

INVESTIGATION OF MOMENTUM AND HEAT TRANSFER IN FLOW PAST SUSPENSIONS OF NON- SPHERICAL PARTICLES

Ze Cao

Dissertation submitted to the faculty of the Virginia Polytechnic Institute and State University in
partial fulfillment of the requirements for the degree of

Doctor of Philosophy

In

Mechanical Engineering

Danesh K. Tafti, Chair

Rui Qiao

Mark R. Paul

Heng Xiao

February 19, 2021

Blacksburg, Virginia, USA

Keywords: PRS simulation, Particulate Flow Systems, drag correlations, lift, torque, heat transfer, ellipsoid, cylinder, preferential orientation

INVESTIGATION OF MOMENTUM AND HEAT TRANSFER IN FLOW PAST SUSPENSIONS OF NON-SPHERICAL PARTICLES

Ze Cao

ABSTRACT

Investigation of momentum and heat transfer between the fluid and solid phase is critical to the study of fluid-particle systems. Dense suspensions are characterized by the solid fraction (ratio of solid volume to total volume), the particle Reynolds number, and the shape of the particle. The behavior of non-spherical particles deviates considerably from spherical particle shapes which have been studied extensively in the literature. Momentum transfer, to first-order, is driven by drag forces experienced by the particles in suspension, followed by lift and lateral forces, and also through the transmission of fluid torque to the particles. The subject of this thesis is a family of prolate ellipsoidal particle geometries of aspect ratios (AR) 2.5, 5.0 and 10.0 at nominal solid fractions (ϕ) between 0.1 and 0.3, and suspensions of cylinders of AR=0.25. The nominal particle Reynolds number (Re) is varied between 10 to 200, representative of fluidized beds. Fluid forces and heat transfer coefficients are obtained numerically by Particle Resolved Simulations (PRS) using the Immersed Boundary Method (IBM). The method enables the calculation of the interstitial flow and pressure field surrounding each particle in suspension leading to the direct integration of fluid forces acting on each particle in the suspension.

A substantial outcome of the research is the development of a new drag force correlation for random suspensions of prolate ellipsoids over the full range of geometries and conditioned studied. In many practical applications, especially as the deviation from the spherical shape

increases, particles are not oriented randomly to the flow direction, resulting in suspensions which have a mean preferential orientation. It is shown that the mean suspension drag varies linearly with the orientation parameter, which varies from -2.0 for particles oriented parallel to the flow direction to 1.0 for particles normal to the flow direction. This result is significant as it allows easy calculation of drag force for suspension with any preferential orientation.

The heat transfer coefficient or Nusselt number is investigated for prolate ellipsoid suspensions. Significantly, two methods of calculating the heat transfer coefficient in the literature are reconciled and it is established that one asymptotes to the other. It is also established that unlike the drag force, at low Reynolds number the suspension mean heat transfer coefficient is very sensitive to the spatial distribution of particles or local-to-particle solid fractions. For the same mean solid fraction, suspensions dominated by particle clusters or high local solid fractions can exhibit Nusselt numbers which are lower than the minimum Nusselt number imposed by pure conduction on a single particle in isolation. This results from the dominant effect of thermal wakes at low Reynolds numbers. As the Reynolds number increases, the effect of particle clusters on heat transfer becomes less consequential.

For the 0.25 aspect ratio cylinder, it was found that while existing correlations under predicted the drag forces, a sinusoidal function $F_{d,\theta} = F_{d,\theta=0^\circ} + (F_{d,\theta=90^\circ} - F_{d,\theta=0^\circ})\sin(\theta)$ captured the variation of normalized drag with respect to inclination angle over the range $10 \leq Re \leq 300$ and $0 \leq \varphi \leq 0.3$. Further the mean ensemble drag followed $F_d = F_{d,\theta=0^\circ} + \frac{1}{2}(F_{d,\theta=90^\circ} - F_{d,\theta=0^\circ})$. It was shown that lift forces were between 20% to 80% of drag forces and could not be neglected in models of fluid-particle interaction forces. Comparing the pitching fluid torque to collision torque during an elastic collision showed that as the particle equivalent diameter, density, and

collision velocities decreased, fluid torque could be of the same order of magnitude as collisional torque and it too could not be neglected from models of particle transport in suspensions.

INVESTIGATION OF MOMENTUM AND HEAT TRANSFER IN FLOW PAST SUSPENSIONS OF NON-SPHERICAL PARTICLES

Ze Cao

GENERAL AUDIENCE ABSTRACT

Momentum and heat exchange between the fluids (air, water...) and suspensions of solid particles plays a critical role in power generation, chemical processing plants, pharmaceuticals, in the environment, and many other applications. One of the key components in momentum exchange are the forces felt by the particles in the suspension due to the flow of the fluid around them and the amount of heat the fluid can transfer to or from the particles. The fluid forces and heat transfer depend on many factors, chief among them being the properties of the fluid (density, viscosity, thermal properties) and the properties of the particles in the suspension (size, shape, density, thermal properties, concentration). This introduces a wide range of parameters that have the potential to affect the way the fluid and particles behave and move.

Experimental measurements are very difficult and expensive to conduct in these systems and computational modeling can play a key role in characterization. For accuracy, computational models have to have the correct physical laws encoded in the software. The objective of this thesis is to use very high-fidelity computer models to characterize the forces and heat transfer under different conditions to develop general formulas or correlations which can then be used in less expensive computer models. Three basic particle shapes are considered in this study, a sphere, a disk like cylindrical particles, and particles of ellipsoidal shapes. More specifically, Particle Resolved Simulations of flow through suspensions of ellipsoids with aspect ratio of 2.5, 5, 10 and

cylinders with aspect ratio of 0.25 are performed. The Reynolds number range covered is [10, 200] for ellipsoids and [10, 300] for cylinders with solid fraction range of [0.1, 0.3]. New fluid drag force correlations are proposed for the ellipsoid and cylinder suspensions, respectively, and heat transfer behavior is also investigated.

Table of Contents

List of Tables	xvii
Chapter 1	1
Introduction	1
Chapter 2	6
Development of Drag Correlation for Suspensions of Ellipsoidal Particles	6
2.1. ABSTRACT	6
2.2. INTRODUCTION.....	6
2.3. NUMERICAL METHOD AND SIMULATION SETUP	9
2.3.1. Governing equations	9
2.3.2. Particle Geometry and Immersed Boundary Method.....	10
2.3.3. Computational domain and background mesh	13
2.3.4. Generation of particle suspension.....	14
2.3.5. Pre-processing of the drag data	17
2.4. RESULTS AND DISCUSSION.....	18
2.4.1. Drag results and comparison with literature	18
2.4.2. Development of mean drag correlation	28
2.5. SUMMARY AND CONCLUSIONS	36
2.6. ACKNOWLEDGEMENTS	37
Chapter 3	38
Modeling Drag force in ellipsoidal particle suspensions with preferential orientation	38
3.1. ABSTRACT	38
3.2. INTRODUCTION.....	38

3.3.	NUMERICAL METHOD AND SIMULATION SETUP	42
3.3.1.	Governing equations	42
3.3.2.	Particle Geometry and Immersed Boundary Method.....	44
3.3.3.	Computational domain and mesh	47
3.3.4.	Generation of Particle Suspension	48
3.3.5.	Definition of Orientational Order Parameter	49
3.4.	RESULTS AND DISCUSSION.....	51
3.4.1.	Analysis of pressure and velocity distribution at different Re , φ and S	51
3.4.2.	Fully-Developed Drag force	55
3.4.3.	Variation of Drag Force with Orientation Angle at Different S	57
3.4.4.	Variation of Ensemble Mean Drag Force with S value of the suspension.....	61
3.4.5.	Contribution of Pressure and Viscous Drag forces	65
3.4.6.	Effect of Ellipsoid Aspect Ratio.....	67
3.5.	SUMMARY AND CONCLUSIONS	69
3.6.	ACKNOWLEDGEMENTS	70
	Chapter 4	71
	Convective Heat Transfer in suspensions of prolate ellipsoids.....	71
4.1.	Abstract.....	71
4.2.	Introduction.....	71
4.3.	Numerical method and simulation setup	74
4.3.1.	Governing equations.....	74
4.3.2.	Particle generation and immersed boundary method (IBM)	76
4.3.3.	Simulation setup	77
4.3.4.	Nusselt number definitions.....	80
4.3.5.	Grid independency study and validation	83

4.4.	Results and Discussion	85
4.4.1.	Flow and Thermal fields within particle suspensions	85
4.4.2.	Nusselt number predictions	88
4.4.3.	Comparison with correlations and past results	95
4.5.	Conclusions.....	100
4.6.	ACKNOWLEDGEMENTS	101
	Chapter 5	102
	Fluid forces and torques in suspensions of oblate cylinders with aspect ratio 1:4	102
5.1.	ABSTRACT.....	102
5.2.	INTRODUCTION.....	102
5.3.	SIMULATION METHOD AND SETUP.....	106
5.3.1.	Governing Equations	106
5.3.2.	Particle Definition and Immersed Boundary Method.....	107
5.3.3.	Background Grid and Particle Suspension Generation	111
5.4.	RESULTS AND DISCUSSION	115
5.4.1.	Pre-processing of PRS Results	115
5.4.2.	Analysis of Suspension Drag Force.....	116
5.4.3.	Parameterizing Non-spherical Particles.....	128
5.4.4.	Analysis of Lift, Lateral Forces and Torque.....	132
5.5.	CONCLUSIONS.....	141
5.6.	ACKNOWLEDGEMENTS	142
	References.....	143
	Appendix A	154
	Investigation of drag, lift and torque for fluid flow past a low aspect ratio (1:4) cylinder	154
	Abstract.....	154

Introduction and Literature Review	155
Geometry, Governing Equations, and Numerical Method	158
Object geometry model.....	158
Computational domain and boundary conditions	159
Governing equations and computational method	160
Grid independence study and validation.....	166
Results and Discussion	170
Flow Characteristics.....	170
Drag Coefficient.....	175
Lift coefficient	180
Pitching Torque Coefficient.....	186
Summary and Conclusion.....	188
Acknowledgements.....	189

List of Figures

Figure 2.1. Surface meshes of different particles that are investigated	12
Figure 2.2. Inclination angle of ellipsoid used to define orientation.	12
Figure 2.3. Computational domain and boundary conditions.....	13
Figure 2.4. Randomly placed particles in the computational domain.....	14
Figure 2.5. Variation of normalized particle count with inclination angle for AR10 suspensions	17
Figure 2.6. Drag force on AR5 particles in the suspension at $Re=10$, $\varphi = 0.1$, with respect to their x location.....	18
Figure 2.7. Comparison of drag force between PRS results and correlations in literature for AR2.5 ellipsoid suspensions. H: Holzer[1], O: Ouchene[11], F: Di Felice[21], T: Tenneti[22], R: Rong[25].	24
Figure 2.8. Comparison of drag force between PRS results and correlations in literature for AR10 ellipsoid suspensions. H: Holzer[1], O: Ouchene[11], F: Felice[21], T: Tenneti[22], R: Rong[25].	25
Figure 2.9. Flow field of AR2.5 and AR10 ellipsoid suspension at $Re = 10$, $\varphi = 0.1$	26
Figure 2.10. Ratio between suspension and isolated particle mean drag force (Light blue: Sphere; Red: AR2.5 Ellipsoid; Blue: AR5 Ellipsoid; Green: AR10 Ellipsoid).....	28
Figure 2.11. Comparison of ensemble mean drag force between developed correlation {Fd0 - Eqn 2.10} (Solid lines) and PRS results (Symbols). Spherical particle correlation of Tenneti et al. [22] (Dashed lines) is also shown for comparison; Green: Sphere; Blue: AR2.5; Grey: AR5; Orange: AR10.	31

Figure 2.12. Comparison of drag force dependence on inclination using drag correlation {Ouchene (Table 2.2), $F_{d0, \theta}$ + Eqn. 2.10} with PRS results.	33
Figure 2.13. Comparison of drag force dependence on inclination using new drag correlation {Ouchene (Table 2.2), $F_{d0, \theta}$ + Eqn. 12} with PRS results.	36
Fig. 3. 1. Particle surface mesh and definition of inclination angle.....	44
Fig. 3. 2. Computational domain and boundary conditions.....	47
Fig. 3. 3. Ellipsoid suspensions created using the physics engine PhysX.....	48
Fig. 3. 4. z –directional view of suspensions with all particles (a) perpendicular and (c) parallel to the flow and x –directional view of suspensions with all particles (b) perpendicular and (d) parallel to the flow.	51
Fig. 3. 5. Pressure distribution on particle surfaces and x-z mid-plane and u velocity at x-z mid-plane of the flow field with (a-b): $S = -2.0$, (c-d): $S = 0.21$ and (e-f): $S = 1$	52
Fig. 3. 6 Distribution of u' at different Re and φ of randomly oriented suspensions.....	54
Fig. 3. 7. PDF distribution of u' at different Re, φ and S.....	55
Fig. 3. 8. Drag force on individual ellipsoids in the suspension (a) original data (b) after filtering out data from ellipsoids near inlet and outlet regions.	57
Fig. 3. 9. Variation of drag force on particles in the suspension at Re = 10.....	59
Fig. 3. 10. Variation of drag force on particles in the suspension at Re=200.....	60
Fig. 3. 11. Variation of ensemble mean drag force with respect to S value of suspension at Re = 50.....	63
Fig. 3. 12. Variation of ensemble mean drag force with respect to S value of suspension at Re = 10.....	64

Fig. 3. 13. Variation of ensemble mean drag force with respect to S value of suspension at $Re = 200$	65
Fig. 3. 14. Variation of ensemble mean pressure and viscous drag force with respect to S value of suspension.....	67
Fig. 3. 15. Variation of ensemble mean drag force with respect to S value of aspect ratio 2.5 ellipsoidal suspension. Symbols: PRS predictions; dash line: linear fit between $S = -2$ and 1.0.	68
Fig. 4. 1. Surface meshes of ellipsoid with aspect ratio of 2.5, 5 and 10.....	76
Fig. 4. 2. 3D view of the computational domain	78
Fig. 4. 3. Void fraction and average inclination angle distribution of particles along x –direction. (Dash lines and empty symbols represent suspensions of He and Tafti [53] for AR2.5 particles.)	79
Fig. 4. 4. Validation of Nusselt number for an isolated sphere in uniform flow.....	85
Fig. 4. 5. Flow velocity and temperature fluctuations within AR10 ellipsoid suspensions.....	87
Fig. 4. 6. Variation of $T_{mf}(x)$ and T_{msx} in suspensions of AR2.5(a-b) AR10 ellipsoids (c-d)..	89
Fig. 4. 7. NuA for ellipsoid suspensions using results from one (AR2.5) and two (AR5 and AR10) independent random particle arrangements.	91
Fig. 4. 8. NuB for AR10 ellipsoid suspensions for $\varphi = 0.2$ with corresponding PDF distribution. Dash line shows the mean values in (b) and (d).	92
Fig. 4. 9. Variation of NuB of AR10 ellipsoid suspensions versus shell size, δ	94
Fig. 4. 10. Comparison of NuA and NuB for AR2.5 (a-c), AR5 (d-f) and AR10 (g-i) ellipsoid suspensions at different Re and φ	95
Fig. 4. 11. Comparison of predictions with correlation of Chen and Muller [62]......	96

Fig. 4. 12. Distribution of $Nu_A(x')$ for different particle suspensions at $Re=10$ and $\varphi = 0.1$	98
Fig. 4. 13. Comparison between present AR2.5 suspension and that of He and Tafti [53] (left: $\varphi = 0.1$, right: $\varphi = 0.3$).....	99
Fig. 4. 14. Comparison of individual particle normalized drag between present suspension and that of He and Tafti [53] at $Re=10$ and $\varphi = 0.1$. Normalization is done with Stokes drag on an equivalent diameter sphere.	100
Fig. 5. 1. Particle geometry with local coordinate system and surface mesh.....	108
Fig. 5. 2. 3D computational domain	112
Fig. 5. 3. 3D view of the particle suspension in the computational domain. Every fifth grid line is shown.....	113
Fig. 5. 4. Normalized orientation distribution of different suspensions.	114
Fig. 5. 5. Variation of drag force on particles at different x- locations.	116
Fig. 5. 6. (a) Variation of ensemble mean drag force for different Re and φ . (b) Comparison of pressure drag (dash line) and viscous drag (dash-dot line). (Red: $\varphi = 0.1$; Green: $\varphi = 0.2$; Blue: $\varphi = 0.3$).....	117
Fig. 5. 7. Comparison of drag force between the PRS results and drag correlations (red: $Re=10$; green: $Re=50$; blue: $Re=100$; grey: $Re=200$; orange: $Re=300$.).....	121
Fig. 5. 8. Comparison of PRS drag force with drag correlations using preferentially aligned suspension. (same color legend as Fig. 5.7).....	122
Fig. 5. 9. Particle distribution and the flow velocity in the two suspensions.....	123
Fig. 5. 10. Comparison between PRS data and developed correlation in Eq. (14)-(16). (for legend see Fig. 7).....	127

Fig. 5. 11. Ensemble mean drag force calculated using Eq. (15) – (17). (Red: $\varphi = 0.1$; Green: $\varphi = 0.2$; Blue: $\varphi = 0.3$).....	128
Fig. 5. 12. Comparison of the particle drag force in AR5 ellipsoid and AR0.25 cylinder suspensions at $Re=200$, $\varphi=0.3$	129
Fig. 5. 13. PDF of u' of the flow in AR5 ellipsoid and AR0.25 cylinder suspensions. $Re = 200$ and $\varphi = 0.3$	130
Fig. 5. 14. PDF of the pressure fluctuation in AR5 ellipsoid and AR0.25 cylinder suspensions. $Re = 200$ and $\varphi = 0.3$	132
Fig. 5. 15. Variation of lift and lateral force on individual AR0.25 cylinders at different Re and φ	133
Fig. 5. 16. Variation of lift force on the AR0.25 cylinders under different Re and φ	134
Fig. 5. 17. Variation of pressure and shear contribution to lift force on AR0.25 cylinders.	135
Fig. 5. 18. Ratio of lift-to-drag force ratio at different Re and φ	136
Fig. 5. 19. Variation of directional torque with inclination angle.....	138
Fig. 5. 20. Variation of pitching torque at different Re and φ	139
Fig. 5. 21. Ratio between fluid torque and collisional torque for different materials.....	140
Fig. A. 1. 3D view of the tablet-like cylinder geometry.....	159
Fig. A. 2. View of the 3D domain and position of the cylinder.....	160
Fig. A. 3. Identification of node type in the background mesh defined in IBM.....	162
Fig. A. 4. Surface Pressure and shear stress (velocity gradient) calculation for force calculation (Left plot presents the pressure and right plot presents the velocity of the probe).....	163
Fig. A. 5. Volume grid (green) distribution in the nearfield and surface mesh (black) distribution.	166
Fig. A. 6. Comparison of drag coefficient from the literature and results derived in this study using both IBM and body conforming mesh.....	169

Fig. A. 7. U-velocity and streamlines of the fluid flow near the cylinder at $Re = 50$ and $\theta = 0^\circ$ to 90°	171
Fig. A. 8. Visualization of vorticity behind the cylinder at $Re=200$	173
Fig. A. 9. Drag coefficient as a function of time at Reynolds number of 200 and 300	174
Fig. A. 10. Percentage contribution of pressure and viscous stresses to total drag under different conditions	177
Fig. A. 11. Drag coefficient on the cylinder.	180
Fig. A. 12. Lift coefficient from pressure and shear at different conditions.....	181
Fig. A. 13. Pressure distribution around the cylinder at $\theta = 45^\circ$	184
Fig. A. 14. Lift coefficient on cylinder.	186
Fig. A. 15. Torque coefficient on the cylinder	187

List of Tables

Table 2.1. Number of particles required under different conditions.....	15
Table 2.2. Drag correlations in literature	20
Table 2.3. New drag correlation for ellipsoids/sphere suspensions under different conditions ...	34
Table 3.1. Percentage mean deviation of orientation dependent drag at $S \approx 0.5$ and ≈ -1.0 compared to a random suspension $S \approx 0.0$	61
Table 4. 1. Geometry and surface grid specification of ellipsoidal particles.....	76
Table 4. 2. Nusselt number ($Nu = h * deq */k *$) prediction for single AR10 ellipsoid in uniform flow at $Re=200$	85
Table 5. 1. Drag correlations in literature.....	118
Table 5. 2. Parameters for Eq. (5.15) and Eq. (5.16).....	127
Table 5. 3 Mechanical properties of the three materials.....	139
Table A. 1. Drag coefficient of the flow past the cylinder at different conditions.....	167
Table A. 2. Comparison of drag coefficient from literature and results in this study based on different methods	169

Chapter 1

Introduction

In the study of dense fluid-particle systems, aside from the particle-particle and particle-wall interactions, the drag force induced by the fluid flow also plays a critical role in governing the motion of particles in the flow. To model such systems, Computational fluid Dynamics (CFD) has become an increasingly important tool for design compared to experiments which are comparatively very expensive to perform. Currently two methods: Two-fluid Model (TFM) and Computational Fluid Dynamics Coupled to Discrete Element Method (CFD-DEM) are frequently implemented to model such systems. The Eulerian-Lagrangian approach, CFD-DEM is not only able to capture the fluid-particle interactions, but also track the location, heat and mass transfer condition of each individual particle in the suspension. Therefore, it has become an important tool for modeling such systems. However, because the particles are treated as point masses and not resolved, accurate drag force and heat transfer correlations are fundamental for accurately predicting the momentum and heat exchange between the fluid and solid phase.

Due to the simplicity of geometry and general applicability, early researchers mainly focused on an isolated spherical particle in the flow and proposed drag correlations for a wide range of Reynolds numbers. As natural and engineered particles possess various geometries, and spherical particle drag correlations may not be able to fulfill the accuracy requirement for drag prediction, investigations of other non-spherical particle geometries including cylinders, ellipsoids, cubes, plates, amongst others, have emerged. Among these many drag correlations in the literature, the drag correlation derived by Hölzer and Sommerfeld [1] has been widely implemented by

numerous researchers. In their correlation, sphericities in different orientations are used to represent orientational and geometry difference of particles in the flow, which theoretically has unlimited applicability to different particle geometries. In particle suspensions, in addition to particle geometry, each particle is surrounded by several other particles and the incoming flow experienced by each particle is affected by nearby particles. These effects are not captured in drag correlations for isolated particles, which has motivated studies in recent years to focus on flow through suspensions of non-spherical particles with different geometries. Among these studies, there is a lack of drag correlations for very elongated ellipsoids and low aspect ratio cylinders, or particle shapes that deviate significantly from the spherical shape. In addition, many researchers have observed that in practical systems, non-spherical particles may have different mean orientational preferences as the flow condition varies. Taking elongated ellipsoids as an example, in packed beds of these ellipsoids, they tend to lie with their rotational symmetry axis perpendicular to the flow maintaining minimum potential energy for the whole system. While in a fluidized bed, their orientation tends to be more randomly distributed. However, the effect of preferential orientation on the drag force experienced by either individual particle or the whole suspension has not been characterized in the literature.

Heat transfer between the fluid and solid phase is another important factor since fluidized bed reactors are usually accompanied by heat exchange in the system. Though an increasing number of heat transfer correlations have emerged in recent years, their applicability is always limited to spherical or near-spherical particle geometries. There are two approaches for heat transfer coefficient calculation in particle suspensions. One defines a fluid mixed-mean temperature for each location in the flow direction and uses the average surface temperature of particles at that location to define the heat transfer coefficient. The other approach defines a body conforming

shell around each particle of interest within which the fluid mean temperature is calculated to derive the heat transfer coefficient of each individual particle in the suspension. However, there is a lack of clarity in the literature regarding the difference or similarity between these two approaches.

Though most studies have focused on deriving drag force correlations, which is by far the most consequential force in spherical systems, other fluid forces such as lift and lateral forces and induced fluid moments or torques could also play a consequential role on the translational and rotational motion of particles. In the literature, rotational motions are almost entirely modeled through particle-particle and particle-wall collisions while fluid force induced torque are never considered, but which could also be playing a substantial role. Therefore, it is worthwhile to estimate the lift, lateral forces, and torques along different directions, and investigating their characteristics under different flow conditions and particle inclination angle (θ) to estimate their relative importance against drag and particle-particle or particle-wall collisional forces.

Motivated by the general lack of research in the literature on fluid forces in non-spherical particle suspensions, the overall objective of this work is to characterize and develop general drag and heat transfer correlations, where appropriate, with applicability to various particle geometries. In addition, the relative importance of lift and torque while modeling the motion of the particles is also investigated.

The following are the main contributions of the current work which are described in Chapters 2 to 5.

- **Chapter 2:** Development of a new drag correlations for prolate ellipsoid suspensions covering aspect ratios ranging from 1 (sphere) to 10 under Reynolds number range of

[10, 200] and solid fraction range of [0.1, 0.3]. This is the only correlation in the literature developed specifically for prolate-ellipsoids over the range of geometries and parameters specified.

- **Chapter 3:** Development of a relationship between drag force and suspension preferential orientation for ellipsoidal particle suspensions of AR2.5 to 10. This reduces the large number of characterizations necessary to calculate drag for an arbitrary orientational parameter to just two characterizations at each Reynolds number and solid fraction for each geometry.
- **Chapter 4:** Heat transfer characterization of ellipsoidal particle geometries of AR2.5 to 10 and establishing the relationship between two methods used in the literature to characterize the heat transfer coefficient. It is also established that the mean suspension Nusselt number, unlike drag force, is very dependent on the local solid fraction around each particle at low Reynolds number.
- **Chapter 5:** Drag, lift, lateral force as well as torques along different directions on both isolated and suspensions of AR0.25 cylinders are also investigated. A new drag correlation is proposed after observing that there is no reliable correlation in the literature that can accurately capture variation of drag force on such particle suspensions. The relative significance of lift, lateral force, and torque are also investigated with the observation that lift and pitching torque play important roles in governing the translational and rotational motion of particles in the flow.

The work described in this dissertation has resulted in the following published and submitted peer-reviewed journal publications:

- **Chapter 2: Cao, Z.,** Tafti, D.K. and Shahnam, M., 2020. Development of drag correlation for suspensions of ellipsoidal particles. *Powder Technology*, 369, pp.298-310.
- **Chapter 3: Cao, Z.,** Tafti, D.K. and Shahnam, M., Modeling drag force in ellipsoidal particle suspensions with preferential orientation. *Powder Technology*, 378, pp.274-287.
- **Chapter 4: Cao, Z.** and Tafti, D.K., Convective Heat Transfer in suspensions of prolate ellipsoids. Submitted to *International journal of mass and heat transfer* in January 2021.
- **Chapter 5: Cao, Z.** and Tafti, D.K., 2020. Fluid forces and torques in suspensions of oblate cylinders with aspect ratio 1: 4. *International Journal of Multiphase Flow*, 131, p.103394.
- **Appendix: Cao, Z.** and Tafti, D.K., 2018. Investigation of drag, lift and torque for fluid flow past a low aspect ratio (1: 4) cylinder. *Computers & Fluids*, 177, pp.123-135.

Chapter 2

Development of Drag Correlation for Suspensions of Ellipsoidal Particles

2.1. ABSTRACT

To model drag the current state-of-the-art is to use isolated non-spherical particle drag correlations modified by a solid fraction correlation that is based on experimental or simulation results of spherical particle suspensions. It is shown that this practice can lead to substantial inaccuracies when the particle geometry deviates significantly from a spherical geometry. In this paper particle resolved simulations (PRS) are conducted for ellipsoids of aspect ratio 5 (AR5) and 10 (AR10) in random suspensions with no preferential orientation. Simulations are performed for a Reynolds number $Re = 10$ to 200, and solid fraction $\varphi = 0.1$ to 0.3 and 0.1 to 0.2 for AR5 and AR10 suspensions, respectively. Combined with PRS data from past studies for spherical particle suspensions and ellipsoids with AR2.5, a drag correlation is developed for the mean drag force in suspension as a function of Re , φ , aspect ratio, and inclination angle θ .

Keywords: Particle suspensions; Particle-Resolved Simulation (PRS); prolate ellipsoids; drag correlation.

2.2. INTRODUCTION

Fluid drag forces acting on particles in suspension are of critical importance for capturing the dynamics of fluid-particle systems accurately. Due to the simplicity of the geometry and general applicability, an isolated spherical particle in the flow field has been widely investigated by a number of researches[2–4] and drag correlations have been derived with applicability to a broad range of Reynolds numbers [5–8]. Recently, with the increase in computational power and maturation of numerical techniques and methods in computational fluid dynamics (CFD), highly

resolved Particle Resolved Simulations (PRS) have been performed for non-spherical particles such as ellipsoids [9–12], cylinders [13–15], cubes [16,17], and other complex shapes. In addition to these works, that focus on a specific or on a series of similar geometries, there also have been attempts in the literature that seek to develop a general correlation that can predict drag force on various non-spherical particles. One of the widely used correlation is that by Hölzer and Sommerfeld [1], who fitted 2061 experimental data points for different particle geometries and proposed a drag correlation with a mean deviation of 14.1%.

Unlike the drag on an isolated particle that has been extensively studied in the literature, there are relatively fewer investigations that focus on particle suspensions. Ergun [18] derived a correlation for pressure drop over packed beds of particles based on a large number of experimental data. However, the accuracy decreases at low solid volume fractions (φ). Thus it is combined with the correlation derived by Wen and Yu [19] for φ less than 0.2. The combined drag model is widely used and provides reasonable drag results for flow through spherical particle suspensions [20]. Another widely used correlation is that derived by Di Felice [21] which is based on previous experiments on particle suspensions. In the last decade, these correlations have been augmented by computational investigations of fluid flow through particle suspensions. These have the added advantage of being able to calculate the flow field around each particle in suspension and hence directly calculate the fluid forces acting on the particle. Tenneti et al. [22] did particle resolved simulations of spherical particle suspensions covering a wide range of solid fractions and Reynolds numbers. They found that after normalization, the drag force due to the fluid viscous effect presents a weak power-law dependence on Reynolds number which disproved the previous notion that normalized viscous drag is independent of Reynolds number [23]. They also showed that the normalized pressure drag force varied linearly with Reynolds number. Using Lattice Boltzmann

simulations of spherical particle suspensions, Rong et al. [24] observed that drag force on individual particles fluctuated randomly around the mean with an approximate Gaussian distribution. Similar investigations have also been conducted for specific non-spherical particle suspensions. Rong et al. [25] did Lattice Boltzmann simulation for both oblate and prolate ellipsoid suspensions and based on the drag model of Di Felice [21], they proposed a new correlation that takes the variation in particle geometry into account. Chen and Müller [26] simulated flow in cubic particle suspensions and proposed a drag closure for the specific geometry. To evaluate the accuracy of drag correlations in the literature, He et al. [27,28] investigated fluid flow through suspensions of spheres and ellipsoids with aspect ratio of 2.5 by performing particle resolved simulations and found that drag correlation for isolated particles in the flow proposed by Hölzer and Sommerfeld [1] combined with particle suspension correlation of Tenneti et al. [22] provided drag results on the particles in the suspension with least deviation from the simulation data.

For CFD combined with point-force models for particles such as the discrete element method (DEM), the general lack of available drag models for non-spherical particle suspensions is compensated for by combining drag correlations for isolated non-spherical particle in the flow with a correlation that accounts for the effect of particle density or solid fraction, φ . This has been implemented for suspensions of cylinders [29–31], ellipsoids [32] and cuboids [33]. However, the experimental results of Vollmari et al. [33] observed that though such combinations of drag correlations can reasonably estimate the drag force on suspensions of spheres or particle geometries similar to spheres (sphericity close to unity), much poorer accuracy was found while predicting drag force on suspensions of particles that deviated significantly from a spherical geometry (such as very elongated or flat geometries).

The objective of this paper is to develop a general correlation for prolate ellipsoidal particles ranging in aspect ratios equal to unity (sphere) to 10. In this work, particle resolved simulations are performed for fluid flow through suspensions of prolate ellipsoids with aspect ratio of 10 and 5 (abbreviated as AR5 and AR10 ellipsoid), which is defined as the ratio between length of the particle along the axis of rotational symmetry and the diameter of the equatorial plane. Firstly, the applicability of drag correlations in the literature is evaluated by comparing with our simulation results. Then using drag data for spheres and ellipsoids of AR2.5 from our previous work [27,28], a new drag correlation is proposed that covers ellipsoids in suspension with aspect ratios from 1 to 10, Reynolds number from 10 to 200 and low to intermediate solid fractions.

2.3. NUMERICAL METHOD AND SIMULATION SETUP

2.3.1. Governing equations

The governing flow equations in the particle suspension are given by the incompressible, constant property, continuity and momentum equations. These are solved in the framework of in-house CFD code – GenIDLEST (Generalized Incompressible Direct and Large Eddy Simulation of Turbulence) with the immersed boundary method (IBM). The dimensionless forms of the governing equations have the following form:

Continuity:

$$\frac{\partial u_i}{\partial x_i} = 0 \quad (2.1)$$

Momentum:

$$\frac{\partial u_i}{\partial t} + \frac{\partial}{\partial x_j} (u_i u_j) = -\frac{1}{\rho} \frac{\partial p}{\partial x_i} + \frac{\partial}{\partial x_j} \left(\frac{1}{Re} \left(\frac{\partial u_i}{\partial x_j} \right) \right) \quad (2.2)$$

The above equations are non-dimensionalized by:

$$u_i = \frac{u_i^*}{u_{ref}^*}; \quad x_i = \frac{x_i^*}{l_{ref}^*}; \quad p = \frac{p^* - p_{ref}^*}{\rho_{ref}^* u_{ref}^{*2}};$$

$$\rho = \frac{\rho^*}{\rho_{ref}^*}; \quad \mu = \frac{\mu^*}{\mu_{ref}^*}; \quad Re = \frac{\rho_{ref}^* u_{ref}^* l_{ref}^*}{\mu_{ref}^*} \quad (2.3)$$

where the superscript (*) represents dimensional variables. For the constant property assumption, $\rho = \mu = 1$. In the non-dimensionalization process, the superficial velocity of the flow U_s^* is taken as u_{ref}^* and l_{ref}^* is the equivalent diameter of an equal volume sphere.

The equations are solved using a collocated or non-staggered finite-volume formulation with second-order central (SOC) difference discretization [34,35]. The variables including flow velocities, pressure and temperature are calculated and stored at computational cell center while mass fluxes are calculated and stored at the cell faces. A second order predictor-corrector formulation is implemented for time integration: first an intermediate velocity field is calculated in the predictor step, then a corrector step is carried out based on the calculated pressure field to satisfy the discrete continuity.

2.3.2. Particle Geometry and Immersed Boundary Method

In the present work, simulation for suspensions of ellipsoid with aspect ratio of 5 and 10 are performed and for deriving the new drag correlation, drag force data for spheres and ellipsoids with AR of 2.5 by He et al. [27,28] are also included to extend the applicability of the drag

correlation for different particle geometries. The body conforming surface meshes of the particles investigated are shown in Figure 2.1. From (a) to (d) are sphere, ellipsoid with AR2.5, ellipsoid with AR5, and ellipsoid with AR10.

Particle surfaces are resolved by the Immersed Boundary Method (IBM). Particle surfaces are defined by approximately 4000 (AR5 ellipsoid) and 7500 (AR10 ellipsoid) triangular elements. The much greater number of surface elements of the AR10 ellipsoid results from its relatively larger surface area and surface curvature. A sharp interface indirect forcing method is used for the IBM in which fluid nodes adjoining the particle surface are identified as fluid IB nodes. Boundary conditions on the immersed boundary (IB) surface are implemented in the scheme by using probes normal to the IB surface passing through the IB nodes to determine the appropriate value at the fluid IB node to satisfy the boundary condition at the surface. Details of this implementation and validation can be found in the work of Nagendra et al. [36]. Further, grid independency for non-spherical particles in isolation and suspensions can be found in Cao and Tafti [37], and He et al. [27,28].

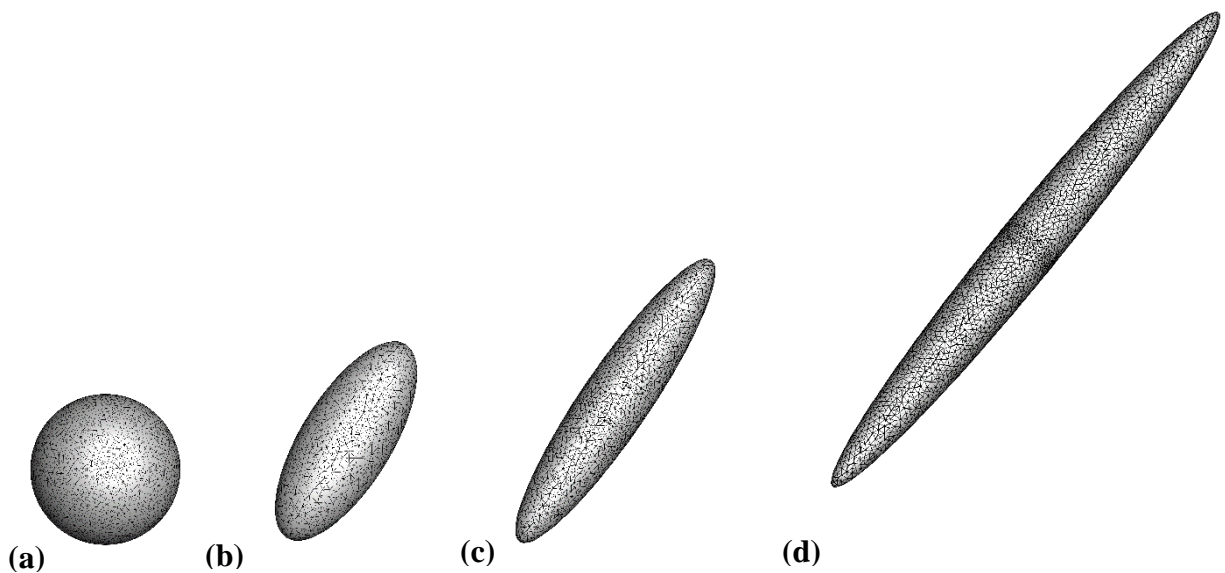


Figure 2.1. Surface meshes of different particles that are investigated

Forces on each individual surface element are calculated by:

$$\vec{F}_e^* = \vec{F}_{viscous}^* + \vec{F}_{pressure}^* \quad (2.4)$$

And the total fluid-particle interaction force on each particle is calculated using:

$$\vec{F}_s^* = \sum_{i=1}^n \vec{F}_{e,i}^* \quad (2.5)$$

The drag force, which is of main interest in this study, is defined as the component of the fluid-particle interaction force in the mean flow direction. To find the effect of particle orientation with respect to the mean flow direction on drag force experienced by each particle, the angle between the particle's rotational symmetry axis and the mean flow direction as shown in Figure 2.2 is used as the singular inclination angle to describe the orientation.

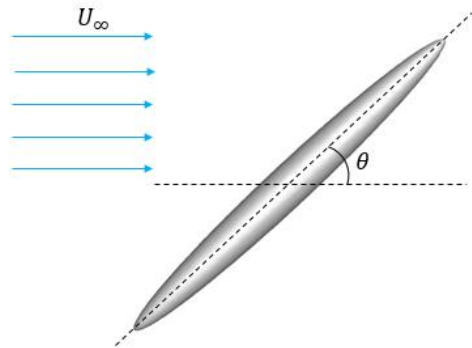


Figure 2.2. Inclination angle of ellipsoid used to define orientation.

2.3.3. Computational domain and background mesh

In this work, a rectangular computational domain is generated as is shown in Figure 2.3. The total length of the domain in the x- or flow direction is 30 non-dimensional units, out of which the ellipsoids are placed in the in the region of length 15 units, 5 units from the inlet plane. The size of the domain is kept to 10 units in the cross-stream, y- and lateral, z-directions. The inlet velocity is set to the target superficial velocity, $u_{ref}^* = U_s^*$ or $U_\infty = 1.0$ in Figure 2.3. At the outlet, outflow or zero gradient conditions are imposed on the velocity and pressure fields. Periodic boundary conditions are specified in the y- and z- directions to simulate an infinite extent of the particle suspension in both directions.

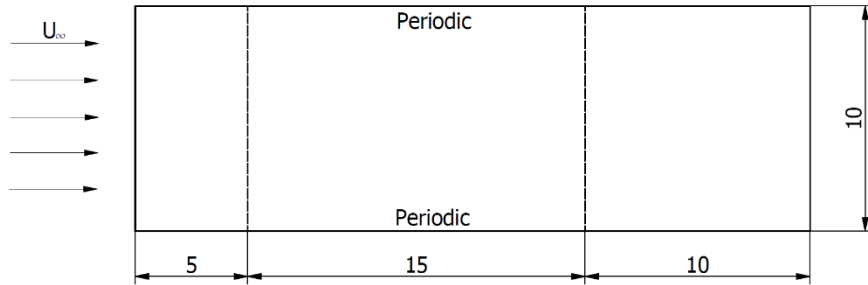


Figure 2.3. Computational domain and boundary conditions

To supplement past grid independency studies [27,28,37], an additional grid independency study is conducted in this study for AR10 particles because of their extreme nature at the highest Reynolds number of 200 at a solid fraction of 0.20. Based on our previous investigations, two of the finest mesh spacings were investigated: 40 and 50 grid cells per equivalent spherical diameter, amounting to a total grid size of 128 and 250 million computational cells in the domain, respectively. With this study it is established that the calculated drag force on over 97% of the

particles had deviations of less than 2.5% between the two grid resolutions while the mean drag force over all particles in the suspension had a deviation of 1.0%, ascertaining grid convergence and the adequacy of the $\frac{1}{40}$ grid spacing. Thus all reported results are on a $\frac{1}{40}$ grid.

2.3.4. Generation of particle suspension

To create the suspension of particles without overlap or orientational preference, a physical simulation engine – PhysX by Nvidia [38] is employed. During this stage each particle defined by a coarse surface mesh is introduced into the packing box with a random velocity. As more particles are introduced into the packing box, overlaps are detected by the PhysX engine and the collision operator moves the particles apart till no overlaps exist in the system. This process is repeated till the desired solid fraction is reached and the system is in a stable state with no overlaps. Figure 2.4 shows an example of the AR10 particle suspension placed in the computational domain.

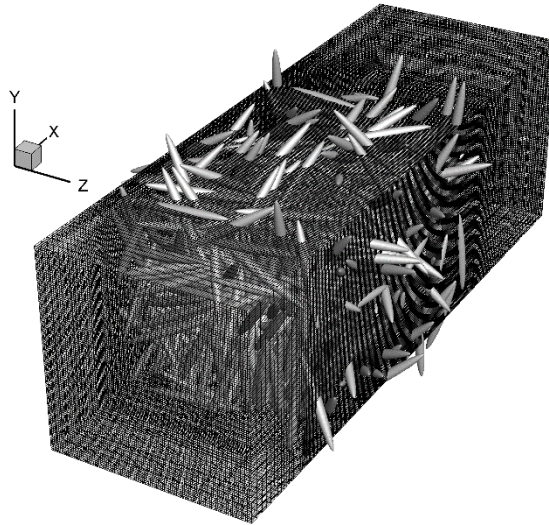


Figure 2.4. Randomly placed particles in the computational domain.

To reach a desired solid volume fraction, with the pre-set region that accommodates the particles, specific number of particles are required, which is calculated by:

$$N = \frac{6\varphi V}{\pi d_p^3} \quad (6)$$

In the equation, N is the total number of particles in the domain. φ is the desired solid fraction and V is the volume of the computational domain with a dimension of $15 \times 10 \times 10$ in x-y-z-directions, respectively. The number of particles for each solid fraction for different ellipsoid shapes are presented in Table 2.1. The difference in the number of particles for the same φ is due to the different domain size implemented in the study of He et al. [27], which had a dimension of $10 \times 10 \times 10$. In this study, two separate and distinct random suspensions are generated for each solid fraction and particle geometry. Because of the large aspect ratio and the elongated shape of the AR10 particles, it was not possible to construct the suspension for $\varphi > 0.2$ without introducing preferential orientation of the particles. Since the objective of this study was to investigate random arrangements, the solid fraction of AR10 particles was limited to 0.2.

Table 2.1. Number of particles required under different conditions

φ	0.1	0.15	0.2	0.3	0.35
Sphere	191	-	382	573	669
AR2.5 ellipsoid	191	-	382	573	669
AR5 ellipsoid	286	-	573	859	-
AR10 ellipsoid	286	430	573	-	-

To ascertain that the AR10 particles are indeed arranged in a random arrangement we make use of the following relationship for a random distribution of ellipsoids

$$\frac{N_{\Delta\theta}}{N_{80^\circ \leq \theta \leq 90^\circ}} \approx \sin\theta \quad (2.7)$$

Here $N_{\Delta\theta}$ are the number of particles present in the interval $\Delta\theta = 10^\circ$ about angle θ , and $N_{80^\circ \leq \theta \leq 90^\circ}$ are the number of particles in the interval $80^\circ \leq \theta \leq 90^\circ$. The expression states that in a random arrangement the number of particles in an interval centered at θ when normalized by the number of particles in an interval near $\theta = 90^\circ$ should approximately equal to $\sin\theta$ [39]. The distribution of the normalized particle count for AR10 ellipsoids with respect to inclination angle is shown in Figure 2.5. In general, the distribution follows the reference sinusoidal curve for the three solid fractions investigated. The larger deviation at low solid fraction is a result of the less number of particles used for $\varphi = 0.1$. A similar distribution is also present for AR5 ellipsoids.

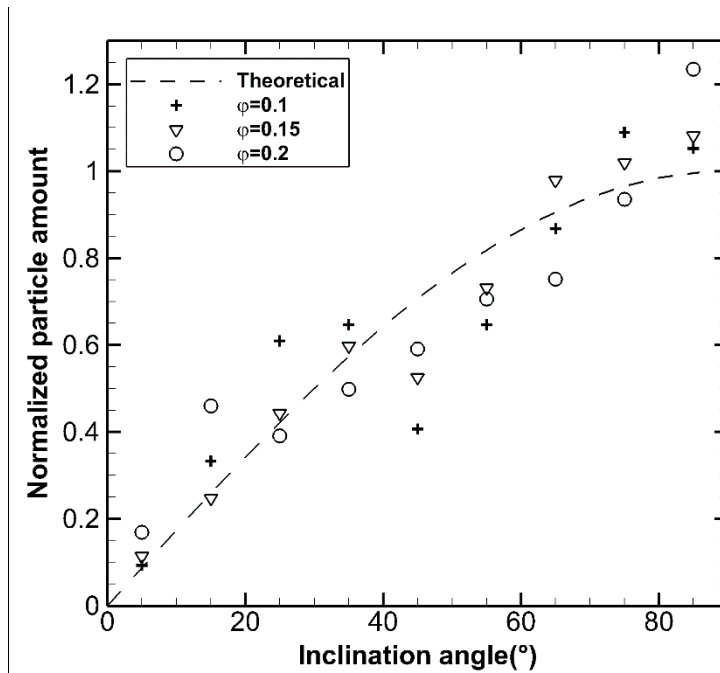


Figure 2.5. Variation of normalized particle count with inclination angle for AR10 suspensions

2.3.5. Pre-processing of the drag data

The drag forces are presented after being normalized by the Stokes drag on an isolated sphere of equivalent diameter, and is calculated as:

$$F_D = \frac{F_D^*}{3\pi\mu^*D_{eq}^*U_\infty^*} \quad (2.8)$$

Due to the developing nature of the flow in the x-direction, flow entrance and exit into and out of the particle suspension (located between $x=5$ and 20) influence the drag forces which will behave differently than in the core of the suspension. Both, upstream effects at the entrance to the suspension and downstream effects at the exit from the suspension will impact the drag forces of particles located near the entrance and exit, respectively. Figure 2.6 shows an example of the normalized drag force on individual particles in the suspension for AR5, at $Re=10$ and $\varphi = 0.1$. The symbols represent the x-location of the particle center and it can be noted that drag on particles near the two ends exhibit different trends compared to the particles in the middle. Therefore, results are only presented for particles that lie in the core of the suspension devoid of entrance and exit effects whose centers lie between $x = 7.5$ to 17.5 for this case. This requirement reduces the sample size, however it is noted that the minimum particle sample size over all the solid fractions still consists of 310 particles over two random distributions which were simulated for each case.

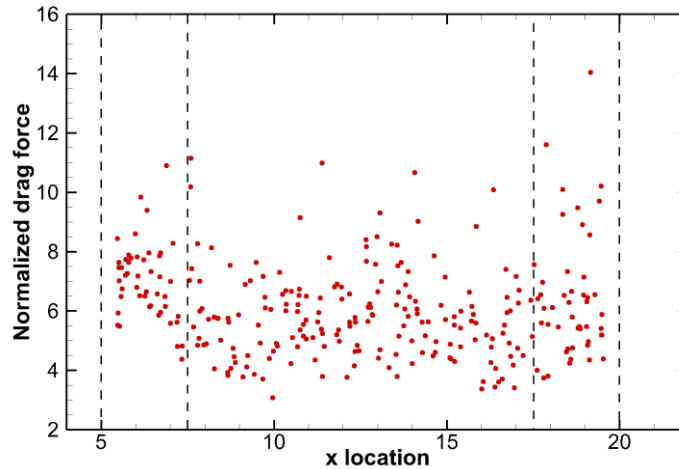


Figure 2.6. Drag force on AR5 particles in the suspension at $Re=10$, $\varphi = 0.1$, with respect to their x location

2.4. RESULTS AND DISCUSSION

2.4.1. Drag results and comparison with literature

In coarse grained simulations of particle mixtures, the particles are modeled as point masses and typically require a model for the drag force. For non-spherical particles in suspension, the drag force is calculated by using the drag force on an isolated particle at different orientations to the flow (*isolated particle drag correlation*) combined with a correlation that accounts for the solid volume fraction (*suspension drag correlation*). In the study of Zhou et al. [32,40], a combination of the isolated particle drag correlation of Hölzer and Sommerfeld [1] and the suspension correlation of Di Felice [21] that takes φ into consideration is used to calculate the drag force on ellipsoids with aspect ratio from 0.5 to 3.5 in the suspension. These correlations are listed in Table 2.2. Due to the general applicability of Hölzer and Sommerfeld's [1] correlation to different particle geometries, this combination has also been used for other particle geometries such as

cylinders [32,41], rod-like particles [30], cuboids [33] and plate-like particles [33]. Among these studies, Vollmari et al. [33] not only did simulations but also experiments for suspensions of particles with different geometries. On comparison, they observed that use of the combined isolated particle plus suspension correlation estimated the pressure drop in the suspension with reasonable accuracy for particles that had geometries similar to a sphere. Particles whose shape deviated considerably from that of a sphere, like cylinders with aspect ratio (height/diameter) 3.5 and elongated cuboids with dimension of $2mm \times 3mm \times 11mm$, showed significant deviation from the experimental results. Their study demonstrated the inadequacy of estimating drag for particles in suspension when the geometry deviated substantially from a spherical geometry.

In addition to these there have been other studies in the literature to either build isolated non-spherical particle correlations at different orientations and Reynolds numbers as well as for particles in suspension. Recently Ouchene et al. (referred to as Ouchene henceforth) [11] did particle resolved simulations (PRS) for isolated ellipsoids with aspect ratios from 1.25 to 32 and derived a drag correlation with applicability in the Reynolds number of up to 240. Tenneti et al. (referred to as Tenneti henceforth) [22] proposed a correlation for spherical particles in suspension based on simulation results. Their drag model for suspensions when combined with the isolated particle drag model of Hölzer and Sommerfeld [1] was found to agree well with simulation results of He et al. [27] for ellipsoids with aspect ratio 2.5. Rong et al. [25] using LBM of flow through suspensions of ellipsoids with aspect ratio from 0.25 to 4 proposed a correlation based on the drag model of Di Felice [21], by considering not only Reynolds number and solid fraction, but also the sphericity of the particle. Drag correlations derived from these studies are listed in Table 2.2. In these correlations, γ represents sphericity of the particle, which is defined as the ratio between surface area of the volume equivalent sphere and the surface area of the non-spherical particle of

interest. γ_{\perp} and γ_{\parallel} respectively are the crosswise and lengthwise sphericity defined by Hölzer and Sommerfeld [1]. ω is the aspect ratio of the ellipsoid and C_D is the drag coefficient for fluid flow over an isolated particle. Both F_{iso} and F_{d0} represents drag force under the condition that there is only one particle in the flow. It is noted that the suspension correlations of Di Felice [21] and Rong et al. [25] do not include the contribution of the mean pressure gradient in the suspension to the drag force, whereas Tenneti et al. [22] include the effect of the change in mean pressure towards the drag force. Since the current PRS calculations and those done previously by He et al. [27,28] include the contribution of the mean pressure gradient in the suspension towards the drag force, during application and use the correlations of Di Felice and Rong et al. are divided by $(1 - \phi)$ for equivalency with the PRS data and the correlation of Tenneti et al.

Table 2.2. Drag correlations in literature

Author	Drag correlation	Applicability
Hölzer and Sommerfeld[1]	$c_D = \frac{8}{Re} \frac{1}{\sqrt{\gamma_{\parallel}}} + \frac{16}{Re} \frac{1}{\sqrt{\gamma}} + \frac{3}{\sqrt{Re}} \frac{1}{\gamma^{\frac{3}{4}}} + 0.42 \times 10^{0.4(-\log \gamma)^{0.2}} \frac{1}{\gamma_{\perp}}$ $F_{d0} = c_D \cdot \frac{1}{2} \rho U_{\infty} \cdot \frac{\pi D_{eq}^2}{4}$	Single particle in the flow field with arbitrary geometry
Ouchene et al. [42]	$c_D = c_{D,\alpha=0^{\circ}} + (c_{D,\alpha=90^{\circ}} - c_{D,\alpha=0^{\circ}}) \cdot \sin^2(\alpha),$ $c_{D,\alpha=0^{\circ}} = \frac{24}{Re} [K_{\alpha=0^{\circ}}(\omega) + 0.15\omega^{-0.80} Re^{0.687} + (\omega - 1)^{0.63} \frac{Re^{0.41}}{24}],$	$Re < 240,$ $\omega \in [1, 32],$ Single ellipsoid in the flow

$$c_{D,\alpha=90^\circ} = \frac{24}{Re} [K_{\alpha=90^\circ}(\omega) + 0.15\omega^{-0.54}Re^{0.687} + \omega^{1.043}(\omega - 1)^{-0.17} \frac{Re^{0.65}}{24}],$$

$$K_{\alpha=0^\circ}(\omega) = \left(\frac{8}{3}\right) \omega^{-\frac{1}{3}} \left[\frac{-2\omega}{\omega^2-1} + \frac{2\omega^2-1}{(\omega^2-1)^{\frac{3}{2}}} \ln \left(\frac{\omega+\sqrt{\omega^2-1}}{\omega-\sqrt{\omega^2-1}} \right) \right]^{-1},$$

$$K_{\alpha=90^\circ}(\omega) = \left(\frac{8}{3}\right) \omega^{-\frac{1}{3}} \left[\frac{\omega}{\omega^2-1} + \frac{2\omega^2-3}{(\omega^2-1)^{\frac{3}{2}}} \ln(\omega + \sqrt{\omega^2-1}) \right]^{-1}.$$

$$F_{d0} = c_D \cdot \frac{1}{2} \rho U_\infty \cdot \frac{\pi D_{eq}^2}{4}$$

Di Felice[21]	$F_d = F_{d0} \varepsilon^{-\chi}$ (ε : void fraction, equals to $(1 - \varphi)$), $\chi = 3.7 - 0.65 \exp \left[-\frac{(1.5 - \log Re)^2}{2} \right].$	Packed beds of spherical particles validated for particle similar to sphere.
Tenneti et al. [22]	$F(\varphi, Re) = \frac{F_{iso}}{(1-\varphi)^3} + F_\varphi(\varphi) + F_{\varphi,Re}(\varphi, Re),$ $F_\varphi(\varphi) = \frac{5.81\varphi}{(1-\varphi)^3} + 0.48 \frac{\varphi^{1/3}}{(1-\varphi)^4},$ $F_{\varphi,Re}(\varphi, Re) = \varphi^3 Re \left(0.95 + \frac{0.61\varphi^3}{(1-\varphi)^2} \right).$	$0.01 \leq Re \leq 300,$ $0.1 \leq \varphi \leq 0.5,$ Spherical particle suspensions.
Rong et al. [25]	$F_d = F_{d0} \varepsilon^{-\beta(\varepsilon, Re) - \lambda(\gamma, Re)},$ $\beta(\varepsilon, Re) = 2.65(\varepsilon + 1) - (5.3 - 3.5\varepsilon) \varepsilon^2 \exp \left[-\frac{1}{2} (1.5 - \log Re)^2 \right],$	Packed beds of ellipsoids, $\omega \in [0.25, 4].$

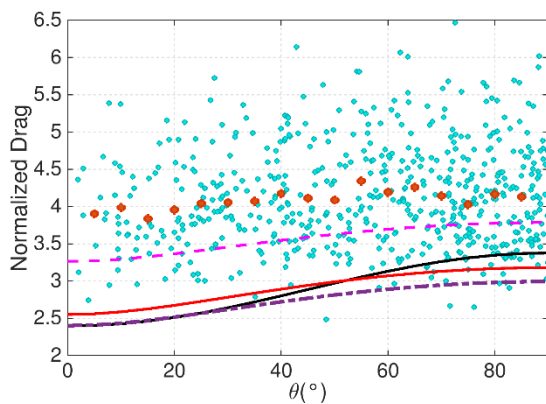
$$\lambda(\gamma, Re) = (1 - \gamma)\{B - A \cdot \exp[-0.5(3.5 - \log Re)^2]\},$$

$$A = 39\gamma - 20.6,$$

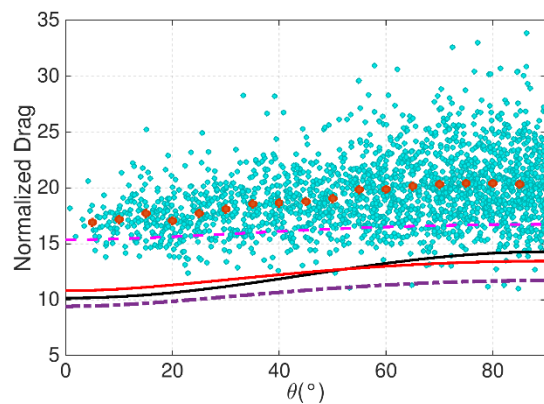
$$B = 101.8(\gamma - 0.81)^2 + 2.4.$$

To evaluate the applicability of these correlations under different Re , φ and particle geometries, comparison of drag force calculated from particle resolved simulation and the combination of different isolated particle and suspension correlations is shown in Figure 2.7 and Figure 2.8 of drag force versus particle inclination angle in suspension. Isolated particle drag correlation of Hölzer and Sommerfeld [1] for general non-spherical particles and that of Ouchene et al. [11] specific to ellipsoidal particles, and suspension correlations due to Di Felice [21], Tenneti et al. [22] and that due to Rong et al. [25] are considered. Four combinations are evaluated, Hölzer-Felice, Hölzer-Tenneti, Hölzer-Rong and Ouchene-Rong. Figure 2.7 are the results for AR2.5 ellipsoid and Figure 2.8 corresponds to AR10 ellipsoid. Each green dot in the figures represents a particle in the suspension while each red dot represents the mean drag force of the particles within an inclination angle range of 5° . In general it can be observed that for both aspect ratios all the correlations always underestimate the drag force at $Re=10$. Out of the different combinations, the Hölzer -Tenneti combination is able to capture the mean variation reasonably well for AR2.5 particles but fails for the AR10 particles with large under predictions. The Ouchene-Rong combination, on the other hand does a reasonable job for AR10 particles but under predicts for the AR2.5 suspension. At $Re=200$, Hölzer-Felice and Hölzer-Tenneti (HT) provide reasonably accurate estimation of the mean drag force for AR2.5 suspensions but tend to under predict the drag for the AR10 suspension. This agrees well with the conclusion drawn by Vollmari et al. [33] that while predicting drag force on particles with geometry similar to that of a sphere, the combination of isolated non-spherical

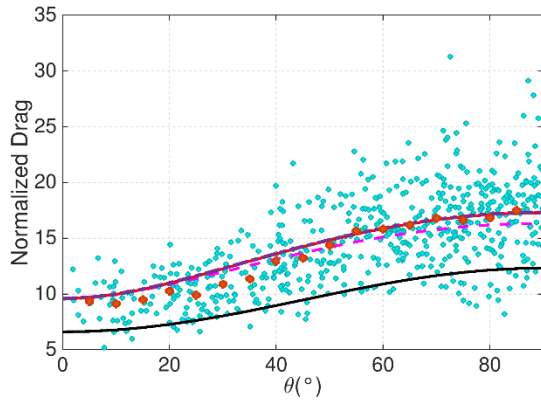
particle drag correlation and spherical suspension drag correlation can provide reasonable estimation of the drag force for particles in a fluidized bed at relatively high Reynolds number in the intermediate flow regime. At $Re=200$, for AR10 particles there is no single combination that can predict mean drag for different solid fractions – at solid fraction 0.1, the Hölzer-Rong combination is best whereas at solid fraction 0.2, Ouchene-Rong gives the best agreement. Rong’s correlation is the only particle suspension drag correlation that takes the effect of particle geometry into consideration. In fact for AR10 particles which deviate substantially from the spherical shape (sphericity of 0.59), results using the Ouchene-Rong correlation show the best overall agreement with the PRS data. On the other hand, the Hölzer-Tenneti combination shows the best overall agreement for the AR2.5 suspensions. The results for AR2.5 conform to the results of He et al. [27] who also found that best agreement with PRS data was given by the Hölzer-Tenneti combined correlation.



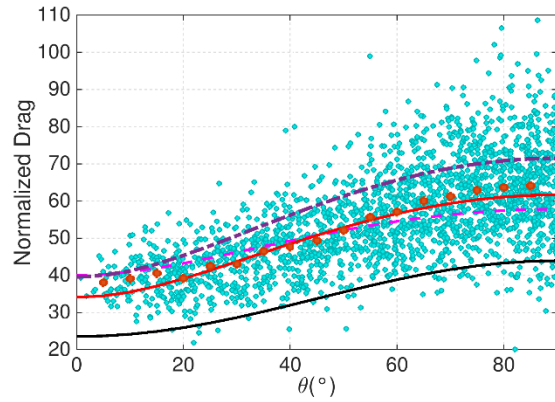
(a) $Re=10, \varphi = 0.1$



(b) $Re=10, \varphi = 0.35$



(c) $Re=200, \varphi = 0.1$



(d) $Re=200, \varphi = 0.35$

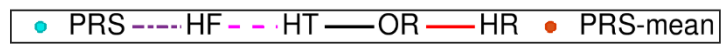
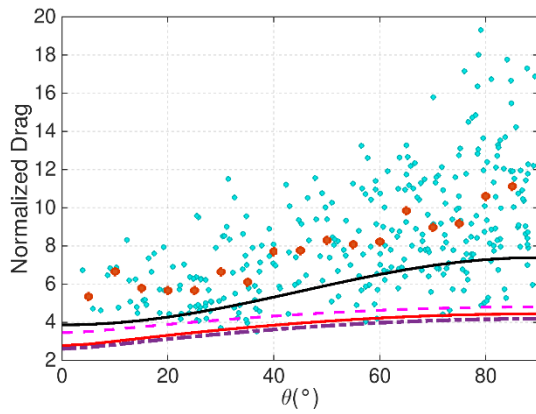
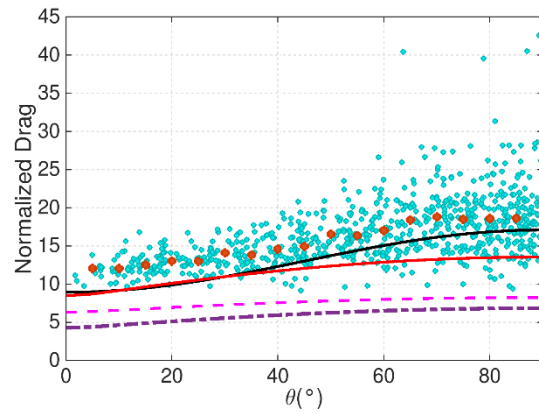


Figure 2.7. Comparison of drag force between PRS results and correlations in literature for AR2.5 ellipsoid suspensions. H: Holzer[1], O: Ouchene[11], F: Di Felice[21], T: Tenneti[22], R: Rong[25].



(a) $Re=10, \varphi = 0.1$



(b) $Re=10, \varphi = 0.2$

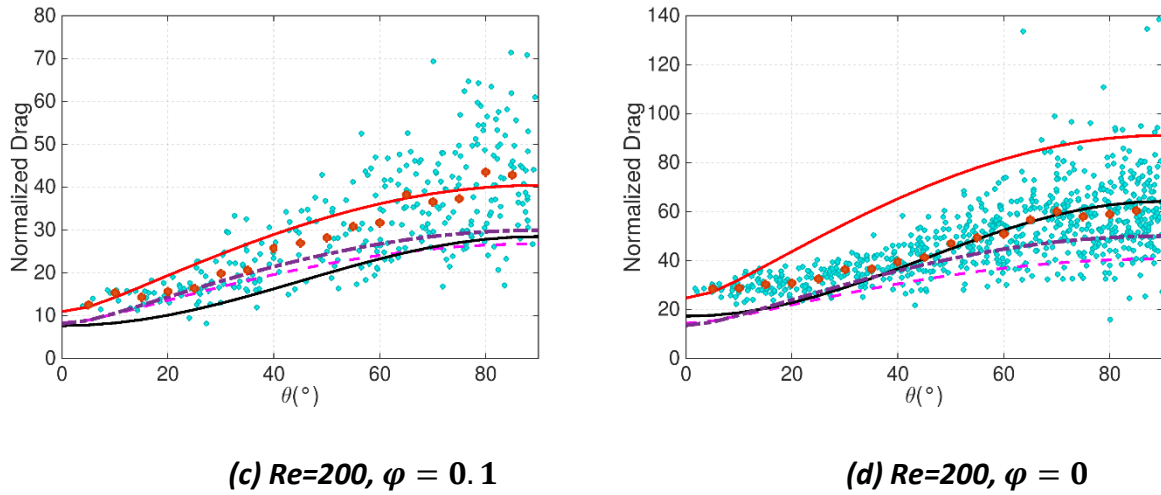


Figure 2.8. Comparison of drag force between PRS results and correlations in literature for AR10 ellipsoid suspensions. H: Holzer[1], O: Ouchene[11], F: Felice[21], T: Tenneti[22], R: Rong[25].

The fact that in Figure 2.8 the Rong et al. [25] suspension correlation developed for packed beds of ellipsoidal particles gives the best overall agreement for AR10 suspensions, conforms to the conclusions of Vollmari et al. [33] that using suspension correlations developed for spherical particles are inadequate as the particle geometry deviates significantly from that of a sphere. Figure 2.9 provides additional insight into this observation by studying the x-directional flow velocity at different planes for AR2.5 (a) – (d) and AR10 (e) – (h) at $Re = 10$ and solid fraction 0.1. It can be observed that in spite of the same solid fraction, due to the very elongated shape of the AR10 ellipsoids, a much greater disturbance is induced in the flow field compared to the AR2.5 ellipsoids. This is because, although these two particles have an identical volume, the AR10 ellipsoid has a much larger surface area that results in more prominent blocking of the incoming flow. As a result, the interstitial fluid velocity is higher resulting in higher drag on the particles.

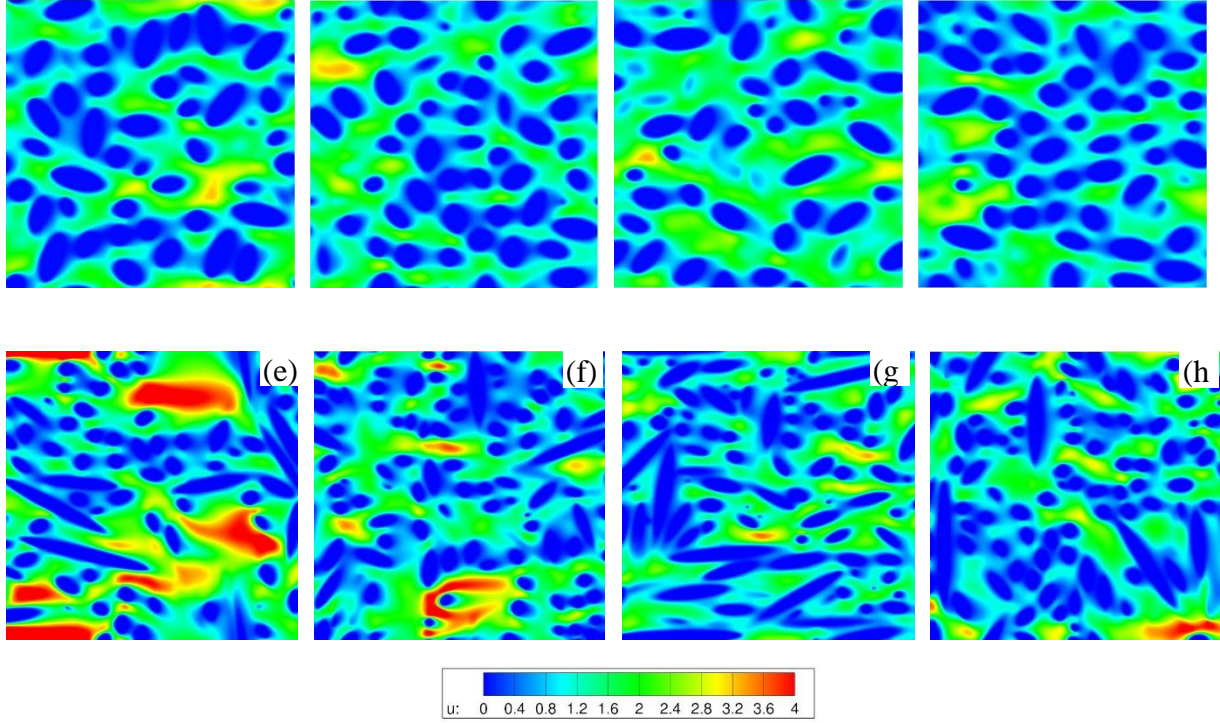


Figure 2.9. Flow field of AR2.5 and AR10 ellipsoid suspension at $Re = 10$, $\varphi = 0.1$.

A more quantitative measure of the effect of particle geometry on drag in suspensions can be obtained by calculating the ratio of the PRS calculated mean drag force per particle in suspension for a given Reynolds number and solid fraction to the weighted isolated particle drag force weighted by number of particles in a given inclination angle range calculated by the following summation.

$$\bar{F}_{d0} = \sum_{\theta=0^{\circ}}^{90^{\circ}} F_{d0,\theta} \cdot k_{\theta} \quad (2.9)$$

In the equation, $F_{d0,\theta}$ is the isolated particle drag force (normalized by Stokes drag) at inclination angle θ calculated using the isolated particle correlation of Ouchene et al. [11] shown in Table 2.2 and k_{θ} is obtained from the theoretical randomly packed suspension, which is the fraction of the

total number of particles at inclination angle of θ , which can be shown to be $\sin\theta$. The weighted mean is used to mimic the fraction of particles with the corresponding inclination angle in the ideal randomly oriented suspension - more specifically the fraction of particles with inclination angle within every 5° is used as k_θ . The ratio between the computed mean drag force per particle in suspension (\bar{F}_d) and the weighted mean isolated particle drag force (\bar{F}_{d0}) is calculated for each solid fraction and particle geometry and the results are shown in Figure 2.10. The ratio gives a measure of the degree to which the presence of the particles in suspension affects the mean drag. In the unlikely scenario that the suspension does not influence the drag on a particle, then the ratio would assume a value close to unity. Any deviation from unity quantifies the effect of the suspension on the average drag force felt by an individual particle in suspension. An increasing ratio indicates that the mean drag per particle in suspension deviates more and more from the mean drag acting on an isolated particle. A strong dependence of the ratio on Reynolds number and solid fraction can be observed. If the shape of the particle were not a strong factor in influencing suspension drag, the ratio would be the same for a given Re and solid fraction across all the particle geometries (AR=1 to 10). However, it is observed that the drag ratio is dependent on the particle aspect ratio as well and it increases with aspect ratio. Figure 2.10 affirms the earlier observation that using spherical particle suspension drag correlations to estimate the drag force on non-spherical particle suspensions leads to increasing errors as the particle shape deviates from that of a sphere. These results demonstrate the importance of considering the effect of particle geometry while proposing suspension drag correlations.

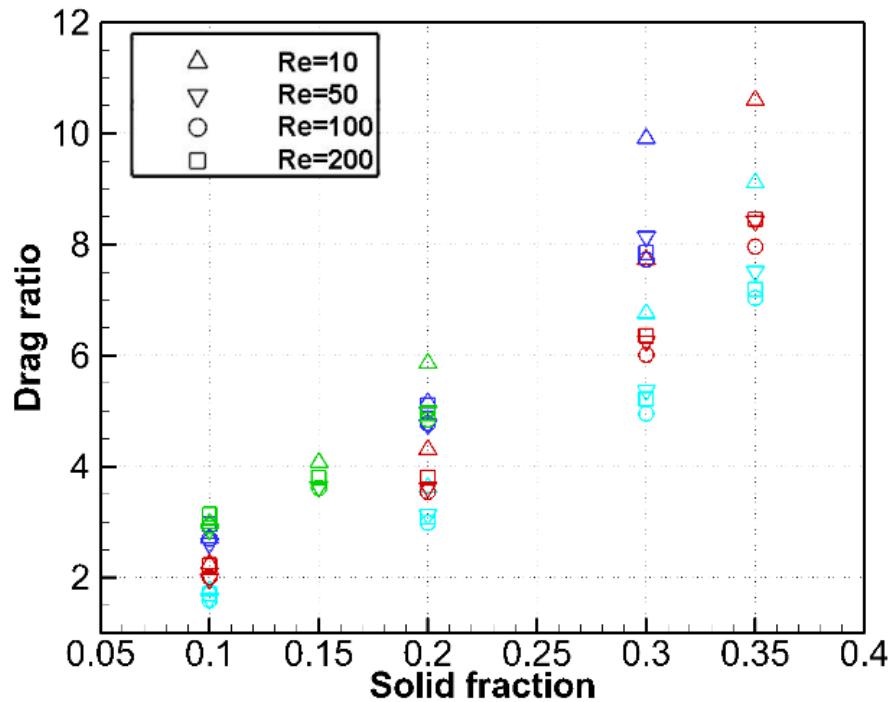


Figure 2.10. Ratio between suspension and isolated particle mean drag force (Light blue: Sphere; Red: AR2.5 Ellipsoid; Blue: AR5 Ellipsoid; Green: AR10 Ellipsoid)

2.4.2. Development of mean drag correlation

Since the analysis above demonstrates that it is hard to find a closure in the literature that can provide reasonably consistent predictions of the drag force for ellipsoidal particle suspensions, here we propose a new correlation for ellipsoids with aspect ratio of 1.0 to 10. There are two basic requirements imposed on the particle suspension drag correlations: when $\varphi \rightarrow 0$, the drag correlation should reproduce the drag force on an isolated particle in the flow; and the drag correlation should be able to predict the correct drag for spherical suspensions as well (AR1). It is the intent of the final correlation to predict the mean drag over the full ensemble of the suspension as well as the variation of drag with inclination angle in suspension. In order to achieve this end

objective, the drag correlation is developed as a combination of isolated particle drag combined with or modified by a suspension drag correlation. A pre-existing isolated particle drag correlation is used and the development focuses on the suspension correlation based on PRS data. First an ensemble mean drag correlation is developed taking into consideration the Re number, the solid fraction, and the particle geometry. This is then modified further by introducing the dependence of particle inclination in suspension.

To build the suspension drag correlation for the ellipsoidal particles a form similar to Di Felice's [21] correlation with parameters modified to match our simulation results is used. Combining this with isolated particle drag correlation, the new drag force correlation is written as:

$$F_d = \bar{F}_{d0} \varepsilon^{-\alpha(Re, \varepsilon) - \beta(\omega, \varepsilon)} \quad (2.10-a)$$

$$\begin{aligned} \alpha = & 4.988(\varepsilon + 0.5139) - (3.175 \\ & - 1.493\varepsilon)\varepsilon^2 \exp\left(-\frac{1}{2}(1.5 - \log_{10}(Re))^2\right) \\ & - 0.5884 \times \log_{10}(Re) \end{aligned} \quad (2.10-b)$$

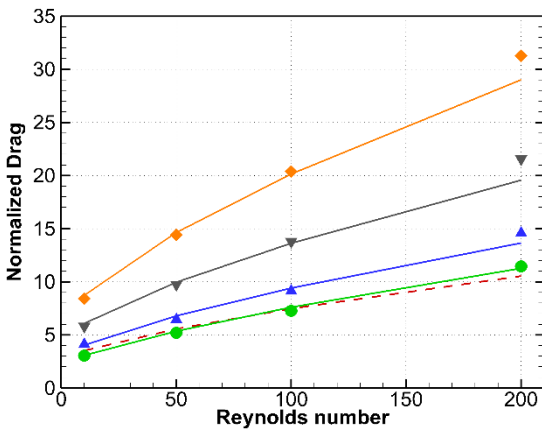
$$\beta(\omega, \varepsilon) = A \times \varepsilon^3 + B \times \varepsilon + C \quad (2.10-c)$$

$$\begin{cases} A = 0.5201\omega^2 + 6.094\omega - 11.74 \\ B = -1.713\omega^2 - 3.467\omega + 12.65 \\ C = 1.056\omega^2 + 0.4316\omega - 4.168 \end{cases}$$

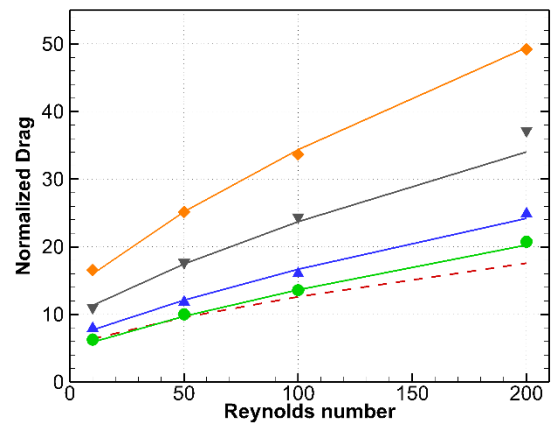
In the equation, ε is the void fraction of the suspension given by $\varepsilon = 1 - \varphi$. \bar{F}_{d0} is calculated using the drag correlation of Ouchene et al. [11,12] (Table 2.2) which covers the range of Re and aspect ratios investigated in this paper. Since Ouchene et al.'s isolated particle correlation for F_{d0}

is sensitive to the inclination angle θ of the ellipsoid with respect to the flow direction, the mean isolated particle drag (\bar{F}_{d0}) is calculated using Eqn (2.9). For spheres (AR1), $\bar{F}_{d0} = F_{d0}$ is the drag force for an isolated spherical particle in the flow, which is calculated using the drag correlation of Ouchene et al. [11,12] (Table 2.2) which in the limit as $AR \rightarrow 1$ reduces to [43]:

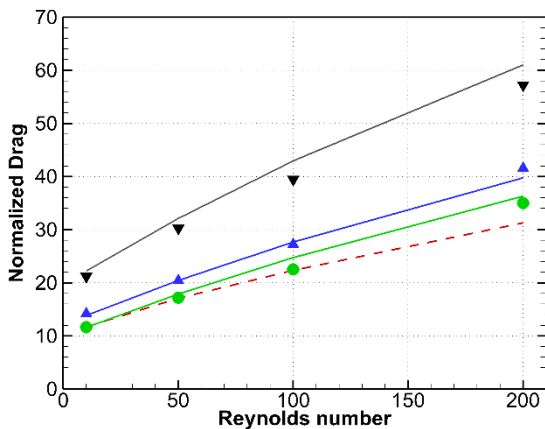
$$C_{D,sphere} = \frac{24}{Re}(1 + 0.15Re^{0.687}) \quad (11)$$



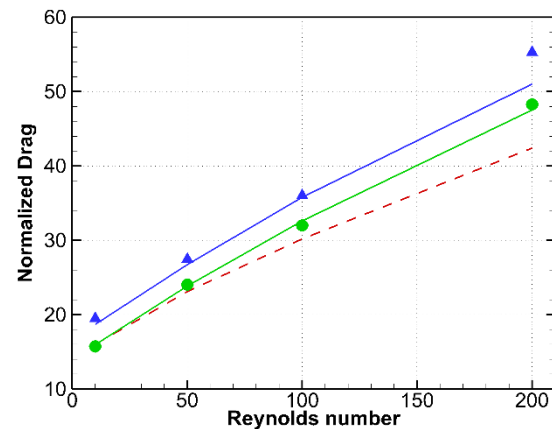
(a) $\phi = 0.1$



(b) $\phi = 0.2$



(c) $\phi = 0.3$



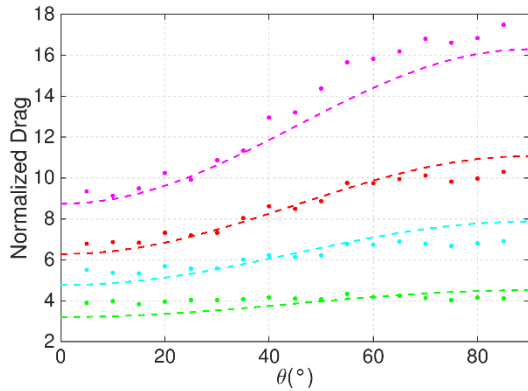
(b) $\phi = 0.35$

Figure 2.11. Comparison of ensemble mean drag force between developed correlation $\{\bar{F}_{d0}$ - Eqn 2.10} (Solid lines) and PRS results (Symbols). Spherical particle correlation of Tenneti et al. [22] (Dashed lines) is also shown for comparison; Green: Sphere; Blue: AR2.5; Grey: AR5; Orange: AR10.

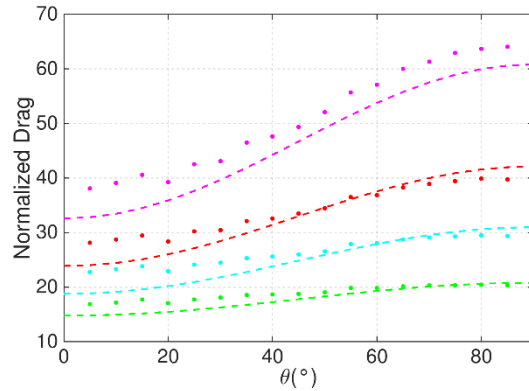
Comparison of PRS results and the correlation is shown in Figure 2.11. To benchmark the proposed drag correlation in Eqn (10) it is compared to the spherical suspension correlation of Tenneti et al. [22] in Figure 2.11. It can be observed that Eqn (10) is in good agreement with Tenneti et al. [22] for spherical suspensions but deviates considerably as the aspect ratio of the particles increases. The discrepancies between Eqn. (10) and Tenneti et al. at high Reynolds number and higher solid fractions for spherical suspensions was also observed by He et al. [27]. Tenneti et al. [22] noted in their paper that their PRS on which their correlation is based always predicted lower drag than previous works at $Re=200$. In Figure 2.11 a strong dependence of the ensemble mean drag force on aspect ratio, emphasizing the importance of including the effect of particle geometry for different non-spherical particle suspensions. The mean deviation of Eqn. (2.10) with PRS results for AR2.5, AR5 and AR10 ellipsoids are 3.24%, 4.96% and 2.24% while relative deviation for the spherical suspension is 2.82%. The small errors indicate that the ensemble mean drag force of ellipsoids with aspect ratio range from 1 to 10 can be well captured by the current correlation within the Reynolds number and solid fraction range investigated.

Since drag force is also a strong function of particle orientation or inclination angle (see Figure 2.7 & Figure 2.8), it is desirable to be able to predict the mean drag force on a particle at a given inclination in suspension. As a first approximation this can be accomplished by using $F_{d0,\theta}$ instead of \bar{F}_{d0} in Eqn. (2.10-a) for each inclination angle. These results are presented in Figure 2.12 (a), (c) and (e) at the lowest solid fraction investigated for AR2.5, AR5 and AR10 ellipsoid,

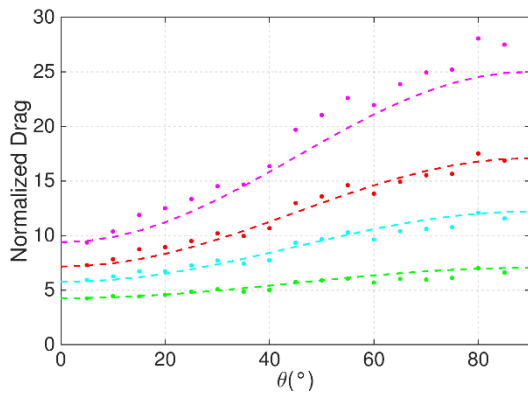
respectively, and Figure 2.12 (b), (d), (f) for the highest solid fraction for these particles. The drag correlation performs reasonably well compared to the PRS results. The mean relative deviation of the three ellipsoid shapes over all inclination angles, Re and φ investigated are 5.78%, 7.47% and 7.43% for AR2.5, 5, and 10, respectively. More specifically, the agreement is better at lower solid fractions, however, at relatively higher solid fractions, significant deviation starts to appear near 0° and 90° . This suggests that for a dilute particle-fluid system, scaling the isolated particle drag force at different θ by the same factor is reasonable for particles in suspension but this becomes less accurate when the solid fraction increases.



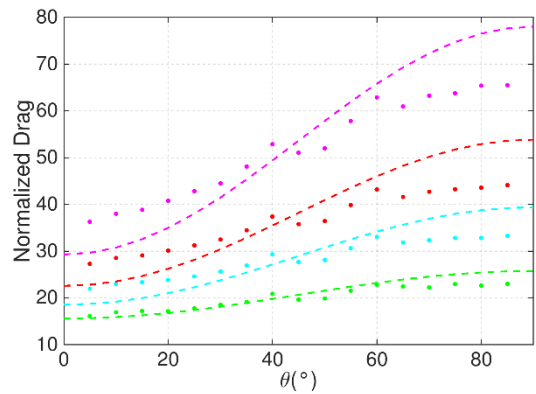
(a) AR2.5 $\varphi = 0.1$



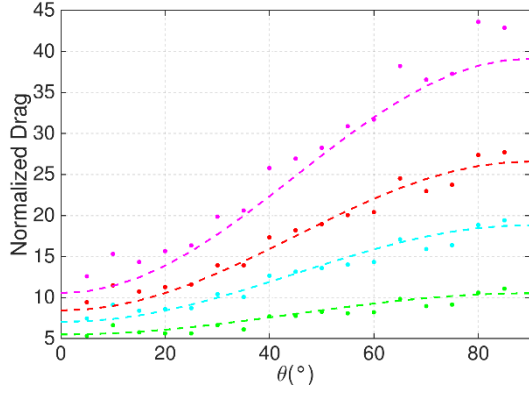
(b) AR2.5 $\varphi = 0.35$



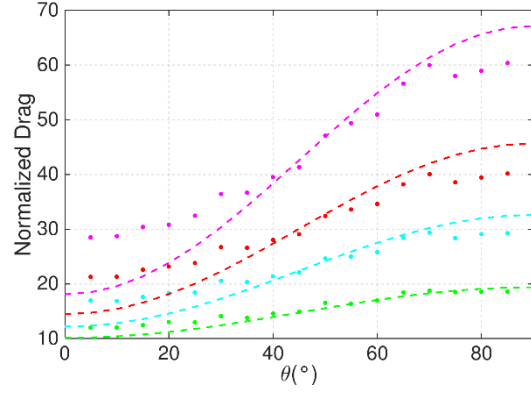
(c) AR5 $\varphi = 0.1$



(d) AR5 $\varphi = 0.3$



(e) AR10 $\varphi = 0.1$



(f) AR10 $\varphi = 0.2$

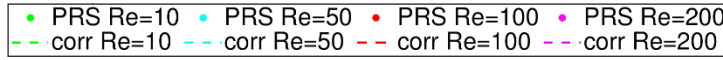


Figure 2.12. Comparison of drag force dependence on inclination using drag correlation {Ouchene (Table 2.2), $F_{d0,\theta}$ + Eqn. 2.10} with PRS results.

The observations in Figure 2.12 suggest that further sensitization of the suspension correlation in Eqn (2.10) to inclination angle could potentially increase accuracy. Error analysis demonstrated that the deviation from PRS data had a strong dependence on solid fraction and aspect ratio of the ellipsoids, with a weak dependence on the Reynolds number. Therefore, a modification term for θ that is a function of φ and AR is proposed and the final drag correlation has the following form:

$$F_d = F_{d0,\theta} \varepsilon^{-\alpha(Re,\varepsilon) - \beta(\omega,\varepsilon)} \cdot \omega^{(a_1 \cdot \theta + a_2)(1-\varepsilon)^{a_3}} \quad (2.12-a)$$

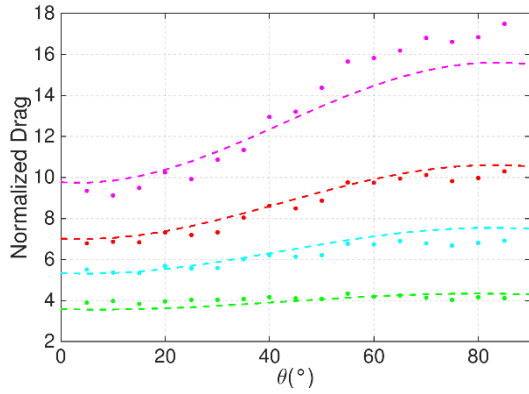
$$\begin{cases} a_1 = 0.0011\omega^2 - 0.0161\omega + 0.0277 \\ a_2 = -0.0405\omega^2 + 0.6296\omega - 0.9672 \\ a_3 = -0.087\omega^2 + 1.2092\omega - 2.0161 \end{cases} \quad (2.12-b)$$

With the additional term $\omega^{(a_1 \cdot \theta + a_2)(1-\varepsilon)^{a_3}}$ included in the drag correlation, comparison between PRS and correlation results are shown in Figure 2.13. The correlation now shows better agreement with PRS data at high solid fractions when previously it did not without the modification. On the

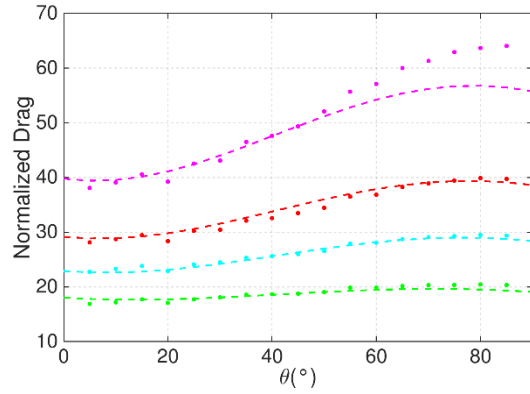
other hand, cases like $Re=200$, $\varphi = 0.35$ seem to have larger deviation at 90° than without the modification term for θ . But there is better agreement for $\theta \leq 60^\circ$. As a result, the weighted deviation, which is based on the proportion of particles under different inclination angles, changed from 6.41% to 7.11%. As for the overall deviation for the 3 particle geometries investigated, the mean deviation become 3.90%, 5.74% and 5.20% for AR2.5, 5, and 10, respectively. To summarize, the proposed drag correlation is reported in Table 2.3.

Table 2.3. New drag correlation for ellipsoids/sphere suspensions under different conditions

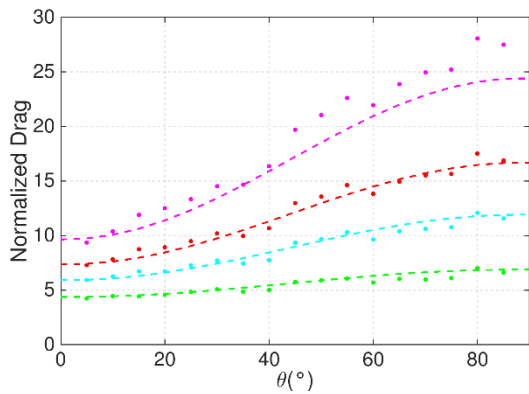
Drag Correlation	Applicability
$F_d = F_{d0,\theta} \varepsilon^{-\alpha(Re,\varepsilon) - \beta(\omega,\varepsilon)} \cdot \omega^{(a_1 \cdot \theta + a_2)(1-\varepsilon)^{a_3}}$ $\alpha = 4.988(\varepsilon + 0.5139) - (3.175$ $- 1.493\varepsilon)\varepsilon^2 \exp\left(-\frac{1}{2}(1.5 - \log_{10}(Re))^2\right)$ $- 0.5884 \times \log_{10}(Re)$ $\beta(\omega, \varepsilon) = A \times \varepsilon^3 + B \times \varepsilon + C$ $\begin{cases} A = 0.5201\omega^2 + 6.094\omega - 11.74 \\ B = -1.713\omega^2 - 3.467\omega + 12.65 \\ C = 1.056\omega^2 + 0.4316\omega - 4.168 \end{cases}$ $\begin{cases} a_1 = 0.0011\omega^2 - 0.0161\omega + 0.0277 \\ a_2 = -0.0405\omega^2 + 0.6296\omega - 0.9672 \\ a_3 = -0.087\omega^2 + 1.2092\omega - 2.0161 \end{cases}$	$Re \in [10,200]$ $1 \leq \omega \leq 10$ $0.1 \leq \varphi \leq 0.35$ (sphere and AR2.5 ellipsoid) $0.1 \leq \varphi \leq 0.3$ (AR5 ellipsoid) $0.1 \leq \varphi \leq 0.2$ (AR10 ellipsoid)



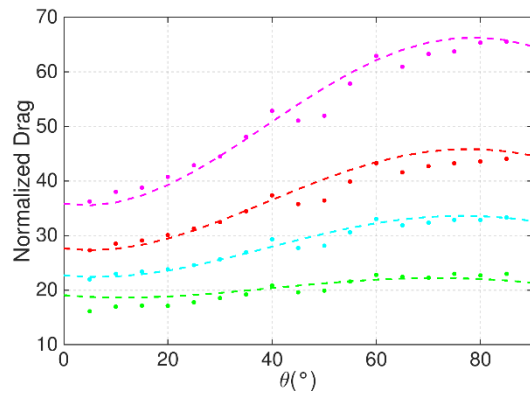
(a) AR2.5 $\varphi = 0.1$



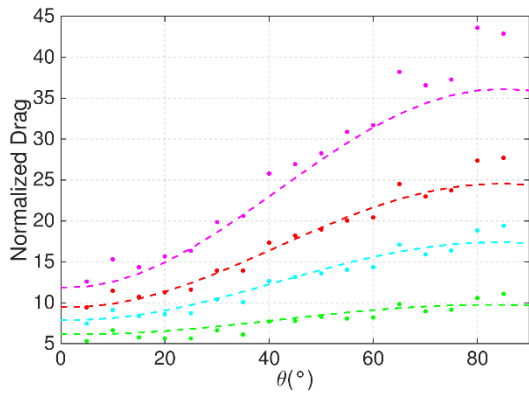
(b) AR2.5 $\varphi = 0.35$



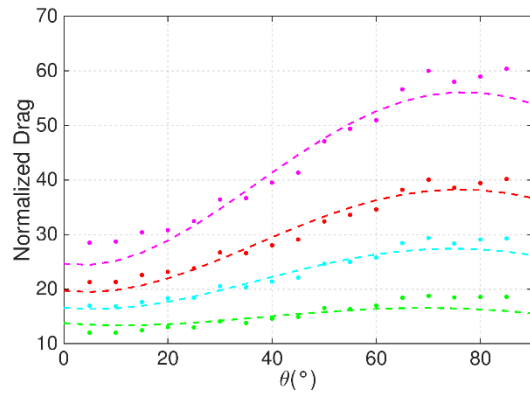
(b) AR5 $\varphi = 0.1$



(d) AR5 $\varphi = 0.3$



(e) AR10 $\varphi = 0.1$



(f) AR10 $\varphi = 0.2$

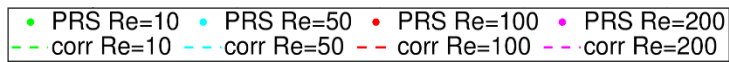


Figure 2.13. Comparison of drag force dependence on inclination using new drag correlation {Ouchene (Table 2.2), $F_{d0,\theta}$ + Eqn. 12} with PRS results.

2.5. SUMMARY AND CONCLUSIONS

The lack of drag correlations for non-spherical particles in suspension makes it difficult to accurately estimate the force on particles in studies that require drag closure to model the fluid-particle dynamics. The current state-of-the-art is to combine isolated non-spherical particle drag correlations and a correlation that takes solid fraction into account, which is based on experimental or simulation results of spherical particle suspensions. It is shown that this practice can lead to substantial inaccuracies when the particle geometry deviates significantly from a spherical geometry, thus motivating the work in this paper which aims to include the effect of particle geometry on drag correlations in suspension. In this study random suspensions (no preferential orientation) of ellipsoids with aspect ratios ranging from 1 (sphere) to 10 are considered in a Reynolds number range from 10 to 200, and solid fractions ranging from 0.1 to 0.35.

In order to achieve this end objective, an incremental approach is taken in the development of the drag correlation. During this exercise, the drag correlation is developed as a combination of isolated particle drag combined with or modified by a suspension drag correlation. In all instances pre-existing isolated particle drag correlation are used and the development focuses on the suspension correlation based on particle resolved simulation data. In this process, an ensemble mean drag correlation is developed for these particles in suspension taking into consideration the Re number, solid fraction and aspect ratio. Then the resulting mean drag correlation is modified further by introducing the dependence of particle inclination in suspension. The final correlation has a maximum mean deviation of approximately 6% from PRS data.

2.6. ACKNOWLEDGEMENTS

Mr. Ze Cao research was supported in part by an appointment to the U.S. Department of Energy (DOE) Postgraduate Research Program at the National Energy Technology Laboratory administered by Oak Ridge Institute for Science and Education. The authors would like to acknowledge the computational resources provided by Advanced Computational Research (ARC) at Virginia Tech.

Chapter 3

Modeling Drag force in ellipsoidal particle suspensions with preferential orientation

3.1. ABSTRACT

High aspect ratio ellipsoidal particle suspensions exhibit preferential orientation under the action of external forces and in the presence of walls. The preferential orientation of the particles has a large effect on the drag force experienced by the suspension. In this paper particle resolved simulations are conducted on ellipsoidal particles of aspect ratio 10 and 2.5 in the Reynolds number range $10 \leq Re \leq 200$ and solid fractions $0.10 \leq \varphi \leq 0.30$. An orientational order parameter $-2.0 \leq S \leq 1$ is used to define the preferential orientation of the suspension. It is shown that in spite of up to 400% variation in mean drag force with S , a simple linear relationship between $S = -2$ and 1 can describe the variation of drag force. This is a significant finding which establishes that only two data points at $S = -2$ and 1 are needed to define mean drag at any preferential orientation exhibited by the suspension. It is also shown that the inclination dependent mean drag is quite independent of S at low Reynolds number and solid fraction but shows increasing dependence at higher values.

Keywords: Particle suspensions; Particle-Resolved Simulation (PRS); prolate ellipsoids; drag correlation; preferential orientation.

3.2. INTRODUCTION

The fluid drag force acting on particle assemblies and suspensions is consequential to the design and operation of many static and dynamic particle systems. In many of these systems, particles are often treated as spherical in shape in spite of their non-sphericity. This is because drag correlations for single spherical particles [2–6,8,44] as well as spherical particles in suspension [18–22] are readily available and relatively easy to use. For non-spherical particles in isolation, not only does the Reynolds number influence drag but also the orientation of the particle with respect to the flow direction [45,46]. Recently, experiments have been augmented with Particle Resolved Simulations (PRS) for single ellipsoids [9–12] and cylinders[13–15] of different aspect ratios, and cubes [16,17] at different orientations to the flow to characterize the orientation dependence. Extensions of drag correlations to non-spherical particle suspensions have been limited. Common practice in the literature has been to combine single particle correlations with suspension correlations developed for spherical particles [21,22]. Recently taking advantage of increased computational power, PRS for different non-spherical particle shapes in suspension have been conducted. He et al. [27,28] performed PRS of flow over randomly oriented suspensions of ellipsoids with aspect ratio of 2.5 and observed the significant variation of drag force experienced by individual particles under different inclination angles. They showed that at a given Reynolds number and solid fraction the mean drag force varied with orientation angle, but there was also considerable scatter of individual particle drag about the mean drag at a given orientation angle. A broader aspect ratio range of 0.25 to 4, which included oblate as well as prolate ellipsoids, was investigated by Rong et al.[24,25] using the Lattice Boltzmann Method (LBM) for flow through a packed bed generated by Discrete Element Method (DEM). With the observed different preferential orientation for oblate and prolate ellipsoids, they demonstrated that drag in these suspensions is quite different from

suspensions that have particles randomly or uniformly oriented. However, this phenomenon was not explicitly investigated in their study.

Buchalter and Bradley [47] simulated the process of pouring hard particles into a three-dimensional container and observed that oblate particles in the packed bed tended to have their rotational symmetry axis parallel to the direction of gravity, while for prolate ellipsoids, the rotational symmetry axis was preferably perpendicular to the direction of gravity. A similar phenomenon was observed by Zhou et al.[40] where they demonstrated that this was consistent with the general understanding of minimizing system potential energy. On the other hand, in fluidized beds, the preferential orientation behavior is different. Detailed orientational distribution was studied in CFD-DEM simulations of Ma and Zhao [31]. They found that in a packed bed of disks with aspect ratio (defined as the ratio between height to diameter) of 1/8, nearly 45% of particles rested with their rotational symmetry axis parallel to the direction of gravity, whereas only 8% of the particles tended to rest with their rotational symmetry axis perpendicular to the direction of gravity, respectively. As the fluidization started and stabilized, an inverse trend was observed with nearly 60% of the particles orienting their axis perpendicular to the flow with very few to no particles orienting their axis parallel to the direction of flow. For prolate rod-like particles with aspect ratio 3, Ma et al. [29] observed that approximately 45% and 1% of the particles were found to rest with their rotational symmetry axis oriented perpendicular and parallel to the flow, respectively. Under fluidized conditions, these two ratios changed to around 22% and 10%, respectively. The influence of non-spherical particle orientation distribution on the momentum transfer between fluid flow and particle suspensions has been reported by Vollmari et al. [33]. They performed both CFD-DEM simulations and experiments of air flow over packed beds of elongated cylinders with aspect ratio of 3.5. They found large differences in pressure drop when

the particles were predominantly positioned with their symmetry axis parallel to the flow versus perpendicular to the flow. However, they did not perform any detailed investigation of the flow field and drag force as influenced by the particle orientation distribution.

While preferential orientation would seem to be the more prevalent and natural condition than random arrangements in static as well as fluidized beds, particularly for large aspect ratio particles, there has been no attempt in the literature to investigate the relationship between drag forces experienced by a randomly oriented suspension versus drag force in a preferentially oriented suspension. Buchalter and Bradley [47] defined an orientational order parameter with respect to the flow direction for both prolate and oblate spheroids. The parameter encapsulates the full range from parallel-to-flow rotational symmetry axis to perpendicular-to-flow orientations and is straightforward to calculate. It has been used by researchers [48,49] performing DEM simulations to quantify the orientational preference for different non-spherical particles. Other researchers, like Woodcock and Naylor [50] use eigenvalue analysis of the 3D orientation data to quantify the orientational preference of the particle suspensions. While this provides quantification of the relative orientation of particles with respect to each other, it does not quantify the relative orientation with respect to the flow direction. Bezrukov and Stoyan [51] implemented an orientation correlation function (OCF), which is a generalization of the definition in a planar case [52]. By calculating the relative orientation for a particle of interest with respect to the surrounding particles, local alignment can be well quantified. However, similar to the eigenvalue analysis of Woodcock and Naylor [50], flow direction is not taken into account.

In summary, there is clear evidence in the literature that preferential orientation of non-spherical particles in suspension is the norm rather than the exception. All past work in the literature on quantifying drag force in suspensions assume a random arrangement of particles with no

preferential orientation. As we will show in this paper this assumption can lead to large errors in specifying the drag force in a suspension with preferential orientation. Thus it would follow that to predict drag forces accurately, drag correlations should not only be function of geometry, Reynolds number, and solid fraction, but also preferential orientation. This study focuses on this aspect for prolate ellipsoidal particles. Our objective is to establish a relationship between drag and preferential orientation, preferably one that is simple and general. In order to establish the effect of preferential orientation on suspension drag, in this work PRS is performed for flow through suspensions of prolate ellipsoids with aspect ratios of 10 and 2.5. Solid fractions from 0.1 to 0.3 and Reynolds numbers from 10 to 200 are considered. The orientational order parameter defined by Buchalter and Bradley [47] is used to quantify the ensemble preferential orientation of the particle suspensions.

3.3. NUMERICAL METHOD AND SIMULATION SETUP

3.3.1. Governing equations

All the simulations performed in this work are using an in-house CFD code – GenIDLEST (Generalized Incompressible Direct and Large Eddy Simulation of Turbulence) [34,35]. The dimensionless form of the governing equations formulated using Cartesian tensor notation are:

Continuity:

$$\frac{\partial u_i}{\partial x_i} = 0 \tag{3.1}$$

Momentum:

$$\frac{\partial u_i}{\partial t} + \frac{\partial}{\partial x_j} (u_i u_j) = -\frac{1}{\rho} \frac{\partial p}{\partial x_i} + \frac{\partial}{\partial x_j} \left\{ \frac{1}{Re} \left(\frac{\partial u_i}{\partial x_j} \right) \right\} \quad (3.2)$$

where the variables are non-dimensionalized by:

$$u_i = \frac{u_i^*}{u_{ref}^*}; \quad x_i = \frac{x_i^*}{l_{ref}^*}; \quad p = \frac{p^* - p_{ref}^*}{\rho_{ref}^* u_{ref}^{*2}};$$

$$\rho = \frac{\rho^*}{\rho_{ref}^*}; \quad \mu = \frac{\mu^*}{\mu_{ref}^*}; \quad Re = \frac{\rho_{ref}^* u_{ref}^* l_{ref}^*}{\mu_{ref}^*}$$

Variables with superscript (*) represent dimensional values. u_{ref}^* is the undisturbed or superficial flow velocity which can also be represented by U_∞ . l_{ref}^* is specified as the diameter of the sphere that has an equivalent volume of the ellipsoid. The flow is assumed to be incompressible with constant properties. Properties of air at 300K are taken for the fluid in the domain.

The governing equations are discretized using second-order central differencing scheme on a non-staggered grid topology. Fluid velocities, pressure and temperature are calculated and stored at the computational cell center whereas the mass flux is calculated and stored at cell faces. A semi-implicit method is implemented for time integration that treats the viscous terms with Crank-Nicolson formulation and the convection terms with Adams-Bashforth method. Firstly, an intermediate velocity field is calculated by a predictor step, then it is corrected in the corrector step using the calculated pressure field to satisfy discrete continuity. A preconditioned BICG-STAB method is implemented to solve the pressure equation.

3.3.2. Particle Geometry and Immersed Boundary Method

The particle geometries of interest are ellipsoids of 2.5 and 10 aspect ratio which is defined as the ratio between length along the rotational symmetry axis and diameter of the particle's largest circular cross-section. Eq. (3) is used to generate the particle geometry. For an aspect ratio of 10, $a = 2.32$, $b = c = 0.232$ and for aspect ratio 2.5, $a = 0.921$, $b = c = 0.368$ are used to give the desired aspect ratio and volume equivalent sphere diameter of unity. During the simulation, each particle is characterized by an inclination angle θ , which is the angle between the particle's rotational symmetry axis and the undisturbed flow direction that ranges from 0° to 90° . Fig. 3. 1. depicts the inclination angle and surface mesh for aspect ratio 10 particle.

$$\frac{x^2}{a^2} + \frac{y^2}{b^2} + \frac{z^2}{c^2} = 1 \quad (3)$$

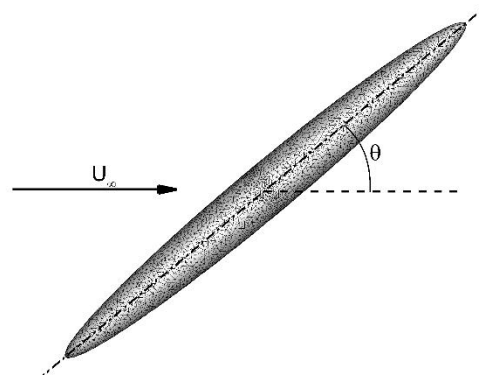


Fig. 3. 1. Particle surface mesh and definition of inclination angle

The Immersed Boundary Method (IBM) is employed to resolve the particle surfaces. In this framework, the computational domain is discretized into a structured Cartesian mesh. The treatment of the cells adjacent to the immersed particle surfaces is modified such that the computation is able to detect the immersed surface. To represent the location and curvature of the

particle surface, a mesh composed by 7538 triangular elements (2172 elements for aspect ratio 2.5) is generated for each particle as shown in Fig. 3. 1.. More details about the IBM procedure and implementation of boundary conditions can be found in the work of Nagendra et al. [36].

Hydrodynamic forces induced by fluid pressure and shear stresses at the surface are calculated at each triangular element of the particle surface mesh along the three primary orthogonal directions in the global $x - y - z$ Cartesian coordinate system [27,28]. As is shown in Eq. (4), drag force on the particle is obtained by the sum of the x -directional force over all surface elements. n is the total number of surface elements of the particle and f_{ix}^* is the x -directional hydrodynamic force on the i th element.

$$F_d^* = \sum_{i=1}^n f_{ix}^* \quad (3.4)$$

The drag force is further normalized by the Stokes drag which is calculated by:

$$F_d = \frac{F_d^*}{3\pi\mu_{ref}^* U_\infty^* d_p^*} \quad (3.5)$$

In this equation, d_p^* is the volume-equivalent sphere diameter.

A critical parameter in IBM is the background grid resolution compared to the size of the object that is immersed in the grid. A number of investigations preceding this study have validated the grid resolution and the overall methodology used in this paper. In He et al. [27], drag force results for suspensions of spheres and ellipsoids of aspect ratio 2.5 were tested at different grid resolutions and with past work in the literature. Predictions of drag forces with grid resolution of 30, 40 and

50 cells per volume equivalent spherical diameter (dimensionless equivalent diameter is always unity) were evaluated. It was found that the maximum difference between the three grids was about 2%. Spherical particle suspension results were compared with the correlation developed by Tenneti et al. [22] using particle resolved simulations. The predictions showed very good agreement with the correlation for $Re < 200$. At Reynolds number of 200, the predicted drag force was 5%~10% higher than the correlation. Tenneti et al. [22] have noted that their predictions, from which the correlation is built, consistently predicted a lower drag at $Re=200$ than that reported by other researchers. In a closely related heat transfer study of 2.5 aspect ratio ellipsoidal suspensions, He and Tafti [53] showed that the mean Nusselt number and its standard deviation varied by 2% and 4%, respectively between 30, 40 and 50 cells per equivalent diameter. In yet another study by Cao and Tafti [37] on single cylinders of aspect ratio 0.25, grids of 1/30, 1/40 and 1/50 were compared for the prediction of the drag coefficient over the range of Re up to 300 and particle inclination angles from 0 to 90 degrees. It was found that the difference in drag coefficient was bounded to within 4% between 1/30 and 1/50 and to within 2% between 1/40 and 1/50 grids. In addition to the grid independency study, the IBM predictions of drag coefficient for flow over a sphere in the $10 \leq Re \leq 300$ range were compared to past correlations [5,7], and to body-fitted grid calculations. Maximum differences were bounded to within 5%.

In all of these past investigations using the IBM method for single particles and particles in suspension, we have established that 40 cells per equivalent diameter captures the physics accurately up to $Re = 300$.

3.3.3. Computational domain and mesh

The 3D computational domain used in this study has a dimension of $30 \times 10 \times 10$ in $x - y - z$ directions, respectively. Flow is in the x -direction with a constant homogeneous velocity specified at the inlet boundary and a zero gradient condition at the outflow. As shown in Fig. 3. 2, particles are located in the region between the two dashed lines, at a distance of 5 units from the inlet and 10 units from the outlet. Periodic boundary conditions are specified in the y - and z - directions to simulate an infinite extent of the suspension in both directions.

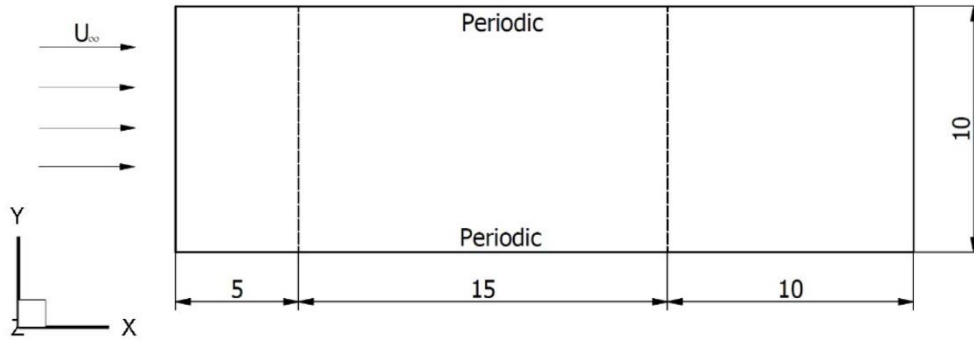


Fig. 3. 2. Computational domain and boundary conditions

A sufficiently refined mesh is necessary to resolve the fluid flow in the region between particles especially at relatively high solid fraction and Reynolds number. To supplement past grid independency studies [27,28,37], an additional grid independency study is conducted at the highest Reynolds number of 200 at a solid fraction of 0.20 for aspect ratio 10 particle suspension. Based on our previous investigations, two of the finest mesh resolutions were investigated: $\frac{1}{40}$ and $\frac{1}{50}$, which amounted to a total grid size of 128 and 250 million computational cells in the domain, respectively. With this study it is established that the calculated drag force on over 97% of the particles had deviations of less than 2.5% between the two grid resolutions while the mean drag

force over all particles in the suspension had a deviation of 1.01%, ascertaining grid convergence and the adequacy of the $\frac{1}{40}$ grid spacing. Thus all reported results are on a $\frac{1}{40}$ grid. A total of 186 calculations are conducted in this study.

3.3.4. Generation of Particle Suspension

A physical simulation engine PhysX by Nvidia [38] is used to create the particle suspension [27]. During this process each particle defined by a coarse surface mesh is introduced into the packing box with a random velocity. As more particles are introduced into the packing box, overlaps are detected by the PhysX engine and the collision operator moves the particles apart till no overlaps exist in the system. To maintain periodicity in the y - and z - directions, if any particle exists at a given location on one side of a periodic boundary, it is replicated on all sides that are periodic with that location. This process is repeated till the desired solid fraction is reached and the system is in a stable state with no overlaps. Fig. 3. 3 shows different views of a particle suspension created from PhysX.

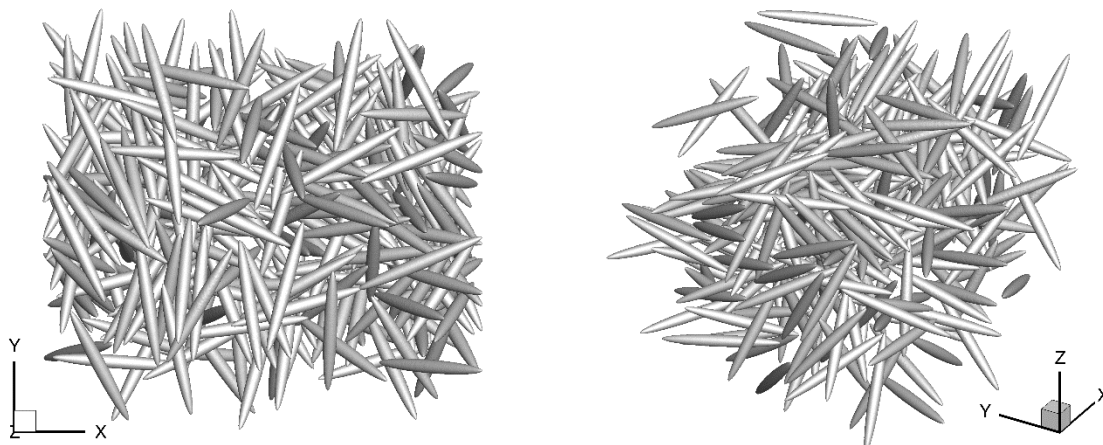


Fig. 3. 3. Ellipsoid suspensions created using the physics engine PhysX

To reach a desired solid volume fraction within the pre-set region that accommodates the particles, the number of particles are calculated by:

$$N = \frac{6\varphi V}{\pi d_p^3} \quad (3.6)$$

In the equation, N is the total number of particles in the domain. φ is the desired solid fraction and V is the volume of the computational domain over which the particles are spread. For the same φ , depending on the actual x - directional length taken by the particle suspension, the exact number of particles may vary. For a random arrangement the number of particles for $\varphi = 0.1, 0.15$ and 0.20 are 286, 430 and 573, respectively for aspect ratio 10 particles.

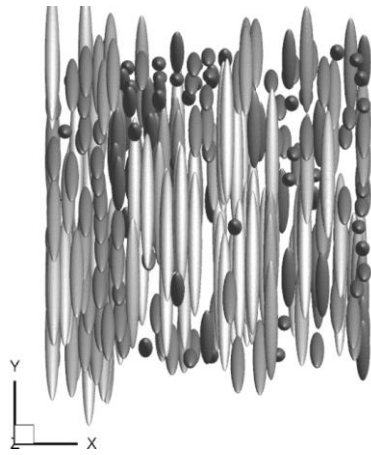
3.3.5. Definition of Orientational Order Parameter

In this study, to investigate the influence of particle orientation with respect to flow on the drag forces, the Orientational Order Parameter defined by Buchalter and Bradley [47] is used to quantify the overall particle orientation distribution in the suspensions. It is represented by S and is calculated using:

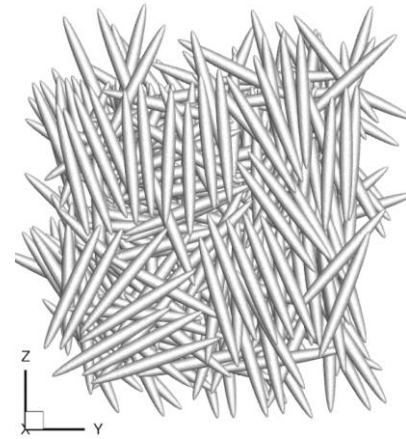
$$S = \frac{3}{2} \left[\frac{1}{N} \sum_{i=1}^N \cos \left(2 \left(\theta_i - \frac{\pi}{2} \right) \right) - \frac{1}{3} \right] \quad (3.7)$$

In this equation, θ_i is the inclination angle of the i^{th} particle while N is the total number of particles in the suspension. Fig. 3.4 shows two special cases with extreme S values. The incoming flow is in the x – direction and Fig. 3.4 (a), (b) shows the arrangement when all particles are perpendicular to the flow with an inclination angle of 90° . However, there is no restriction on the particle orientation in the $y - z$ plane, as can be seen in Fig. 3.4 (b), particles are randomly

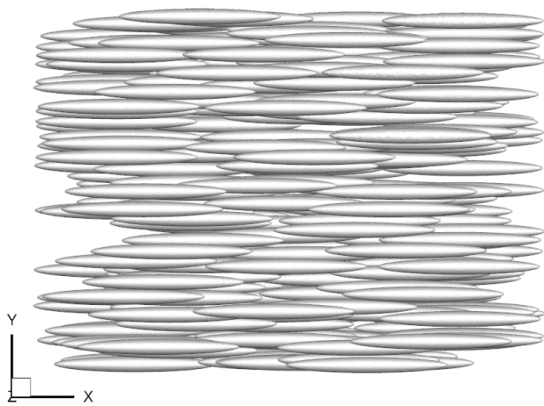
oriented in the $y - z$ plane with some inevitable local alignment. The S value for this case assumes the maximum value of 1.0. Conversely when all particles are aligned with the flow direction with an inclination angle of 0° , as shown in Fig. 3.4 (c), (d), the S value for the suspension will reach its minimum value of -2.0. Due to the monotonic increasing nature of the cosine function in Eq. (7) as $2(\theta - \pi/2)$ increases from -180° to 0° , an increasing S value indicates that particles are preferentially oriented towards a larger orientation angle. A value of $S = 0$ indicates that the distribution is random with no preferential orientation.



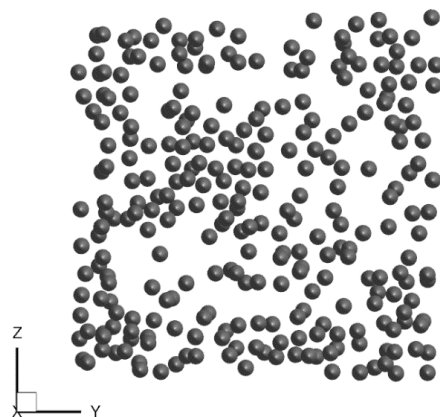
(a)



(b)



(c)



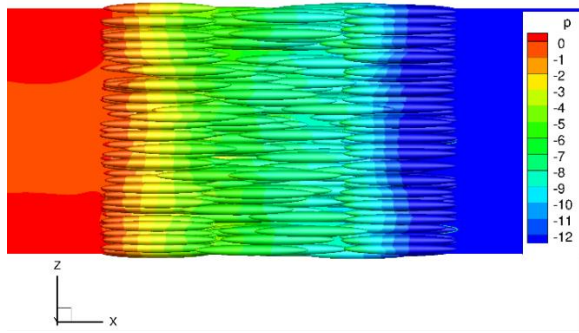
(d)

Fig. 3. 4. z –directional view of suspensions with all particles (a) perpendicular and (c) parallel to the flow and x –directional view of suspensions with all particles (b) perpendicular and (d) parallel to the flow.

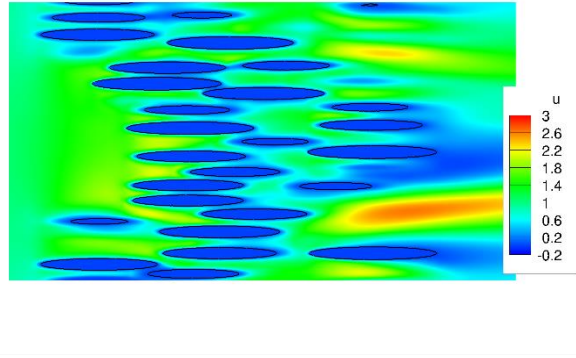
3.4. RESULTS AND DISCUSSION

3.4.1. Analysis of pressure and velocity distribution at different Re , φ and S

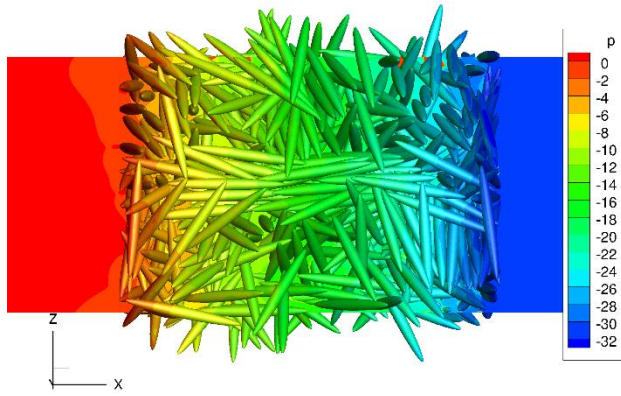
Fig. 3. 5 shows the pressure and velocity distribution in suspensions with $S = -2, 0.21, \text{ and } 1.0$, $Re = 50$ and $\varphi = 0.2$. The dimensionless pressure field on the particle surfaces as well as a planar view of the $x - z$ mid-plane and a planar $x - z$ view of the streamwise velocity is shown. At $S = -2.0$, by virtue of the particles being aligned parallel to the flow, the dimensionless pressure varies from 0.0 at the inlet to approximately -12.0 downstream of the suspension. At the same time the velocity field is quite ordered as the flow channels through the suspension. At the other extreme, at $S = 1.0$ all the particles are aligned normal to the flow but with arbitrary orientations in the $y - z$ plane. This results in blocking the incoming flow and a pressure drop of approximately 30 dimensionless units is 2.5 times that at $S = -2.0$. Compared to the two extreme arrangements, $S = -2.0$ and 1.0, $S = 0.21$ represents a near-random arrangement with some preferential orientation towards higher orientation angles. This leads to a tortuous flow path with accelerating and decelerating regions of velocity and high pressure drop. Note that for $S = 1.0$, because of the ordered arrangement, less number of particles can be used in a smaller x -distance to construct the suspension for a given solid fraction. Thus, in spite of the pressure drop per particle being the highest at $S = 1.0$, the overall pressure drop through the suspension is slightly less than that for $S = 0.21$ which has more particles spread across a larger x -distance.



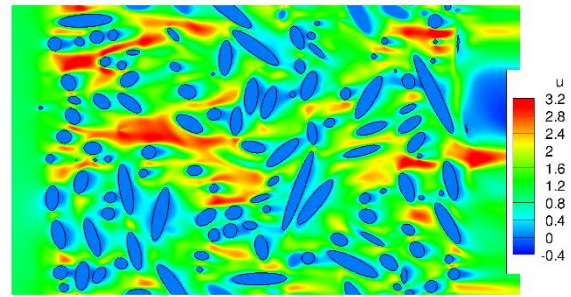
(a)



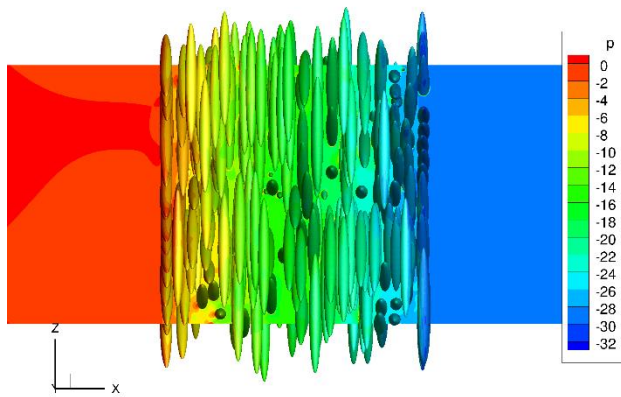
(b)



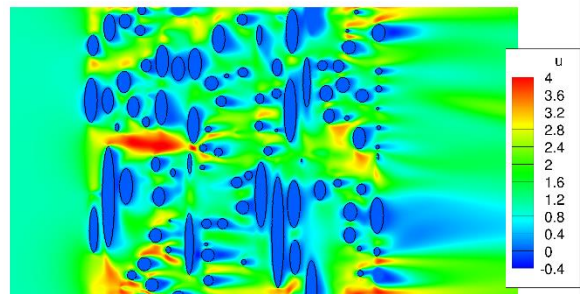
(c)



(d)



(e)



(f)

Fig. 3. 5. Pressure distribution on particle surfaces and x - z mid-plane and u velocity at x - z mid-plane of the flow field with (a-b): $S = -2.0$, (c-d): $S = 0.21$ and (e-f): $S = 1$.

To encapsulate the effect of Re , φ , and S on the flow field, we look at the Probability Density Function (PDF) of velocity fluctuations in the suspension defined by

$$u' = \frac{u - u_m}{u_m} \quad (8)$$

where u_m is the volumetric mean streamwise velocity of the fluid within the fully developed region as defined in Section 3.3.2. As a baseline, the PDF distribution of u' for a random distribution of particles ($S \sim 0$) for $Re = 10$ and 200 at $\varphi = 0.1, 0.15$ and 0.20 are presented in Fig. 3.6. A peak at/near $u' = -1.0$ can be found for all the cases which is caused by the low velocity boundary layers that are formed on the particles. Additionally, as Re decreases from 200 to 10 , a larger positive tail with $u' > 1.5$ develops that is caused by the combined effect of thicker boundary layers and large recirculating regions at $Re = 10$, resulting in more frequent occurrence of negative as well as larger positive velocities from mass conservation principles. As the solid fraction increases, for both $Re = 10$ and 200 , the peaks at $u' = -1$ increase, and because of the greater flow blockage with less void space, flow channeling effects lead to more high flow velocity regions. As a result, large positive excursions from the mean velocity also increase.

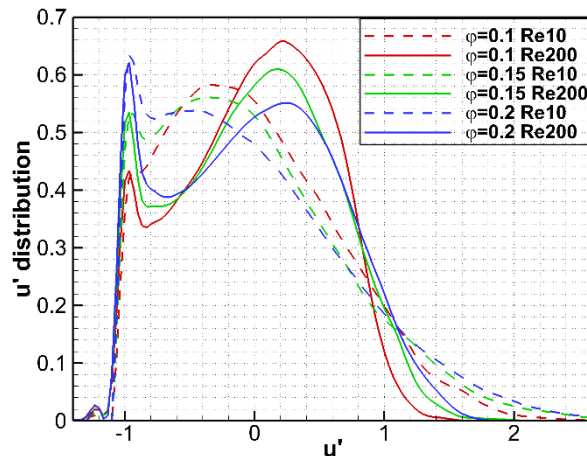
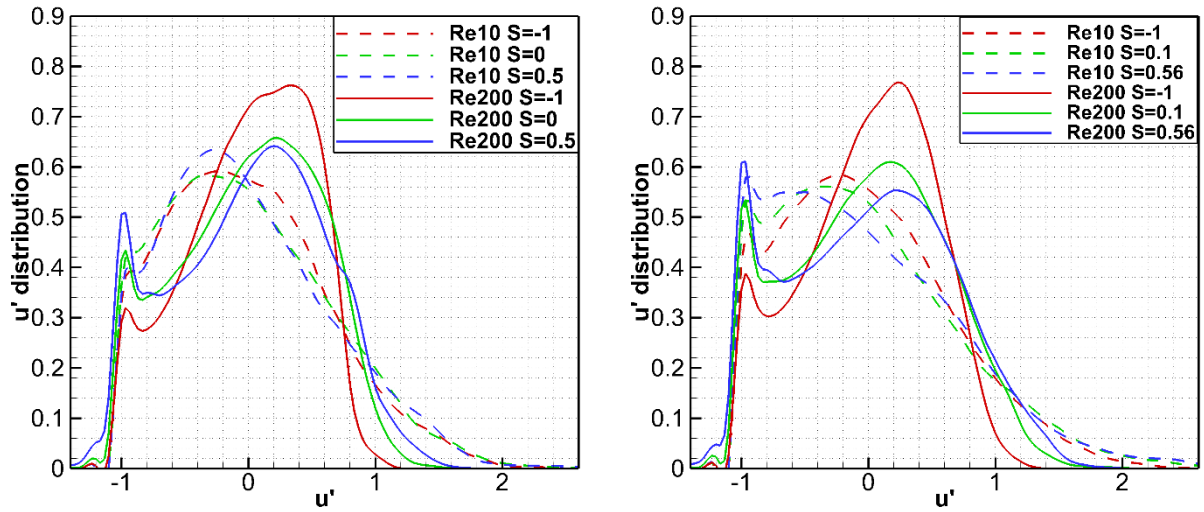


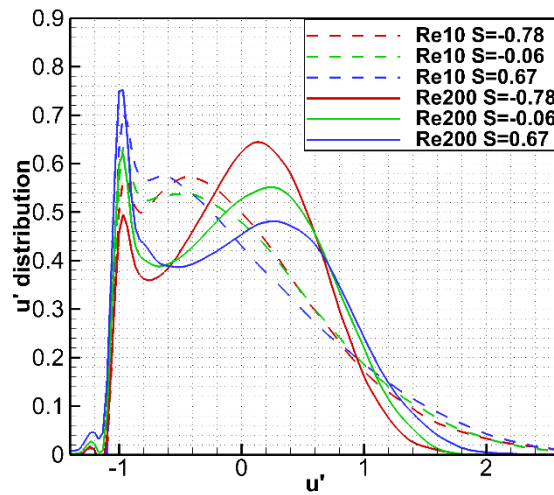
Fig. 3. 6 Distribution of u' at different Re and φ of randomly oriented suspensions

Having established the baseline trends for random arrangements, Fig. 3.7 compares the effect of the orientation parameter, S , on the PDF of velocity fluctuations. $Re = 10$ and 200 and $\varphi = 0.1, 0.15$ and 0.2 are compared for $S = -1, \sim 0$, and ~ 0.5 . $S = -1$ correspond to suspensions in which the rotational symmetry axis of the particles is predominantly aligned with the flow direction, $S = 0$ has no preferential orientation, and $S = 0.5$ describes a suspension predominantly aligned in a direction normal to the flow. In general, the orientation parameter has a much larger effect on the flow field as Re increases. At $Re = 10$ and $\varphi = 0.1$, the orientation parameter has little influence on the PDF distribution with peak occurrences between -0.4 and -0.2 . This is because at $\varphi = 0.1$, the particles are not in close proximity to each other and in the viscosity dominated flow the change in particle orientation does not have a large influence on the velocity field. As φ increases to 0.15 and to 0.2 , increasing S shifts the PDF to the left signaling the presence of more energetic wakes with larger and more frequent negative fluctuations. The velocity field is much more sensitive to the orientation parameter at $Re = 200$ at all solid fractions. As S increases from -1 to ~ 0.5 , independent of the solid fraction, the peak in the PDF at $0.2 \leq u' \leq 0.4$ decreases with a corresponding increase in large positive fluctuations $u' > 1$. This trend is very similar to that observed when φ increases, i.e. the overall velocity fluctuations in the suspension increase in magnitude as the particle orientation changes from aligned to the flow field to perpendicular to the flow field.



(a) $\phi = 0.1$

(b) $\phi = 0.15$



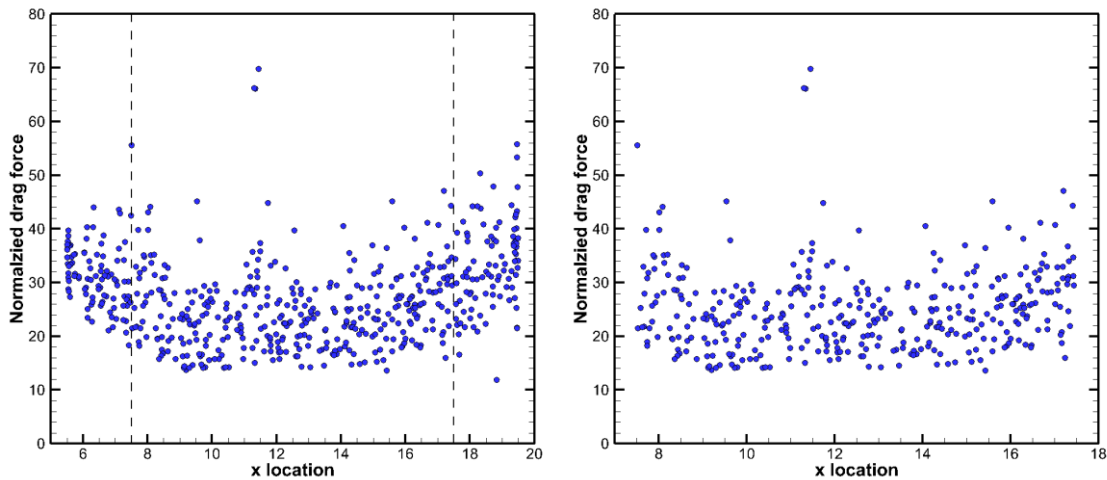
(c) $\phi = 0.2$

Fig. 3. 7. PDF distribution of u' at different Re , ϕ and S .

3.4.2. Fully-Developed Drag force

Drag force on individual particles in a suspension with $\phi = 0.2$, $Re = 50$ and $S = 0.21$ is shown in Fig. 3.8 (a) as a function of x -distance. Each point in the figure represents a particle in the domain and is located at the geometric centroid of a particle. The large scatter in drag forces at a

given x -location is a result of the randomness of the particle distribution and its effect on the pressure and velocity field surrounding each particle. It can also be observed that the mean drag calculated over some interval Δx is not uniform with x but is high at the entrance and exit regions of the suspension. This is because the flow experienced by these particles is not typical of the flow experienced by a particle deep in the suspension. We denote these as entrance and exit effects much like in the hydrodynamics of internal flows and only obtain force data from within the suspension in the “fully-developed” region (dashed lines in Fig. 3.8 (a)). Fig. 3.8 (b) presents the drag force data that is extracted for further analysis with the observation that the mean drag force has a near constant value with x . For the rest of the cases, we observed that the cut off length of 2 on either side is enough for most particle suspensions to effectively eliminate end effects from the drag force. The decrease in sample size is countered by doing multiple simulations at a given S or in the vicinity of the same S whenever possible. At least 2 different suspensions are calculated for the cases with $S \approx 0$. The calculated mean drag force for these different cases at the same solid fraction and Reynolds number are all within 6% of each other. This gives us sufficient confidence that the number of particles used for each case to analyze the behavior of drag forces are statistically significant and meaningful.



(a)

(b)

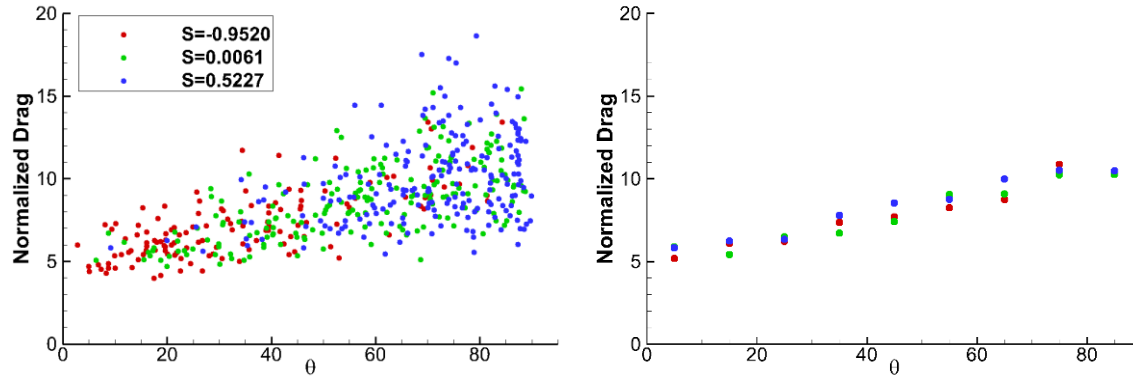
Fig. 3. 8. Drag force on individual ellipsoids in the suspension (a) original data (b) after filtering out data from ellipsoids near inlet and outlet regions.

3.4.3. Variation of Drag Force with Orientation Angle at Different S

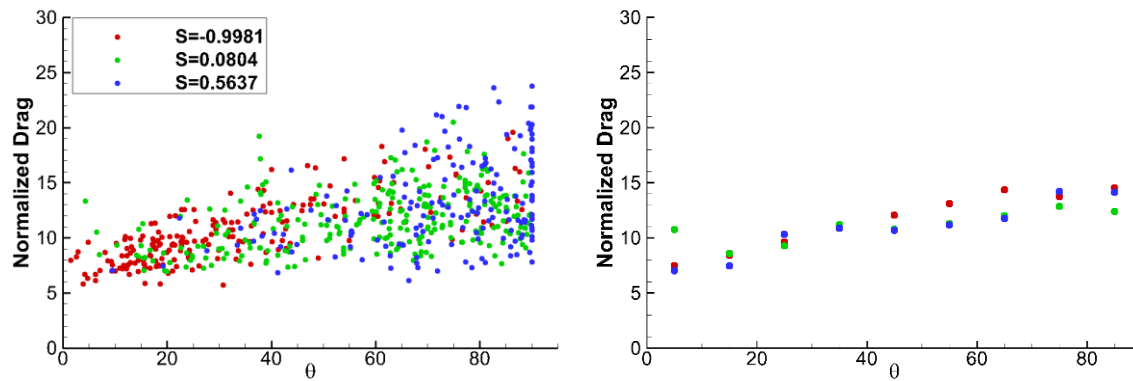
As shown in Section 3.3.1 the preferential orientation of particles has a large impact on the flow through the suspension. To further investigate its influence on drag force experienced by particles in the suspension, drag on particles at a given inclination angle is first investigated. i.e., under the same conditions of Re and φ , how will the composite S -value affect the mean drag experienced by particles inclined at a given angle θ to the flow? Drag results corresponding to the suspensions presented in Fig 3.5 are shown in Fig. 9 for $Re = 10$; $\varphi = 0.10 - 0.20$ and in Fig. 10 for $Re = 200$; $\varphi = 0.10 - 0.20$. Each symbol in the left column represents a particle in the suspension and the right column plots the mean drag within a $\pm 5^\circ$ range. At each solid fraction, drag results with three different S values are presented to show how the overall particle orientation preference influences the drag on individual particles.

In general, as the orientation angle increases, the drag force increases with increasing variation in magnitude. At $Re = 10$ in Fig. 3.9, the results indicate that at $\varphi=0.1$ and 0.15 , mean drag force for a particle at a given orientation is quite independent of the suspension's preferential orientation (S value) – i.e., a particle oriented at angle θ will experience the same approximate drag force irrespective of the preferential orientational bias of the full suspension. However, this changes at $\varphi=0.2$ which shows that the mean drag is not only dependent on the individual particle

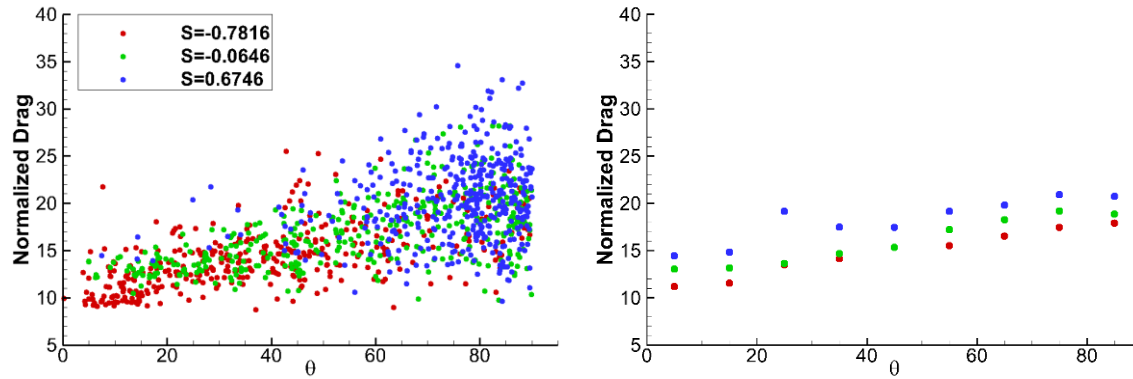
orientation but also on the orientational bias of the full suspension – larger the S value, larger is the mean drag force experienced by the particle at any given particle orientation angle.



(a) $\phi=0.1$



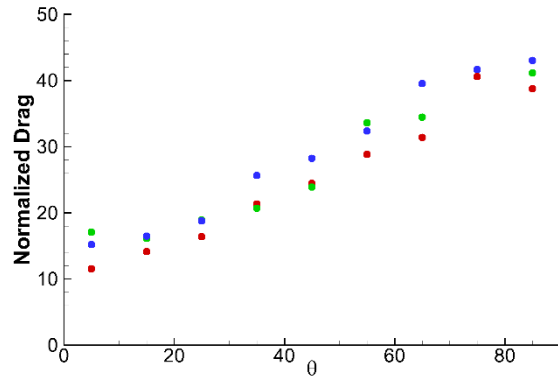
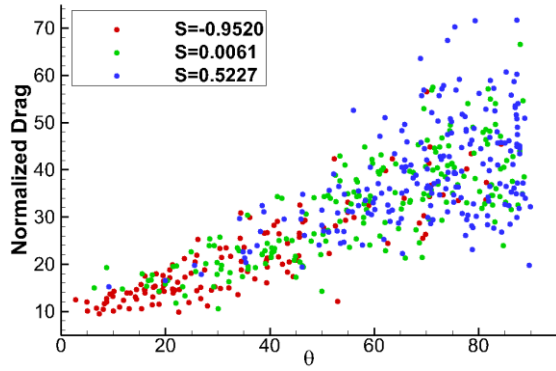
(b) $\phi=0.15$



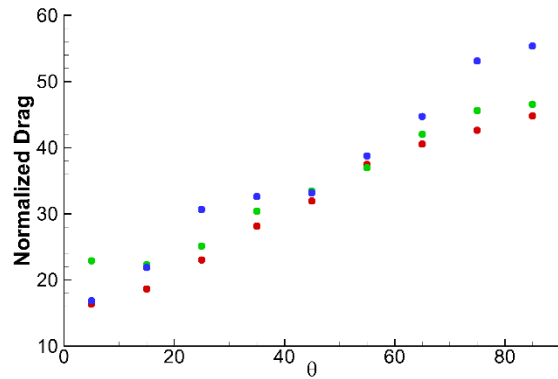
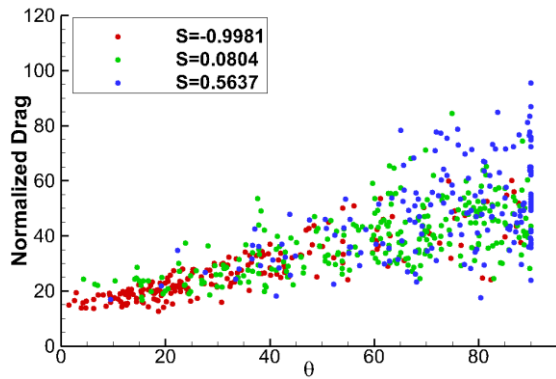
(c) $\varphi=0.20$

Fig. 3. 9. Variation of drag force on particles in the suspension at $Re = 10$.

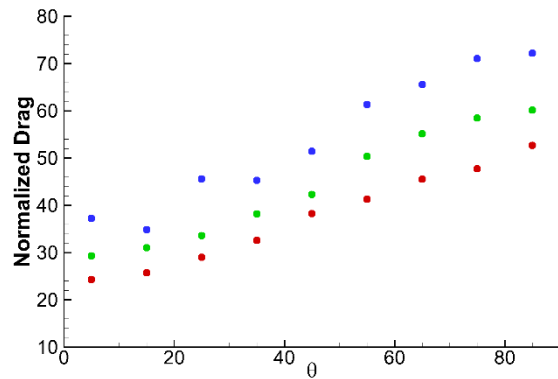
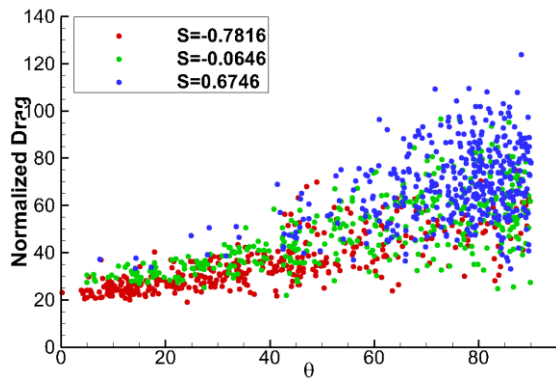
Fig. 3.10 at $Re = 200$ shows the same approximate trend at $\varphi=0.1$ and 0.15 , while the sensitivity to S at $\varphi = 0.2$ is somewhat larger than at $Re = 10$. The overall behavior can be explained by the observation that at low solid fractions and Reynolds numbers, the relative void space between particles is large enough that the effect of neighboring particle orientations is not as strongly felt. This situation changes as the solid fraction and Reynolds number increase and the flow perturbation created by neighboring particles propagates through the suspension. Since a particle aligned perpendicular to the flow creates the largest perturbation, the influence of increasing suspension S -value will increase the drag force felt by a particle independent of its inclination angle.



(a) $\varphi=0.1$



(b) $\varphi=0.15$



(c) $\varphi=0.20$

Fig. 3. 10. Variation of drag force on particles in the suspension at $Re=200$

The mean deviation of orientation dependent drag force between suspensions at $S \approx 0.5$ and $S \approx -1.0$ from the drag force at $S \approx 0$ is expressed as:

$$dev_{,\theta} = \frac{|\overline{F}_{d\theta,S} - \overline{F}_{d\theta,S \approx 0}|}{\overline{F}_{d\theta,S \approx 0}} \times 100\% \quad (3.8)$$

and tabulated in Table 3.1. At low solid fraction $\varphi=0.1$, the differences are bounded within 10%, which increases to about 12% at $\varphi=0.15$ and to 22% at $\varphi=0.20$.

Table 3. 1. Percentage mean deviation of orientation dependent drag at $S \approx 0.5$ and ≈ -1.0 compared to a random suspension $S \approx 0.0$.

Re		$\varphi=0.1$	$\varphi=0.15$	$\varphi=0.2$
10	S=-0.952	7.0	12.3	7.0
	S=0.523	7.5	10.0	15.0
50	S=-0.998	7.4	8.5	10.5
	S=0.564	8.2	10.6	15.7
200	S=-0.782	10.5	8.6	15.4
	S=0.675	8.8	11.7	22.0

3.4.4. Variation of Ensemble Mean Drag Force with S value of the suspension

In Lagrangian methods of representing the solid phase as point-mass particles such as Discrete-Element Method (DEM) and Euler-Euler methods such as the Two Fluid Model (TFM), it is the ensemble mean drag force that is mostly modeled based on local particle Reynolds number and solid fraction. In this section, the ensemble mean drag force of the suspension is related to the

orientational order parameter, S . Fig. 3.11 shows the variation of ensemble mean drag force with respect to S at $Re=50$ at different solid fractions. Each point in the plot represents the average drag force over all particles in the suspension. It can be observed that there is a strong positive correlation between the ensemble mean drag force and the S value – as S varies from -2.0 to 1.0 the drag force increases almost monotonically barring some local fluctuations. This is consistent with the expectation that particles parallel to the flow will have less drag force than particles perpendicular to the flow. The relative difference between the cases with $S = 1.0$ and $S = -2.0$ also varies at different solid fractions. Using the drag at $S = -2.0$ as reference, the relative difference between $S = -2.0$ and $S = 1.0$ at $\varphi = 0.10$ is 206%. It increases to 216% at $\varphi = 0.15$ and to 227% at $\varphi = 0.20$. The more than tripling of the drag force indicates that while modeling ensemble mean drag force of ellipsoidal particle suspensions, not only should the solid fraction and Reynolds number be considered, but due consideration should also be given to the overall suspension orientational preference.

Most importantly, from Fig. 3.11 an approximate linear relationship is observed between drag force and S . In order to construct the relationship one option would be to do a linear least-squares fit through all the data points, or the other option, which is taken, is to constrain the line to pass through the two end points at $S = -2.0$ and $S = 1$. The usefulness of the second option is significant as it greatly simplifies the task of constructing the dependence for other geometries using PRS – it would suffice to only perform two simulations at $S = -2.0$ and at $S = 1.0$ for a given Reynolds number and solid fraction to define the dependence of drag force on S . The linear function passing through the two end points is shown by the dashed lines in Fig. 3.11 (note that when more than one data point is available at the end points, the mean value is used). The linear approximation at $\varphi = 0.1$ has an R^2 value of 0.9631, at $\varphi = 0.15$ the R^2 becomes 0.9744, and at $\varphi = 0.2$, it is

0.9894. The mean relative deviations of the linear approximation are 4.56%, 4.52% and 4.04% for solid fraction at 0.10, 0.15 and 0.20, respectively.

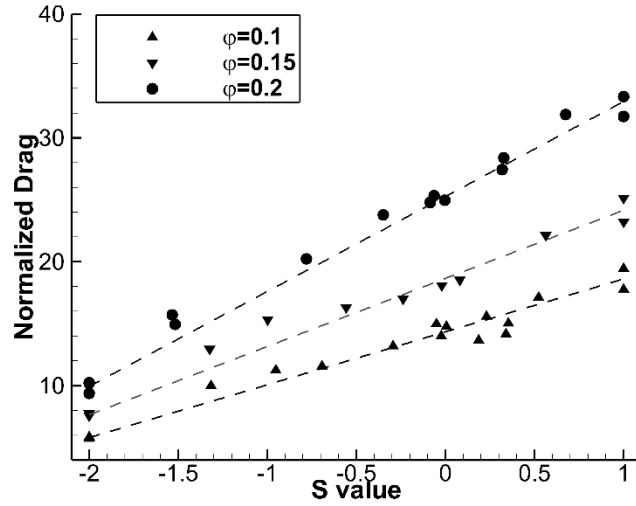


Fig. 3. 11. Variation of ensemble mean drag force with respect to S value of suspension at $Re = 50$.

Fig. 3.12 shows the results of drag force at $Re = 10$. Compared to $Re = 50$, the increase in drag force is smaller ($\cong 100\%$) between $S = -2.0$ and 1.0 and the linearity of the correlation between ensemble mean drag force and S is somewhat weaker. The mean relative deviation of the line fit with PRS is 5.96%, 6.85% and 8% for solid fractions of 0.10, 0.15 and 0.20, respectively. From the figure it can be observed that the linear fit tends to under-predict the drag force especially for $S < 0.0$. The deviation from linearity will be discussed further in the next section.

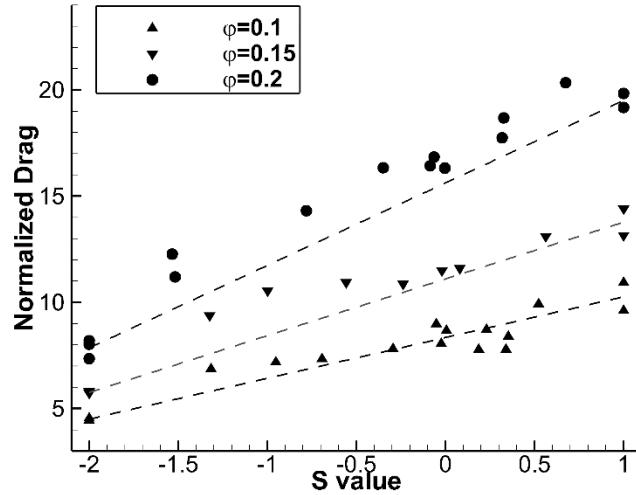


Fig. 3. 12. Variation of ensemble mean drag force with respect to S value of suspension at $Re = 10$.

Fig. 3.13 shows the results of mean drag force versus S for $Re = 200$. As the Reynolds number increases, the effect of the orientational parameter on the mean drag force increases – the drag increases by over 400% compared to particles oriented parallel versus normal to the flow direction. Once again the linear fit approximates the variation quite well with some over prediction at S values near zero. The mean relative deviations are 5.22%, 5.91% and 5.86% for $\phi = 0.10$, 0.15, and 0.20, respectively.

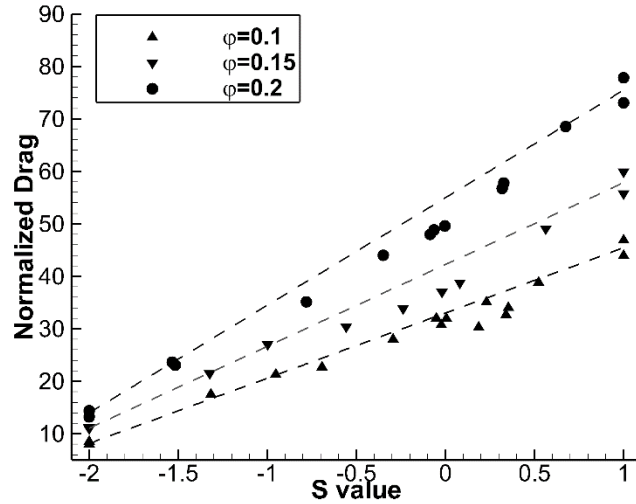


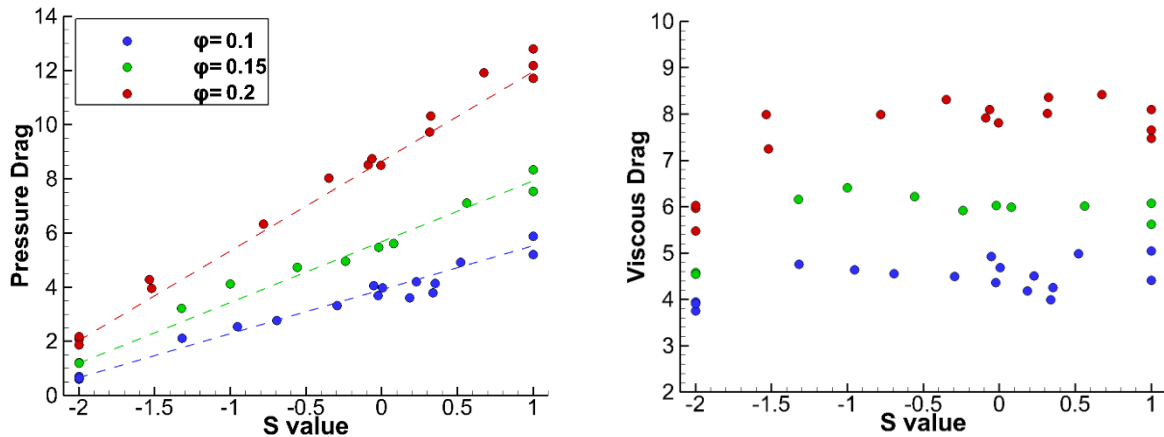
Fig. 3. 13. Variation of ensemble mean drag force with respect to S value of suspension at $Re = 200$.

It is noted that although the ensemble mean drag force is well represented by a linear trend with S , there is some scatter in the mean drag force at near-identical values of S . This is a result of statistical variance caused by different arrangements of a finite number of particles for each simulation (even for near-identical S -values).

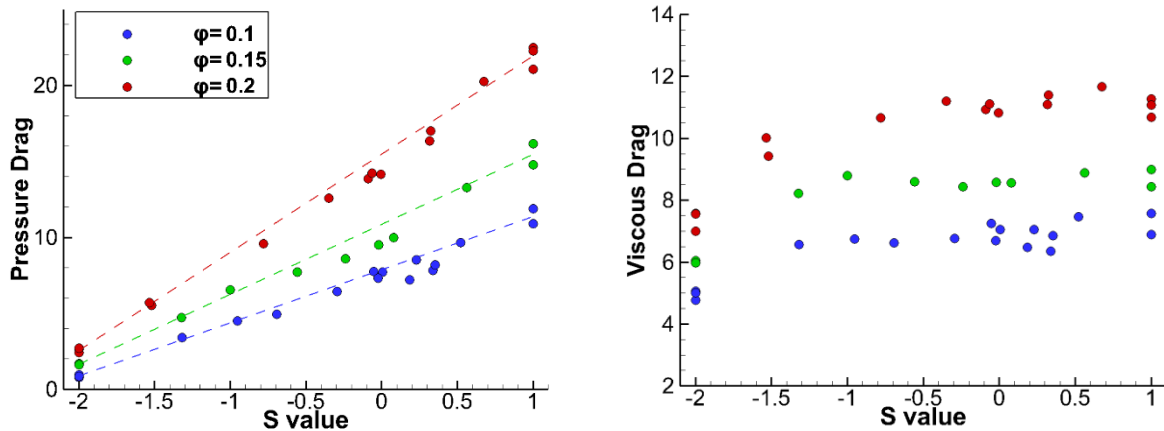
3.4.5. Contribution of Pressure and Viscous Drag forces

Though the variation of the ensemble mean drag force of the suspension is approximately linear with S , it is informative to investigate the effect of S on pressure and viscous drag in light of the observation that the deviation from linearity is most at low Re when viscous forces are important. The effect of preferential orientation on normalized pressure and viscous forces which make up total drag is investigated in Fig. 3.14 for all cases. At all Reynolds numbers normalized pressure drag increases monotonically with S whereas viscous drag exhibits a different behavior in which after an initial sharp increase between $-2 < S < -1.5$ the normalized drag increases minimally

for $S > -1.5$ in all the cases. Contrary to this trend normalized pressure drag exhibits a near linear increase. At $Re = 10$ and $S = -2.0$, viscous drag contributes between 70 – 80% of the total drag for all solid fractions, decreasing to between 40 – 50% at $S = 1.0$. Thus at $Re = 10$, because the viscous forces are significant and do not follow a linear variation with S , the total drag force shows the largest deviations from a linear relationship in Fig. 3.12. At $Re = 50$ and 200 however, the contribution of viscous forces to total drag steadily decreases and the total drag variation shows better agreement with the assumed linear variation with S . It is observed that at $Re = 200$ and $\phi = 0.15$ and 0.20 the pressure drag starts deviating from the linear relationship. However the total drag in Fig. 3.13 still maintains a fairly linear variation with S .



(a) $Re=10$



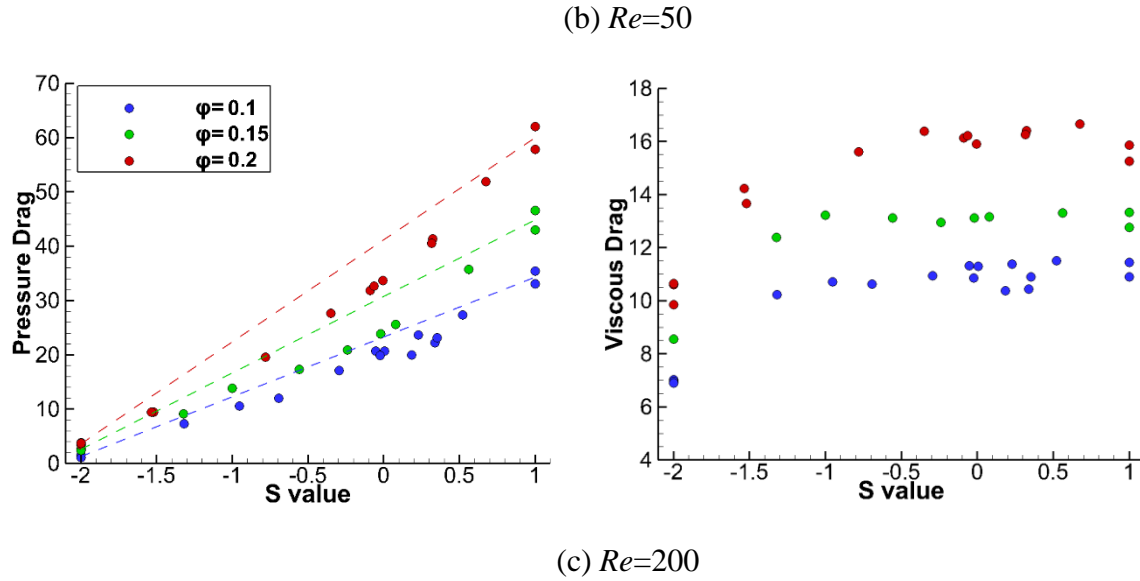
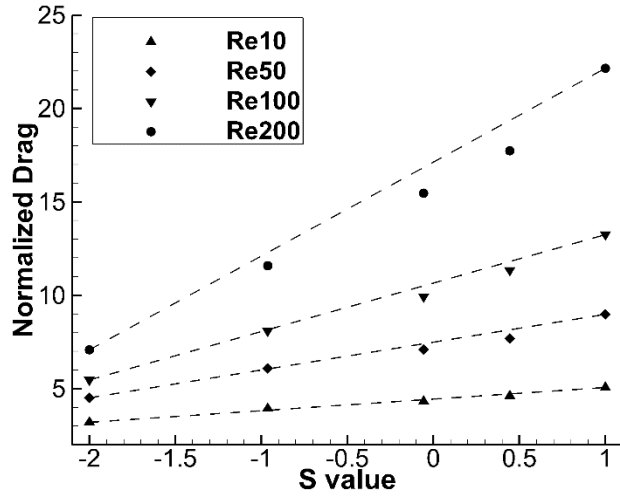


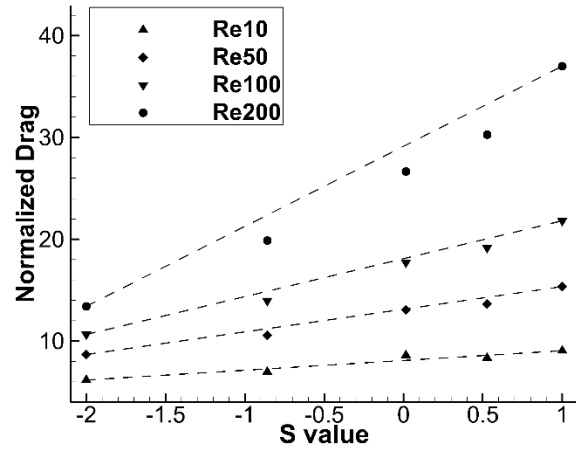
Fig. 3. 14. Variation of ensemble mean pressure and viscous drag force with respect to S value of suspension.

3.4.6. Effect of Ellipsoid Aspect Ratio

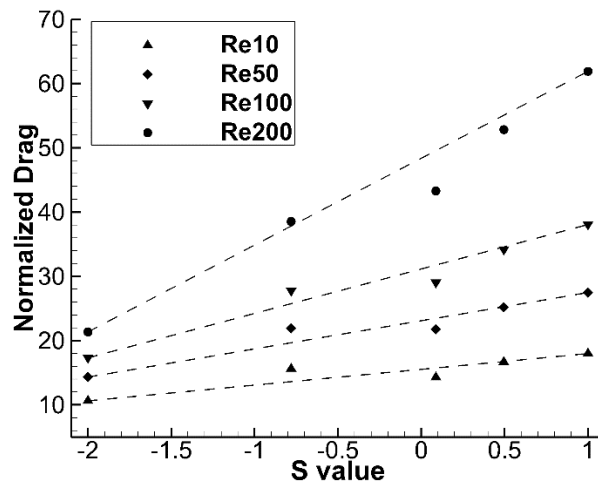
The above results establish the existence of an approximate linear correlation between mean drag force for suspensions of elongated ellipsoids with aspect ratio 10 and the suspension orientational preference. In order to establish that the linear relationship is not peculiar to the elongated high aspect ratio particles and to establish the generality of this trend, the relationship is tested for aspect ratio 2.5 particle suspensions for $Re = 10, 50, 100$ and 200 and $\varphi = 0.1, 0.2$ and 0.3 and the results are shown in Fig. 3.15. The results show that the linear variation between $S = -2$ and $S = 1$ predicts the drag force with a mean error of 4.4%, 7.5% and 6.8% for $\varphi = 0.1, 0.2$ and 0.3 , respectively, thus establishing the generality of the linear trend for prolate ellipsoidal suspension up to aspect ratio 10.



(a) Drag force at $\varphi = 0.10$



(b) Drag force at $\varphi = 0.20$



(c) Drag force at $\varphi = 0.30$

Fig. 3. 15. Variation of ensemble mean drag force with respect to S value of aspect ratio 2.5 ellipsoidal suspension. Symbols: PRS predictions; dash line: linear fit between $S = -2$ and 1.0.

3.5. SUMMARY AND CONCLUSIONS

The paper develops a broadly applicable simple relationship between suspension preferential orientation and drag force by performing 186 particle resolved simulations on suspensions of ellipsoidal particles with aspect ratio 10 and 2.5 for Reynolds numbers from 10 to 200 and solid fractions ranging from 0.10 to 0.30. An orientational parameter S is used such that it varies from -2.0 for all particles aligned with the flow to $S = 1.0$ for all particles lying normal to the flow direction with $S = 0$ specifying a random orientation in suspension. It is shown that to characterize the variation of suspension drag with orientational preference it is sufficient to specify the normalized drag force at $S = -2.0$ and $S = 1.0$ at each Reynolds number and solid fraction. By using a linear variation of drag with S between these two values, the drag at any preferential orientation parameter can be obtained. It is established that for the high aspect ratio ellipsoids the linear fit satisfies PRS results with mean deviation of less than 6% and for the low aspect ratio suspension to within 10%. These errors are miniscule in comparison to the large variation in drag forces experienced at different preferential orientations. It may not be unreasonable to deduce that the linear relationship would be a good approximation for any aspect ratio between 2.5 and 10.

This study has two major findings with respect to modeling drag in DEM-CFD and TFM simulations.

1. If the ensemble mean particle drag is to be used to model the drag force on a particle in suspension then the mean drag need only be calculated at $S = -2.0$ and $S = 1$ for a given Reynolds number, void fraction, and aspect ratio. Using these two values the mean drag force can be calculated for any other suspension with preferential orientation to within 10%.

2. If a correlation describing the variation of drag with orientation angle is available for a random suspension ($S = 0$) then at low solid fractions ($\varphi \leq 0.15$) and low Reynolds numbers ($Re \leq 50$) this relationship can be directly used to predict the orientation based drag (within 10-12%) on a particle at the same orientation existing in a suspension with $S \neq 0$. However, as Reynolds number and solid fraction increase the drag is overpredicted for $S < 0$ and underpredicted for $S > 0$ independent of the orientation angle of the particle by as much as 20%.

3.6. ACKNOWLEDGEMENTS

Ze Cao's research was supported in part by an appointment to the U.S. Department of Energy (DOE) Postgraduate Research Program at the National Energy Technology Laboratory administered by Oak Ridge Institute for Science and Education. The authors would also like to acknowledge the computational resources provided by Advanced Computational Research (ARC) at Virginia Tech.

Chapter 4

Convective Heat Transfer in suspensions of prolate ellipsoids

4.1. Abstract

Particle Resolved Simulations (PRS) using the Immersed Boundary Method (IBM) are performed for flow through suspensions of ellipsoids with aspect ratios of 2.5, 5, and 10 for solid volume fractions from 0.1 to 0.3 in the Reynolds number range from 10 to 200. The mean Nusselt number increases as $Re^{1/2}$ but shows only a weak dependence on the aspect ratio while increasing between 10-15% with an increase in solid fraction from 0.1 to 0.3. Two common practices of calculating Nusselt number in past literature are reconciled. It is shown that the suspension mean Nusselt number based on individual particles, by definition is always greater than or at the least equal to the Nusselt number based on the internal developing flow analogy. It is established that for $Re \leq 50$, the suspension heat transfer coefficient is very sensitive to the spatial distribution of particles or local-to-particle solid fractions. For the same mean solid fraction, suspensions dominated by particle clusters or high local solid fractions can exhibit Nusselt numbers which are lower than the minimum Nusselt number imposed by pure conduction on a single particle in isolation. This results from the dominant effect of thermal wakes at low Reynolds numbers. As the Reynolds number increases to 100 and beyond, the effect of particle clusters on heat transfer becomes less consequential. Unlike heat transfer, particle clustering has an insignificant effect on mean fluid forces such as drag.

Keywords: Heat transfer; Ellipsoidal particle suspensions; Particle Resolved Simulations; Immersed Boundary Method (IBM)

4.2. Introduction

Heat transfer in particle suspensions in packed as well as fluidized beds play an important role in many industrial processes. To investigate the heat transfer between fluid flow and

suspensions/packed beds of spherical/non-spherical particles, particle-resolved numerical simulations have become the *de facto* method for a growing number of researchers. To model these systems, different approaches of calculating the heat transfer coefficient or Nusselt number have been proposed. Tenneti et al. [54] used the internal developing flow analogy by imposing a constant temperature on the particle surface. Analogous to internal flow in a pipe or duct, the thermal state of the flow undergoes a region of development followed by a fully-developed region considering that the thermal environment in a homogeneous random mixture of particles would reach a statistical mean over many particles at a given streamwise location. Similar to that observed in internal flow, a rapidly decreasing Nusselt number is followed by a statistically constant Nusselt number in the fully-developed region. The Nusselt number is calculated based on the heat flux at the particle surface averaged over multiple particles and a reference fluid temperature based on the mixing cup [55] or mixed mean temperature [53] at each x – location. Using the Immersed Boundary Method (IBM), Tenneti et al. [1] simulated fluid flow through suspensions of spherical particles for solid fractions (φ) of 0.2 and 0.4 with Reynolds number range of [1, 100]. In a follow-up investigation [56] with extended φ range from 0.1 to 0.5, they proposed a new heat transfer correlation for spherical particle suspensions. Based on the same Nusselt number calculation approach, Tavassoli et al. [57] investigated the same Re range of [1, 100] for spherical particle suspensions with φ from 0.1 to 0.5 and good agreement was observed with the results of Tenneti et al. [54]. Aside from particle suspensions, Singhal et al. [58] simulated a packed beds of spheres in the Reynolds number range of [9, 180] and developed a correlation for Nusselt number. As for research on non-spherical particles, ellipsoid suspensions with aspect ratio 2.5 under solid fraction range of [0.1, 0.35] with Re of [10, 200] have been simulated by He and Tafti [53]. They modified Gunn’s [55] Nusselt number correlation, to develop a correlation for the 2.5 aspect ratio ellipsoidal suspension. Singhal et al. [59] simulated flow over packed beds of cylinders with aspect ratios 2, 4, and 6 and proposed a general heat transfer correlation applicable to packed beds of not only cylinders, but also spherical particles. Simulation results for spherocylinders with aspect ratio of 2, 3 and 4 for $\varphi \in [0.1, 0.6]$ from Tavassoli et al. [60] indicated that with the sphere equivalent particle diameter chosen as reference length, spherical particle heat transfer correlation [55] is also applicable for suspensions of spherocylinders.

While the above method expresses Nusselt number as a function of the streamwise distance, it does not define the Nusselt number for individual particles. This is an important quantity because

individual particle heat transfer could vary substantially from the mean value obtained over many particles. Therefore, instead of using the mixing cup temperature as the reference temperature, Chen and Müller [61] defined a cubic box of size $3d$ (d – diameter) around each spherical particle in the suspension (their cubic domain size varied from $\sim 4d$ to $\sim 7d$ to accommodate different solid fractions with 54 to 61 particles) and used the mixed mean temperature of the fluid within the box as reference temperature to calculate the Nusselt number for each particle. They [61], under fully-developed conditions (periodic boundary conditions in all three directions) compared their results with those derived by Tavassoli et al. [57] and Sun et al. [56] using the mixing cup temperature. Tavassoli et al. [57] used a cubic domain of size ranging from $\sim 4d$ to $\sim 7d$ with 54 particles under developing flow conditions. Sun et al. [56] also used a cubic domain of size $\sim 4d$ to $\sim 7d$ with number of particles ranging from 61 to 161 under fully-developed conditions (periodic in all three directions). On comparison, Chen and Müller observed good agreement with Tavassoli et al. [57] for $\varphi = 0.1$ and 0.3 . For $\varphi = 0.5$, significant deviation appeared which was attributed to the possible underestimation of the thermal developing region in the Nusselt number calculation by Tavassoli et al. [57], resulting in higher values. On comparing their results with Sun et al. [56], Sun et al.'s predictions were lower over the whole range of φ and Re . This was attributed by Chen and Müller to the invalidity of the assumed similarity used by Sun et al. [56] between a thermally fully-developed pipe flow with isothermal walls and a packed bed. In contrast, using thermally developing flow, He and Tafti [53] observed that their Nusselt numbers calculated using the mixing cup temperature agreed well with Sun et al. [56] up to $Re=100$ indicating that there could be other factors contributing to the deviation of Chen and Müller [61] with Tavassoli et al. [60] and Sun et al. [56].

Following this, Chen and Müller [62] investigated heat transfer in a suspension of cubic particles and concluded that a box size of $3d_p$, where d_p is the cube's volume equivalent sphere diameter, is representative enough of the surrounding fluid for estimating the heat transfer coefficient. Besides, it was found in their paper that with Re and Nu defined based on the hydraulic and Sauter diameter of the particle, respectively, their proposed correlation is not only applicable for cubes, but also ellipsoids [53] and cylinders [59]. Furthermore, by implementing the same method for Nusselt number calculation and choosing a cubic box of size $5d$ as suggested in the literature [63–65], Lu et al. [66] investigated the correlation between the heat transfer rate and the local flow

velocity around the particles in the suspension and concluded that there was no correlation between the two quantities. In yet another study to investigate the local heat transfer coefficient on the particle surface, Kravets and Kruggel-Emden [67] introduced a different procedure for Nusselt number calculation in a spherical suspension which can be regarded as a hybrid of the above mentioned two methods. In their calculation, they used the cup mixing temperature as the fluid reference temperature, and calculated the local Nusselt number at each lattice node defining the particle surface making it possible to investigate not only the Nusselt number of each particle in the suspension, but also the local heat transfer rate on the particle surface at different polar angles. Their calculated Nusselt number is validated in [68] through comparisons with correlations [55,60,69] in literature.

In past work, most heat transfer investigations have been performed in spherical particle suspensions with a few in non-spherical particle suspensions such as sphero-cylinders of aspect ratio 2 to 4 [60], packed beds of cylindrical particles [59], and by Chen and Müller [62] for square super-ellipsoid suspensions. The current paper extends the investigation of He and Tafti [53] for an aspect ratio 2.5 ellipsoidal suspension by covering a broader range of geometries. In this paper we investigate the heat transfer coefficient in random suspensions of ellipsoids by repeating some of the calculations of He and Tafti [53], albeit in a larger domain with more particles, and with additional aspect ratios 5 and 10. The Reynolds number range covered is 10 to 200 and solid fractions vary from 0.1 to 0.3. The relationship between particle based Nusselt number and the Nusselt number derived through an analogy with the fully developed flow assumption borrowed from internal flows is investigated in detail together with the effect of particle distribution on heat transfer characteristics of the suspension.

4.3. Numerical method and simulation setup

4.3.1. Governing equations

Under the assumption of constant property, incompressible flow, the governing equations are solved in the framework of an in-house CFD code – GenIDLEST (Generalized Incompressible Direct and Large Eddy Simulation of Turbulence) using the Immersed Boundary Method (IBM). The equations describing mass, momentum, and energy conservation are solved in their dimensionless form given by

Continuity:

$$\frac{\partial u_i}{\partial x_i} = 0 \quad (4.1)$$

Momentum:

$$\frac{\partial u_i}{\partial t} + \frac{\partial}{\partial x_j} (u_i u_j) = -\frac{1}{\rho} \frac{\partial p}{\partial x_i} + \frac{\partial}{\partial x_j} \left(\frac{1}{Re} \left(\frac{\partial u_i}{\partial x_j} \right) \right) \quad (4.2)$$

Energy:

$$\frac{\partial T}{\partial t} + \frac{\partial}{\partial x_j} (u_j T) = \frac{\partial}{\partial x_j} \left(\frac{1}{Re \cdot Pr} \left(\frac{\partial T}{\partial x_j} \right) \right) \quad (4.3)$$

with the following non-dimensionalizations

$$u_i = \frac{u_i^*}{u_{ref}^*}; \quad x_i = \frac{x_i^*}{l_{ref}^*}; \quad p = \frac{p^* - p_{ref}^*}{\rho_{ref}^* u_{ref}^{*2}}; \quad t = \frac{t^* u_{ref}^*}{l_{ref}^*}$$

$$T = \frac{T^* - T_{ref}^*}{T_0^*}; \quad Re = \frac{\rho_{ref}^* u_{ref}^* l_{ref}^*}{\mu_{ref}^*}; \quad Pr = \frac{c_{pref}^* \mu_{ref}^*}{k_{ref}^*}$$

where superscript (*) represents dimensional variables. In the process of non-dimensionalization, the superficial fluid velocity U_{in}^* is taken as u_{ref}^* and diameter d_{eq}^* of the ellipsoid's volume equivalent sphere is taken as l_{ref}^* . T_{ref}^* is the inlet flow temperature T_{in}^* , and $T_0^* = \frac{q_s''^* l_{ref}^*}{k_{ref}^*}$, where $q_s''^*$ is the uniform heat flux applied at the particle surface.

The governing equations are solved using a collocated or non-staggered finite volume formulation with implementation of second-order central (SOC) difference discretization scheme [34,35]. Variables including flow velocities, pressure and temperature are calculated and stored at computational cell center whereas fluxes are calculated and stored at cell faces. A predictor-corrector formulation is used for time integration of the velocity: an intermediate velocity field is calculated in the predictor step followed by a pressure correction applied to the velocity field to satisfy discrete continuity.

4.3.2. Particle generation and immersed boundary method (IBM)

The ellipsoidal particle shape investigated in this research is generated using:

$$\left(\frac{x}{a}\right)^2 + \left(\frac{y}{b}\right)^2 + \left(\frac{z}{c}\right)^2 = 1 \quad (4.4)$$

Prolate ellipsoidal particles are investigated with aspect ratio 2.5 (abbreviated as AR2.5), 5 (AR5) and 10 (AR10) with sphericities (ratio of surface area of equal volume sphere to particle surface area) ranging from 0.887 to 0.593, respectively. The number of elements used to resolve the surface area of each particle ranges from 2100 to 7500 as shown in Table 4.1. It is noted that the element size is commensurate with the background grid resolution and the number of elements increase as the surface area of the particle. The particle surface grids are shown in Fig. 4.1 for the three aspect ratios.

Table 4. 1. Geometry and surface grid specification of ellipsoidal particles.

Aspect ratio (AR)	AR2.5	AR5	AR10
(a,b,c) in Eqn. 4	(0.92,0.37,0.37)	(1.46,0.29,0.29)	(2.32,0.232,0.232)
Sphericity (Φ)	0.887	0.735	0.593
Surface elements	2172	4176	7538

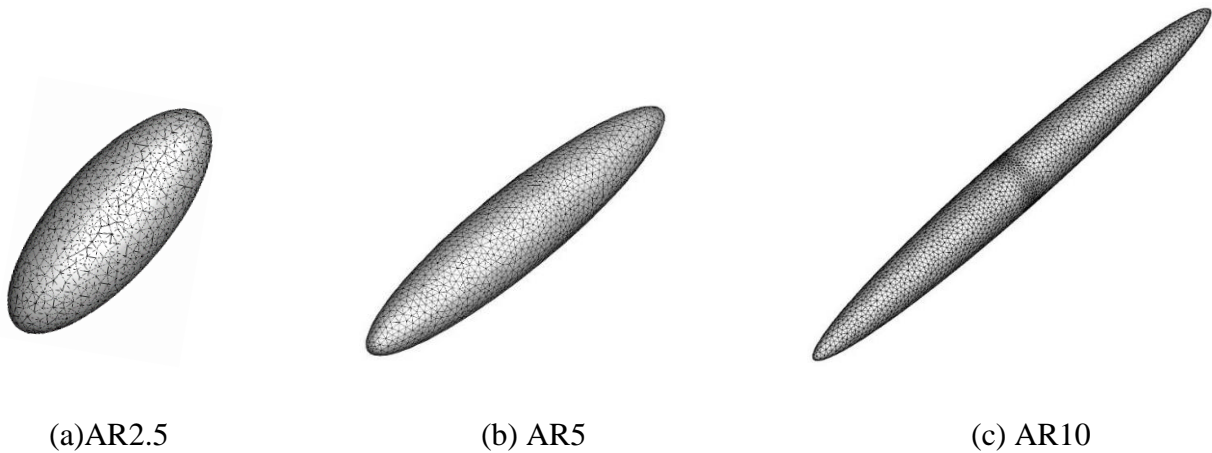


Fig. 4. 1. Surface meshes of ellipsoid with aspect ratio of 2.5, 5 and 10.

The particles defined by their individual surface meshes are immersed in a background multi-block volume mesh composed of structured non-uniform orthogonal cells. The IBM method is implemented in generalized coordinate system and is fully described in Nagendra *et al.* [36]. It uses a sharp-interface indirect forcing method. In this implementation, no additional forcing term is used in the governing equations. Instead, solution to the governing equations is suitably modified at grid nodes that lie in the immediate vicinity of the immersed surface. The major steps in the implementation can be listed as follows: (1) identify the location of the immersed surface and designate surrounding nodes as fluid or solid; fluid nodes immediately adjacent to the IB surface are labelled as IB nodes (2) solve the governing equations at all nodes in the domain except at the IB nodes, and (3) apply a special treatment to reflect the presence of an immersed surface with specified boundary conditions at the IB nodes.

In (1) above, three primary node types are defined – fluid, solid and IB. The fluid and solid node definitions are trivial – any node that lies in the fluid region is a fluid node and if not, it is a solid node. An IB node, on the other hand, is any fluid node that lies in the immediate vicinity of the immersed boundary. To implement the boundary conditions in step (3) two probes are projected into the flow field, on lines normal to the IB surface and passing through the IB nodes [22,23]. In the context of the present study, no slip, no penetration Dirichlet boundary conditions are implemented at the IB surface for the velocity field in the momentum equations, and Neumann conditions for the solution of the pressure Poisson equation and the energy equation. Similarly, to determine the Nusselt number, the particle surface temperature is obtained at each surface element centroid by projecting a normal into the flow and using temperature values at two probe locations to satisfy the constant heat flux boundary condition at the surface.

4.3.3. Simulation setup

Ellipsoidal particle suspensions from Cao *et al.* [70] are directly adopted in this work. An identical rectangular computational domain of size $30 \times 10 \times 10$ in the x -, y -, and z - directions is employed as shown in Fig. 4.2. In each calculation, 286, 430, 573, and 859 randomly distributed particles are placed between $5 \leq x \leq 20$ for solid fractions $\phi = 0.1, 0.15, 0.2$ and 0.3 , respectively. Solid fractions $\phi = 0.1, 0.2$ and 0.3 are calculated for AR2.5 and AR5 particle shapes whereas $\phi = 0.1, 0.15$ and 0.2 are calculated for AR10 particle shapes. For each case, four Reynolds numbers $Re = 10, 50, 100,$ and 200 are calculated. Each condition is simulated for two independent particle arrangements and the average results are reported.

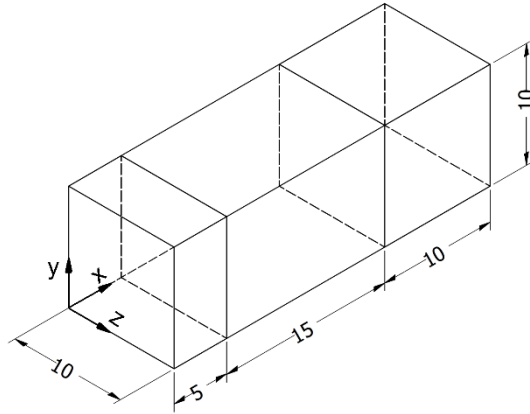
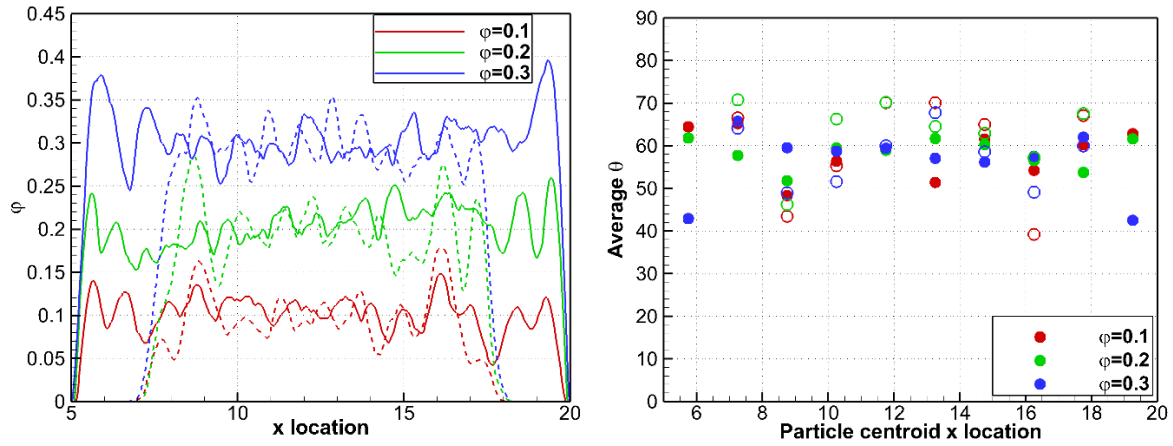
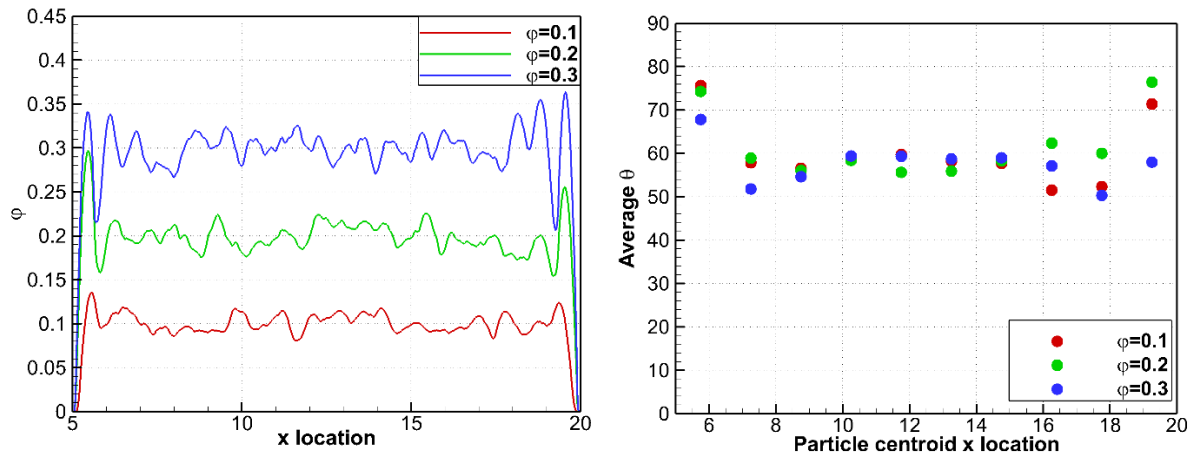


Fig. 4. 2. 3D view of the computational domain

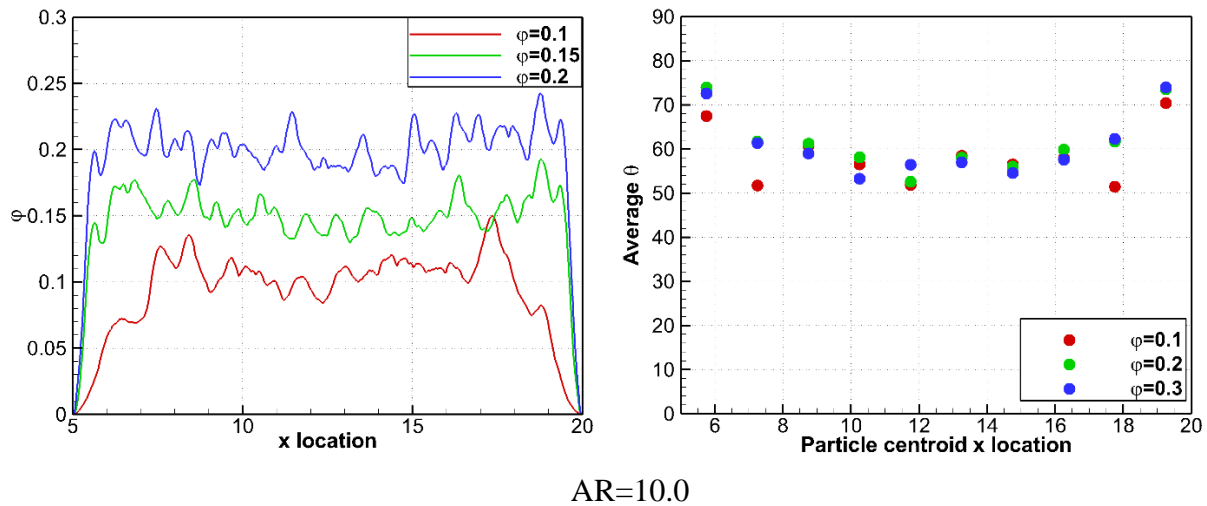
An incoming flow with homogeneous dimensionless x –velocity and temperature of 1.0 and 0, respectively, is specified at the entrance to the domain. At the outlet, zero gradients of pressure, velocity, and temperature are used. Periodic boundary conditions in y - and z - directions simulate a particle suspension with infinite extent in these two directions. Fig 4.3 presents the distribution of solid fraction (defined as ratio of solid cells over total number of cells at a given x –location) and mean inclination angle of particle (θ , defined as the angle between the major axis of particle and streamwise x –direction). Also shown for comparison are the corresponding distributions of He and Tafti [53] for AR=2.5 particle suspensions. In all cases the local solid fraction fluctuates about the intended nominal mean value. There are no perceptible systemic differences between He and Tafti [53] and the current suspensions with the exception that in He and Tafti [53] the suspension extends 10 units in x versus 15 units in the current work. In the random suspensions generated, the mean inclination angle is expected to be 57.3 degrees which is closely reproduced in all particle arrangements over the length of the region. However, there are local variations in mean orientation angle. In the current suspensions, all solids are contained within $5 \leq x \leq 20$. Because of the high aspect ratio particles, this results in particles being placed at high inclination angles in the entrance and exit regions of the suspension followed by lower angular orientations in the interior. This requirement was not enforced by He and Tafti [53] thus allowing particles with major axis more closely aligned with the x –direction.



(a) AR=2.5



(b) AR=5.0



AR=10.0

Fig. 4. 3. Void fraction and average inclination angle distribution of particles along x –direction. (Dash lines and empty symbols represent suspensions of He and Tafti [53] for AR2.5 particles.)

No slip velocity boundary conditions and constant dimensionless heat flux, $q_s'' = 1$ are specified at the particle surface. Although constant temperature has been widely implemented by previous researchers [54,56–60], it has been reported by Sun et al. [56] and confirmed by our own experiments [53], that under relatively high solid fractions and low Reynolds numbers, the fluid temperature develops quickly to approach the particle surface temperature. As this happens, not only does the fluid - solid temperature difference approach zero but so does the heat flux from the surface resulting in spurious numerical noise in the calculation of the heat transfer coefficient. Previous works typically have used much smaller domain lengths in the flow direction. For example, Tavassoli et al. [57] and Chen and Müller [62] mostly use a fixed number of particles (54 to 61) and vary the domain size to simulate different solid fractions. As a consequence, their domain length in the flow direction decreases as the solid fraction increases thus mitigating the issue of the fluid temperature approaching the particle temperature. On the other hand, a smaller domain used with the thermally developing flow assumption as in Tavassoli et al. [57], could also increase the likelihood that the calculated heat transfer coefficients will include effects from the thermally developing region. Similarly, under the thermally fully-developed periodic flow assumption (Sun et al. [56]), a small domain size in the flow direction could admit solutions in which the temperature field remains spatially correlated over the periodic length and the thermal wake of a particle could unduly influence its own thermal environment. For these reasons, in the current study, a much larger domain is used to accommodate a statistically significant number of particles and to ascertain that the heat transfer is indeed reported in the thermally fully-developed region¹. To avoid temperature saturation, a constant heat flux boundary condition is specified at the particle surface. As discussed in He and Tafti [53], the average Nusselt number calculated from these two boundary conditions presents reasonable agreement at different Reynolds numbers.

4.3.4. Nusselt number definitions

One method used in the literature [54], which we will denote Method A, is based on the analogy between heat transfer in a statistically homogeneous particle suspension and convective heat

¹ It will be shown in the results that the thermally fully-developed region is never fully achieved at $Re=10$ and $\phi=0.1$ in spite of the large streamwise length of suspension.

transfer of internal flow. In this, a mixed mean fluid temperature is defined along the flow direction (x) which is calculated using:

$$T_{mf}(x) = \frac{\iint_A |u(\vec{x})| \cdot T(\vec{x}) \rho dydz}{\iint_A |u(\vec{x})| \rho dydz} \quad (4.5)$$

Note that in Eqn 4.5, the absolute velocity is used to prevent negative contributions to the sum. The average particle surface temperature $T_{ms}(x)$ is calculated as follows

$$T_{ms}(x) = \frac{1}{\sum_1^{N_x} \Omega_n} \sum_{n=1}^{N_x} \Omega_n T_s(x, n) \quad (4.6)$$

where N_x denotes the number of surface elements over multiple particles whose centroid lies within $x \pm 1/80$ and Ω_n is the area of the surface element. Using Eqns. (4.5) and (4.6) the Nusselt number is calculated as

$$Nu_A(x) = \frac{q_s''}{T_{ms}(x) - T_{mf}(x)} \quad (4.7)$$

where $q_s'' = \frac{q_s''^*}{\frac{k_{ref}^* T_o^*}{l_{ref}^*}} = 1$ is the dimensionless heat flux applied at the particle surface. The average

Nusselt number \overline{Nu}_A is calculated by taking the arithmetic mean of $Nu_A(x)$ over the x –range of interest which can be written as:

$$\overline{Nu}_A = \frac{q_s''}{\overline{T}_{ms} - \overline{T}_{mf}} \quad (4.8)$$

where

$$\bar{T}_{mf} = \frac{\iiint_{\forall_x} |u(\vec{x})| \cdot T(\vec{x}) \rho \cdot d\forall_x}{\iiint_{\forall_x} |u(\vec{x})| \cdot \rho \cdot d\forall_x} \quad (4.9)$$

and

$$\bar{T}_{ms} = \frac{1}{\sum_1^N \Omega_n} \sum_{n=1}^N \Omega_n T_s(x, n) \quad (4.10)$$

where \forall_x is the volume of the domain and N are the total number of surface elements spread over all particles in the x –range of interest.

Method A does not allow the specification of the heat transfer coefficient associated with individual particles, so Chen and Müller [61] to investigate the local heat transfer coefficient for each individual particle in the suspension used a different method by calculating the fluid mixed mean temperature near the particle. They did that by associating a volume surrounding each particle over which the fluid mixed mean temperature is calculated. The method, which we refer to as Method B is implemented in our case by using an ellipsoidal shaped shell of thickness δ around each particle defined as:

$$\left(\frac{x}{a+\delta}\right)^2 + \left(\frac{y}{b+\delta}\right)^2 + \left(\frac{z}{c+\delta}\right)^2 = 1 \quad (4.11)$$

The bulk mean fluid temperature within this shell of volume \forall_b is calculated by:

$$T_{pf}(n_p) = \frac{\iiint_{\forall_b} |u(\vec{x})| T(\vec{x}) \rho \cdot d\forall_b}{\iiint_{\forall_b} |u(\vec{x})| \rho \cdot d\forall_b} \quad (4.12)$$

together with the average particle surface temperature

$$T_{ps}(n_p) = \frac{1}{\sum_1^{N_e} \Omega_n} \sum_{n=1}^{N_e} \Omega_n T_s(n) \quad (4.13)$$

where n_p is the particle number and N_e is the total number of surface elements on particle n_p and Ω_n is the surface area of each element.

The Nusselt number of each individual particle in the suspension is then calculated as:

$$Nu_B(n_p) = \frac{q_s''}{T_{ps}(n_p) - T_{pf}(n_p)} \quad (4.14)$$

Note that because of the nature of the definition of the heat transfer coefficient in Eqn. 4.14, the conditions local to a particle may result in extremely high or negative Nusselt numbers if $T_{ps} \leq T_{pf}$. It is quite likely and physical that in the shell of thickness δ around the particle of interest, the mixed mean temperature of the fluid may be greater than or nearly equal to the particle surface temperature because of the influence of other particles in the vicinity. This scenario becomes more prominent at low Re and high ϕ but is admissible and physical in the context of calculating the average Nusselt number over all particles given by

$$\overline{Nu}_B = \frac{1}{\frac{1}{N} \sum_{n_p=1}^{n_p=N} (1/Nu_B(n_p))} \quad (4.15)$$

While both methods of calculating Nusselt number ($\overline{Nu}_A, \overline{Nu}_B$) have been used in the literature, no study has established a formal relationship between the two definitions. In fact, Eqns. 8 and 15 become identical if the hypothetical shell size (δ) around each particle is chosen such that \forall_b in Eqn 4.12 approaches \forall_x in Eqn 9 for each particle. As will be shown later, this leads to the condition that $\overline{Nu}_B \geq \overline{Nu}_A$.

4.3.5. Grid independency study and validation

The background grid used in this work has been adopted from our previous investigations of hydrodynamic forces and heat transfer in particle suspensions [27,28,53,71]. Noting that suspension heat transfer prediction is derived from individual particles in suspensions, grid qualification on an isolated particle is a valid means for establishing grid independency of the suspension.

Cao and Tafti [37] validated heat transfer predictions on an isolated spherical particle with other IBM calculations [72,73], with their own body conforming grid calculations, and empirical

correlations in the literature [74]. The result in Fig. 4.4 shows excellent agreement with other IBM calculations and correlations with deviations of less than 5%. For the IBM calculations they tested a resolution of $1/40$ (or $d_{eq}/40$) and $1/20$ and found that at $Re=200$, the predicted Nusselt number at $1/20$ resolution was within 3.3% of the $1/40$ resolution.

Accompanying fluid force calculations on an isolated cylindrical shaped particle with aspect ratio of 0.25, Cao and Tafti [37] also simulated heat transfer for different Reynolds numbers and particle inclination angles. Grid resolutions of $1/30$, $1/40$ and $1/50$ of the particle's volume equivalent sphere diameter were tested. Using the particle Nusselt number derived from grid spacing of $1/50$ as reference, the maximum deviation for meshes with $1/30$ and $1/40$ resolutions was 3.30% and 1.83%, respectively.

For the high aspect ratio AR10 ellipsoid, which is the most extreme geometry investigated in this paper, grid independency studies are done on a single particle placed parallel (inclination 0° within a domain size of $24 \times 15.5 \times 15.5$) and perpendicular (inclination 90° within a domain size of $20 \times 17.5 \times 13.5$) to the flow for three background grid resolutions of $1/40$, $1/60$ and $1/80$ at the highest Reynolds number used in this investigation, $Re=200$. The results presented in Table 4.2, show that the $1/40$ grid resolution is within 2% of the Nusselt number using $1/80$ grid resolution for both orientations.

Finally to supplement the single particle grid independency study, an additional grid independency study is also conducted on a suspension of AR10 particles at $\varphi = 0.2$ and $Re=200$. Both Nu_A and Nu_B are calculated for the suspension on background grids of $1/40$ and $1/50$ resulting in 128 million and 250 million total grid sizes, respectively. A relative deviation of 2.37% is observed in $\overline{Nu_A}$. For individual particle Nu_B , 92% of the particles present deviations of less than 5%, with a mean deviation in $\overline{Nu_B}$ of 2.48%.

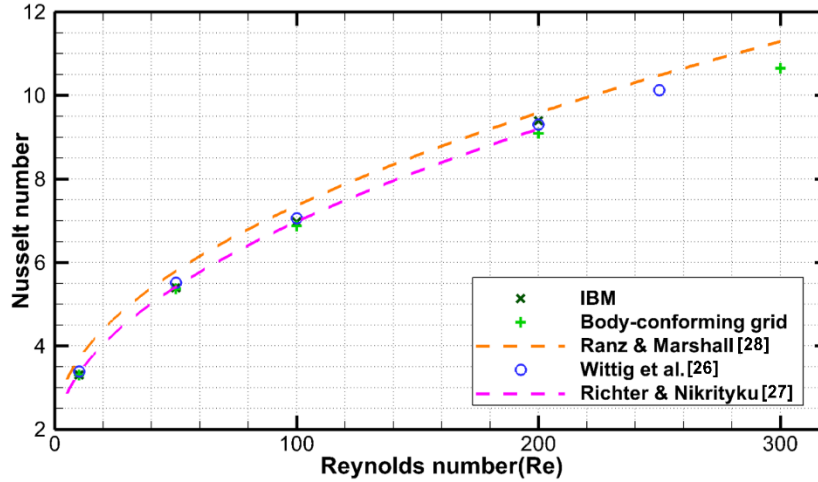


Fig. 4. 4. Validation of Nusselt number for an isolated sphere in uniform flow.

Based on the numerous grid independency studies done, balancing both computational efficiency and simulation accuracy, a grid resolution of 1/40 is employed between $5 \leq x \leq 20$ to resolve the particles with a total grid of size of 128 million cells over a domain size of $30 \times 10 \times 10$ for the PRS results presented in this paper.

Table 4. 2. Nusselt number ($Nu = h^* d_{eq}^* / k^*$) prediction for single AR10 ellipsoid in uniform flow at Re=200.

<i>Volume grid (Δ)</i>	1/40	1/60	1/80	% difference
<i>Surface grid size (N)</i>	7538	7538	28500	
Parallel to flow, 0°	6.47	6.50	6.56	<1.5%
Normal to flow, 90°	12.05	11.85	11.85	1.7%

4.4. Results and Discussion

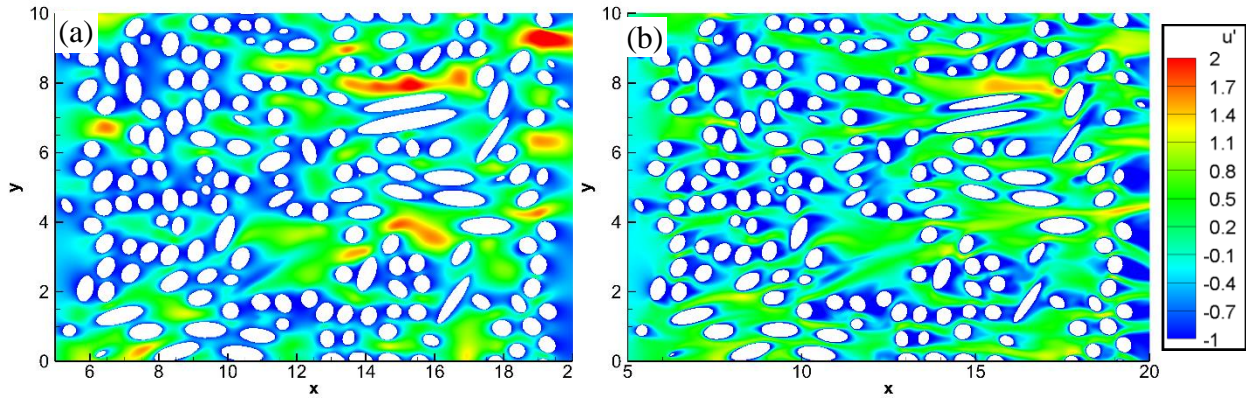
4.4.1. Flow and Thermal fields within particle suspensions

The general characteristics of the velocity and temperature field are first investigated. As the flow traverses the suspension, the random particle locations and orientations give rise to strong interstitial flow accelerations and decelerations which influence energy transport and heat transfer.

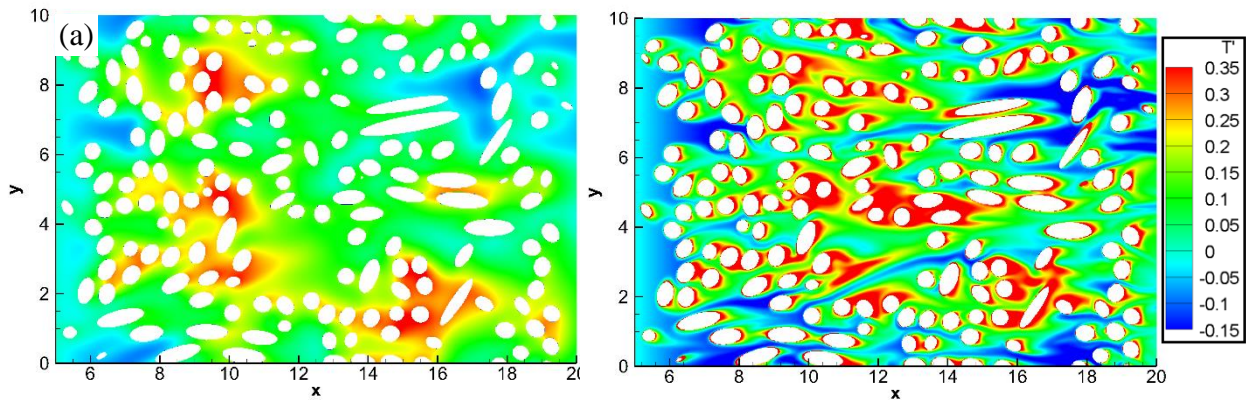
Fig. 4.5(a) shows x –directional flow velocity fluctuation in AR10 ellipsoid suspensions at $\varphi = 0.2$, $Re=10$ and 200 which is calculated using:

$$u' = \frac{u - u_{mean}}{u_{mean}} \quad (4.16)$$

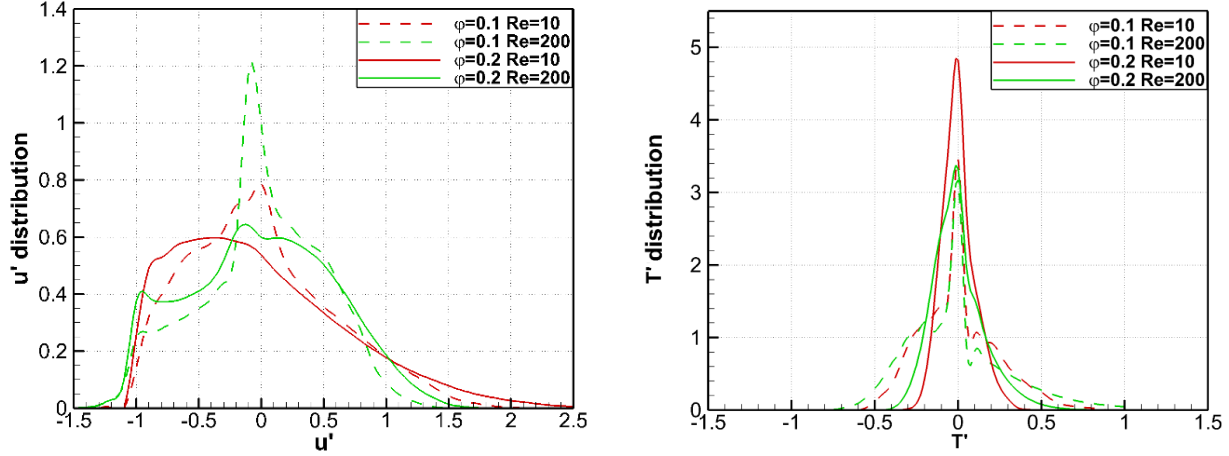
where u_{mean} is the mean fluid velocity through the particle suspension. It can be seen that at $Re=10$, the flow is dominated by viscous effects resulting in thick boundary layers on particle surfaces. Consequently, continuous, bridged low velocity regions can be found especially within particle clusters. At $Re=200$, the bridged low velocity regions are replaced by channels of higher velocity fluid between particles as the boundary layers become thinner. Interestingly, $Re=10$ exhibits larger extreme deviations from the mean than does $Re=200$. These features of the velocity field are more generally characterized by studying the Probability Density Functions (PDF) of u' distribution in the three-dimensional computational domain.



(a) $x - y$ planes of the x –directional flow velocity fluctuation (left: $Re=10$, right: $Re=200$)



(b) $x - y$ planes of fluid temperature fluctuation (left: $Re=10$, right: $Re=200$)



(c) Probability Density Function of u' (left) and T' (right) distribution

Fig. 4. 5. Flow velocity and temperature fluctuations within AR10 ellipsoid suspensions.

The PDFs of u' distribution for AR10 ellipsoid suspensions under different flow conditions are presented in Fig. 4.5(c). Both, effects of Reynolds number and solid fraction are shown. Comparing the effect of Reynolds number at $\phi = 0.2$, $Re=10$ has a higher probability of producing large fluctuations, $-1 < u' < 0$ and $u' > 1.5$ than $Re=200$. At $Re=200$, the extreme fluctuations are tempered and somewhat homogenized and are concentrated at and near zero (the mean value) much more so than at $Re=10$. These trends are consistent with the observations made in a single $x - y$ plane in Fig 4.5 (a). The same general trends are reflected at the lower $\phi = 0.1$ between $Re=10$ and 200. As the solid fraction decreases to $\phi = 0.1$, less of the fluid volume is affected by the presence of particles and thus the probability of fluctuations at or near zero (mean value) increases for both Reynolds numbers.

Since the temperature field is largely influenced by the velocity field, the fluid temperature fluctuations defined as:

$$T' = \frac{T - T_{mf}(x)}{T_{out} - T_{in}} \quad (4.17)$$

where T_{in} and T_{out} represent the spatially averaged inlet and outlet fluid temperatures and $T_{mf}(x)$ is the mixed mean temperature defined in Eqn. 4.5. Fig. 4.5(b) presents T' slices at $x - y$ planes identical to Fig 4.5 (a) to facilitate comparison. Generally, regions of negative or low velocity fluctuation are correlated to regions of high positive temperature fluctuation at a given

x – location, and vice versa. Regions of high positive temperature fluctuations surrounding particles result in heat transfer coefficients lower than the mean at a given x –location. Thus at $Re=10$, the preponderance of negative velocity fluctuations in particle wakes and particle clusters at $8 < x < 10$ and $14 < x < 16$ results in the local temperature being higher than the mixed mean temperature. Conversely, high velocity regions resulting from flow acceleration in the interstitial spaces results in temperatures lower than the mixed mean temperature. As Re increases to 200, the trends remain the same with the notable differences that the range of temperature fluctuations about the mean increase. This is due to the combined effect of thinner thermal boundary layers and extended high temperature wakes that significantly influence the fluctuations about the mixed mean. Notably, this is contrary to velocity fluctuations which reduce with increase in Reynolds number from $Re=10$ to 200.

For a more complete picture, PDFs of T' over the whole computational domain are presented in Fig. 4.5(c). The $x - y$ planar trends observed in Fig 4.5 (b) are confirmed by the volume PDFs. As Re increases from 10 to 200, the temperatures spread out to larger values as the fluctuations intensify, with less concentration near the mixed mean at $T' = 0$. As φ decreases to 0.1, there are less pronounced differences between the two Reynolds numbers. For both $Re=10$ and 200, the frequency of large positive and negative fluctuations increases because of the relative sparsity of the particles and the weaker mixing.

4.4.2. Nusselt number predictions

Method A assumes similarity with heat transfer in internal flow and calculates the evolution of the fluid mixed mean temperature $T_{mf}(x)$ and the particle surface temperature $T_{ms}(x)$ to obtain the Nusselt number $Nu_A(x)$ using Eqn. 4.7. As the flow traverses the heated suspension of particles, both $T_{mf}(x)$ and $T_{ms}(x)$ increase with x . Based on the analogy with internal flow subject to a constant heat flux boundary condition, a fully-developed state is reached when $(T_{ms}(x) - T_{mf}(x))$ reaches a constant value. Examples of development of these temperatures is presented in Fig 4.6 for AR2.5 and AR10 ellipsoid suspensions at $Re=10$ and $Re=200$ for the lowest and highest solid fractions investigated, respectively. Unlike internal flows we note that while the development of $T_{mf}(x)$ is smooth because of the large sample size (400×400 fluid cells in each $y-z$ plane), the development of $T_{ms}(x)$ fluctuates about a linear increase because of a limited and changing sample

size of particle surface elements at any given x –location. Comparing the two Reynolds numbers, $Re=10$ and 200 , we find that the fully-developed state is never completely achieved at $Re=10$ and $\varphi = 0.1$, whereas at $Re=200$, in spite of the perturbations superimposed on the linear increase, there is a discernable classical fully-developed region in which $T_{ms}(x) - T_{mf}(x)$ remains approximately constant. In spite of the large extent of the suspension in the flow direction, the lack of clear convergence to a fully-developed regime is most evident at low Reynolds numbers.

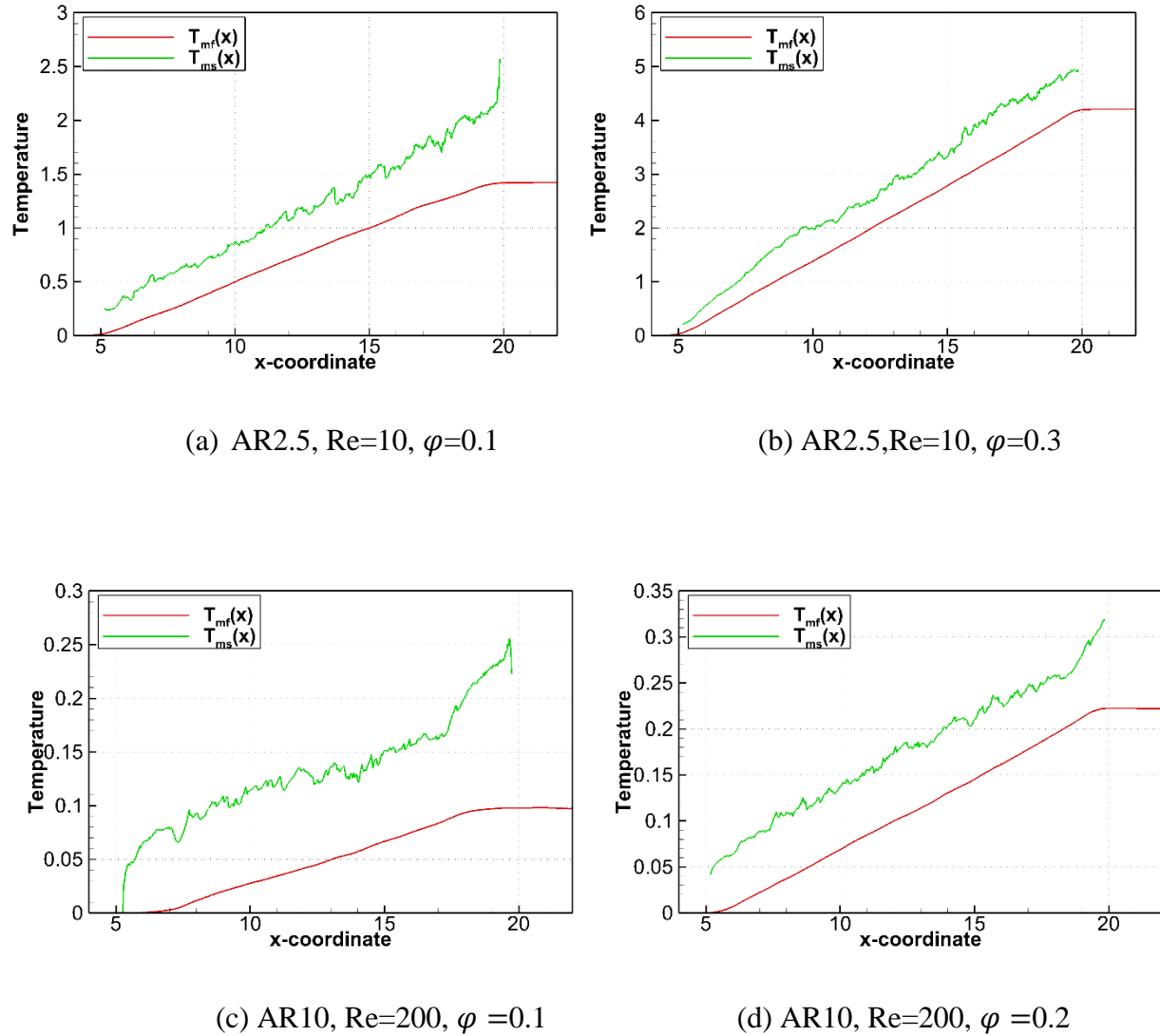
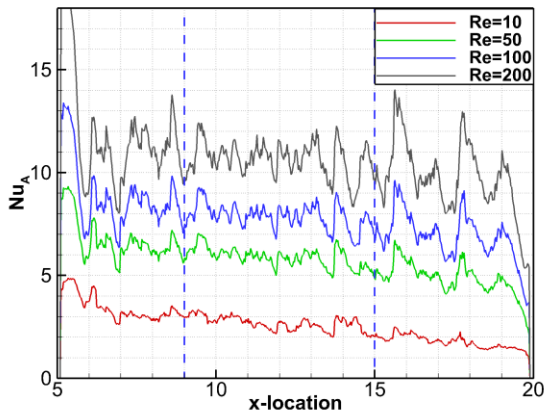


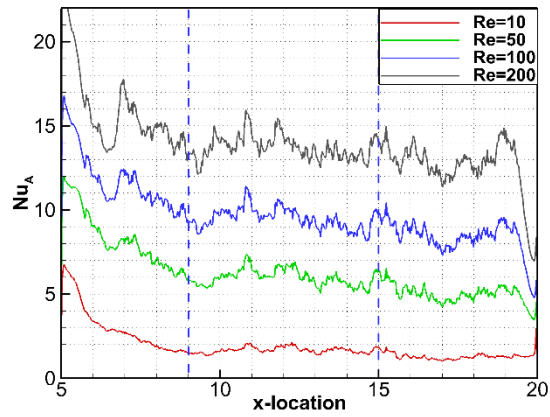
Fig. 4. 6. Variation of $T_{mf}(x)$ and $T_{ms}(x)$ in suspensions of AR2.5(a-b) AR10 ellipsoids (c-d).

The spatial development of $Nu_A(x)$ for ellipsoid suspensions is presented in Fig. 4.7. In all cases it is observed that the high Nusselt number in the initial development region of the suspension

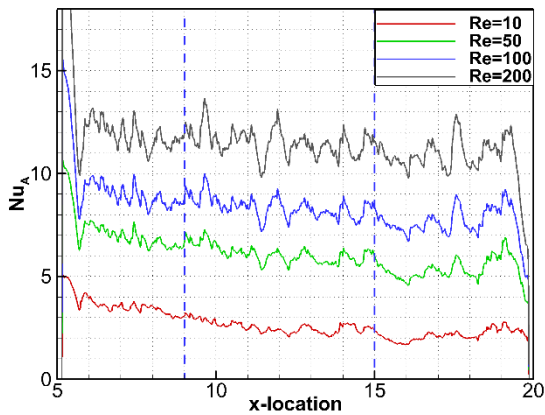
decays to what could be considered the fully developed value. However, the rate of decay does not show any strong consistent trend with AR, Re, or ϕ except possibly that the development length is consistently higher for AR10 suspensions over AR2.5 and 5.0 particles. On the other hand, similar trends in developing length observed over all Re for a given suspension, indicates that particle arrangement may be a dominant factor in the evolution of $Nu_A(x)$. It is noted that in spite of the large length of the domain in the flow direction, and the large number of particles and multiple particle arrangements, $Nu_A(x)$ in many of the cases does not settle to a stationary value representative of a fully-developed thermal region. Therefore for consistency, to specify the mean Nusselt number \overline{Nu}_A at a given condition, a subset of the $Nu_A(x)$ distribution between $x = 9$ and 15 is used for all cases as indicated by the dashed lines in Fig. 4.7.



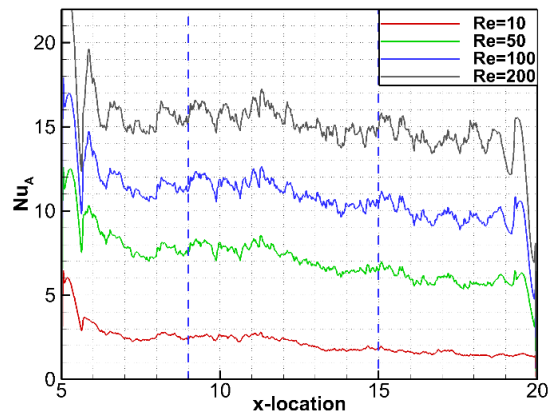
(a) AR2.5, $\phi=0.1$



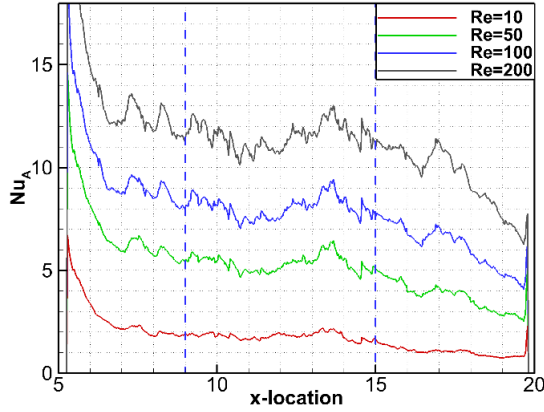
(b) AR2.5 $\phi=0.3$



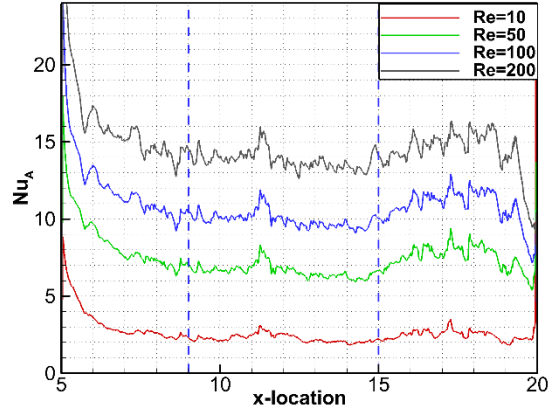
(c) AR5, $\phi=0.1$



(d) AR5, $\phi=0.3$



(e) AR10, $\varphi = 0.1$



(f) AR10, $\varphi = 0.2$

Fig. 4. 7. Nu_A for ellipsoid suspensions using results from one (AR2.5) and two (AR5 and AR10) independent random particle arrangements.

Individual particle Nusselt numbers (Method B) is calculated by using the average surface temperature of a particle with the mixed mean fluid temperature in a shell of finite-width surrounding the particle (Eqns. 4.12-4.14). Examples of Nu_B on individual AR10 particles is presented in Fig 4.8 for a shell size of $\delta = 1.5d_{eq}$ around each particle at $Re=10$ and 200 and $\varphi = 0.2$. Also shown are the corresponding PDFs of the normalized deviation from the mean value of Nusselt number. Because of the inherent randomness in the suspension and the large influence of interstitial flow on thermal fields around each particle, there are large variations in the calculated Nusselt numbers which are represented at the location of the particle geometric center. As stated earlier in section 2.4, very large or negative Nu_B can result on individual particles. Approximately 30% of the cases run had between 1% to 3% of the particles with very large (more than 5 times the mean) and negative values. These values are not plotted in Fig 4.8 nor are they included in the construction of the PDFs. Studying the PDFs which specify the variation about the mean, for both Reynolds numbers the PDFs are positively skewed, much more so at $Re=10$ at which many particles experience values as large as 1.5 to 2 times the mean value. At $Re=100$, the individual particle Nusselt numbers experience comparatively less fluctuations about the mean value and the distribution is more uniform. This leads to the conclusion that Nu_B is much more sensitive to the particle arrangement at low Re than at higher Re .

Unlike Nu_A , the distribution of Nu_B is quite insensitive to x –location, i.e., entrance and exit effects are barely perceptible. This is because even though the geometric center of the particle is

located near the entrance or exit, because of the high aspect ratio, the AR10 ellipsoid extends over a range of x -values and thus any sharp variations in the local mixed mean fluid and surface temperatures are smoothed out when averaged over the outer shell surrounding the particle and over the particle surface, respectively. Taking advantage of this inherent smoothing, particles with geometric centers between $8 < x < 17$ are used for defining the mean Nusselt number \overline{Nu}_B at each condition.

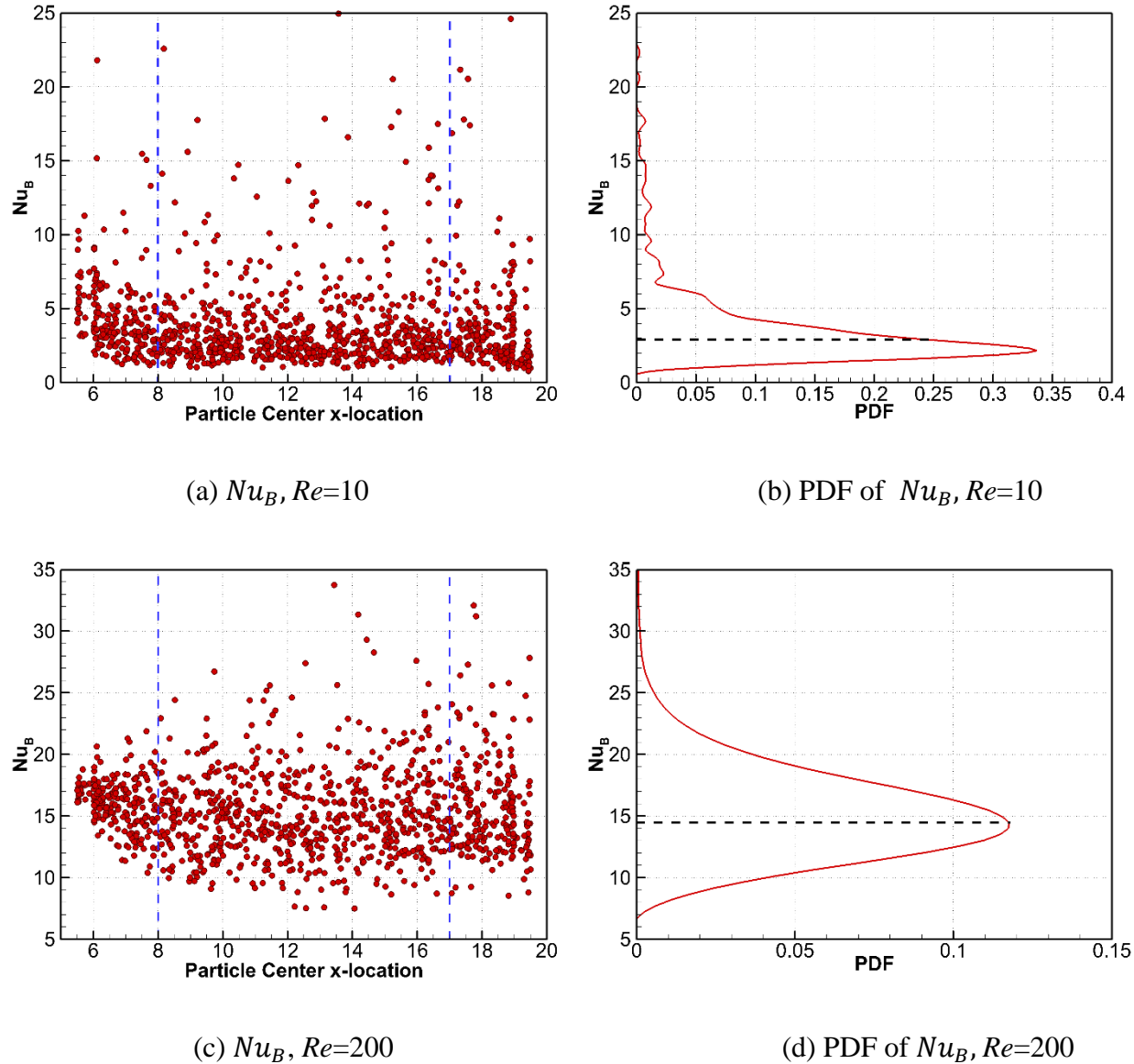
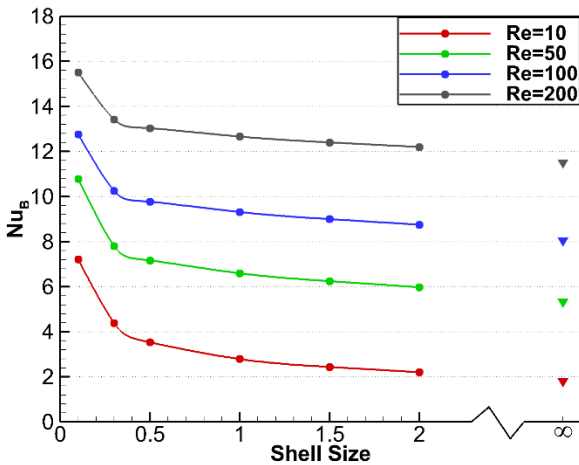
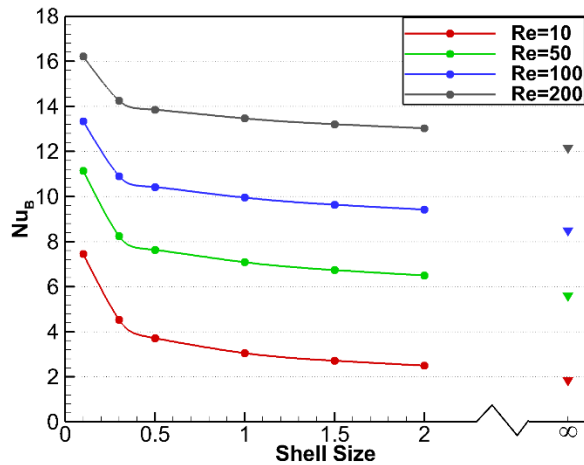


Fig. 4. 8. Nu_B for AR10 ellipsoid suspensions for $\varphi = 0.2$ with corresponding PDF distribution. Dash line shows the mean values in (b) and (d).

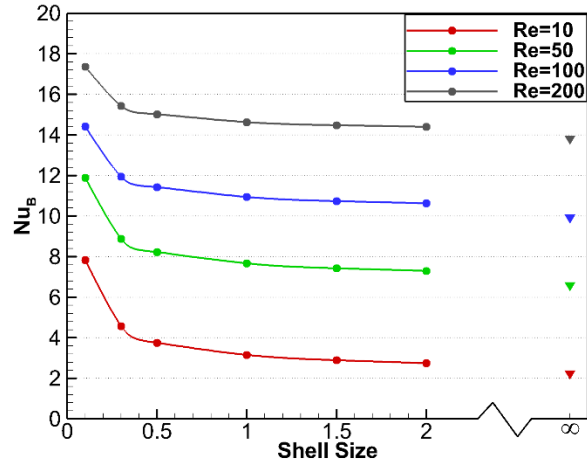
An important parameter in determining the particle Nusselt number, Nu_B , is the size of the shell over which the fluid mixed mean temperature T_{pf} is calculated. For very thin shells the fluid and surface temperature approach each other and under constant heat flux conditions lead to high Nusselt numbers. As the shell size increases, the calculated temperature is more representative of the surrounding fluid temperature, however progressively more of the presence of other particles is also included in the calculation of the fluid temperature. This is similar to calculating the fluid mixed mean temperature at any given x –location– where the effect of other particles on the fluid temperature is implicitly included in the reference fluid temperature. To show that as the shell size gets larger, the mean particle Nusselt number \overline{Nu}_B approaches \overline{Nu}_A , different shells sizes of $\delta/d_{eq} = 0.1, 0.3, 0.5, 1, 1.5$ and 2 are tested (Eqn. 4.11). These results are presented in Fig. 4.9 showing the effect of δ on the mean Nusselt number, \overline{Nu}_B , for AR10 ellipsoid suspensions at different Re and φ . At $\delta = 0.1$, the predicted mean Nusselt number starts at a high value, but drops sharply by $\delta = 0.5$, gradually decreasing further as the shell size increases. In the limit that the shell size approaches the volume of the fluid domain, \overline{Nu}_B approaches \overline{Nu}_A as both become equivalent. Similar trends are also observed for AR2.5 and AR5 ellipsoid suspensions (not shown).



(a) Nu at $\varphi=0.1$



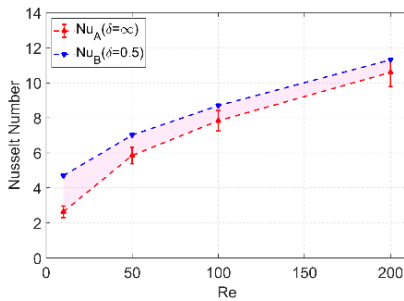
(b) Nu at $\varphi=0.15$



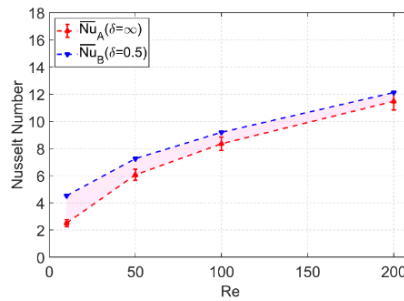
(c) Nu at $\varphi=0.2$

Fig. 4. 9. Variation of \overline{Nu}_B of AR10 ellipsoid suspensions versus shell size, δ .

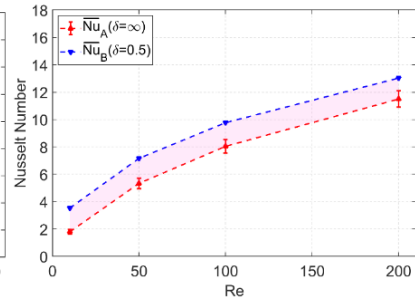
To expand on the relationship between \overline{Nu}_B and \overline{Nu}_A further, Fig. 4.10 presents both quantities at different Reynolds numbers and solid fractions for AR2.5, AR5 and AR10 geometries. The vertical range bars on \overline{Nu}_A represent the standard deviation in the thermally fully-developed region between $9 \leq x \leq 15$. \overline{Nu}_B is plotted at shell size $\delta/d_{eq} = 0.5$ and the shaded region represents the admissible possible values of \overline{Nu}_B as the shell size increases with the lower bound given by \overline{Nu}_A . As Reynolds number increases, the Nusselt number increases approximately as $Re^{1/2}$. The difference between $\overline{Nu}_B|_{0.5}$ and \overline{Nu}_A is nearly 100% at $Re = 10$ but reduces to between 15%-20% at $Re = 200$ for the different cases investigated.



(a) AR2.5, $\varphi = 0.1$



(d) AR5, $\varphi = 0.1$



(g) AR10, $\varphi = 0.1$

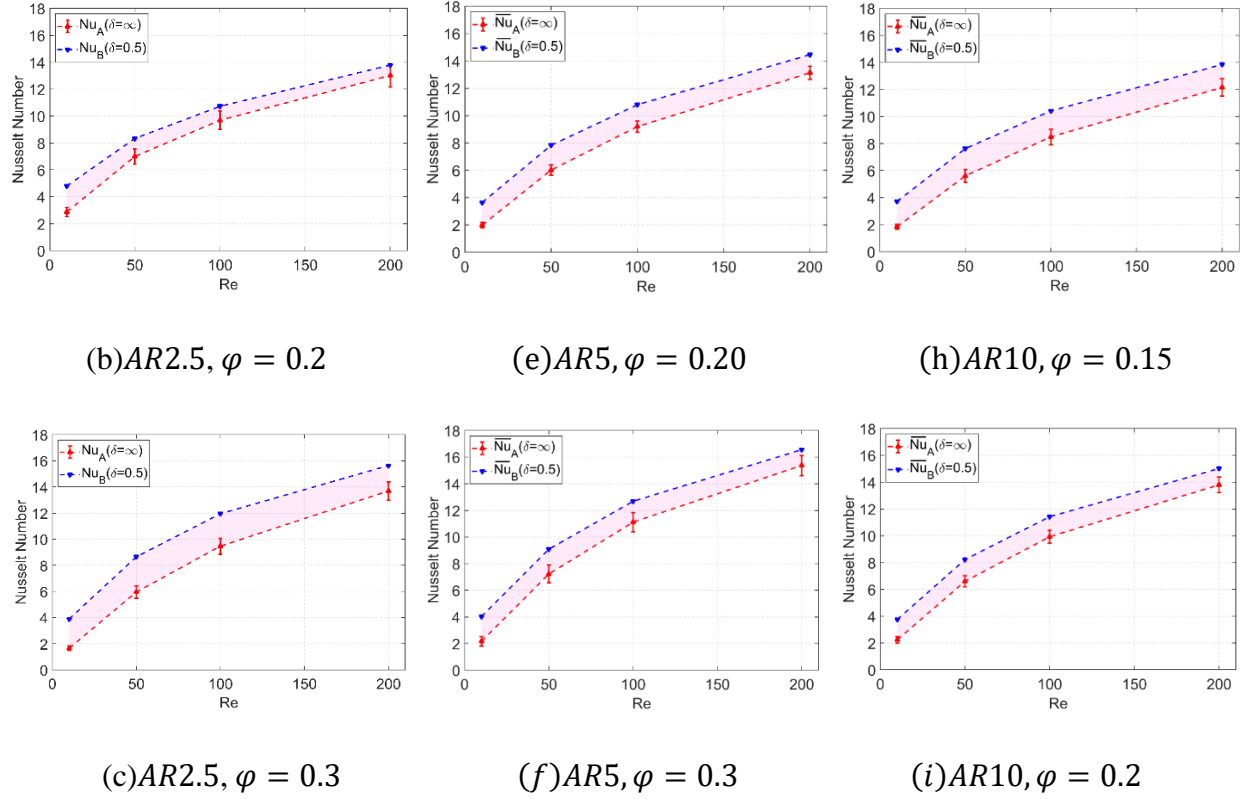


Fig. 4. 10. Comparison of \overline{Nu}_A and \overline{Nu}_B for AR2.5 (a-c), AR5 (d-f) and AR10 (g-i) ellipsoid suspensions at different Re and ϕ .

4.4.3. Comparison with correlations and past results

Both, \overline{Nu}_A and \overline{Nu}_B are quite independent of the shape of the particle, i.e., there are no strong trends with changing aspect ratio of the ellipsoids over the range of Re and ϕ investigated in this study. Note that the default length scale in the Reynolds number and Nusselt number is based on the volume equivalent diameter, thus when expressed in this form, the shape or geometry is subsumed in the volume equivalent diameter. The results are in agreement with Tavassoli et al. [60] who also observed that heat transfer coefficients were quite independent of the aspect ratio of sphero-cylinders ranging from 2 to 4. This is quite unlike hydrodynamic forces such as drag and lift which exhibit a strong dependence on shape and increase with aspect ratio or deviation from sphericity. On the other hand, the Nusselt number increases slightly (between 15-20%) as ϕ changes from 0.1 to 0.3. Chen and Muller [62] modified a spherical suspension correlation, to develop a correlation for non-spherical particles by explicitly accounting for the shape of the

particle in the definition of the Nusselt number by defining, $Nu_S = \frac{h^* d_S^*}{k^*}$, where the Sauter diameter, $d_S^* = \Phi d_{eq}^*$, with Φ defining the sphericity of the particle shape.

$$\overline{Nu}_s = \Phi \left[2 + 0.77\phi + 0.64\phi^2 + (0.6 + 1.1\phi) Re_{D_h}^{0.5} Pr^{1/3} \left(\frac{3\phi}{2(1-\phi)\Phi} \right)^{0.5} \right] \quad (4.18)$$

where the Reynolds number is based on the hydraulic diameter given by $D_h^* = \frac{4(1-\phi)V^*}{\Omega^*}$. Here V^* is the volume of the suspension domain and Ω^* is the total surface area of the particles in the volume V^* . Fig. 4.11 compares the present predictions with the correlation.

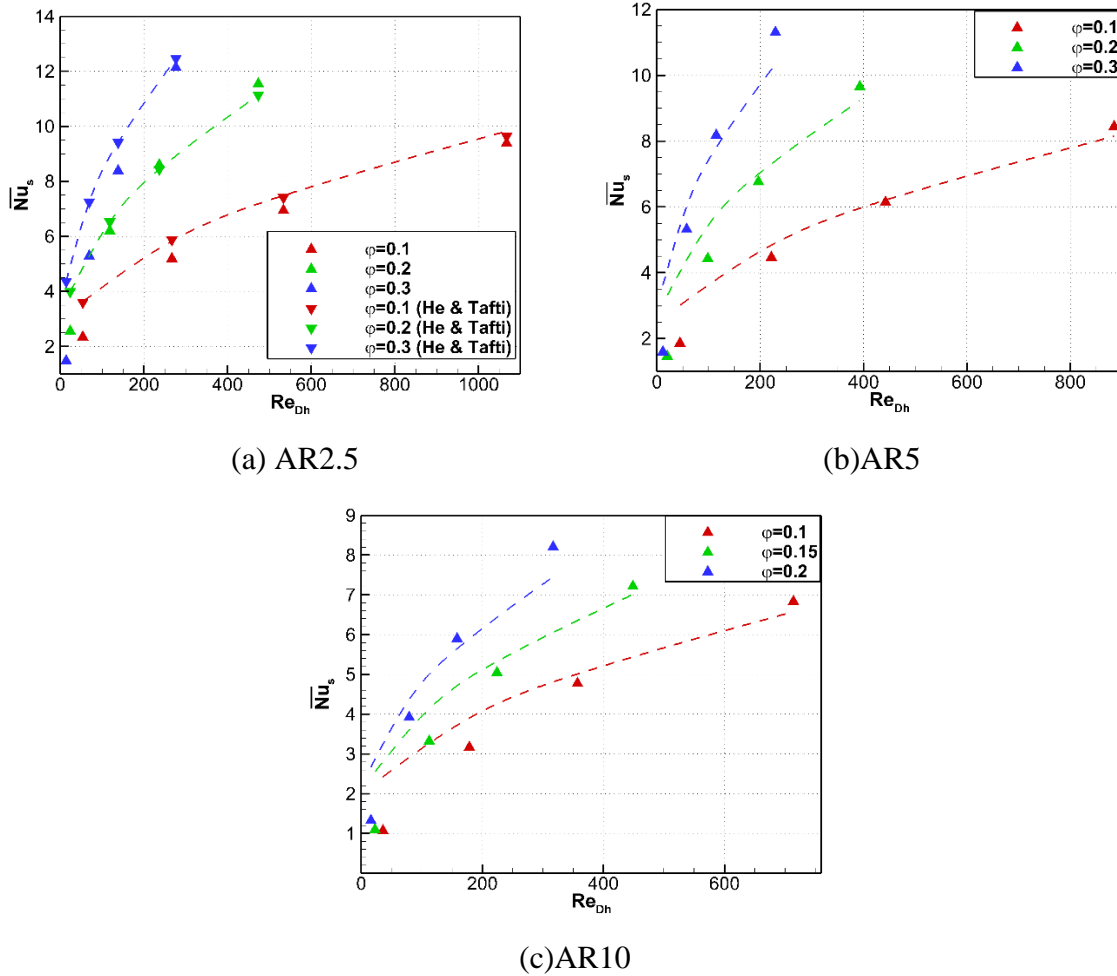


Fig. 4. 11. Comparison of predictions with correlation of Chen and Muller [62].

Nusselt number values obtained from the correlation agree quite well with the current predictions for $Re_{D_h} > 100$ but tend to over predict the values at lower Reynolds numbers, $Re=10$ and 50 (based on sphere equivalent diameter). On comparing the current predictions with the results of He and Tafti for AR2.5 particles, it is observed that He and Tafti [53] systemically predict higher values of Nusselt number at $Re=10$ and 50 . In order to identify the source of these differences we checked the reproducibility of the He and Tafti [53] results by using their particle distribution in the software version used to compute the current cases and found exact reproducibility of their Nu_A distribution. This was followed by additional tests of using one of the current distributions of AR2.5 $\varphi = 0.1$ suspension and truncating its streamwise extent from $5 \leq x \leq 20$ to $5 \leq x \leq 15$ and to $10 \leq x \leq 20$ by selectively removing particles to make the suspensions have a development length of $10d_{eq}^*$ as in He and Tafti [53]. In addition to these modifications to the existing suspension, a new suspension is created without strictly restricting the solid phase to $5 \leq x \leq 20$ as in He and Tafti (only particle centers are restricted to lie between $5 \leq x \leq 20$). The resulting Nusselt number distribution Nu_A distributions are shown in Fig. 4.12. It is noted that none of the suspensions reach a truly fully-developed state. While Nu_A decreases continuously with x' for the original suspensions in this study, He and Tafti's and the new suspension, while not decreasing continuously, do not reach a nominal constant value characteristic of a fully – developed regime either. In spite of making the above modifications in the original suspension and generating a new suspension, the current results consistently under predict the Nusselt number compared to He and Tafti [53].

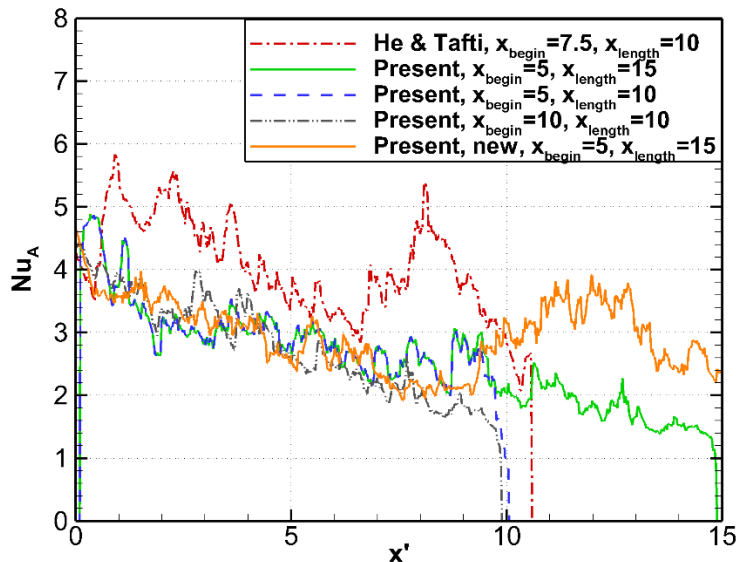


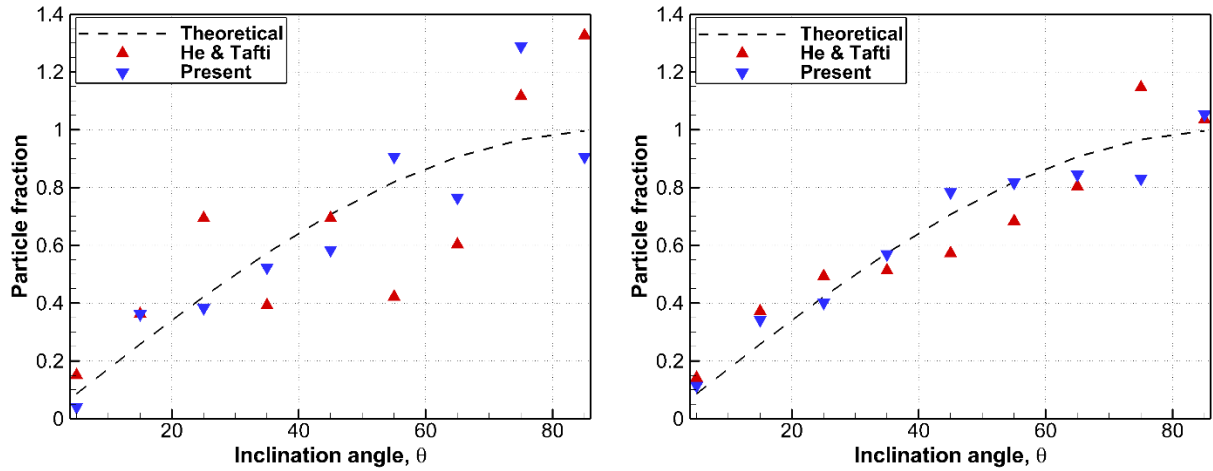
Fig. 4. 12. Distribution of $Nu_A(x')$ for different particle suspensions at $Re=10$ and $\varphi = 0.1$.

To further investigate the systemic under prediction at low Reynolds number, Fig. 4.13(a) presents the orientation distribution of particles in suspension and the calculated local solid fraction as perceived by individual particles in the suspension. In a random ellipsoidal suspension the following relationship between number of particles and inclination angle θ is satisfied

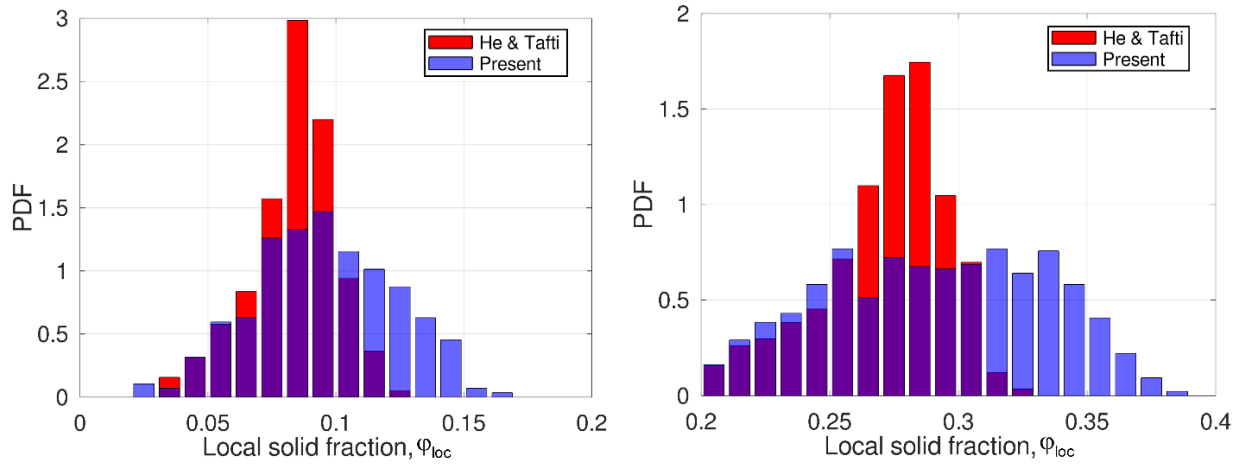
$$\frac{N_{\Delta\theta}}{N_{80^\circ \leq \theta \leq 90^\circ}} \approx \sin\theta \quad (4.19)$$

Here $N_{\Delta\theta}$ are the number of particles present in the interval $\Delta\theta = 10^\circ$ about angle θ , and $N_{80^\circ \leq \theta \leq 90^\circ}$ are the number of particles in the interval $80^\circ \leq \theta \leq 90^\circ$. Both distributions follow the trends of a random arrangement within the limits imposed by the smaller sample size of particles at $\varphi = 0.1$. He and Tafti show more scatter with fewer particles in the mid-range of inclination angles between $30^\circ \leq \theta \leq 70^\circ$, whereas the current distribution shows less scatter with more particles between $70^\circ \leq \theta \leq 80^\circ$. The more illuminating result is the PDF distribution of local solid fraction, φ_{loc} in Fig. 4.13 (b), which is calculated by finding the ratio of grid cells designated as solid to the total number of grid cells in an envelope or ellipsoidal shell size of $1.5d_{eq}^*$ surrounding each particle in the suspension. We find that compared to He and Tafti, the current suspension has more clusters of particles (indicated by the PDF skewed towards higher φ_{loc}) in spite of the randomness and same mean solid fraction in both distributions.

This leads to the conclusion that the lower predicted Nusselt numbers in the present study are due to the effect of thermal wakes which engulf many of the particles in close proximity to each other. At low Reynolds numbers, the thermal wakes are particularly strong but diminish in spatial extent as the Reynolds number increases. Notably, particle clustering only affects the heat transfer coefficient but has very little effect on fluid forces, such as drag, within the variations imposed by the randomness of the suspension,. Fig. 4.14 presents the calculated normalized drag force on individual particles for the two distributions. The present results exhibit a larger range of drag values because of the larger variation in local solid fraction experienced by individual particles. However, unlike the heat transfer coefficient, the mean suspension drag is only marginally different within 3% of each other at 4.43 for He and Tafti and 4.31 for the present arrangement.



(a) Particle inclination angle distribution



(b) PDF of local solid fraction

Fig. 4. 13. Comparison between present AR2.5 suspension and that of He and Tafti [53] (left: $\varphi = 0.1$, right: $\varphi = 0.3$)

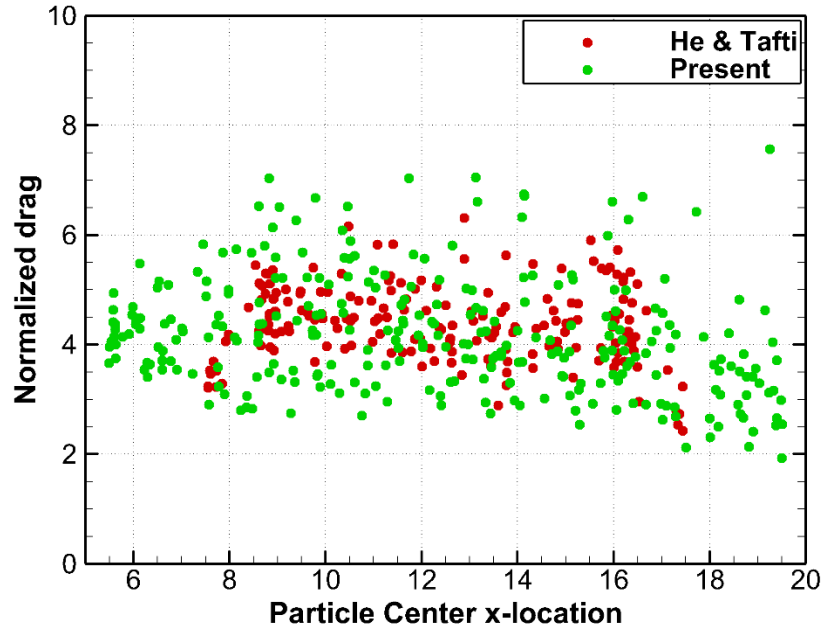


Fig. 4. 14. Comparison of individual particle normalized drag between present suspension and that of He and Tafti [53] at $Re=10$ and $\varphi = 0.1$. Normalization is done with Stokes drag on an equivalent diameter sphere.

4.5. Conclusions

In this study, Particle-Resolved Simulations (PRS) are performed to calculate the Nusselt number through random suspensions of ellipsoidal particles of aspect ratio 2.5, 5 and 10, solid fractions between 0.1 and 0.3, and Reynolds number in the range 10 to 200.

The mean Nusselt number based on the equivalent diameter of the particle increases with Reynolds number roughly to the $\frac{1}{2}$ power. It shows only a weak dependence on the aspect ratio while increasing between 10-15% with an increase in solid fraction from 0.1 to 0.3. Both these trends are in sharp contrast to fluid drag forces which increase with increase in aspect ratio and solid fraction.

Two Nusselt numbers are defined and calculated, one analogous to developing internal flow (Nu_A) as a function of the streamwise distance and another based on individual particles, Nu_B . It is shown that by definition the suspension mean $\overline{Nu_B}$ is always greater than or equal to the mean $\overline{Nu_A}$ and that it approaches $\overline{Nu_A}$ as the fluid mixed mean temperature pertaining to a particle is calculated over a larger volume of the suspension.

It is shown that at $Re \leq 50$, the suspension heat transfer coefficient is very sensitive to the spatial distribution of particles or local-to-particle solid fraction. This is because of the strong thermal wakes that form at low Re in the presence of clusters of particles and the role the wakes play in reducing the heat transfer coefficient. Because of this effect, the Nusselt number (based on equivalent diameter) can drop below the nominal minimum limiting value of 2.0 used in most correlations that is imposed by conduction heat transfer in the absence of any convection. Notably, the effect of particle clustering and hydrodynamic wakes, while influencing individual particle fluid forces, do not have any substantial effect on suspension mean fluid forces such as drag.

4.6. **ACKNOWLEDGEMENTS**

Ze Cao's research was supported in part by an appointment to the U.S. Department of Energy (DOE) Postgraduate Research Program at the National Energy Technology Laboratory administered by Oak Ridge Institute for Science and Education. The authors would like to acknowledge the computational resources provided by Advanced Computational Research (ARC) at Virginia Tech.

Chapter 5

Fluid forces and torques in suspensions of oblate cylinders with aspect ratio 1:4

5.1. ABSTRACT

Fluid forces and torques in a random stationary suspension of oblate cylinder-like particles of AR0.25 are investigated in the Reynolds number range $10 \leq Re \leq 300$ and solid fraction range $0.1 \leq \varphi \leq 0.3$ using Particle Resolved Simulations with the Immersed Boundary Method (IBM). While existing correlations were found to grossly under predict the drag forces, a sinusoidal function $F_{d,\theta} = F_{d,\theta=0^\circ} + (F_{d,\theta=90^\circ} - F_{d,\theta=0^\circ})\sin(\theta)$ captured the variation of normalized drag with respect to inclination angle over the range $10 \leq Re \leq 300$ and $0 \leq \varphi \leq 0.3$. Further the mean ensemble drag followed $F_d = F_{d,\theta=0^\circ} + \frac{1}{2}(F_{d,\theta=90^\circ} - F_{d,\theta=0^\circ})$. Lift forces varied between 20% and 80% of drag forces over the range of Reynolds numbers studied. Comparing the pitching fluid torque to collision torque in an elastic collision showed that as the particle equivalent diameter, density, and collision velocity decrease, fluid torque can be of the same order of magnitude as collisional torque and cannot be neglected.

5.2. INTRODUCTION

The collective dynamic behavior of particles in suspension is strongly dependent on their interaction with each other and with the interstitial fluid flow. Particle-particle interactions are nominally dominated by collision forces, whereas particle-fluid interactions are dominated by the fluid forces. The particle-particle interaction can be modeled based on solid mechanics that

resolves collision and momentum exchange for both spherical and non-spherical particles (Zhu et al., 2007, 2008; Zhou et al., 2011). For the fluid-particle interaction, due to the various flow conditions and particle geometries encountered, there is no general formulation available. Because of the simplicity afforded by the spherical shape assumption, initial experimental and computational work in characterizing fluid forces has mostly been done for single (Turton and Levenspiel, 1986; Flemmer and Banks, 1986; Clift et al., 1978) and suspensions of spherical particles (Ergun, 1952; Wen and Yu, 1962; Tenneti et al., 2011). Most of these studies have focused on developing drag force correlations. In the last decade, because of the limitation of the spherical shape assumption, investigations on the effect of non-sphericity on fluid forces have gained considerable attention. Among the various particle geometries, ellipsoids and cylinders are commonly chosen because of their defined geometry compared to irregular shaped particles and in their ability to mimic particles from plate-like to fiber-like shapes by varying their aspect ratios (AR). One of the important enabling technologies has been the increase in computational power which has made Particle Resolved Simulation (PRS) possible. Using PRS fluid forces can be directly integrated on the particle surface. Zastawny et al. (2012) used PRS to derive correlations for drag, lift force and torque on single particle under different inclination angles in the intermediate Reynolds number range for ellipsoids with aspect ratio of 1.25 and 2.5 and spherocylinders of aspect ratio of 5. Similarly, Richter and Nikrityuk (2013) simulated flow over single ellipsoid with aspect ratio of 2 and demonstrated through statistical analysis, that there exists an apparent sin-square relation between the drag force and the particle inclination angle, which was later found to be applicable for ellipsoids with aspect ratio up to 32 in the study of Ouchene et al. (2016). Vakil and Green (2009) simulated flow over an individual cylinder with aspect ratio range of [2, 20] with $1 \leq Re \leq 40$ and proposed a drag correlation. When it comes to the study of

particle suspensions, only a few studies can be found in the literature. He et al. (2017) did PRS for flow within suspensions of ellipsoids with aspect ratio of 2.5 and tested the ability of existing correlations to predict the drag force of the suspension. They found that the combination of the Hölzer and Sommerfeld's (2008) correlation for an isolated non-spherical particle in the flow and the correlation of Tenneti et al. (2011) to include the effect of solid fraction provided the best estimation of suspension drag force. Similarly, Sanjeevi and Padding (2019) simulated flow through suspensions of spherocylinders with aspect ratio of 4 and they found that similar to single prolate spheroids, the drag of particles in the suspension also approximately followed the sin-squared distribution with respect to their inclination angles. In addition to drag force, lift as well as torque on prolate particles in suspension have been investigated by He and Tafti (2018) and Sanjeevi and Padding (2019).

As for oblate particles, based on previous computational and experimental results, Militzer et al. (1989) developed a drag correlation for a single ellipsoid in the flow with minimum aspect ratio of 0.2. A much lower aspect ratio of 0.05 for cylindrical shaped particle (disk) was studied by Unnikrishnan and Chhabra (1991) through free falling experiments and they also proposed a drag correlation that is applicable in the range $0.2 \leq Re \leq 180$. However, both of these studies didn't include the effect of particle orientation, which is found to play an important role in determining the drag force in the study of Zastawny et al. (2012). In addition to prolate shapes, Zastawny et al. (2012) also simulated flow over an oblate ellipsoid with aspect ratio of 0.2 and derived drag, lift and torque correlations with particle inclination angle included. Similarly, an ellipsoid with aspect ratio of 0.25 was included in the study of Ke et al. (2018) and they proposed a drag correlation over an aspect ratio range of $0.25 \leq AR \leq 2.5$. A more general study was carried out by Hölzer and Sommerfeld (2008) that proposed a drag correlation based on 2061 experimental data of

various particle geometries. When it comes to investigations of oblate particle suspensions, though researchers like Eshghinejadfard et al. (2019) and Fonseca and Herrmann (2004) performed PRS for flow through oblate ellipsoidal suspensions, neither of them explicitly presented the drag force results in their work. The lack of drag correlations for non-spherical particle suspensions in the literature has resulted in a trend of combining isolated or single non-spherical particle drag correlations with spherical suspension drag correlations in coarse-grained simulations (Gan and Zhou, 2016; Shrestha et al., 2019; Ma and Zhao, 2018). The applicability of this was evaluated by Vollmari et al. (2016) through comparison with experimental results. They concluded that the accuracy of this practice was compromised as the particle geometry deviated substantially from a spherical geometry.

In light of the scarcity of fluid force formulations for oblate particle shapes in suspension, the current investigation contributes to the literature by formulating fluid force and torque results in a stationary suspension of particle of cylindrical shape with aspect ratio 0.25 (AR0.25) in a Reynolds number range $10 \leq Re \leq 300$ and solid fraction $0.1 \leq \phi \leq 0.3$. Firstly, select drag correlations from the literature most applicable to the AR0.25 cylinder geometry are compared against the PRS results. It is shown that inevitable preferential orientation in suspension correlations derived from packed bed experiments leads to under prediction of PRS drag in a random orientation. A new drag correlation is proposed that covers both isolated AR0.25 cylinder and suspensions with much better agreement with the PRS data. This is followed by an investigation of the difference in velocity and pressure fields and in drag force for particles of the same sphericity, which is used to characterize particle non-spherical shape in drag correlations. Finally, the variation of lift and lateral forces, as well as torque is investigated and their relative magnitude with respect to drag forces are calculated.

5.3. SIMULATION METHOD AND SETUP

5.3.1. Governing Equations

The dimensionless governing equations given the fluid under incompressible and constant property assumption are written as:

Continuity:

$$\frac{\partial u_i}{\partial x_i} = 0 \quad (5.1)$$

Momentum:

$$\frac{\partial u_i}{\partial t} + \frac{\partial}{\partial x_j} (u_i u_j) = -\frac{1}{\rho} \frac{\partial p}{\partial x_i} + \frac{\partial}{\partial x_j} \left(\frac{1}{Re} \left(\frac{\partial u_i}{\partial x_j} \right) \right) \quad (5.2)$$

The above equations are non-dimensionalized by:

$$u_i = \frac{u_i^*}{u_{ref}^*}; \quad x_i = \frac{x_i^*}{l_{ref}^*}; \quad p = \frac{p^* - p_{ref}^*}{\rho_{ref}^* u_{ref}^{*2}};$$
$$\rho = \frac{\rho^*}{\rho_{ref}^*}; \quad \mu = \frac{\mu^*}{\mu_{ref}^*}; \quad Re = \frac{\rho_{ref}^* u_{ref}^* l_{ref}^*}{\mu_{ref}^*} \quad (5.3)$$

Variables with superscript (*) represents dimensional variables. In the process of non-dimensionalization, superficial approach flow velocity U_∞^* is taken as u_{ref}^* and diameter d_p^* of the sphere that has an equivalent volume as the AR0.25 cylinder is chosen to be l_{ref}^* . The governing equations are solved using an in-house CFD code – GenIDLEST (Generalized Incompressible

Direct and Large Eddy Simulation of Turbulence) with Immersed Boundary Method (IBM) implemented to perform the PRS simulations.

The governing equations are solved based on a non-staggered finite-volume formulation using second-order central (SOC) differencing scheme [34,35]. The fluid velocity and pressure are calculated at computational cell centers while the mass fluxes are solved and stored at cell faces. The time integration is done by a predictor-corrector formulation: the predictor step calculates an intermediate velocity which is then modified in the corrector step based on the calculated pressure field to satisfy discrete continuity.

5.3.2. Particle Definition and Immersed Boundary Method

The AR0.25 cylindrical particle is created based on the super-ellipsoid equation that is written as:

$$(|a \times x|^r + |b \times y|^r)^{t/r} + |c \times z|^t = 1 \quad (5.4)$$

In this equation, x , y and z represent coordinates in the Cartesian coordinate system with a , b and c correspondingly controlling the semi-diameters of the particle in the respective directions. The exponentials, r and t adjust the surface curvature of the particle. In this work, r and t are specified as 2 and 20 for the cylindrical geometry. a , b and c are chosen to be 1.438, 1.438 and 5.752 respectively to derive the desired aspect ratio of 0.25 with the particle volume equivalent spherical diameter of unity. As is shown in Fig. 5.1, the particle aspect ratio is defined as the ratio between the height (h) along its rotational symmetry axis and the diameter (d) of its circular cross section. A local coordinate system is defined for each individual particle in the suspension, as can be seen from Fig. 5.1, x' is defined along the direction of the superficial approach flow velocity U_∞ . The y' is specified within the plane that contains both x' and the cylinder rotational symmetry axis l' and perpendicular to x' . z' is perpendicular to $x' - y'$ to make a right-handed coordinate system.

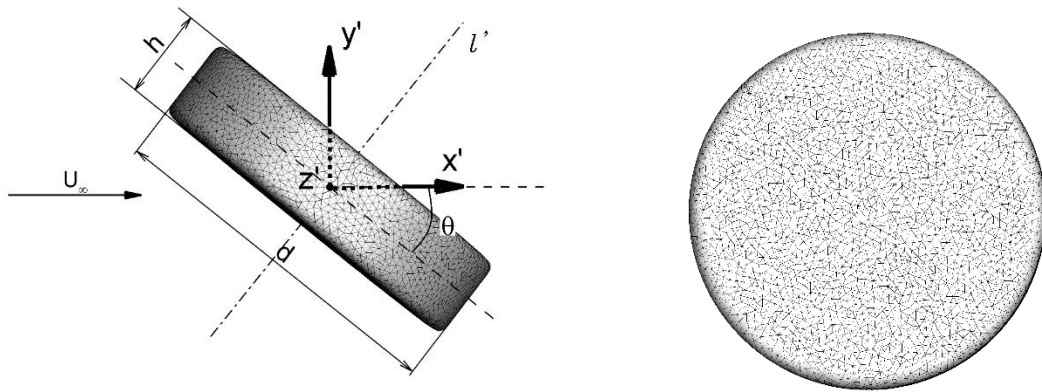


Fig. 5. 1. Particle geometry with local coordinate system and surface mesh.

Following our previous work using the Immersed Boundary Method (IBM) on a single cylindrical particle of AR0.25 in the same Reynolds number range (Cao and Tafti, 2018), the surface of each particle in the suspension is resolved with 11698 triangular elements and placed in the background volume grid. The no slip boundary condition on each particle in the suspension is implemented by the IBM boundary treatment. Probes passing through the fluid IB nodes and normal to the surface are projected into the flow. The interpolated flow variables at the probes are used with the specified boundary condition at the surface and Taylor series expansions to calculate the variable value at the IB node which acts as the boundary condition. Following Cao and Tafti (2018), second-order accurate boundary conditions are used in this investigation. More detailed discussion is given in the original paper by Nagendra et al. (2014) and specifically to PRS in subsequent investigations by He et al. (2017), He and Tafti (2018), and Cao and Tafti (2018).

In our previous work on spherical and ellipsoidal particle suspensions (He et al., 2017; He and Tafti, 2018), and Cao and Tafti (2018) on a single particle of the same shape as used to construct the suspension in this study, the background grid is constructed to have a resolution of 1/40 cells

(40 cells per equivalent sphere diameter). In Cao and Tafti (2018), grids of 1/30, 1/40 and 1/50 were compared for the prediction of the drag coefficient over the full range of Reynolds numbers and particle inclination angles. It was found that the difference in drag coefficient was bounded to within 4% between 1/30 and 1/50 and within 2% between 1/40 and 1/50 grids. Additionally by using the same three grid spacings, He et al., (2017) simulated flow through suspensions of spheres at solid fraction of 0.1 for a Reynolds number range from 10 to 200, and reported a maximum deviation of the ensemble mean drag force of around 2% between 1/30 and 1/50 grids and 1.6% between 1/40 and 1/50 grids. The grid spacing of 1/40 and 1/50 was also evaluated by Cao and Tafti (2020) for suspensions of ellipsoids with aspect ratio of 10 at $\varphi = 0.2$. They found that 97% of particles had deviations less than 2.5% and the deviation of the ensemble mean drag was 1.01% between the two grids.

In addition to the grid independency study, the IBM predictions of drag coefficient for flow over a sphere in the Re range [10,300] were compared to past correlations (Clift et al., 1978; Brown and Lawler, 2003), and to body-fitted grid calculations. Maximum differences were bounded to within 5%. Validation has also been done by He et al. (2017) for spherical suspensions for $0.1 \leq \varphi \leq 0.45$ and $10 \leq Re \leq 200$ by comparing with the suspension drag correlation proposed by Tenneti et al. (2011) based on their simulation for flow through sphere suspensions. Good agreement was observed from the comparison indicating the current simulational setup and IBM framework is not only able to calculate the drag on isolated particle in the flow, but also the drag on suspensions of particles. Therefore, considering both computational efficiency and simulation accuracy, a grid spacing of 1/40 is finally chosen for this research.

The fluid-particle interaction force is calculated for each surface element using:

$$\vec{F}_e^* = \vec{F}_{viscous}^* + \vec{F}_{pressure}^* \quad (5.5)$$

In Eq. (5.5), $\vec{F}_{pressure}^*$ and $\vec{F}_{viscous}^*$ are the forces due to pressure and viscous effect. Then, the total force on an individual particle is calculated by:

$$\vec{F}_S^* = \sum_{i=1}^n \vec{F}_{e,i}^* \quad (5.6)$$

The drag force is defined as the component of the total fluid-particle interaction force in the direction of U_∞^* , while the lift force is defined along y' as shown in Fig. 5. 1. The lateral force is part of the fluid-particle interaction force with direction of z' . All of the three force components are normalized using the Stokes drag as:

$$F = \frac{F^*}{3\pi\mu^*d_p^*U_S^*} \quad (5.7)$$

In addition to the forces that are responsible for the translational movement of the particles in the flow, torques along the three directions of the local coordinate system are also calculated to investigate the rotational motion of particles induced by the fluid flow. In this case, similar to the calculation of hydrodynamic force, torque on each surface element is calculated using:

$$\vec{T}_e^* = |r|\vec{e} \times \vec{F}_e^* \quad (5.8)$$

where $|r|$ is the distance and \vec{e} is the unit vector with direction pointing from the particle geometrical center to the centroid of the surface element. \vec{T}_e^* is the elemental contribution to total torque \vec{T}^* which is obtained by integrating over all the elements on the surface of the particle. The normalized torque \vec{T} is expressed as:

$$\vec{T} = \frac{\vec{T}^*}{3\pi\mu^*d_p^*U_s^* \cdot \frac{d_p^*}{2}} \quad (5.9)$$

5.3.3. Background Grid and Particle Suspension Generation

The domain employed in this simulation has dimension of $30 \times 10 \times 10$ in $x - y - z$ directions, respectively, as shown in Fig. 5.2. A uniform velocity with dimensionless value of unity in the $+x$ direction is specified at the inlet with a zero gradient of both pressure and velocity imposed at the outlet. Periodic boundary conditions are specified in $y -$ and $z -$ directions to simulate an infinite extent of the suspension in these directions. Particle suspensions are placed in the middle region with dimension of $15 \times 10 \times 10$ with the number of particles for a specified solid volume fraction φ calculated using:

$$N = \frac{6\varphi V}{\pi d_p^3} \quad (5.10)$$

In Eq. (5.10), d_p is the non-dimensional volume equivalent sphere diameter with value of unity. V is volume of the domain that contains the particles, which is $15 \times 10 \times 10$ in this study. With solid fraction of 0.1, 0.2 and 0.3 investigated, the corresponding number of particles are 286, 573 and 859, respectively. Two unique but random cylinder suspension arrangements are created for each solid fraction.

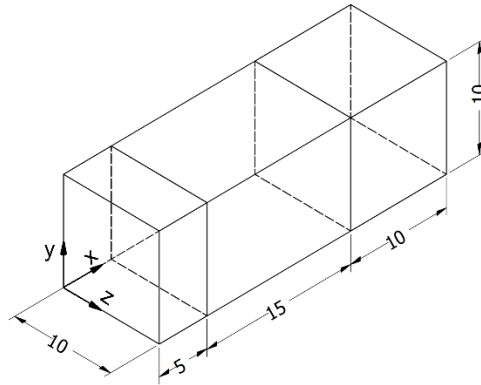


Fig. 5. 2. 3D computational domain

With the known amount of particles required for each solid fraction, particle suspensions are generated using a physical simulation engine – PhysX by Nvidia (Nvidia). During this process, particles approximated by a coarse grid are successively placed in the packing box with random velocities. During this process, particle overlaps are detected and resolved in PhysX by assigning opposing velocities to the particles to separate them. This process is repeated till the desired solid fraction is reached and particles in the domain achieve equilibrium without any overlap. An example of the particle suspension and its location in the computational domain is shown in Fig. 5. 3.

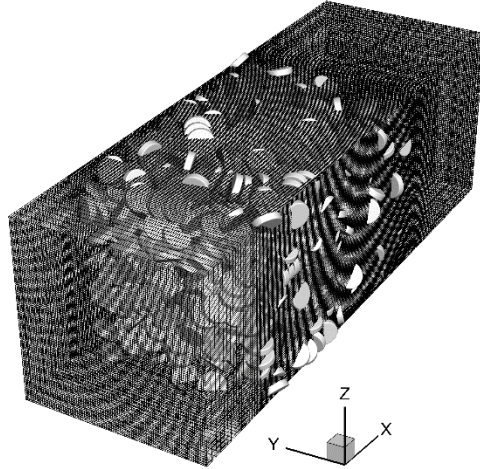


Fig. 5. 3. 3D view of the particle suspension in the computational domain. Every fifth grid line is shown.

To confirm the random orientation of particles in the suspension we show that the inclination angle, $\theta = 90^\circ - \gamma$, where $\gamma \leq 90^\circ$ is the angle made by the unit vector along the rotational symmetry axis with the x -axis, follows $\sin(\gamma)$ or $\cos(\theta)$ distribution [50]. The particle count within each $\Delta\theta = 10^\circ$ interval normalized by the total number of particles shown in Fig. 5.4(a) is found to satisfy the desired $\cos(\theta)$ distribution. In contrast, Fig. 4(b) shows the corresponding distribution of a suspension which is preferentially oriented perpendicular to the flow that will be discussed later.

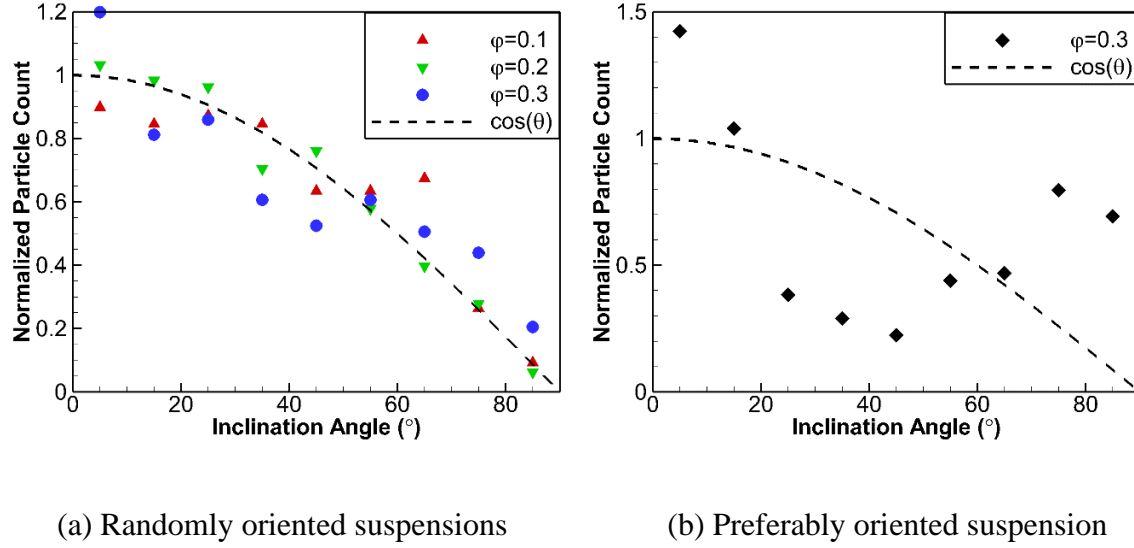


Fig. 5. 4. Normalized orientation distribution of different suspensions.

To further demonstrate the random distribution of cylinders in the suspensions, the orientation tensor \mathbf{S} is calculated by:

$$\mathbf{S} = \langle \vec{\alpha}^T \vec{\alpha} \rangle \quad (5.11)$$

where $\vec{\alpha}$ is the unit vector along the rotational symmetric axis of the cylinder and $\langle \rangle$ represents dyadic mean over all particles in the suspension. In a 3D randomly oriented suspension (isotropic), the diagonal components of the tensor should have values of $1/3$ with the off-diagonal values as 0. It was found that this condition was satisfied within 0.33 ± 0.01 for $\varphi = 0.2$ and 0.3 . The largest deviation from isotropy was observed for $\varphi = 0.1$ as 0.37 . This is attributed to the sparsity of the packing and the small sample of particles. Conversely, for the preferably oriented suspension in Fig. 5.4, the diagonal components, $S_{11} = 0.487 > S_{22} = 0.24 \approx S_{33} = 0.27$, indicate that the particle axes are not only preferentially aligned with the x -axis (flow direction), but also randomly oriented when projected on the $y - z$ plane.

A total of 30 calculations were performed to cover the range of Re , φ , and particle arrangements. For $Re \leq 100$, the flow through the suspension remained steady, but exhibited unsteadiness for $Re \geq 200$. Under these conditions, the simulations are run till the time-averaged drag force reaches a constant value, then the averaged drag force of each individual particle in the suspension is taken for further analysis.

5.4. RESULTS AND DISCUSSION

5.4.1. Pre-processing of PRS Results

Because the suspension experiences flow entrance and exit effects, the fluid forces experienced by the particles at the entrance to and exit from the suspension are different than those encountered by particles in the core of the suspension. The drag force on individual particles in the suspension at $Re=200$, $\varphi=0.3$ is presented in Fig. 5.5 versus the streamwise distance x . The calculated drag force on particles in the entrance and exit regions is smaller than in the center of the suspension. This is due to the particles experiencing a different flow and also the fact that PhysX during the generation of the suspension has a tendency to place particles at lower inclination angles near the entrance and exit. In order to eliminate these effects from the desired calculation of mean forces in a random suspension, only particles whose geometric centers lie between $x = 8$ and 17 are included in the force calculations for further analysis.

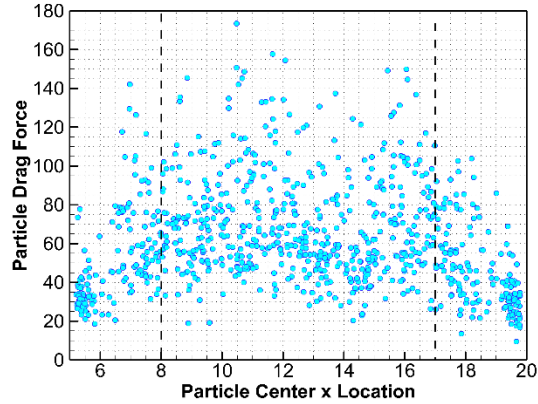


Fig. 5. 5. Variation of drag force on particles at different x - locations.

5.4.2. Analysis of Suspension Drag Force

Based on the pre-processed drag data, ensemble mean drag force of each suspension is calculated and the results are presented in Fig. 5. 6 (a). The ensemble average drag force increases with Reynold number as well as solid fraction. A notable trend is the near-linear increase in normalized total drag with Reynolds number for all solid fractions. This observation is supported by the variation of pressure drag and viscous drag on the particles. Pressure drag exhibits a super-linear trend with Reynolds number and dominates the total drag as Re increases making up 83% of the total at $Re = 300$. Viscous drag, on the other hand exhibits a sub-linear increase with Reynolds number and increases only slightly after $Re = 200$.

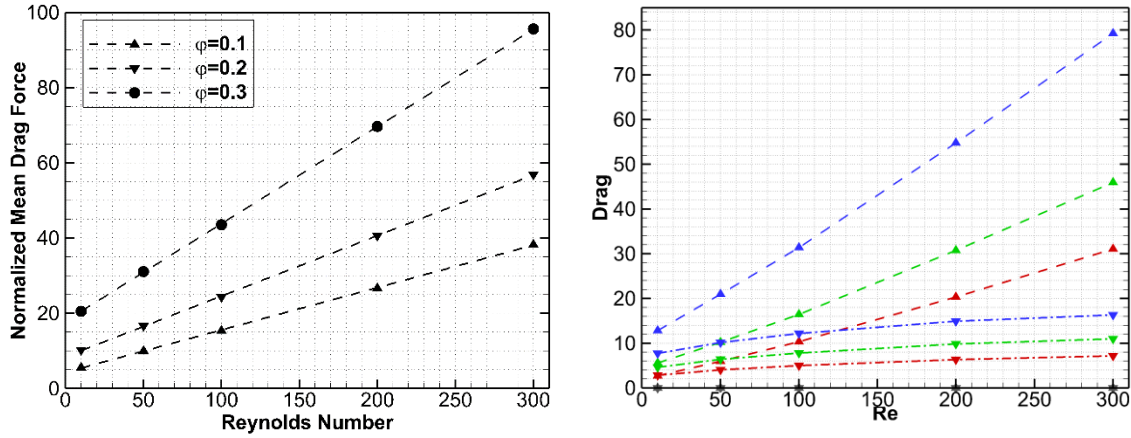


Fig. 5. 6. (a) Variation of ensemble mean drag force for different Re and ϕ . (b) Comparison of pressure drag (dash line) and viscous drag (dash-dot line). (Red: $\phi = 0.1$; Green: $\phi = 0.2$; Blue: $\phi = 0.3$)

In the absence of specific correlations for suspension of particles of different non-spherical shapes there is a trend in the literature to use single particle non-spherical particle drag correlation modified for a suspension of particles (Felice, 1994). While the single particle drag correlation used is relatable to the non-spherical particle shape and inclination in some form [1], the modification for suspension is usually derived from correlations developed for spherical particle suspensions [31,33,86]. In this study, the accuracy of these combined correlations is evaluated versus the PRS drag data. For that purpose we obtain the single particle drag from the widely used correlation developed by Hölzer and Sommerfeld (2008) (referred to as Hölzer henceforth) and the suspension correlations from Di Felice (1994), Tenneti et al. (2011) and Rong et al. (2015). Tenneti et al. proposed a suspension drag correlation for spheres based on their PRS results. He et al. (2017) found that combining the Hölzer-Tenneti correlations gave reasonable predictions of drag in suspensions of ellipsoids with aspect ratio of 2.5. [25] performed particle resolved simulations for packed beds of ellipsoids in the aspect ratio range between [0.25, 4] and proposed a geometry-specific suspension drag correlation based on the model of Felice (1994). The different

drag correlations are listed in Table 5. 1. Among the variables used, γ is the sphericity, γ_{\perp} is the crosswise sphericity defined in the research of Hölzer and Sommerfeld. Three combinations are tested Hölzer-Di Felice (HF), Hölzer-Tenneti (HT) and Hölzer-Rong (HR) and the results are shown in Fig. 5.7 of predicted drag force versus particle inclination angle. The PRS results are plotted by taking the mean drag of particle in $\pm 5^{\circ}$ interval about a given inclination.

Table 5. 1. Drag correlations in literature

Author	Drag correlation	Applicability
Hölzer and Sommerfeld (2008)	$c_D = \frac{8}{Re} \frac{1}{\sqrt{\gamma_{\perp}}} + \frac{16}{Re} \frac{1}{\sqrt{\gamma}} + \frac{3}{\sqrt{Re}} \frac{1}{\gamma^{\frac{3}{4}}} + 0.42 \times 10^{0.4(-\log\gamma)^{0.2}} \frac{1}{\gamma_{\perp}}$ <p>γ: sphericity.</p>	Single particle in the flow field with arbitrary geometry
Felice (1994)	$F_d = F_{d0} \varepsilon^{-\chi} \quad (\varepsilon: \text{void fraction, equals to } (1 - \varphi)),$ $\chi = 3.7 - 0.65 \exp \left[-\frac{(1.5 - \log Re)^2}{2} \right].$	Packed beds of spherical particles validated for particle similar to sphere.
Tenneti et al. (2011)	$F(\varphi, Re) = \frac{F_{iso}}{(1-\varphi)^3} + F_{\varphi}(\varphi) + F_{\varphi, Re}(\varphi, Re),$ $F_{\varphi}(\varphi) = \frac{5.81\varphi}{(1-\varphi)^3} + 0.48 \frac{\varphi^{1/3}}{(1-\varphi)^4},$	$0.01 \leq Re \leq 300,$ $0.1 \leq \varphi \leq 0.5,$

$$F_{\varphi,Re}(\varphi, Re) = \varphi^3 Re \left(0.95 + \frac{0.61\varphi^3}{(1-\varphi)^2} \right).$$

Spherical particle suspensions.

[25]

$$F_d = F_{d0} \varepsilon^{-\beta(\varepsilon, Re) - \lambda(\gamma, Re)},$$

$$\beta(\varepsilon, Re) = 2.65(\varepsilon + 1) - (5.3 - 3.5\varepsilon)\varepsilon^2 \exp \left[-\frac{1}{2}(1.5 - \log Re)^2 \right],$$

$$\lambda(\gamma, Re) = (1 - \gamma) \{ B - A \cdot \exp [-0.5(3.5 - \log Re)^2] \},$$

$$A = 39\gamma - 20.6,$$

$$B = 101.8(\gamma - 0.81)^2 + 2.4.$$

Packed beds of ellipsoids, Aspect ratio \in [0.25, 4].

It can be observed in Fig. 5.7 that all three correlations under predict the PRS data. The relative deviation, which is calculated by:

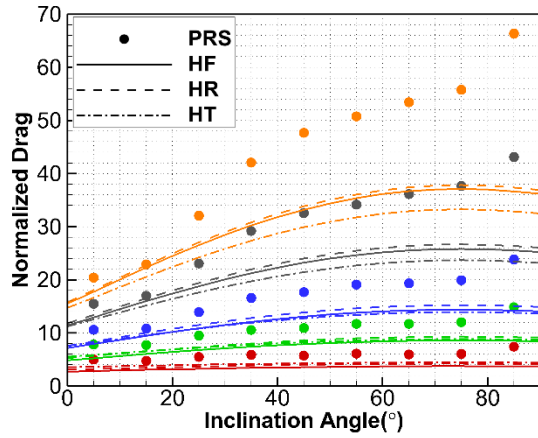
$$dev = \frac{|F_{D,PRS} - F_{D,correlation}|}{F_{D,PRS}} \times 100\% \quad (5.12)$$

reaches more than 50% for $Re = 10$ for the HF correlation. The other two correlations, HT and HR, are slightly better but still exhibit significant deviation in the range from 20% to 40% for $Re = 10$. Using the suspension correlation of Tenneti (Tenneti et al., 2011) (HT) results in the largest deviation compared to the correlation of [21] (HF) and Rong et al. (2015) (HR) particularly at higher $Re > 10$. The inaccurate predictions of these models for the oblate cylindrical particle of this study are not due to inherent shortcomings of the suspension models but more due to the fact that they are applied outside of their domain of validity. For example, the Tenneti [22] correlation was developed for suspensions of spherical particles, and in fact it was shown by He

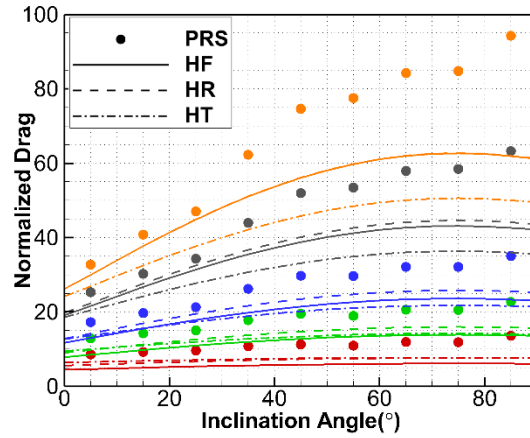
et al. (2017) that the HT combination gave reasonable predictions of the drag force in suspensions of ellipsoids with aspect ratio 2.5 which are closer to the spherical shape. Similarly, Sanjeevi and Padding (2019) while modeling drag on suspensions of spherocylinders with aspect ratio of 4, found that the suspension drag correlation derived for spherical particles by Tang et al. (2015) was sufficiently accurate for $Re \geq 100$ with $\varphi \leq 0.3$. However, as the particle shape deviates from that of a sphere, the applicability of spherical suspension correlations becomes progressively tenuous – this is in spite of having a reasonable prediction of single non-spherical particle drag.

Fig. 5.7 shows that the correlations of both Di Felice (1994) and Rong et al. (2015) give similar drag force distributions with significant underestimation comparing with the PRS results. While this can be expected from Di Felice's correlation which is for spherical particle suspensions, Rong's correlation is expected to do better since it includes flow through suspension of 0.25 aspect ratio ellipsoids. However, it does not do any better than Di Felice in predicting the PRS results. A closer look at Rong et al.'s work reveals that their correlation was developed for packed beds. In the packed bed configuration, the 0.25 aspect ratio ellipsoids are preferentially oriented with their rotational symmetry axis parallel to gravity and the flow velocity [21], whereas the suspension in this work has random orientation. To investigate the influence brought by particle preferential orientation on the drag force, another AR0.25 cylinder suspension under solid fraction of 0.3 was generated with particles having a tendency of aligning their rotational symmetry axis parallel to the flow direction. Its normalized orientation distribution is shown in Fig. 5.4(b). The simulated drag force along with the correlation results are presented in Fig. 5.8. A much better agreement can be observed compare with the results shown in Fig. 5.7. More specifically, the drag predictions from the combination of Hölzer [1] and [25] (HR) show an average deviation of 36.0%, 22.3%, 15.5% and 14.0% for $Re = 10, 50, 100$ and 200 , respectively for the randomly oriented suspension

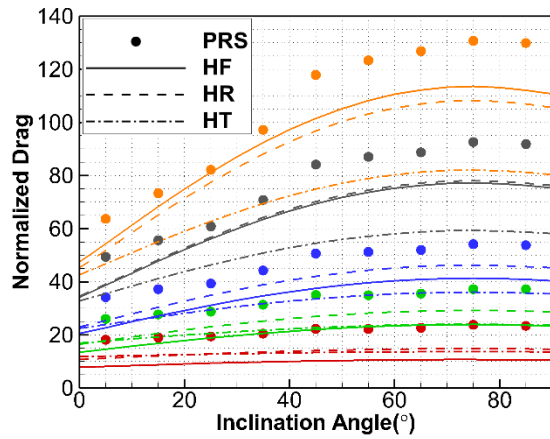
in Fig. 5.7. While for the suspension with preferential orientation the deviation is much less at 15.0%, 8.2%, 12.5% and 9.8%.



(a) $\varphi = 0.1$



(b) $\varphi = 0.2$



(c) $\varphi = 0.3$

Fig. 5. 7. Comparison of drag force between the PRS results and drag correlations (red: $Re=10$; green: $Re=50$; blue: $Re=100$; grey: $Re=200$; orange: $Re=300$.)

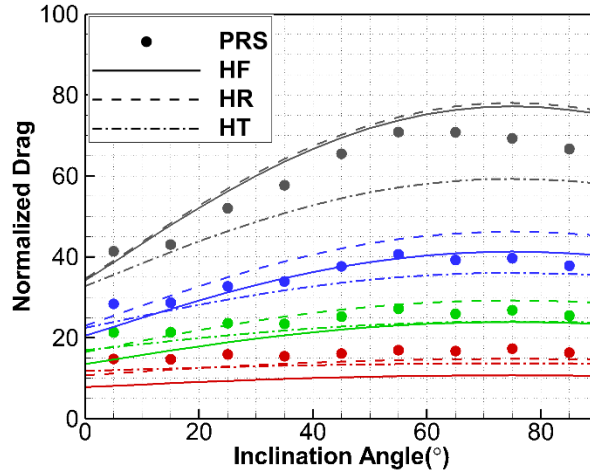


Fig. 5. 8. Comparison of PRS drag force with drag correlations using preferentially aligned suspension. (same color legend as Fig. 5.7).

The implication that by preferentially orienting the rotational symmetry axis in the flow direction for the AR0.25 cylinders reduces the drag force is counter-intuitive if one considers that this configuration maximizes the frontal area of the particle and that drag should increase. However, a closer look at the flow field in the suspension in Fig. 5.9 explains why this is the case. Fig. 5.9 plots the x – directional velocity for an arbitrary $y - z$ slice in the random and preferential suspensions. It can be seen that particles in the relatively ordered packing show significant alignment with their rotational symmetry axis approximately parallel to the flow direction. Taking particle 1 to 5 as examples, they experience a normalized drag force of 113.7, 16.4, 13.8, 102.9 and 37.0, respectively, indicating that even at similar inclination angles, particles that lie in the wake (2,3, and 5) of another particle (1 and 4) experience significantly smaller drag forces than the leading particles because of the large blocking effect. As a result, oblate particle suspensions that possess preference towards large inclination angles may not necessarily experience high drag forces as a whole.

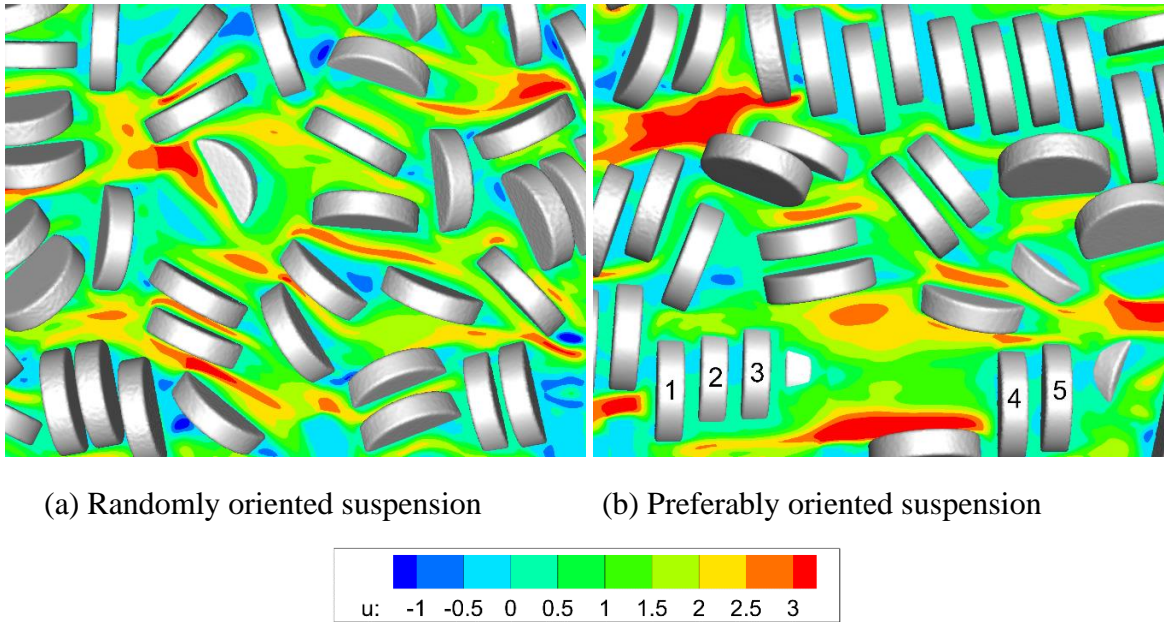


Fig. 5. 9. Particle distribution and the flow velocity in the two suspensions.

The trends in Fig. 5.7 and Fig. 5.8 show that the inclination angle has a large influence on the drag force. Conventionally, the effect of inclination angle is only included in the single particle drag correlation leaving the suspension correlation to scale the orientation dependent single particle drag by a constant factor which is only dependent on Re and φ (suspension correlation). The trends in Fig. 5.7 show that this may not be adequate for the oblate cylinders of AR0.25 investigated in this study. At solid fractions $\varphi \leq 0.2$, the deviation between the correlations and PRS data increases with increasing θ , while at $\varphi = 0.3$, the deviations become approximately independent of θ . The observations imply that a constant scaling of single particle drag independent of orientation, as is conventional practice in suspension correlations, may not be sufficient to accurately capture the orientation dependent drag in suspensions of oblate-shaped particles. In other words, suspension correlations may need to include the effect of Re , φ , and θ .

As demonstrated in Fig. 5.7 the drag forces on the AR0.25 cylinder suspension has a strong dependence on θ . Happel and Brenner (1983) found that within the Stokes flow regime, the drag coefficient of an isolated particle in the flow can be calculated using:

$$C_{d,\theta} = C_{d,\theta=0^\circ} + (C_{d,\theta=90^\circ} - C_{d,\theta=0^\circ})\sin^2(\theta) \quad (5.13)$$

Ouchene et al. (2016) found that Eq. (5.13) described the drag on isolated prolate ellipsoids with aspect ratios up to 32 and $Re < 240$ based on their PRS results. Sanjeevi and Padding (2017) reached the same conclusion for prolate ellipsoids up to $Re=2000$. They also found that Eq. (5.13) was valid for oblate ellipsoids of AR0.25 with relative deviation less than 10%. Our previous study [37] found that for an isolated AR0.25 cylinder, Eq. (5.13) predicted the drag coefficient for $Re \leq 50$ within 10% but the deviations increased for $Re \geq 100$. Sanjeevi and Padding, (2019) found that Eq. (5.13) was valid even for a suspension of spherocylinders with aspect ratio of 4 under solid fractions up to 0.5. However, there is no research in the literature that correlates the drag of oblate particle suspension with inclination angle. In this study, Eq. (5.13) was not able to capture the variation of drag on AR0.25 cylinders with inclination angle θ in the suspension.

In light of the above observations, in this work a correlation for the AR0.25 cylindrical geometry as a function of Re , φ , and θ , applicable to a single isolated particle in flow as well as to suspensions ($0 \leq \varphi \leq 0.3$) is derived. Further investigation reveals that a sinusoidal variation with inclination angle θ can capture the variation of drag force on both single particle and suspensions of the AR0.25 cylinders. Notably the $\sin(\theta)$ variation closely follows the variation of the frontal area with θ and points to a bluff body like behavior of drag force.

Based on these findings the drag force correlation is sought in the form:

$$F_{d,\theta} = F_{d,\theta=0^\circ} + (F_{d,\theta=90^\circ} - F_{d,\theta=0^\circ})\sin(\theta) \quad (5.14)$$

where $F_{d,\theta=0^\circ}$ and $F_{d,\theta=90^\circ}$ is the drag force at inclination $\theta = 0^\circ$ and 90° , respectively formulated as:

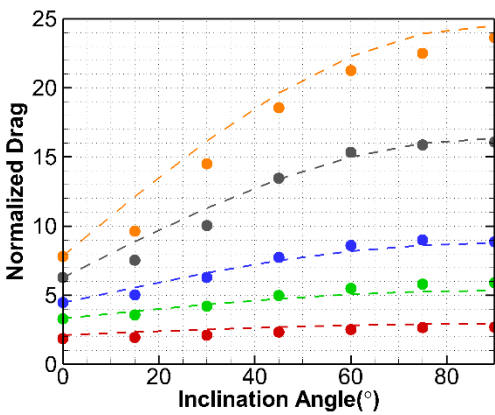
$$F_{d,\theta=0^\circ} = (a_1 Re^{b_1} + c_1(1 - \varphi)) \cdot (1 - \varphi)^{d_1} + e_1(1 - \varphi) \quad (5.15)$$

$$F_{d,\theta=90^\circ} = (a_2 Re^{b_2} + c_2\varphi) \cdot (1 - \varphi)^{d_2} + e_2(1 - \varphi)(Re \cdot \varphi + f_2(1 - \varphi)) \quad (5.16)$$

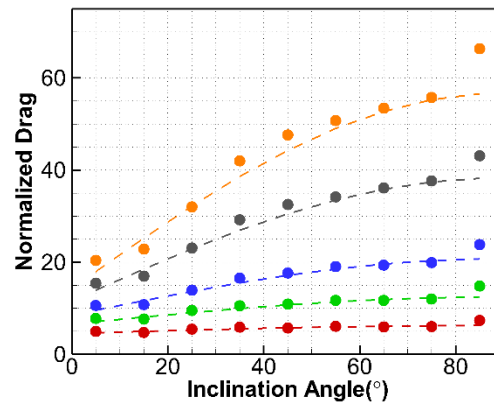
The correlation is valid in the range $0 \leq \varphi \leq 0.3$, $10 \leq Re \leq 300$, and $0^\circ \leq \theta \leq 90^\circ$. Drag forces for an isolated particle ($\varphi = 0$), were obtained from a companion study [37]. However, to develop the correlation, accurate PRS values of $F_{d,\theta=0^\circ}$ and $F_{d,\theta=90^\circ}$ are needed. $F_{d,\theta=0^\circ}$ is not readily available in suspension since there may not be any particles inclined exactly at $\theta = 0^\circ$ to the flow in the suspension (the inclination dependent drag calculated at $\theta = 5^\circ$ uses PRS data for particles between $0^\circ < \theta < 10^\circ$). The same is true for $F_{d,\theta=90^\circ}$ with the added challenge that in a random arrangement there are few particles in the range between $80^\circ < \theta < 90^\circ$ (see particle distribution function in Fig. 5.4(a)). As a result the mean drag force plotted at $\theta = 85^\circ$ for particles in the range $80^\circ < \theta < 90^\circ$ in Fig. 5.7, particularly for $\varphi \leq 0.2$, does not follow the same trend as for $\theta < 85^\circ$ but has a much higher value due to the small sample size. Because of these reasons, drag at $\theta = 0^\circ$ and $\theta = 90^\circ$ of the particle suspensions are extrapolated based on a least-squares curve fit of PRS results in the interval $\theta \in [5^\circ, 85^\circ]$. Using this technique, the coefficients a through f are listed in Table 5.2.

Comparison of the correlation with the PRS results in Fig. 5.10 shows that the $\sin(\theta)$ function can reasonably capture the variation of drag with respect to θ with little deviation. The mean

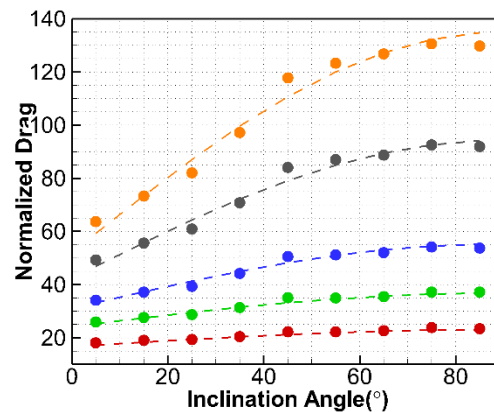
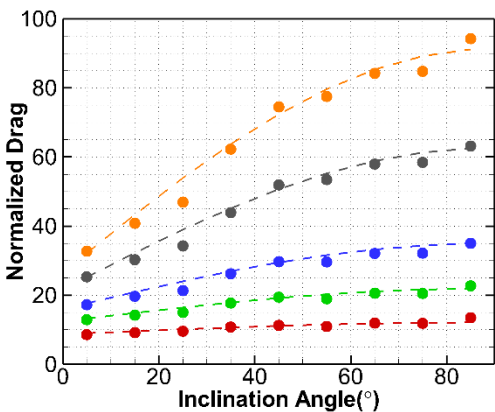
relative deviation for an isolated cylinder is 7.54% considering all Re studied. For suspensions, the relative deviation weighted by the theoretical particle number ratio as shown in Fig. 5.4(a) are 5.39%, 4.53% and 2.75% for $\varphi = 0.1, 0.2$ and 0.3 , respectively. The largest deviation appears at $Re = 10$ for isolated particle with a value of 14%. This is because of the large range of fitted PRS drag values (2 – 130) and the difficulty of fitting a function with equal relative sensitivity at the high and low end of the range of values. As the drag at $Re = 10$ for isolated particle possesses the smallest values, the relative deviation becomes more significant. Except for this case, the deviations over all the φ and Re studied are less than 10%.



(a) Isolated cylinder ($\varphi = 0.0$)



(b) $\varphi = 0.1$



(c) $\varphi = 0.2$ (d) $\varphi = 0.3$ **Fig. 5. 10. Comparison between PRS data and developed correlation in Eq. (14)-(16). (for legend see Fig. 7)****Table 5. 2. Parameters for Eq. (5.15) and Eq. (5.16).**

	$F_{d,\theta=0^\circ}$	$F_{d,\theta=90^\circ}$
<i>a</i>	0.1143	0.03304
<i>b</i>	0.7029	1.14
<i>c</i>	3.347	21.41
<i>d</i>	-5.1	-3.028
<i>e</i>	-1.803	0.7951
<i>f</i>		3.126

Eq. (5.14) – (5.16) can be readily extended to a correlation for the mean ensemble drag by integrating the mean drag force $F_{d,\theta}$ (Eq. (5.14)) weighted by the theoretical particle fractional distribution given by $\cos\theta$ over the interval from $0 \rightarrow \frac{\pi}{2}$ to give

$$F_d = F_{d,\theta=0^\circ} + \frac{1}{2}(F_{d,\theta=90^\circ} - F_{d,\theta=0^\circ}) \quad (5.17)$$

Comparison with the PRS results fitted with a line is presented in Fig. 5.11. Both the drag values and linear relationship with Re are well replicated by the correlation with a maximum relative deviation of 7% appearing at $Re = 300$, $\varphi = 0.1$. The mean deviation over all the cases investigated is 3.6%.

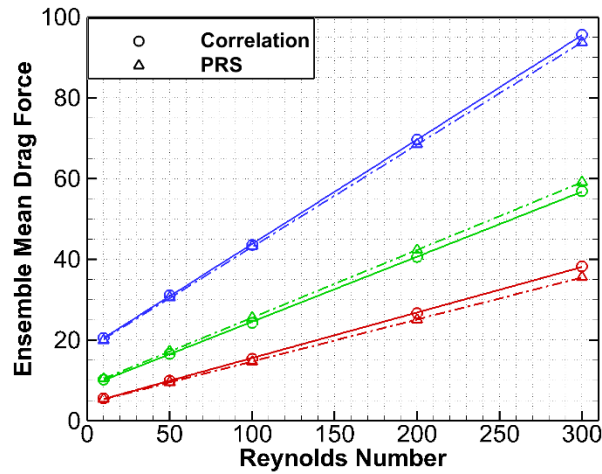


Fig. 5. 11. Ensemble mean drag force calculated using Eq. (15) – (17). (Red: $\varphi = 0. 1$; Green: $\varphi = 0. 2$; Blue: $\varphi = 0. 3$)

5.4.3. Parameterizing Non-spherical Particles

In past research, non-spherical particles have been classified using parameters such as aspect ratio and sphericity. Aspect ratio has mostly been used for classifying rotationally symmetric particles like cylinders [15,78,89] and ellipsoids [11,81]. Besides having the ability to describe particles from very elongated to very flat shapes, aspect ratio provides no detailed information about the geometry of the particle and needs an additional classifier pertaining to the type of particle like cylinder or ellipsoid, etc. Thus aspect ratio by itself is not a unique identifier. Sphericity, defined as the ratio between surface area of the volume equivalent sphere and the particle of interest, is usually employed for irregular shaped particles [6,90,91] and characterizes the deviation of the particle from the spherical shape. However, it cannot distinguish between different particle shapes. This has often been pointed to in the literature as a shortcoming of using sphericity in drag correlations for non-spherical particles. To elucidate further on this aspect, here we compare drag

force between a prolate ellipsoid of aspect ratio 5 with the oblate cylindrical shape of this study, having nearly the same sphericity of 0.735 and 0.718, respectively. The drag force, velocity and pressure fields are investigated for a representative case at $Re = 200$ and $\varphi = 0.3$ for the two geometries.

Fig. 5.12 compares the drag force of individual particles (blue dots) and mean drag force within inclination angle range of $\pm 5^\circ$ (red dots) in the two suspensions. It is observed that in spite of the two shapes having the same sphericity, the drag force experienced by the AR0.25 cylinder is much larger than AR5 ellipsoids at the same inclination over the whole range of angles. Not only is the mean drag force higher, but the relative variation or scatter from the mean is also much larger for the cylinder AR0.25 suspension.

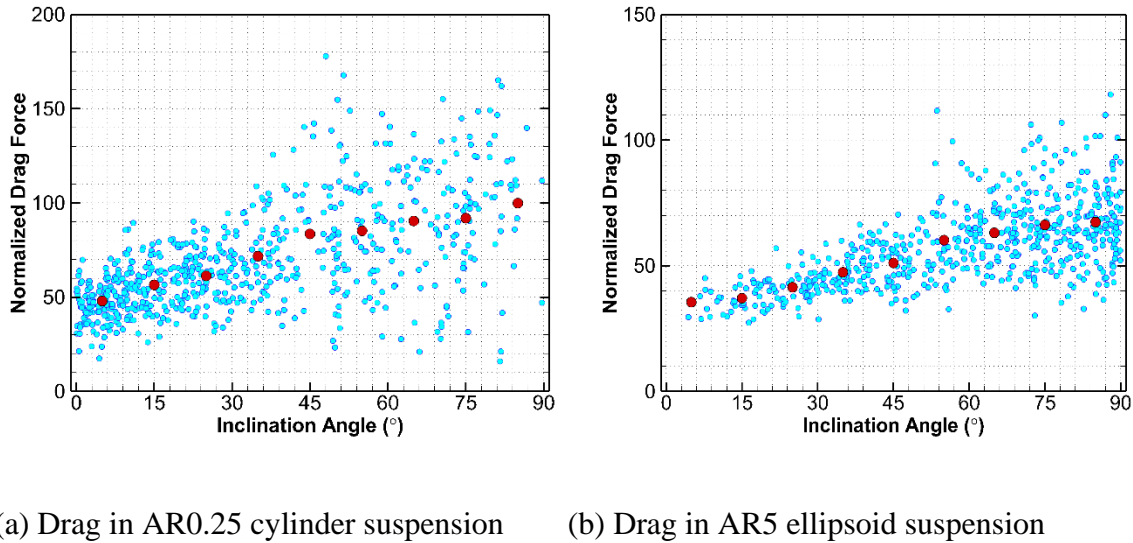


Fig. 5. 12. Comparison of the particle drag force in AR5 ellipsoid and AR0.25 cylinder suspensions at $Re=200$, $\varphi=0.3$

The larger variation in drag force can be understood by investigating the fluctuating velocity and pressure fields in the two suspensions. The normalized fluctuating velocity field (u') is computed

by subtracting the volume-averaged mean interstitial velocity (u_m) within $5 \leq x \leq 20$ from the total velocity (u) as

$$u' = \frac{u - u_m}{u_m} \quad (5.18)$$

The Probability Density Function (PDF) of u' is plotted in Fig. 5.13. The range of u' for both geometries ranges from -1.5 to 1.5. However, there are considerable differences in the respective PDF distributions. The occurrence of velocity in the range from -0.5 to 0.5 is much higher for the AR5 ellipsoids indicating a flow with smaller excursions around the mean value, whereas the occurrence of velocity outside of this range is more probable for the AR0.25 cylinders indicating more prevalent flow acceleration and deceleration. From the geometry perspective these results are consistent with the expectation that the AR0.25 cylinders will cause more abrupt blockages with stronger accelerations around the particle and stronger wakes.

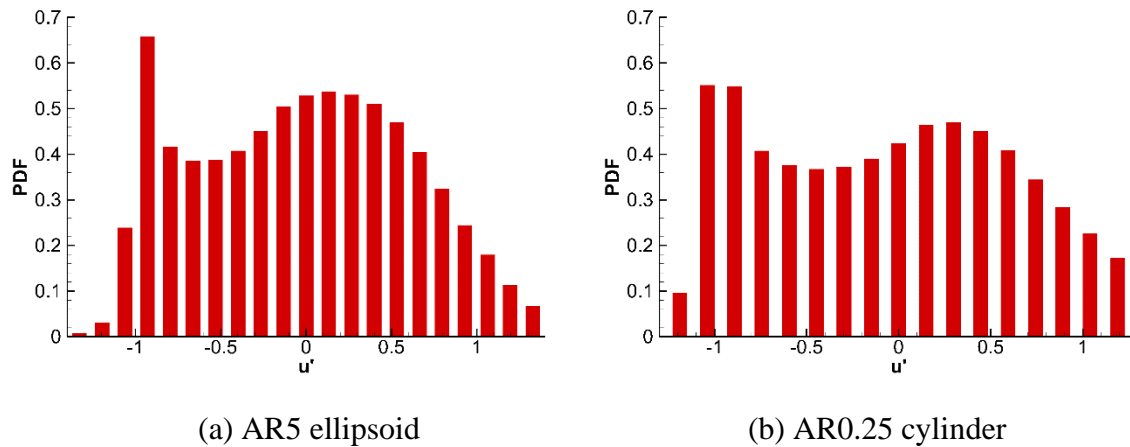


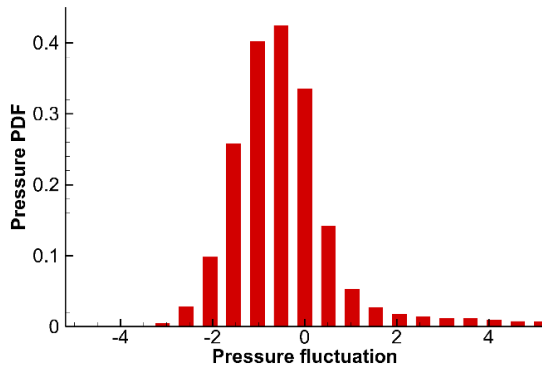
Fig. 5. 13. PDF of u' of the flow in AR5 ellipsoid and AR0.25 cylinder suspensions. $Re = 200$ and $\varphi = 0.3$.

Pressure fluctuations follow the same trends as the velocity fluctuations about a mean value. The pressure fluctuations are calculated by subtracting the mean pressure at a given x-location to account for the near-linear drop in mean pressure from the local pressure as

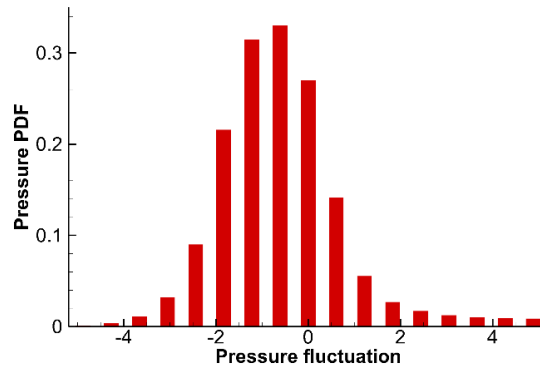
$$p' = p - p_{x,m} \quad (5.19)$$

Note that pressure is normalized by $\rho^*U_\infty^{*2}$. The PDF of p' for the two particle suspensions are shown in Fig. 5.14. The general PDF distribution between the two geometries is similar to that observed for u' . The AR5 particle suspension has a narrower spread with the largest probability of occurrence between -1 and 0 (mean value), whereas the probability of fluctuations outside this range are higher for the AR0.25 cylinders. This is consistent with the observations made earlier about the AR0.25 cylinders creating much stronger wakes with lower velocities and pressures more dominant in the flow through the suspension.

This section categorically shows that the use of sphericity to differentiate particle geometries while developing drag models is insufficient. Therefore, additional parameters characterizing the particle shape and orientation with respect to flow, such as those used by Hölzer and Sommerfeld (2008) who incorporated lengthwise and crosswise sphericity are necessary to formulate fluid forces.



(a) AR5 ellipsoid

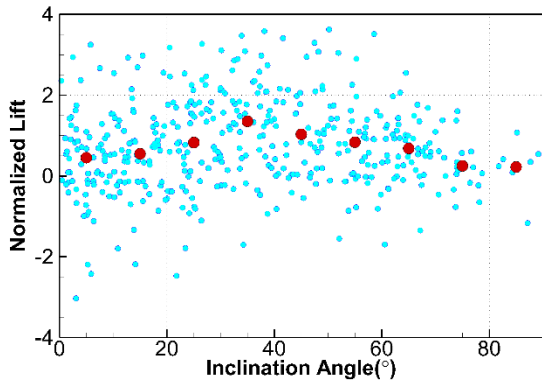


(b) AR0.25 cylinder

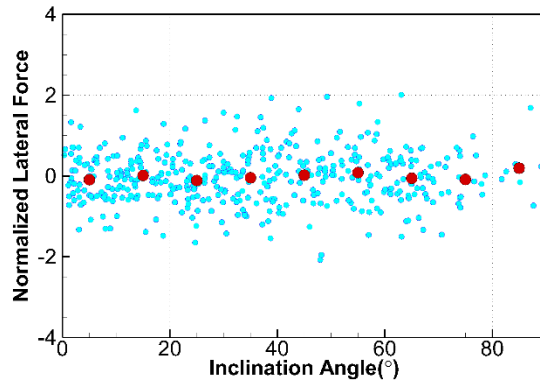
Fig. 5. 14. PDF of the pressure fluctuation in AR5 ellipsoid and AR0.25 cylinder suspensions. $Re = 200$ and $\varphi = 0.3$.

5.4.4. Analysis of Lift, Lateral Forces and Torque

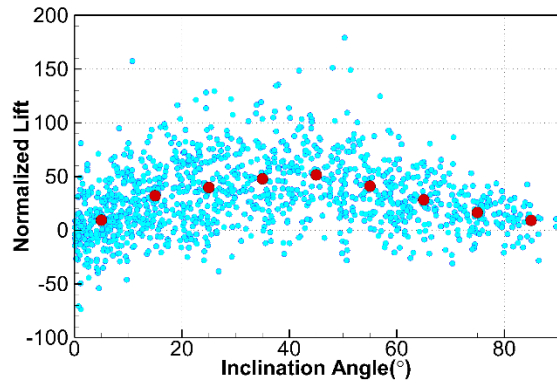
As demonstrated in previous research [28,39], both fluid lift and pitching torque play an important role in the momentum transfer between the fluid and the particle phase for prolate ellipsoidal particles. To investigate these effects on AR0.25 cylinders in suspension, both lift and lateral force on each individual particle in the suspension defined in the local-to-particle coordinate system (see Fig. 5.1) are calculated and results under two representative conditions are presented in Fig. 5.15. Each blue dot in the figure represents a particle in the suspension while the red dots represent the mean for particles within $\Delta\theta \pm 5^\circ$ of θ . Individual particles exhibit strong positive and negative variations in lift and lateral forces. While the inclination dependent mean lift varies substantially with inclination angle, the mean lateral force is close to zero as it should be in a random arrangement.



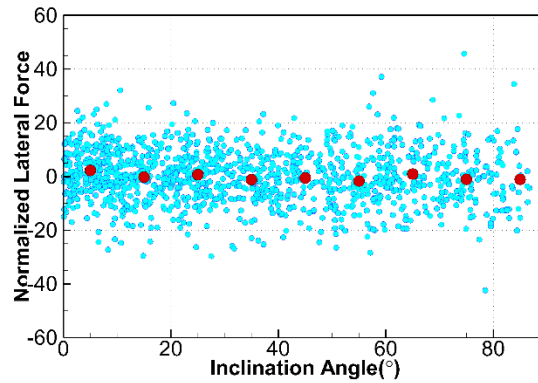
(a) Lift at $Re = 10$, $\varphi=0.1$



(b) Lateral force at $Re = 10$, $\varphi=0.1$



(c) Lift at $Re = 300$, $\varphi=0.3$



(d) Lateral force at $Re = 300$, $\varphi=0.3$

Fig. 5. 15. Variation of lift and lateral force on individual AR0.25 cylinders at different Re and φ .

Fig. 5.16 shows the variation of mean normalized lift force as a function of inclination angle for all the cases calculated. It is noted that the lift force increases with Reynolds number and solid fraction. Interestingly, the maximum lift force is experienced at $\theta = 35^\circ$ at $\varphi = 0.1$ which shifts to $\theta = 45^\circ$ at $\varphi = 0.3$. This trend is in contrast to that found by Cao and Tafti (2018) for a single isolated cylinder. In that study, it was found that at $Re = 10$ the lift force was symmetric about $\theta = 45^\circ$ where it reached a peak value. At higher Reynolds numbers up to 300, the peak in lift was still observed at $\theta = 45^\circ$ but the distribution of lift became somewhat asymmetrical. This was attributed to the respective non-symmetrical contributions of shear and pressure forces to lift. However, in suspension the distribution of lift is far from a symmetric distribution, much more so than a single particle. Even when the peak appears at $\theta = 45^\circ$, there is a sharper drop-off in lift for $\theta > 45^\circ$ for all Reynolds numbers. To investigate this trend further, representative pressure induced and shear induced lift forces are plotted in Fig. 5.17 against inclination angle. The plot reveals that the mean lift generated by shear forces is always negative over all inclination angles and the lift force is dominated by pressure forces which are asymmetric about the peak value.

Surveying the full range of Re and φ it is found that at $Re = 10$, the magnitude of pressure contribution to peak lift is about 3 to 4 times the magnitude of peak shear induced negative lift at $\theta = 35^\circ$. This increases to 23, 12 and 10 times at $Re = 300$ for $\varphi = 0.1, 0.2$, and 0.3 , respectively. Notably, the negative contribution of shear to peak lift increases as the solid fraction increases due to the larger flow accelerations/decelerations in the flow field at higher solid fractions that induce larger velocity gradients.

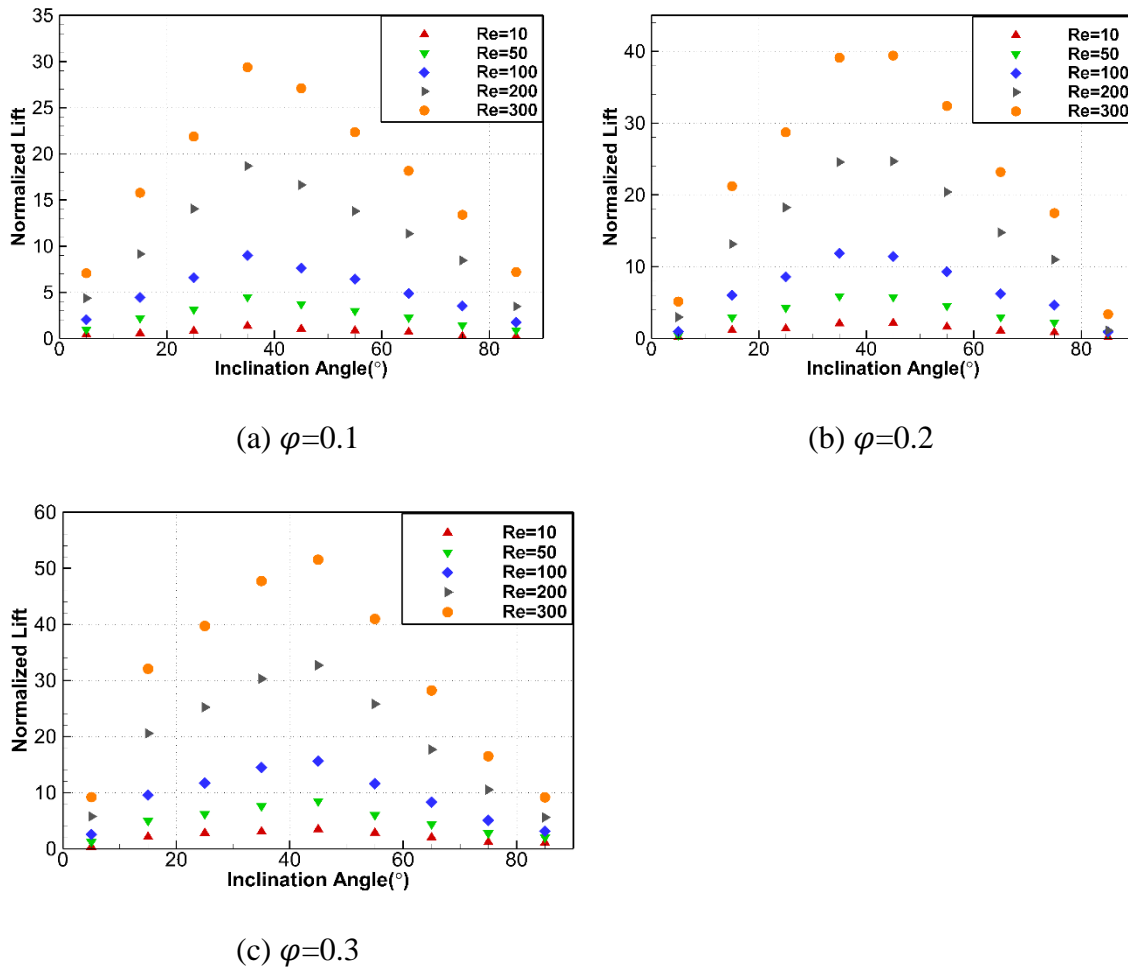


Fig. 5. 16. Variation of lift force on the AR0.25 cylinders under different Re and φ

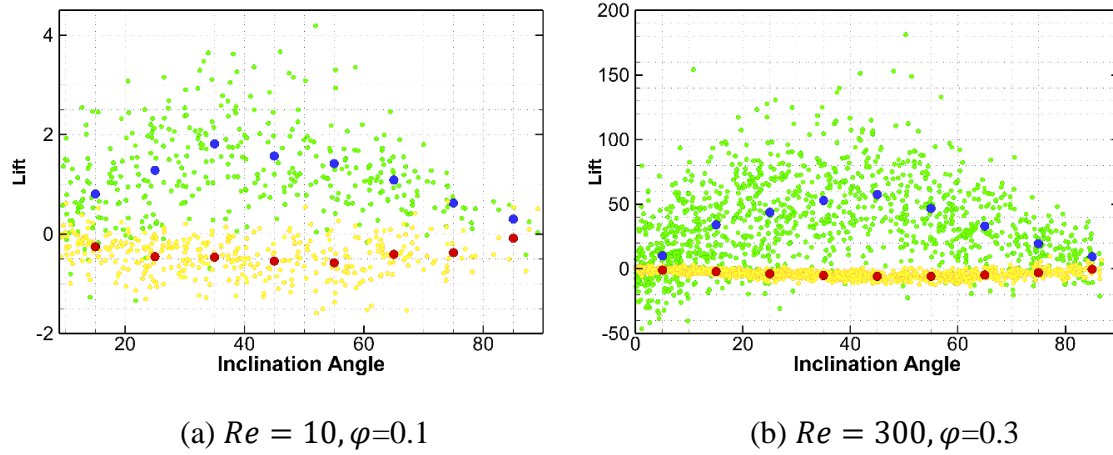


Fig. 5. 17. Variation of pressure and shear contribution to lift force on AR0.25 cylinders.

In most all studies which model particles as point masses, only drag force is considered and all other directional fluid forces are neglected. To investigate the significance of lift force under different conditions, the ratio calculated using:

$$r = \frac{|F_l(\theta)|}{F_d(\theta)} \quad (5.20)$$

with respect to particle inclination angle is presented in Fig. 5.18. The results indicate that as Re increases, effect of F_l becomes increasingly prominent as it assumes values from up to 20% of the drag at $Re=10$ to 60% of the drag at $Re=300$. This implies that inclusion of lift forces will result in more vigorous motion of the particle resulting in stronger mixing in the system. The effect of solid fraction on the lift-to-drag ratio is weak – as the solid fraction increases, there is a slight decrease in the ratio. Finally, considering the effect of particle inclination, moderate increase of the ratio can be observed reaching a maximum near 35° followed by an approximate linear decrease as θ becomes larger than 35° , finally reducing to near 0.1 among all the Re and φ investigated. To summarize, while modeling the momentum exchange between the flow and the

particles in suspension, lift force has a non-negligible effect especially at relatively high Reynolds numbers and low particle inclination angles.

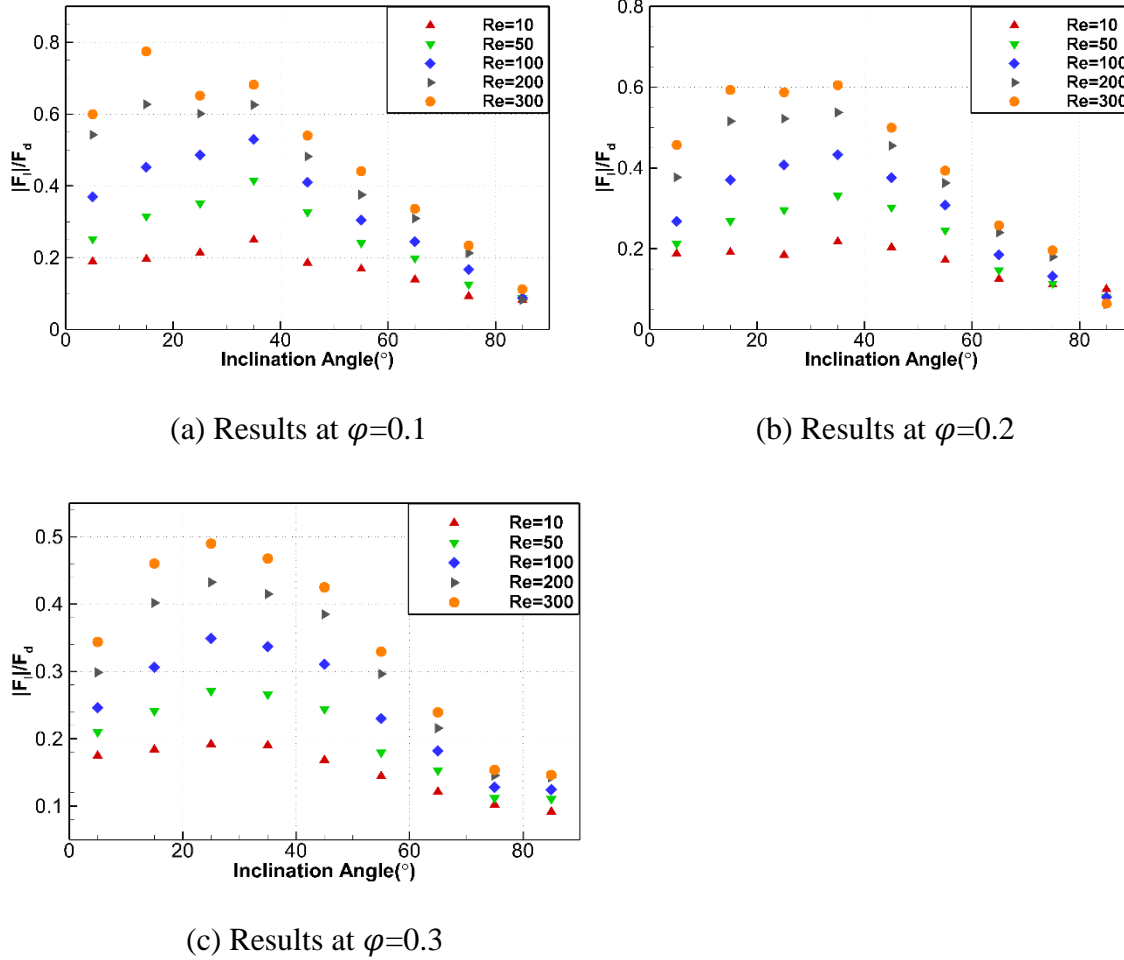
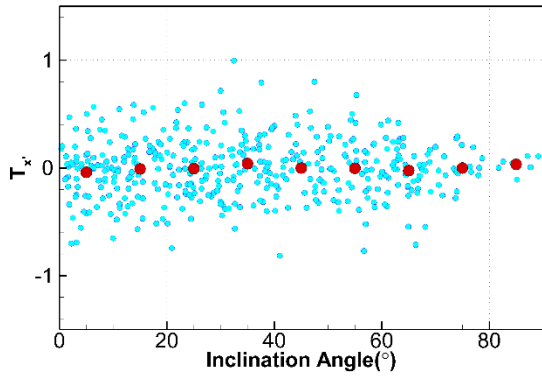


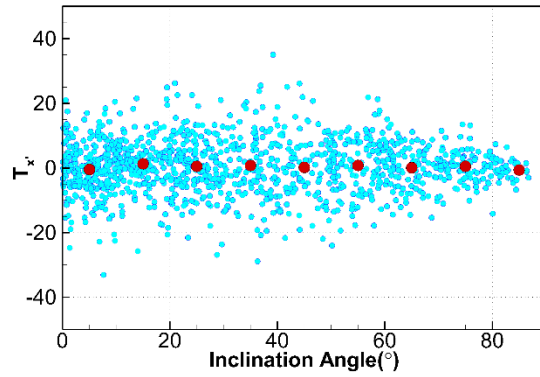
Fig. 5. 18. Ratio of lift-to-drag force ratio at different Re and φ

In dense fluid particulate systems, in current practice, angular momentum transfer is exclusively modeled through particle-particle collisional dynamics. While this is a good approximation for spherical particles, fluid moments or torques imparted by fluid forces could potentially create comparable moments in non-spherical systems. To investigate this aspect, normalized fluid torques along the three principle axes of the local coordinate system (Fig. 5.1) are calculated and shown in Fig. 5.19. Both T_x and T_y , have near-zero mean values resulting from the random distribution

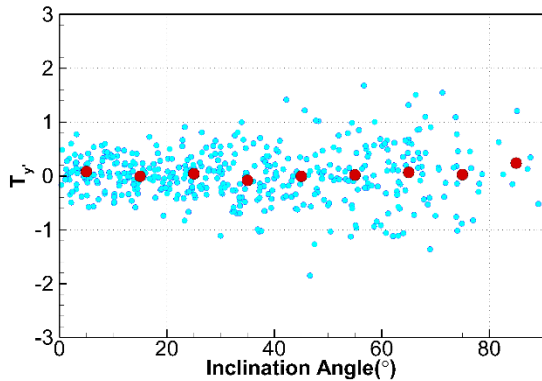
of the particle orientations. They both exhibit opposite trends with respect to the inclination angle. $T_{x'}$ has maximum variation at low angles whereas the variations in $T_{y'}$ increases with inclination angle. The mean pitching torque, $T_{z'}$, has a non-zero negative mean value with respect to inclination angle and exhibits the same trend as the lift force. It varies significantly with respect to θ , φ and Re and is analyzed further.



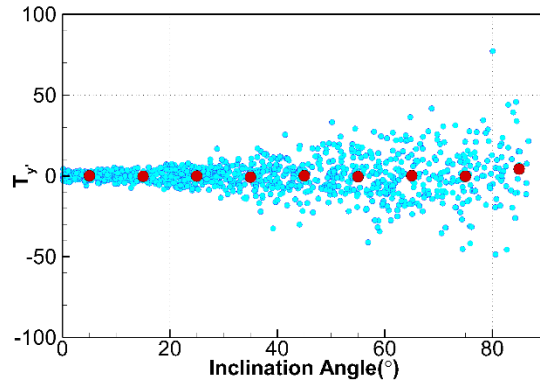
(a) $T_{x'}$ at $Re=10$, $\varphi=0.1$



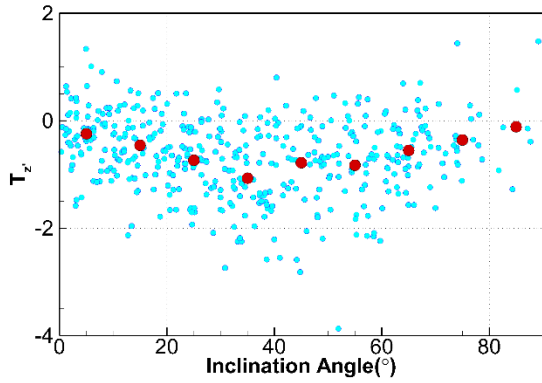
(b) $T_{x'}$ at $Re=300$, $\varphi=0.3$



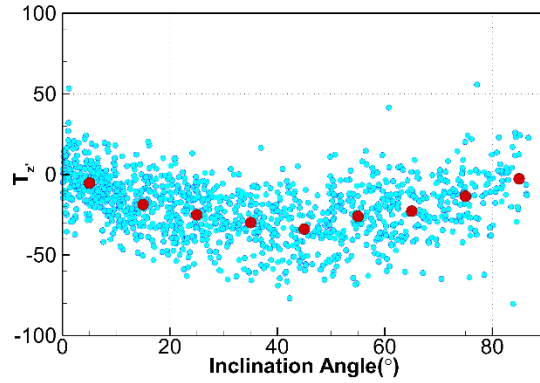
(c) $T_{y'}$ at $Re=10$, $\varphi=0.1$



(d) $T_{y'}$ at $Re=300$, $\varphi=0.3$



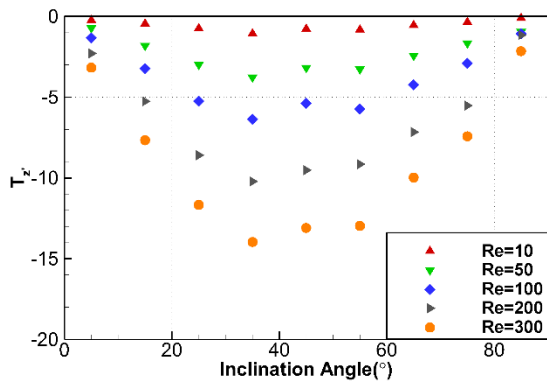
(e) $T_{z'}$ at $Re=10$, $\varphi=0.1$



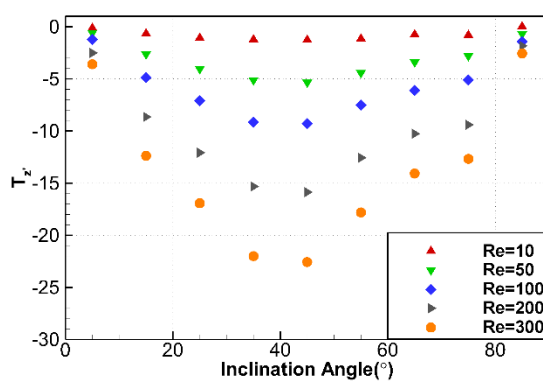
(f) $T_{z'}$ at $Re=300$, $\varphi=0.3$

Fig. 5.19. Variation of directional torque with inclination angle.

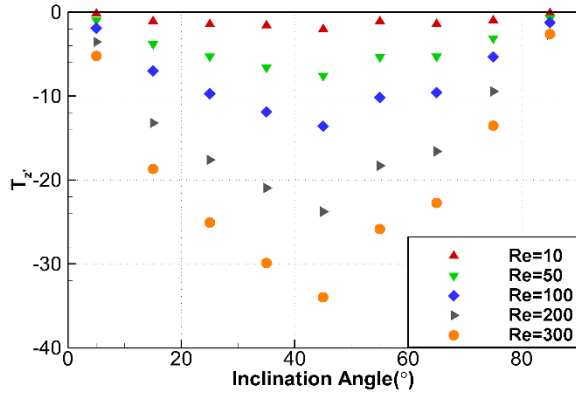
The results of mean $T_{z'}$ versus inclination angle are shown in Fig. 5.20 for all the cases. The results show that similar to both lift and drag, pitching torque increases with respect to Re and φ and it follows trends similar to that followed by the lift force. Similar to the observation for lift force, the maximum torque appears near $\theta = 35^\circ$ at $\varphi = 0.1$, and shows a tendency of shifting to larger inclination angles as φ increases, peaking at $\theta = 45^\circ$ at $\varphi = 0.3$.



(a) Results at $\varphi=0.1$



(b) Results at $\varphi=0.2$



(c) Results at $\varphi=0.3$

Fig. 5. 20. Variation of pitching torque at different Re and φ

In order to estimate the relative importance of fluid torque in relation to collisional torque, the collisional torque is estimated using Hertz theory (Stronge, 2000) at the elastic limit. In the absence of a known collision force, the normal collision force of a sphere of diameter d_p^* colliding with a flat surface is estimated by the yield stress acting over a contact area just before it enters the plastic regime. To mimic the maximum elastic torque produced in the AR0.25 cylinder geometry, the normal force is applied at a radius $r^* = d_p^*/2$ which is the largest moment arm about the particle local z –axis. The calculated torque is further normalized using Eq. (5.9) and the ratio between maximum fluid torque and collisional torque for $500 \mu m \leq d_p^* \leq 5000 \mu m$ at $Re = 300$, $\varphi = 0.3$ shown in Fig. 5.20(c) is presented in Fig. 5.21. Three bed materials of interest are tested, soft wood (white pine), hard wood (white oak), and sand. 5.3 gives the relevant properties.

Table 5. 3 Mechanical properties of the three materials

	White Pine [93–95]	White Oak [93,95]	Sand [96]
Poisson Ratio	0.33	0.618	0.3

Young's Modulus (<i>MPa</i>)	8500	12300	20000
Yield Stress (<i>MPa</i>)	3.5	9.1	400

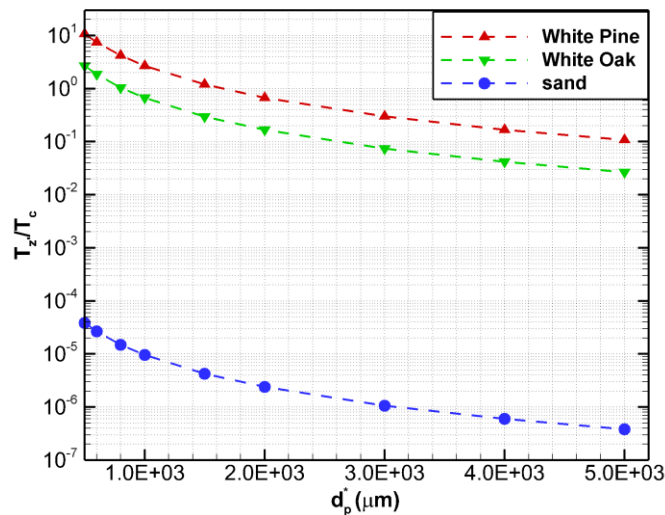


Fig. 5. 21. Ratio between fluid torque and collisional torque for different materials

It is found that for sand particles, the collision torque is between 5 to 6 orders-of-magnitude larger than the fluid torque, whereas for soft and hard wood the fluid torque is competitive with collision torque and even up to 10 times larger for soft wood at $d_p^* = 500 \mu\text{m}$. Generalization of the trends in Fig 5. 21 lead to the conclusion that fluid torque is competitive with collision torque for small diameter, lower density particles colliding at low velocities. Therefore, although neglecting fluid torque may be justifiable in many systems, it cannot be neglected in all non-spherical systems. However, we note that not all collisions will reach the elastic limit and while collisional torque only acts for a very short time interval, fluid torque is persistent over the flight of the particle. Fig. 5.21 should be viewed with these assumptions in mind. Nevertheless, it does give an order of magnitude estimate of the relative importance.

5.5. CONCLUSIONS

Fluid forces in a suspension of oblate cylinder-like particles of AR0.25 is investigated in the range $10 \leq Re \leq 300$ and $0.1 \leq \varphi \leq 0.3$ using particle resolved simulations. The following major conclusions are made.

1. Existing single particle drag correlation (Hölzer and Sommerfeld, 2008) combined with suspension correlations for spherical (Tenneti et al., 2011) as well as AR0.25 ellipsoidal particles (Rong et al., 2015) under predict the PRS drag force between 20% to 40% over the full range of Re and φ investigated. It is shown that the Rong et al. suspension correlation, developed for a fixed bed of particles with preferential orientation, agrees much better with PRS done in a suspension of similar preferential orientation. Unlike prolate spheroids, preferential orientation near 90° of the oblate cylindrical geometry results in lower drag force because of large wake sheltering effects in the suspension.
2. A sinusoidal function $F_{d,\theta} = F_{d,\theta=0^\circ} + (F_{d,\theta=90^\circ} - F_{d,\theta=0^\circ})\sin(\theta)$ was found to capture the variation of normalized drag with respect to particle inclination angle over the range $10 \leq Re \leq 300$ and $0 \leq \varphi \leq 0.3$. It is also shown that the mean ensemble normalized drag force can be expressed as a linear function given by $F_d = F_{d,\theta=0^\circ} + \frac{1}{2}(F_{d,\theta=90^\circ} - F_{d,\theta=0^\circ})$. Therefore, only two values of drag force, at $\theta = 0^\circ$ and $\theta = 90^\circ$ are needed at a given (Re, φ) to define the ensemble mean and inclination dependent drag.
3. By comparing the drag force and the statistical nature of flow and pressure field of oblate AR0.25 cylinder geometry of the current work to a suspension of prolate ellipsoids, it is shown that in spite of having nearly the same sphericity, considerable differences exist in the flow structure and drag force between the two. Thus it is concluded that sphericity by

itself is not a good indicator of drag force on non-spherical particles and its use in drag correlations may not be correct.

4. Comparison of fluid forces and torque on the AR0.25 cylinders in different directions indicates that lift and pitching torque are the most prominent in addition to drag force. The lift force is 20% of the drag force at $Re=10$ and reaches up to 80% of the drag force at $Re=300$ under inclination angle less than 35. Pressure contribution to lift force dominates even at $Re = 10$. Unlike the lift force on prolate particle suspensions that can be scaled using a $\sin(\theta) \cdot \cos(\theta)$ distribution, the lift force in the current study exhibits asymmetries about its peak value and drops off faster as θ increases beyond the peak location. It is shown that the pitching torque follows the same trend with inclination angle as lift force. Comparing the pitching fluid torque to collision torque in an elastic collision shows that as the particle equivalent diameter, density, and collisional velocity decrease fluid torque can be of the same order of magnitude as collisional torque and cannot be summarily neglected.

5.6. ACKNOWLEDGEMENTS

The authors would like to acknowledge the computational resources provided by Advanced Computational Research (ARC) at Virginia Tech.

References

- [1] Hölzer, A., and Sommerfeld, M., 2008, “New Simple Correlation Formula for the Drag Coefficient of Non-Spherical Particles,” *Powder Technol.*, **184**(3), pp. 361–365.
- [2] Roos, F. W., and Willmarth, W. W., 1971, “Some Experimental Results on Sphere and Disk Drag,” *AIAA J.*, **9**(2), pp. 285–291.
- [3] Bailey, A. B., and Hiatt, J., 1971, “Free-Flight Measurements of Sphere Drag at Subsonic, Transonic, Supersonic, and Hypersonic Speeds for Continuum, Transition, and near-Free-Molecular Flow Conditions.”
- [4] Achenbach, E., 1972, “Experiments on the Flow Past Spheres at Very High Reynolds Numbers,” **54**, pp. 565–575.
- [5] Clift, R., Grace, J.R., Weber, M. E., 1978, “Bubbles, Drops and Particles,” *J. Fluid Mech.*, **94**(04), p. 795.
- [6] HAIDER, A., and LEVENSPIEL, O., 1989, “Drag Coefficient and Terminal Velocity of Spherical and Nonspherical Particles,” **58**, pp. 63–70.
- [7] Brown, P. . P., and Lawler, D. F., 2003, “Sphere Drag and Settling Velocity Revisited,” *J. Environ. Eng.*, **129**(March), pp. 222–231.
- [8] Turton, R., and Levenspiel, O., 1986, “A Short Note on the Drag Correlation for Spheres,” *Powder Technol.*, **47**, pp. 83–86.
- [9] Zastawny, M., Mallouppas, G., Zhao, F., and van Wachem, B., 2012, “Derivation of Drag and Lift Force and Torque Coefficients for Non-Spherical Particles in Flows,” *Int. J. Multiph. Flow*, **39**, pp. 227–239.
- [10] Kishore, N., and Gu, S., 2011, “Effect of Blockage on Heat Transfer Phenomena of Spheroid Particles at Moderate Reynolds and Prandtl Numbers,” *Chem. Eng. Technol.*, **34**(9), pp. 1551–1558.

- [11] Ouchene, R., Khalij, M., Arcen, B., and Tanière, A., 2016, “A New Set of Correlations of Drag, Lift and Torque Coefficients for Non-Spherical Particles and Large Reynolds Numbers,” *Powder Technol.*, **303**, pp. 33–43.
- [12] Ouchene, R., Khalij, M., Tanière, A., and Arcen, B., 2015, “Drag, Lift and Torque Coefficients for Ellipsoidal Particles: From Low to Moderate Particle Reynolds Numbers,” *Comput. Fluids*, **113**, pp. 53–64.
- [13] Shenoy, a. R., and Kleinstreuer, C., 2008, “Flow over a Thin Circular Disk at Low to Moderate Reynolds Numbers,” *J. Fluid Mech.*, **605**(2008), pp. 253–262.
- [14] Yang, J., Liu, M., Wu, G., Liu, Q., and Zhang, X., 2015, “Low-Frequency Characteristics in the Wake of a Circular Disk,” *Phys. Fluids*, **27**(6).
- [15] Chrust, M., Dauteuille, C., Bobinski, T., Rokicki, J., Goujon-Durand, S., Wesfreid, J. E., Bouchet, G., and Dušek, J., 2015, “Effect of Inclination on the Transition Scenario in the Wake of Fixed Disks and Flat Cylinders,” *J. Fluid Mech.*, **770**(2015), pp. 189–209.
- [16] Saha, A. K., 2004, “Three-Dimensional Numerical Simulations of the Transition of Flow Past a Cube,” *Phys. Fluids*, **16**(5), pp. 1630–1646.
- [17] Saha, A. K., 2006, “Three-Dimensional Numerical Study of Flow and Heat Transfer from a Cube Placed in a Uniform Flow,” *Int. J. Heat Fluid Flow*, **27**(1), pp. 80–94.
- [18] Ergun, S., 1952, “Fluid Flow through Packed Columns,” *Chem. Eng. Prog.*, **48**, pp. 89–94.
- [19] Wen, C., and Yu, Y., 1962, “Mechanics of Fluidization,” *Chem Eng Prog Symp*, **62**, pp. 100–111.
- [20] Gidaspow, D., 1986, “Hydrodynamics of Fluidization and Heat Transfer: Supercomputer Modeling,” *Screen*, **39**(1), pp. 1–23.
- [21] Felice, R. D. I., 1994, “THE VOIDAGE FUNCTION FOR FLUID-PARTICLE INTERACTION SYSTEMS,” *Int. J. Multiph. Flow*, **20**(I), pp. 153–159.
- [22] Tenneti, S., Garg, R., and Subramaniam, S., 2011, “Drag Law for Monodisperse Gas-Solid Systems Using Particle-Resolved Direct Numerical Simulation of Flow Past Fixed

- Assemblies of Spheres,” *Int. J. Multiph. Flow*, **37**(9), pp. 1072–1092.
- [23] Hill, R. J., Koch, D. L., and Ladd, A. J. C., 2001, “The First Effects of Fluid Inertia on Flows in Ordered and Random Arrays of Spheres,” *J. Fluid Mech.*, **448**(2001), pp. 243–278.
- [24] Rong, L. W., Dong, K. J., and Yu, A. B., 2013, “Lattice-Boltzmann Simulation of Fluid Flow through Packed Beds of Uniform Spheres: Effect of Porosity,” *Chem. Eng. Sci.*, **99**, pp. 44–58.
- [25] Rong, L. W., Zhou, Z. Y., and Yu, A. B., 2015, “Lattice-Boltzmann Simulation of Fluid Flow through Packed Beds of Uniform Ellipsoids,” *Powder Technol.*, **285**, pp. 146–156.
- [26] Chen, Y., and Müller, C. R., 2018, “Development of a Drag Force Correlation for Assemblies of Cubic Particles: The Effect of Solid Volume Fraction and Reynolds Number,” *Chem. Eng. Sci.*, **192**, pp. 1157–1166.
- [27] He, L., Tafti, D. K., and Nagendra, K., 2017, “Evaluation of Drag Correlations Using Particle Resolved Simulations of Spheres and Ellipsoids in Assembly,” *Powder Technol.*, **313**, pp. 332–343.
- [28] He, L., and Tafti, D., 2018, “Variation of Drag, Lift and Torque in a Suspension of Ellipsoidal Particles,” *Powder Technol.*, **335**, pp. 409–426.
- [29] Ma, H., Xu, L., and Zhao, Y., 2016, “CFD-DEM Simulation of Fluidization of Rod-like Particles in a Fluidized Bed,” *Powder Technol.*
- [30] Ma, H., Zhao, Y., and Cheng, Y., 2019, “CFD-DEM Modeling of Rod-like Particles in a Fluidized Bed with Complex Geometry,” *Powder Technol.*, **344**, pp. 673–683.
- [31] Ma, H., and Zhao, Y., 2018, “Investigating the Fluidization of Disk-like Particles in a Fluidized Bed Using CFD-DEM Simulation,” *Adv. Powder Technol.*, **29**(10), pp. 2380–2393.
- [32] Zhou, Z. Y., Pinson, D., Zou, R. P., and Yu, A. ., 2009, “CFD-DEM SIMULATION OF GAS FLUIDIZATION OF ELLIPSOIDAL PARTICLES,” *CFD-DEM SIMULATION OF*

- [33] Vollmari, K., Jasevičius, R., and Kruggel-Emden, H., 2016, “Experimental and Numerical Study of Fluidization and Pressure Drop of Spherical and Non-Spherical Particles in a Model Scale Fluidized Bed,” *Powder Technol.*, **291**, pp. 506–521.
- [34] Tafti, D. K. D. K., 2001, “GenIDLEST: A Scalable Parallel Computational Tool for Simulating Complex Turbulent Flows,” *ASME-PUBLICATIONS-FED*, pp. 347–356.
- [35] Tafti, D. K., 2010, “Time-Accurate Techniques for Turbulent Heat Transfer Analysis in Complex Geometries,” *Comput. fluid Dyn. heat Transf.*, **41**, pp. 217–264.
- [36] Nagendra, K., Tafti, D. K., and Viswanath, K., 2014, “A New Approach for Conjugate Heat Transfer Problems Using Immersed Boundary Method for Curvilinear Grid Based Solvers,” *J. Comput. Phys.*, **267**, pp. 225–246.
- [37] Cao, Z., and Tafti, D. K., 2018, “Investigation of Drag, Lift and Torque for Fluid Flow Past a Low Aspect Ratio (1:4) Cylinder,” *Comput. Fluids*, **177**, pp. 123–135.
- [38] Nvidia, “NVIDIA PhysX SDK 3.3.4 Documentation.”
- [39] Sanjeevi, S. K. P., and Padding, J. T., 2019, “Hydrodynamic Forces on Assemblies of Non-Spherical Particles: Orientation and Voidage Effects.”
- [40] Zhou, Z. Y., Pinson, D., Zou, R. P., and Yu, A. B., 2011, “Discrete Particle Simulation of Gas Fluidization of Ellipsoidal Particles,” *Chem. Eng. Sci.*, **66**(23), pp. 6128–6145.
- [41] Vollmari, K., Oschmann, T., Wirtz, S., and Kruggel-Emden, H., 2015, “Pressure Drop Investigations in Packings of Arbitrary Shaped Particles,” *Powder Technol.*, **271**, pp. 109–124.
- [42] Arcen, B., Ouchene, R., Khalij, M., and Tanière, A., 2017, “Prolate Spheroidal Particles’ Behavior in a Vertical Wall-Bounded Turbulent Flow,” *Phys. Fluids*, **29**(9).
- [43] Schiller, L., and Neumann, A., 1933, “Fundamental Calculations in Gravitational Processing,” *Zeitschrift Des Vereines Dtsch. Ingenieure*, **77**, pp. 318–320.

- [44] Brown, P. P. . P. P. . P., and Lawler, D. F., 2003, "Sphere Drag and Settling Velocity Revisited," *J. Environ. Eng.*, **129**(3), pp. 222–231.
- [45] Carranza, F., and Zhang, Y., 2017, "Study of Drag and Orientation of Regular Particles Using Stereo Vision , Schlieren Photography and Digital Image Processing," *Powder Technol.*, **311**, pp. 185–199.
- [46] Bagheri, G., and Bonadonna, C., 2016, "On the Drag of Freely Falling Non-Spherical Particles," *Powder Technol.*, **301**, pp. 526–544.
- [47] Buchalter, B. J., and Bradley, R. M., 1994, "Orientational Order in Amorphous Packings of Ellipsoids," *Epl*, **26**(3), pp. 159–164.
- [48] Gong, J., and Liu, J., 2017, "Effect of Aspect Ratio on Triaxial Compression of Multi-Sphere Ellipsoid Assemblies Simulated Using a Discrete Element Method," *Particuology*, **32**, pp. 49–62.
- [49] Gan, J., and Yu, A., 2019, "DEM Study on the Packing Density and Randomness for Packing of Ellipsoids," *Powder Technol.*, pp. 12–18.
- [50] Woodcock, N. H., and Naylor, M. A., 1983, "Randomness Testing in Three-Dimensional Orientation Data," *J. Struct. Geol.*, **5**(5), pp. 539–548.
- [51] Bezrukov, A., and Stoyan, D., 2007, "Simulation and Statistical Analysis of Random Packings of Ellipsoids," *Part. Part. Syst. Charact.*, **23**(5), pp. 388–398.
- [52] Stoyan, D., and Stoyan, H., 1994, "Fractals, Random Shapes, and Point Fields: Methods of Geometrical Statistics," Wiley.
- [53] He, L., and Tafti, D. K., 2017, "Heat Transfer in an Assembly of Ellipsoidal Particles at Low to Moderate Reynolds Numbers," *Int. J. Heat Mass Transf.*, **114**, pp. 324–336.
- [54] Tenneti, S., Sun, B., Garg, R., and Subramaniam, S., 2013, "Role of Fluid Heating in Dense Gas-Solid Flow as Revealed by Particle-Resolved Direct Numerical Simulation," *Int. J. Heat Mass Transf.*, **58**(1–2), pp. 471–479.
- [55] Gunn, D. J., 1978, "Transfer of Heat or Mass to Particles in Fixed and Fluidised Beds," *Int.*

- J. Heat Mass Transf., **21**(4), pp. 467–476.
- [56] Sun, B., Tenneti, S., and Subramaniam, S., 2015, “Modeling Average Gas-Solid Heat Transfer Using Particle-Resolved Direct Numerical Simulation,” *Int. J. Heat Mass Transf.*, **86**, pp. 898–913.
- [57] Tavassoli, H., Kriebitzsch, S. H. L., van der Hoef, M. A., Peters, E. A. J. F., and Kuipers, J. A. M., 2013, “Direct Numerical Simulation of Particulate Flow with Heat Transfer,” *Int. J. Multiph. Flow*, **57**, pp. 29–37.
- [58] Singhal, A., Cloete, S., Radl, S., Quinta-Ferreira, R., and Amini, S., 2017, “Heat Transfer to a Gas from Densely Packed Beds of Monodisperse Spherical Particles,” *Chem. Eng. J.*, **314**, pp. 27–37.
- [59] Singhal, A., Cloete, S., Radl, S., Quinta-Ferreira, R., and Amini, S., 2017, “Heat Transfer to a Gas from Densely Packed Beds of Cylindrical Particles,” *Chem. Eng. Sci.*, **172**, pp. 1–12.
- [60] Tavassoli, H., Peters, E. A. J. F. J. F., and Kuipers, J. A. M. M., 2015, “Direct Numerical Simulation of Fluid-Particle Heat Transfer in Fixed Random Arrays of Non-Spherical Particles,” *Chem. Eng. Sci.*, **129**, pp. 42–48.
- [61] Chen, Y., and Müller, C. R., 2019, “Lattice Boltzmann Simulation of Gas-Solid Heat Transfer in Random Assemblies of Spheres: The Effect of Solids Volume Fraction on the Average Nusselt Number for $Re \leq 100$,” *Chem. Eng. J.*, **361**(February 2018), pp. 1392–1399.
- [62] Chen, Y., and Müller, C. R., 2020, “Gas-Solid Heat Transfer in Assemblies of Cubes for $ReV \leq 100$,” *Chem. Eng. Sci.*, **216**, p. 115478.
- [63] Link, J. M., Cuypers, L. A., Deen, N. G., and Kuipers, J. A. M., 2005, “Flow Regimes in a Spout-Fluid Bed: A Combined Experimental and Simulation Study,” *Chem. Eng. Sci.*, **60**(13), pp. 3425–3442.
- [64] Deen, N. G., Kriebitzsch, S. H. L., van der Hoef, M. A., and Kuipers, J. A. M., 2012, “Direct Numerical Simulation of Flow and Heat Transfer in Dense Fluid-Particle Systems,” *Chem.*

- Eng. Sci., **81**, pp. 329–344.
- [65] Jackson, R., 1997, “Locally Averaged Equations of Motion for a Mixture of Identical Spherical Particles and a Newtonian Fluid,” Chem. Eng. Sci., **52**(15), pp. 2457–2469.
- [66] Lu, J., Peters, E. A. J. F., and Kuipers, J. A. M., 2019, “Direct Numerical Simulation of Fluid Flow and Dependently Coupled Heat and Mass Transfer in Fluid-Particle Systems,” Chem. Eng. Sci., **204**, pp. 203–219.
- [67] Kravets, B., and Kruggel-Emden, H., 2017, “Investigation of Local Heat Transfer in Random Particle Packings by a Fully Resolved LBM-Approach,” Powder Technol., **318**, pp. 293–305.
- [68] Kravets, B., Rosemann, T., Reinecke, S. R., and Kruggel-Emden, H., 2019, “A New Drag Force and Heat Transfer Correlation Derived from Direct Numerical LBM-Simulations of Flown through Particle Packings,” Powder Technol., **345**, pp. 438–456.
- [69] Wakao, N., Kaguei, S., and Funazkri, T., 1979, “Effect of Fluid Dispersion Coefficients on Particle-to-Fluid Heat Transfer Coefficients in Packed Beds: Correlation of Nusselt Numbers,” K GK Kautschuk Gummi Kunststoffe, **34**(3)(1–2), pp. 325–336.
- [70] Cao, Z., Tafti, D. K., and Shahnam, M., 2020, “Development of Drag Correlation for Suspensions of Ellipsoidal Particles,” Powder Technol., **369**, pp. 298–310.
- [71] Cao, Z., and Tafti, D. K. K., 2020, “Fluid Forces and Torques in Suspensions of Oblate Cylinders with Aspect Ratio 1:4,” Int. J. Multiph. Flow, **131**, p. 103394.
- [72] Wittig, K., Richter, A., and Golia, A., 2014, “CD and Nu Closure Relations for Spherical and Nonspherical Particles,” Gasif. Process. Model. Simul., pp. 73–104.
- [73] Richter, A., and Nikrityuk, P. A., 2013, “New Correlations for Heat and Fluid Flow Past Ellipsoidal and Cubic Particles at Different Angles of Attack,” Powder Technol., **249**, pp. 463–474.
- [74] Ranz, W. E., and Marshall, W. R., 1952, “Evaporation from Drops - Part 1,” Chem. Eng. Prog., **48**, pp. 141–148.

- [75] Zhu, H. P., Zhou, Z. Y., Yang, R. Y., and Yu, A. B., 2007, “Discrete Particle Simulation of Particulate Systems: Theoretical Developments,” *Chem. Eng. Sci.*, **62**(13), pp. 3378–3396.
- [76] Zhu, H. P., Zhou, Z. Y., Yang, R. Y., and Yu, A. B., 2008, “Discrete Particle Simulation of Particulate Systems: A Review of Major Applications and Findings,” *Chem. Eng. Sci.*, **63**(23), pp. 5728–5770.
- [77] Flemmer, R. L. C., and Banks, C. L., 1986, “On the Drag Coefficient of a Sphere,” *Powder Technol.*, **48**(3), pp. 217–221.
- [78] Vakil, A., and Green, S. I., 2009, “Drag and Lift Coefficients of Inclined Finite Circular Cylinders at Moderate Reynolds Numbers,” *Comput. Fluids*, **38**(9), pp. 1771–1781.
- [79] Militzer, J., Kan, J. M., Hamdullahpur, F., Amyotte, P. R., and Al Taweel, A. M., 1989, “Drag Coefficient for Axisymmetric Flow around Individual Spheroidal Particles,” *Powder Technol.*, **57**(3), pp. 193–195.
- [80] Unnikrishnan, A., and Chhabra, R. P., 1991, “An Experimental Study of Motion of Cylinders in Newtonian Fluids: Wall Effects and Drag Coefficient,” *Chem. Eng. Process. Process Intensif.*, **30**(1985), pp. 61–67.
- [81] Ke, C., Shu, S., Zhang, H., Yuan, H., and Yang, D., 2018, “On the Drag Coefficient and Averaged Nusselt Number of an Ellipsoidal Particle in a Fluid,” *Powder Technol.*, **325**, pp. 134–144.
- [82] Eshghinejadfard, A., Hosseini, S. A., and Thévenin, D., 2019, “Effect of Particle Density in Turbulent Channel Flows with Resolved Oblate Spheroids,” *Comput. Fluids*, **184**, pp. 29–39.
- [83] Fonseca, F., and Herrmann, H. J., 2004, “Sedimentation of Oblate Ellipsoids at Low and Moderate Reynolds Numbers,” *Phys. A Stat. Mech. its Appl.*, **342**(3–4), pp. 447–461.
- [84] Jieqing Gan, Zongyan Zhou, and A. Y., 2016, “CFD–DEM Modeling of Gas Fluidization of Fine Ellipsoidal Particles,” *VTT Publ.*, **62**(504), pp. 3–194.
- [85] Shrestha, S., Kuang, S., Yu, A., and Zhou, Z., 2019, “Bubble Dynamics in Bubbling

- Fluidized Beds of Ellipsoidal Particles,” *AIChE J.*, **65**(11), pp. 1–17.
- [86] Gan, J., Zhou, Z., and Yu, A., 2016, “Particle Scale Study of Heat Transfer in Packed and Fluidized Beds of Ellipsoidal Particles,” *Chem. Eng. Sci.*, **144**, pp. 201–215.
- [87] Happel, J., and Brenner, H., 1983, “Low Reynolds Number Hydrodynamics,” Englewood Cliffs NJ, **40**(1), pp. 25–45.
- [88] Sanjeevi, S. K. P., and Padding, J. T., 2017, “On the Orientational Dependence of Drag Experienced by Spheroids,” *J. Fluid Mech.*, **820**(May), p. R1.
- [89] Hölzer, A., and Sommerfeld, M., 2009, “Lattice Boltzmann Simulations to Determine Drag, Lift and Torque Acting on Non-Spherical Particles,” *Comput. Fluids*, **38**(3), pp. 572–589.
- [90] Ganser, G. H., 1993, “A Rational Approach to Drag Prediction of Spherical and Nonspherical Particles,” *Powder Technol.*, **77**(2), pp. 143–152.
- [91] Wang, Y., Zhou, L., Wu, Y., and Yang, Q., 2018, “New Simple Correlation Formula for the Drag Coefficient of Calcareous Sand Particles of Highly Irregular Shape,” *Powder Technol.*, **326**, pp. 379–392.
- [92] Stronge, W. J., 2000, *Impact Mechanics*.
- [93] Green, D. W., Winandy, J. E., and Kretschmann, D. E., 1999, “Mechanical Properties of Wood,” *Mater. Res. Soc. Symp. - Proc.*, **546**, pp. 213–218.
- [94] Modena, C., Lourenco, P. B., and Roca, P., 2004, *Structural Analysis of Historical Constructions-2 Volume Set: Possibilities of Numerical and Experimental Techniques- Proceedings of the IVth Int. Seminar on Structural Analysis of Historical Constructions*.
- [95] Clauser, H. R., Donald, E., and Manning, A. V., 1975, *Industrial and Engineering Materials*.
- [96] Yu, K., and Tafti, D., 2016, “Impact Model for Micrometer-Sized Sand Particles,” *Powder Technol.*, **294**, pp. 11–21.
- [97] Bailey, A. B., 1931, “Sphere Drag Coefficients for a Broad Range of Mach and Reynolds

- Numbers,” **10**(11), pp. 1436–1440.
- [98] Barati, R., Neyshabouri, S. A. A. S., and Ahmadi, G., 2014, “Development of Empirical Models with High Accuracy for Estimation of Drag Coefficient of Flow around a Smooth Sphere: An Evolutionary Approach,” *Powder Technol.*, **257**, pp. 11–19.
- [99] Ui, T. J., Hussey, R. G., and Roger, R. P., 1984, “Stokes Drag on a Cylinder in Axial Motion,” *Phys. Fluids*, **27**(4), p. 787.
- [100] Marchildon, E. K., Clamen, A., and Gauvin, W. H., 1964, “Drag and Oscillatory Motion of Freely Falling Cylindrical Particles,” *Can. J. Chem. Eng.*, **42**(4), pp. 178–182.
- [101] Fernandes, P. C., Risso, F., Ern, P., and Magnaudet, J., 2007, “Oscillatory Motion and Wake Instability of Freely Rising Axisymmetric Bodies,” *J. Fluid Mech.*, **573**(2007), pp. 479–502.
- [102] Auguste, F., Fabre, D., and Magnaudet, J., 2010, “Bifurcations in the Wake of a Thick Circular Disk,” *Theor. Comput. Fluid Dyn.*, **24**(1–4), pp. 305–313.
- [103] Yow, H. N., Pitt, M. J., and Salman, a. D., 2005, “Drag Correlations for Particles of Regular Shape,” *Adv. Powder Technol.*, **16**(4), pp. 363–372.
- [104] Rosendahl, L., 2000, “Using a Multi-Parameter Particle Shape Description to Predict the Motion of Non-Spherical Particle Shapes in Swirling Flow,” *Appl. Math. Model.*, **24**(1), pp. 11–25.
- [105] Cleary, P. W., 2010, “DEM Prediction of Industrial and Geophysical Particle Flows,” *Particuology*, **8**(2), pp. 106–118.
- [106] Guan, Y., Guadarrama-Lara, R., Jia, X., Zhang, K., and Wen, D., 2017, “Lattice Boltzmann Simulation of Flow Past a Non-Spherical Particle,” *Adv. Powder Technol.*, (April), pp. 1–9.
- [107] Richter, A., and Nikrityuk, P. A., 2012, “Drag Forces and Heat Transfer Coefficients for Spherical, Cuboidal and Ellipsoidal Particles in Cross Flow at Sub-Critical Reynolds Numbers,” *Int. J. Heat Mass Transf.*, **55**(4), pp. 1343–1354.

- [108] Jones, D. A., and Clarke, D. B., 2008, "Simulation of Flow Past a Sphere Using the Fluent Code," p. 35.
- [109] Pearson, J. R. A., 1966, *Low Reynolds Number Hydrodynamics*.
- [110] In, K. M., Choi, D. H., and Kim, M. U., 1995, "Two-Dimensional Viscous Flow Past a Flat Plate," *Fluid Dyn. Res.*, **15**, pp. 13–24.

Appendix A

Investigation of drag, lift and torque for fluid flow past a low aspect ratio (1:4) cylinder

(Published at *Computers & Fluids*, volume: 177, pp.123-135.)

Abstract

Non-spherical objects exist in many multiphase applications but there is very limited data available on the fluid forces acting on these different shapes. This work derives correlations for drag, lift and torque coefficients for a single low aspect ratio 1:4 cylinder (tablet shaped object) placed at different incidence angles to the approach flow using direct numerical simulations (DNS). An Immersed Boundary Method (IBM) is used for deriving the force coefficients for $10 \leq Re \leq 300$ and incidence angles $0^\circ \leq \theta \leq 90^\circ$. The method is validated by comparisons to existing data on spheres, to results from a body conforming grid, and through a grid independency study. The flow around the cylinder remains steady till $Re=200$ $\theta \leq 30^\circ$. The general correlation of Hölzer and Sommerfeld [1] for non-spherical particles, over predicts the drag coefficient for $0^\circ < \theta < 90^\circ$ and the degree of over prediction increases with Reynolds number. The lift coefficient has a symmetric distribution about the maximum value at $\theta = 45^\circ$ at $Re=10$ but develops asymmetries in θ as Reynolds number increases. Contributions of pressure force and shear to drag and lift for each case is presented to provide a detailed view of the hydrodynamic forces on the object. The trends in the torque coefficient are similar to the lift coefficient reaching a maximum value near 45 degrees. Correlations based the Reynolds number and incidence angle are developed for drag, lift and torque coefficients.

Keywords: Low aspect ratio cylinder, drag coefficient, lift coefficient, torque coefficient, IBM

Introduction and Literature Review

Prediction of the behavior of fluid flow past objects of various shapes is of great relevance to many industrial processes such as gasification, combustion, refining and processing of chemicals and ores, drying feedstock, separation technologies, etc. It is also of importance in many natural systems undergoing erosion and sedimentation, transport of particulate matter in the atmosphere and oceans, etc. Most early work in characterizing fluid-bluff body interaction was performed for spherical shape because of the geometrical simplicity [2–4,6,97]. The majority of early research characterized the drag force. Based on available experimental data in the literature, Clift et al.[5] developed a drag correlation for different ranges of Reynolds numbers. The Reynolds number is defined as $Re = \frac{\rho^* u^* d_0^*}{\mu^*}$. In the definition, ρ^* is the density of the fluid, u^* is the undisturbed approach flow velocity, μ^* is the dynamic viscosity of the fluid and d_0^* is the equivalent spherical diameter. Later in 2003, Brown and Lawler[7] developed a single correlation to fit 480 experimental data points with 178 of them being corrected for wall proximity effect for Reynolds number up to 2×10^5 . Many other researchers have also proposed correlations for the drag on a sphere[6,8,77,98].

As computational fluid dynamics has matured and computational power has increased, computational research in characterizing drag over non-spherical objects has gained traction. Militzer et al.[79] developed a correlation for drag coefficient on a spheroid based on previous numerical and experimental results. Their correlation covered the Reynolds number range from 1 to 200 and the spheroid aspect ratio(ratio between the axis of the spheroid that is parallel and perpendicular to the axis of rotational symmetry) from 0.2 to 5. Kishore and Gu[10] did

simulations for a spheroid with aspect ratio from 0.25 to 2.5 in the Reynolds number range from 1 to 200 and developed a correlation with average error of $\pm 5.8\%$ to fit their simulation results. However, in both studies, the object is placed normal to the approach flow and no data is available for the spheroid placed at an angle to the approach velocity. Zastawny et al. [9] developed a correlation for drag as well as lift and torque on a spheroid based on Direct Numerical Simulation (DNS) using the immersed boundary method (IBM). They considered the cases with different inclinations ranging from 0° to 90° . Similarly, Richter and Nikrityu [73] did simulations on a spheroid at varying incidence angles using a body conforming mesh for the object. Although the two studies mentioned above studied the behavior of the object in the flow field more comprehensively, Zastawny et al [9] only studied three aspect ratios of the spheroid: 0.2, 1.25 and 2.5 while Richter and Nikrityu[73] only studied a spheroid with an aspect ratio of 2. To broaden the range of data available, Ouchene et al. [11] did simulations using DNS with a body conforming mesh for spheroids with aspect ratio ranging from 1 to 32 and derived a correlation for drag, lift and torque coefficient for incidence angles from 0° to 90° and Reynolds numbers from 1 to 240.

For fluid flow past cylindrical objects, Ui et al. [99] performed free falling experiments for cylinders with aspect ratio (ratio between height and diameter of the cylinder) from 4 to 100 and disks with aspect ratio from 0.019 to 0.26. Sharma and Chhabra [80] did similar experiments for cylinders with aspect ratio from 0.05 to 2 at Reynolds number from 0.2 to 180. Although both Ui et al. [99] and Sharma and Chhabra[80] studied the drag comprehensively for different cylinders, the orientation of the cylinder is always fixed with its axis of symmetry parallel to the motion of the cylinder. A notable factor in free falling experiments is that when a certain critical Reynolds number is reached, the wake becomes unstable and the cylinder starts oscillating [100,101], e.g. for a cylinder with aspect ratio of 1/3 studied by Fernandes et al [101], the critical Reynolds number

is around 167. Under such conditions, the results obtained for drag and other parameters will be different from that of a fixed non-oscillating object in the flow field. Among computational studies about stationary objects, Auguste et al. [102] performed DNS to investigate the dynamics in the wake of a disk with aspect ratio of 1/3, which is similar to the object studied in this research. Instead of forces and torque, they focused on identifying different bifurcations in the wake of the disk and the critical Reynolds number of transition of different bifurcations. Shenoy and Kleinstreuer [13] using a body conforming mesh to resolve the cylinder with aspect ratio of 0.1 derived not only the critical Reynolds number for different bifurcations, but also time dependent drag force on the object. Yang et al. [14] studied drag, lift and vortex shedding frequency characteristic for flow past a cylinder with aspect ratio of 0.2 at Reynolds number of 250, 300, 3000 and 1×10^4 . All the three research works mentioned above studied the hydrodynamic forces with fixed orientation of the object. In the work of Chrust et al. [15], they did DNS simulations for a cylinder with aspect ratio of 1/6 at incidence angle ranging from 0° to 60° . Instead of forces and torque on the object, they focused on the influence of incidence angle on the vortex shedding behind the cylindrical object and discovered that a small inclination tends to promote vortex shedding, whereas the opposite effect is observed when incidence angle exceeds 20° . The drag, lift and torque on a cylinder at incidence angle from 0° to 90° has been investigated by Vakil and Green [78]. In their research slender cylinders with aspect ratio between 2 and 20 are investigated under Reynolds number range of 1 to 40. Considering research about cylinders with smaller aspect ratios, Hölzer and Sommerfeld [89] used Lattice Boltzmann simulations to calculate the drag, lift and torque coefficient on cylinders with aspect ratio of 1 and 1.5 at incidence angles from 0° to 90° in the Reynolds number range from 0.3 to 240. Yow et al. [103] collected experimental data of drag coefficient for object shapes including spheres, cubes, disks, and cylinders and developed a drag correlation while the

orientation of the object is fixed. Hölzer and Sommerfeld [1], based on drag data for various geometries, including spheres, spheroids, disks, plates, etc., proposed a drag correlation for non-spherical objects that took the sphericity and orientation of the object into account and showed a mean error of 14.4% comparing to the 2061 experimental data points. However, little research on hydrodynamics forces and torque on cylinders with aspect ratio less than 1 can be found in the literature.

The literature review demonstrates the lack of hydrodynamic force data on low aspect ratio cylinders. The current study investigated a low aspect ratio (0.25) cylindrical geometry. The super-ellipsoidal geometry is constructed analytically with smooth edges to replicate a cylinder of aspect ratio 0.25 and takes on the shape of a tablet. The smoothed edges are a consequence of the analytical construction, which however more closely replicate the geometry of real cylindrical objects. The Immersed Boundary Method (IBM) is implemented to specify boundary condition on the cylinder surface. The main objective of the current study is to derive drag, lift, and torque correlations for the cylinder at different incidence angles and Reynolds numbers to add to the existing database of forces acting on non-spherical objects. These can not only be used to develop better correlations for non-spherical objects but also add to our understanding of the behavior of non-spherical objects in suspension.

Geometry, Governing Equations, and Numerical Method

Object geometry model

The cylinder geometry is constructed using the super-ellipsoid formula, which enables construction of spherical as well as non-spherical objects of different shapes [29,104,105]. This formula has a simple form and can be applied to create various geometries including traditional

geometries like a sphere, cube, ellipsoid and complex geometries like rod shaped objects [29] and the cylinder shaped objects studied in this research. The standard formula of a super-ellipsoid is written as:

$$(|a \times x|^r + |b \times y|^r)^{t/r} + |c \times z|^t = 1 \quad (\text{A.1})$$

where, x, y, z represent the three coordinates in a Cartesian coordinate system. a, b and c represent semi-diameters of the object and r and t control the surface curvature condition. In this research, to create the cylinder geometry, r and t are set to be 2 and 20, respectively. With the remaining parameters specified as: $a = 1.438; b = 1.438; c = 5.752$, the cylinder shaped object with aspect ratio of 0.25 and volume equivalent sphere diameter of unity is created. The geometry is shown in Fig. A.1. The aspect ratio is defined as h/d and the incidence angle θ is defined as the angle between the undisturbed flow direction and the transverse cross-section of the cylinder.

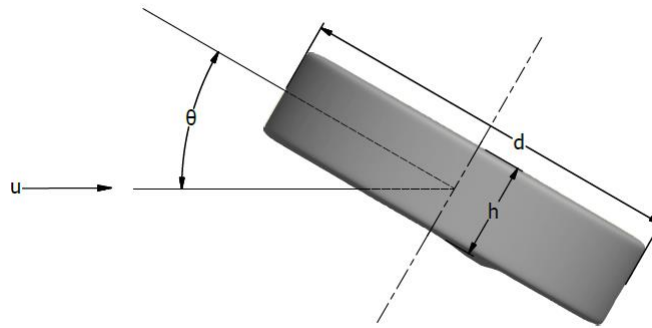


Fig. A. 1. 3D view of the tablet-like cylinder geometry

Computational domain and boundary conditions

The domain size is chosen such that the boundary conditions do not affect the flow field in the vicinity of the cylinder from that of a uniform approach flow. The domain used in the current study

is of size $30d_0 \times 28d_0 \times 28d_0$ (d_0 is the volume equivalent sphere diameter of unity) and is presented in Fig. A.2. The inlet and outlet boundaries are in the stream-wise directions with distance of $8d_0$ and $22d_0$ from the cylinder. In the cross-stream direction, the four boundaries are assigned the free-stream flow velocity at a distance of $14d_0$ from the cylinder. U_∞^* represents the approach velocity in the x-direction. In comparison, past studies of Guan et al. [106] used $12d_0 \times 10d_0 \times 10d_0$ to study the drag at Re between 0.01 and 3000 on different non-spherical shapes, and Richter and Nikrityuk [107] used $28d_0 \times 20d_0 \times 20d_0$ for investigating drag on spherical as well as ellipsoidal objects in a Re range between 10 and 250.

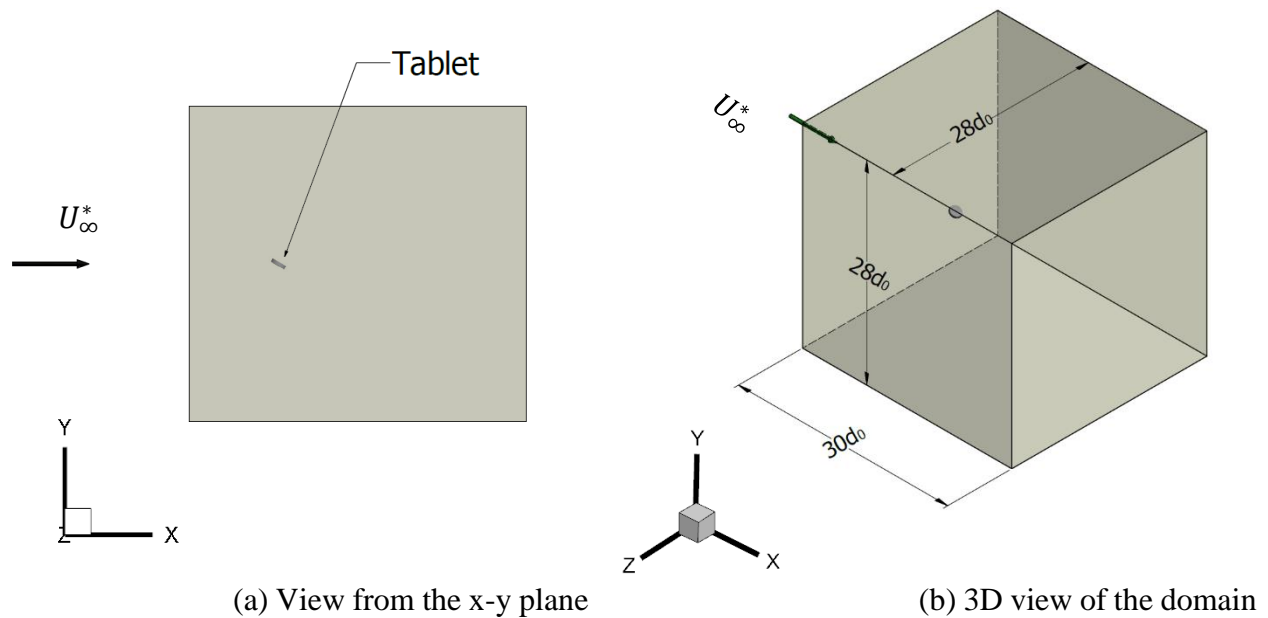


Fig. A. 2. View of the 3D domain and position of the cylinder

Governing equations and computational method

The calculation is based on our in-house code – GenIDLEST (Generalized Incompressible Direct and Large Eddy Simulation of Turbulence) [34][35]. It solves the unsteady incompressible Navier-

Stokes and energy equation. The constant property dimensionless governing equations formulated using Cartesian tensor notation are:

$$\frac{\partial u_i}{\partial x_i} = 0 \quad (\text{A.2})$$

$$\frac{\partial u_i}{\partial t} + \frac{\partial}{\partial x_j} (u_i u_j) = -\frac{\partial p}{\partial x_i} + \frac{\partial}{\partial x_j} \left(\frac{1}{Re} \left(\frac{\partial u_i}{\partial x_j} \right) \right) \quad (\text{A.3})$$

where the variables are nondimensionalized by:

$$u_i = \frac{u_i^*}{u_{ref}^*}; \quad x_i = \frac{x_i^*}{l_{ref}^*}; \quad p = \frac{p^* - p_{ref}^*}{\rho_{ref}^* u_{ref}^{*2}};$$

$$\rho = \frac{\rho^*}{\rho_{ref}^*}; \quad \mu = \frac{\mu^*}{\mu_{ref}^*}; \quad Re = \frac{\rho_{ref}^* u_{ref}^* l_{ref}^*}{\mu_{ref}^*}$$

In the nondimensionalization process, u_{ref}^* is the free stream or approach velocity of the fluid, i.e., U_∞^* . The reference length, l_{ref}^* is the volume equivalent sphere diameter d_0^* and ρ_{ref}^* , μ_{ref}^* , are the properties of the fluid (air) at 300K.

Eqs. (A.2) and (A.3) are discretized using a second-order accurate central differencing scheme on a non-staggered grid topology. Velocities, pressure and other scalar fields are calculated and stored at the cell center, whereas the mass flux is calculated and stored at cell faces. For time integration, a fractional step semi-implicit method is employed in which the viscous terms are treated implicitly by a Crank-Nicolson formulation and the convection terms explicitly with Adams-Bashforth. Firstly, a predictor step solves an intermediate velocity field and the corrector step uses the calculated pressure field to correct the velocity such that discrete continuity is satisfied. The pressure equation is solved using a preconditioned BiCG-STAB method. The preconditioner employed is a sub-structured Jacobi smoother.

Immersed Boundary Method (IBM) is employed to specify the boundary conditions on the cylinder surface in the flow field. The IBM has been developed and validated in Nagendra et al. [36] and applied to DNS of ellipsoidal object suspensions in [27]. In this implementation, there are two sets of meshes - the fluid background volume mesh which is structured and Cartesian in this case, and the triangular surface mesh of the cylinder immersed in the fluid mesh.

The first step in the IBM procedure is to identify background nodes that lie in the fluid or solid region or at the interface between the two. A two-dimensional example is shown in **Fig. A.3**. Any node that lies in the fluid region is assigned to be a fluid node, whereas nodes inside the immersed boundary are assigned to be solid nodes. Moreover, nodes that lie in the immediate vicinity of the immersed boundary and have at least one face sharing a neighboring fluid node are marked as fluid IB nodes.

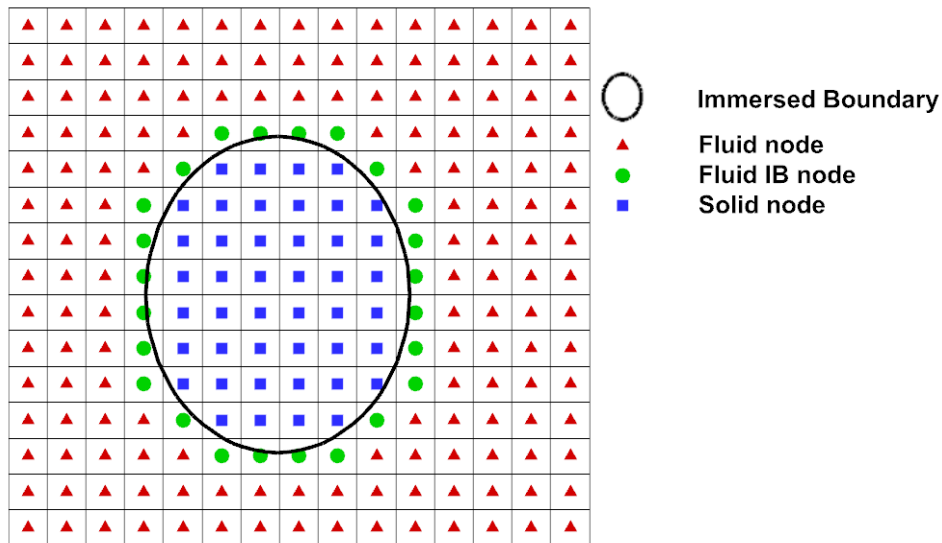


Fig. A. 3. Identification of node type in the background mesh defined in IBM

Boundary conditions at the IB surface are implemented by assigning appropriate values to the IB node for the primitive variables. These values are calculated by assigning probes to each IB node, projected outward, normal to the IB surface. The distance between the probe and the fluid IB node is the length of the longest diagonal of the background mesh near the immersed boundary. Primitive flow variables at the probe are interpolated based on the values at surrounding fluid nodes. The interpolated value at the probe is used to obtain the appropriate boundary condition at the fluid IB node such that the boundary condition at the IB surface is satisfied. The IBM procedure has been shown to be second-order accurate in Nagendra et al. [36] .

Fluid forces and torques are calculated using a procedure similar to that used for implementing the boundary conditions. For each surface element, a probe is assigned that lies along the surface element normal from the element centroid as shown in Fig. A.4. The same tri-linear interpolation method used for IB node probes (but with a different surrounding node stencil) is employed to determine the value of the desired primitive flow variable at the probe location.

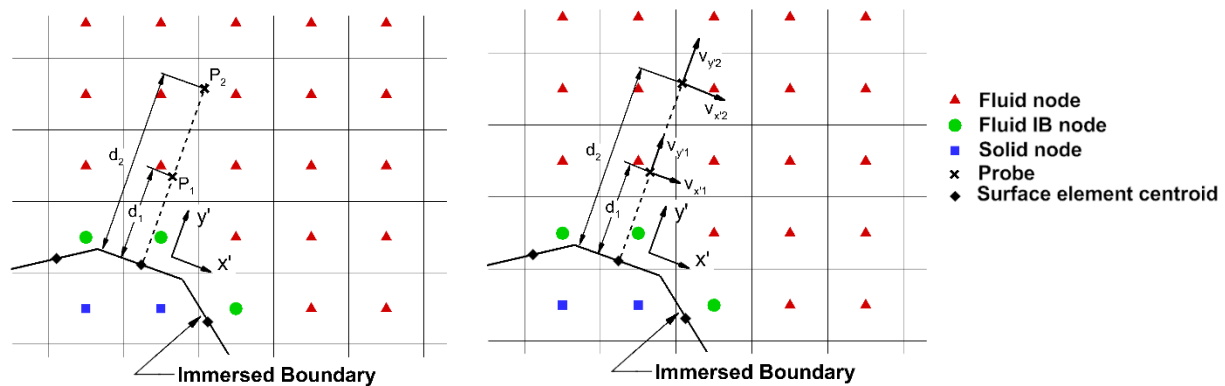


Fig. A. 4. Surface Pressure and shear stress (velocity gradient) calculation for force calculation (Left plot presents the pressure and right plot presents the velocity of the probe)

The force on each element consists of pressure and viscous forces. Under steady, no-slip, impenetrable condition at the cylinder surface, normal viscous stresses and pressure are the only contributors to the normal momentum transfer at the surface. Because the velocity normal to the object surface is small, the contribution of the gradient of normal velocity is neglected in the normal momentum balance to give

$$\frac{\partial P}{\partial y'} \Big|_s = 0 \quad (\text{A.4})$$

Taylor series expansion is implemented for pressure at probe 1 (P_1) and probe 2 (P_2) that are defined about pressure at immersed surface (P_S). After eliminating $\frac{\partial^2 P}{\partial y'^2} \Big|_s$ and neglecting higher order terms, P_S can be obtained by:

$$P_S = \frac{d_1 d_2 (d_1 - d_2) \frac{\partial P}{\partial y'} \Big|_s + d_2^2 P_{P1} - d_1^2 P_{P2}}{d_2^2 - d_1^2} \quad (\text{A.5})$$

Shear stress is derived from the velocity gradient along the surface normal of each surface element.

It is calculated by:

$$\vec{\tau} = \mu \frac{d\vec{u}_{x'}}{dy'} \Big|_s = \mu \frac{u_{x'2} d_1^2 - u_{x'1} d_2^2 + (d_2^2 - d_1^2) u_{x's}}{d_1 d_2 (d_1 - d_2)} \vec{e}_{x'} \quad (\text{A.6})$$

In Eq. (A.6), $u_{x's}$ is the tangential velocity at the immersed surface, which in this case is zero. Hence total hydrodynamic force applied on a single surface element can be calculated by:

$$\vec{F}_e = (\vec{\tau} - P_S \cdot \vec{e}_{y'}) A_e \quad (\text{A.7})$$

The total force is the integration of forces on each element, i.e., summation of force on each surface element, the equation can be written as:

$$\vec{F} = \sum_{surface} \vec{F}_e \quad (A.8)$$

Definitions of drag, lift and torque coefficients are:

$$\text{Drag coefficient: } C_D = \frac{F_D^*}{\frac{1}{2}\rho_{ref}^* u_{ref}^{*2} A^*}. \quad (A.9)$$

In this equation, A^* is the cross-sectional area of equal volume sphere calculated by $\frac{\pi d_0^{*2}}{4}$. F_D^* is the total force in the streamwise x-direction.

$$\text{Lift coefficient: } C_L = \frac{F_L^*}{\frac{1}{2}\rho_{ref}^* u_{ref}^{*2} A^*}. \quad (A.10)$$

F_L^* is the force that lies in the plane formed by the x-axis and the axis of rotational symmetry of the cylinder in a direction perpendicular to the x-axis. In this study, the cylinder is only inclined about the z-axis, therefore the lift will be in the y-direction, i.e., along the y-axis as is shown in Fig. A.11.

$$\text{Torque coefficient: } C_T = \frac{T^*}{\frac{1}{2}\rho_{ref}^* u_{ref}^{*2} A^* \frac{d_0^*}{2}}. \quad (A.11)$$

Here T^* is the pitching torque aligned with an axis perpendicular to both drag and lift. In this case, it is in the direction parallel to the z-axis. The calculation of non-dimensional torque is carried out using:

$$\vec{T} = \sum_{surface} (\vec{r}_e \times \vec{F}_e) \quad (13)$$

where \vec{r}_e is the vector pointing from the cylinder's center of mass to the center of the element.

Grid independence study and validation

The grid needs to be fine enough to resolve the boundary layer formed near the cylinder surface. With the purpose of finding a reasonable grid size, three grids are chosen and the results of drag coefficient of the cylinder at different Reynolds number and incidence angle are presented to show the effect of grid size. The grid sizes are 1/30, 1/40 and 1/50. The near field distribution of the volume grid of size 1/40 is shown in Fig. A.5 including the mesh defining the surface of the cylinder. The surface grid and volume grid have approximately the same cell size.

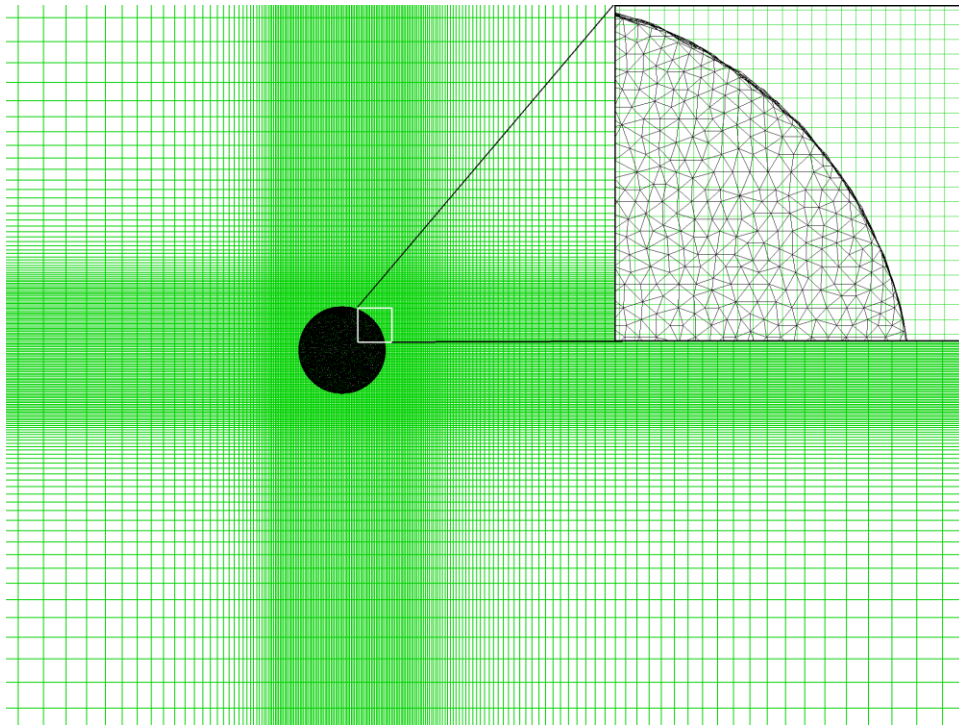


Fig. A. 5. Volume grid (green) distribution in the nearfield and surface mesh (black) distribution.

Table A.1 shows the results for drag coefficient. It can be seen that at different Reynolds number and incidence angle, the drag coefficient derived from the three grid sizes have no significant discrepancy. Using the results from grid size of 1/50 as reference, the largest discrepancy for grid

size of 1/30 appears at $Re=200$, $\theta=90^\circ$ with a value of 4.45%, with an average difference of 2.16%. For the grid size of 1/40, the largest discrepancy is 1.7% that appears at $Re=10$, $\theta=0^\circ$. The grid independency results from this study closely match the results from He and Tafti [27] who used the same grid densities in a suspension of ellipsoidal objects. It was found that the maximum difference between the three grids was about 2%. To summarize, the grid independency results suggest that the three grid resolutions are within a range that can accurately capture the hydrodynamic boundary layers on the cylinder for the range of Reynolds numbers of interest in this study.

Table A. 1. Drag coefficient of the flow past the cylinder at different conditions

Grid size	Re=10				Re=200			
	0°	30°	60°	90°	0°	30°	60°	90°
1/30	4.443	5.019	6.028	6.420	0.748	1.215	1.862	1.987
1/40	4.515	5.073	6.077	6.498	0.756	1.207	1.841	1.930
1/50	4.593	5.104	6.117	6.531	0.763	1.203	1.829	1.902

Further comparison of results from the literature and this study is necessary to validate the computational algorithm and domain defined in this study. Since drag coefficient of fluid flow past a single stationary sphere has already been comprehensively studied in the literature, separate simulations for spheres were done in order to do the validation. Based on experimental data in the literature, Clift et al. [5] developed a set of correlations for the drag coefficient on a single

stationary sphere in cross flow at different Reynolds number. Their correlations are shown in Eqs.(A.13) - .(A.16).

$$C_D = \frac{24}{Re} (1 + 0.1315Re^{(0.82-0.05w)}) \quad 0.01 < Re \leq 20 \quad (\text{A.13})$$

$$C_D = \frac{24}{Re} (1 + 0.1935Re^{0.6305}) \quad 20 \leq Re \leq 260 \quad (\text{A.14})$$

$$\log_{10} C_D = 1.6435 - 1.1242w + 0.1558w^2 \quad 260 \leq Re \leq 1500 \quad (\text{A.15})$$

In the equations above $w = \log_{10} Re$. Moreover, Brown & Lawler's [7] correlation after eliminating wall effects can be written as:

$$C_D = \frac{24}{Re} (1 + 0.150Re^{0.681}) + \frac{0.470}{1 + \frac{8710}{Re}} \quad Re \leq 2 \times 10^5 \quad (\text{A.16})$$

Fig. A.6 shows the comparison of the results of this study using IBM and that of Clift et al. [5] and Brown & Lawler[7]. Computational results from Wittig et al. [72] using body conforming mesh is also presented. In order to further validate the correctness of our IBM calculation, we also performed simulations using a body conforming mesh around the sphere. From **Fig. A.6** it can be seen that both current IBM and body conforming mesh show good agreement with the literature.

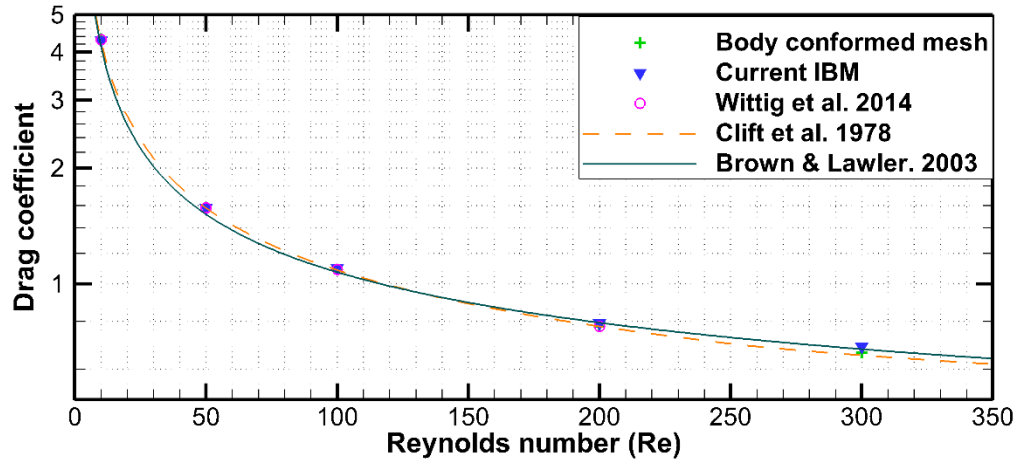


Fig. A. 6. Comparison of drag coefficient from the literature and results derived in this study using both IBM and body conforming mesh

Data for the drag coefficient is shown in Table A.2. Using results derived in this study as reference, comparing with literature, the largest discrepancy for the simulations using a body conforming mesh is 4.47% while this becomes to 4.81% for IBM. Comparing to Brown & Lawler’s correlation [7], the average discrepancy with IBM is 2.16%.

Table A. 2. Comparison of drag coefficient from literature and results in this study based on different methods

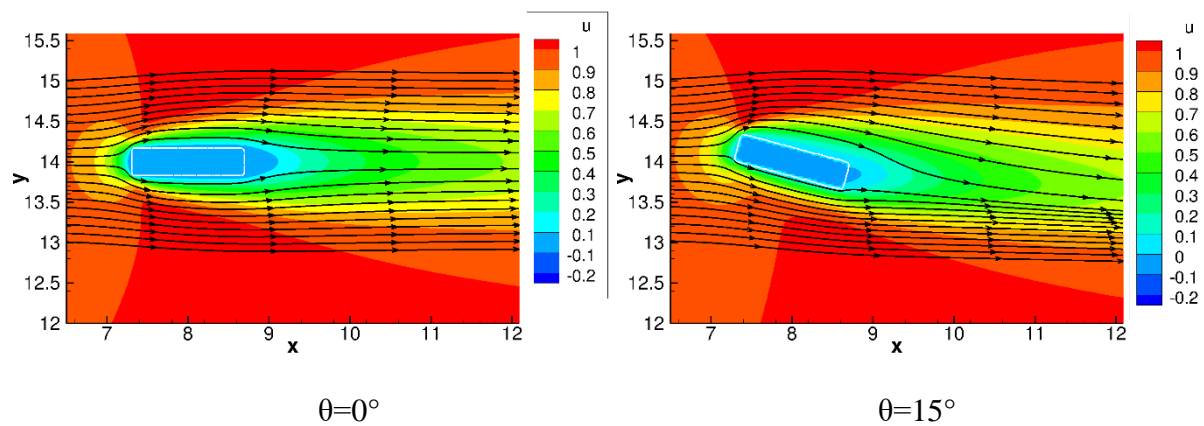
Reynolds number	Clift et al. [5]	Wittig et al. [72] (IBM)	Brown & Lawler[7]	Current (Body conforming mesh)	Current (IBM)
	C_D	C_D	C_D	C_D	C_D
10	4.258	4.312	4.128	4.321	4.287

50	1.574	1.577	1.516	1.576	1.574
100	1.087	1.090	1.073	1.089	1.096
200	0.7756	0.776	0.7933	0.7729	0.7899
300	0.6527	-	0.6738	0.6626	0.6857

Results and Discussion

Flow Characteristics

For the most part, in the range of Reynolds numbers investigated in this study, the flow remains steady around the cylinder as well in the wake. Velocity of the fluid in the free stream direction near the cylinder at Reynolds number of 50 is shown in Fig A.7. From $\theta = 0^\circ$ to 15° the flow remains attached to the cylinder surface. At $\theta \geq 30^\circ$, the flow separates and large recirculation zones start to appear on the leeward side or wake of the cylinder.



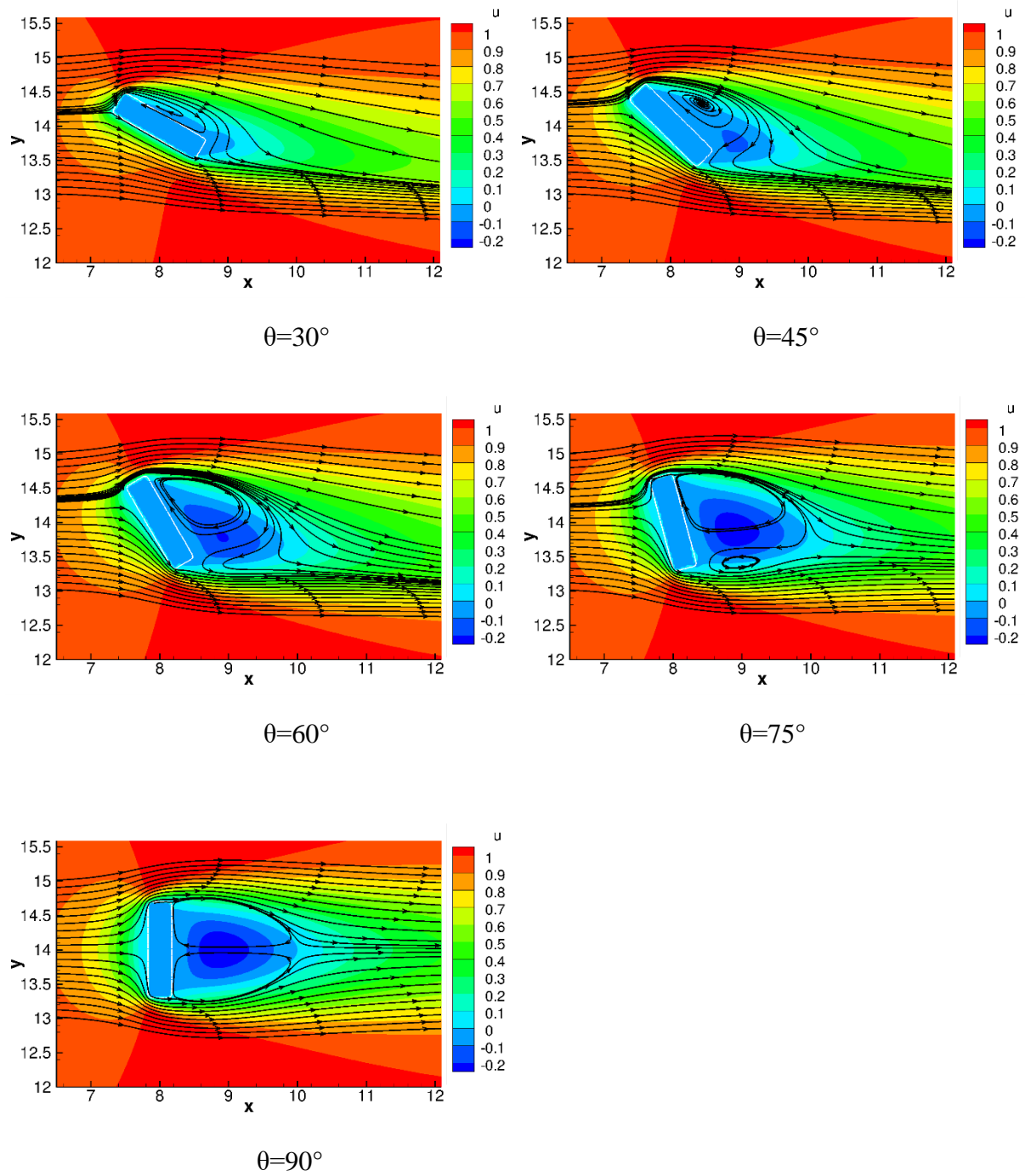
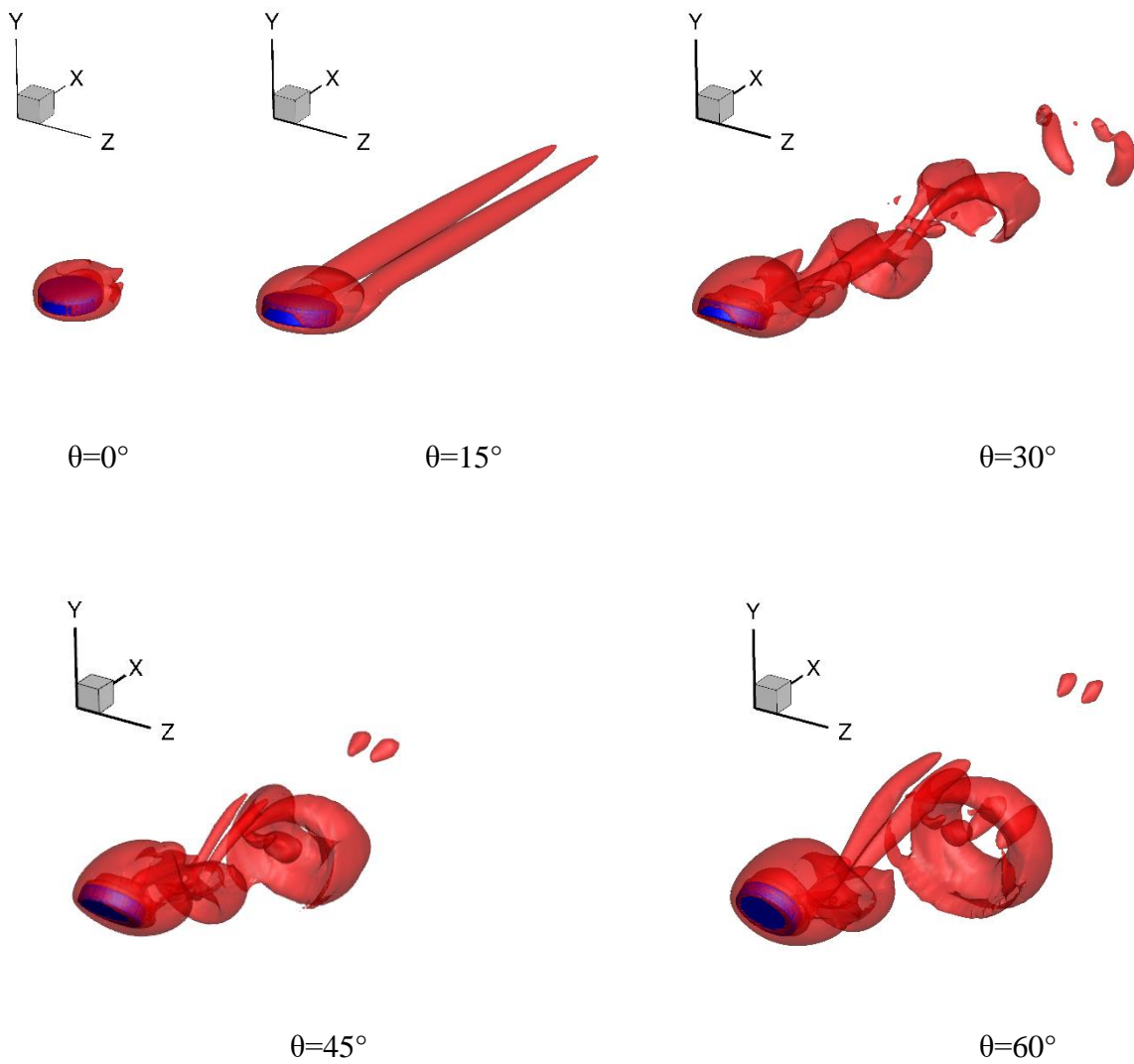


Fig. A. 7. U-velocity and streamlines of the fluid flow near the cylinder at $Re = 50$ and $\theta = 0^\circ$ to 90°

At Reynolds number of 200, the wake becomes unsteady for $\theta \geq 30^\circ$. In Fig A.8, at $\theta = 15^\circ$, two tubular vortex structures extend into the wake of the cylinder from the two lateral extremities of the tablet. These become unstable at $\theta=30^\circ$ to form and shed ring shaped vortices in the wake. The size of the ring vortex increases from $\theta = 30^\circ$ to 60° , whereas from 60° to 90° , the opposite trend is observed. This is similar to the observation of Chrust et al. [15] of flow over a disk. This trend results from the projected area of the cylinder, which reaches a maximum at around $\theta = 75^\circ$ and then decreases, which manifests in the flow structures as well.



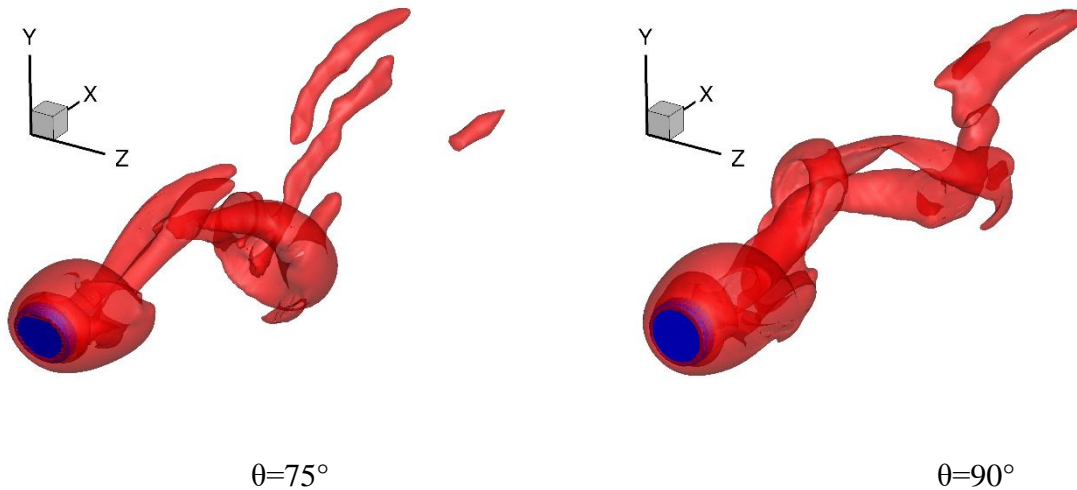
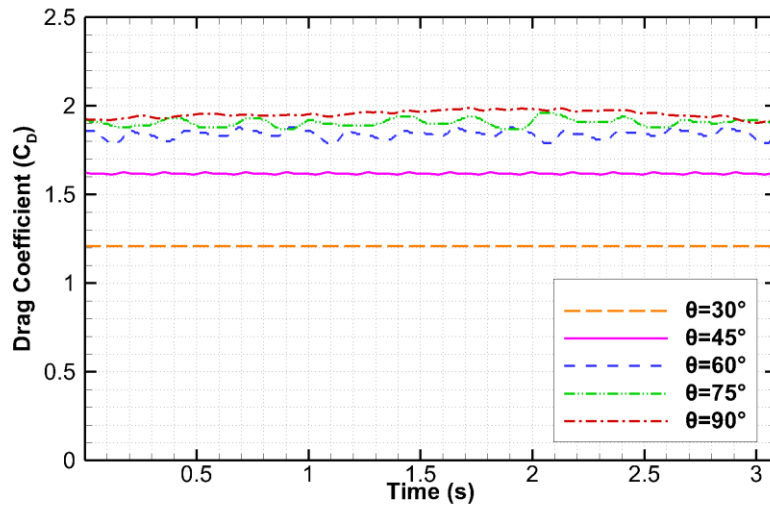


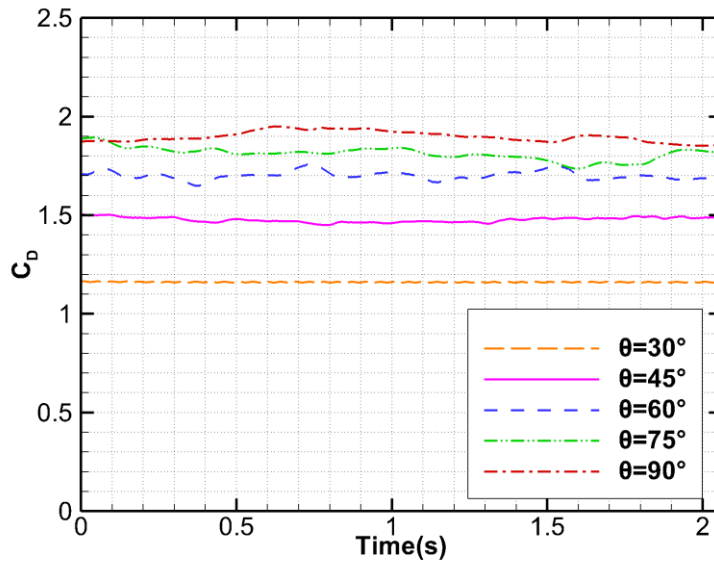
Fig. A. 8. Visualization of vorticity behind the cylinder at Re=200

Due to the oscillation of the flow, hydrodynamic forces including drag and lift become unsteady and start to show periodic oscillations with time. Fig A.9 (a) shows the behavior of drag coefficient in time at Reynolds number of 200. It can be observed that at $\theta = 30^\circ$, the unsteady wake has insignificant effect on the drag coefficient which remains at a near constant value. At $\theta = 45^\circ$, the drag coefficient exhibits periodic fluctuations and at $\theta = 60^\circ$ exhibits traces of chaos. At $\theta = 75^\circ$ and 90° , the signal becomes chaotic. Interestingly, the characteristic frequency of oscillation decreases as the angle increases from 45° to 90° . Time dependent drag coefficient for Reynolds number of 300 is presented in Fig A.9 (b). The flow remains steady at $\theta=0^\circ$ and 15° . At $\theta =30^\circ$, the drag coefficient exhibits small periodic fluctuations which become chaotic for $\theta \geq 45^\circ$.

To compare the results from different Reynolds number and incidence angle, the unsteady signal is averaged to get a representative value. Averaging is initiated by locating a probe in the wake of the cylinder and started when the velocity signal at the probe location reaches a stationary or quasi-periodic state.



(a) Re=200



(b) Re=300

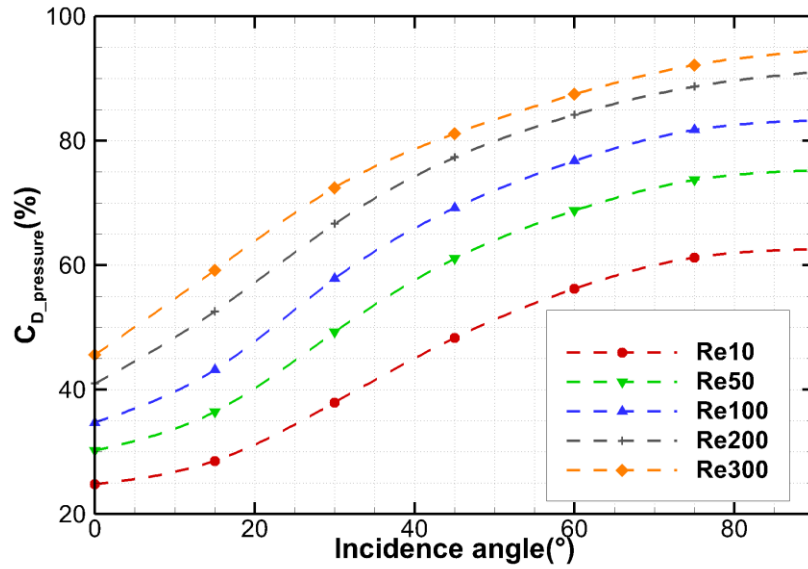
Fig. A. 9. Drag coefficient as a function of time at Reynolds number of 200 and 300

Drag Coefficient

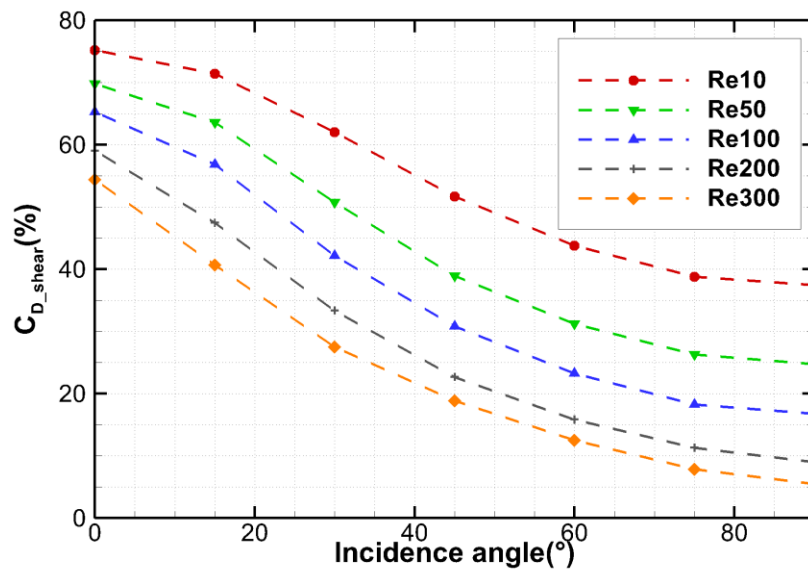
In this study, drag on the cylinder at different Reynolds numbers (10, 50, 100, 200 and 300) and incidence angles (0° , 15° , 30° , 45° , 60° , 75° and 90°) are calculated. There are two components that contribute to the total drag coefficient, i.e., drag resulting from pressure difference or form drag coefficient that is denoted as $C_{D_pressure}$, and drag resulting from viscous shear or friction drag coefficient that is denoted as C_{D_shear} . Contribution of pressure and shear to the total drag coefficient is shown in Fig A.10 (a) and Fig A.10 (b). As the Reynolds number increases, the percentage contribution of pressure drag to total drag increases because of the increase in the dynamic pressure which varies to the square of the approach velocity, whereas shear stresses vary linearly. Thus as the Reynolds number increases, pressure drag dominates the total drag. Friction drag contributes nearly 75% to the total drag at $Re=10$ and $\theta=0^\circ$, whereas pressure drag contributes nearly 95% at $Re=300$ and $\theta=90^\circ$.

The contribution of pressure drag also increases with incidence angle because an increase in incidence angle intensifies the pressure difference between the windward side on which the flow stagnates and the leeward side which experiences separation and low pressures. In addition, as the incidence angle increases, the projected area of the cylinder that is normal to the approach flow increases and reaches a maximum around an incidence angle of 75° , thus increasing the pressure contribution to the total drag and results in the drag coefficient at 75° to have a higher value than that of 90° at the higher Reynolds numbers in this study. This is shown in Fig A.11. In the Reynolds number range between 10 to 200, the drag coefficient decreases with increasing Re , whereas between Re of 200 and 300, the decreasing trend becomes less significant. Similar observations are also made for an ellipsoid of aspect ratio 2 as the Reynolds number approaches 200 [73]. The trend of the drag coefficient becoming independent of Reynolds number is commonly found with

bluff bodies. For example, the drag coefficient of a single sphere becomes independent of Reynolds number for Re greater than 800 till the critical Reynolds number [108], where it encounters the drag crises.



(a) Pressure contribution to the total drag coefficient



(b) Viscous contribution to the total drag coefficient

Fig. A. 10. Percentage contribution of pressure and viscous stresses to total drag under different conditions

To provide context the computed results are compared to the correlation developed by Hölzer and Sommerfeld [1] who have used drag data for ellipsoids, plates, disks and other non-spherical geometries over a range of Reynolds numbers and at different incidence angle to provide a means of predicting the drag on any non-spherical object. In their formula, the variables are sphericity φ , lengthwise sphericity φ_{\parallel} and crosswise sphericity φ_{\perp} . Their formula is:

$$C_D = \frac{8}{Re} \frac{1}{\sqrt{\varphi_{\parallel}}} + \frac{16}{Re} \frac{1}{\sqrt{\varphi}} + \frac{3}{\sqrt{Re}} \frac{1}{\varphi^{\frac{3}{4}}} + 0.42 \times 10^{0.4(-\log\varphi)^{0.2}} \frac{1}{\varphi_{\perp}} \quad (\text{A.17})$$

The sphericity, φ , is the ratio between the surface area of the volume equivalent sphere and the surface area of the object. The crosswise sphericity, φ_{\perp} is the ratio between the cross-sectional area of the volume equivalent sphere and the object's projected cross-sectional area perpendicular to the flow. And the lengthwise sphericity, φ_{\parallel} is the ratio between the cross-sectional area of the volume equivalent sphere and the difference between half the surface area and the mean longitudinal (i.e. parallel to the direction of relative flow) projected cross-sectional area of the object. A comparison of the drag coefficient between the value derived from their formula and the DNS simulation results of this study is shown in Fig A.11. It can be seen that the results of this study agree well with the results from Hölzer and Sommerfeld around incidence angles of 0° and 90° , however there are differences at other incidence angles. The possible reason could be that in the data used by Hölzer and Sommerfeld for disks (similar to tablet) was biased towards these two positions. Since other incidence angles were not considered in building the correlation, the discrepancy increases at incidence angles between 0° and 90° .

To evaluate the accuracy of their correlation, the mean square error (MSE) between their predicted value and our simulation results is calculated with a value of 0.0583. The relative error, which is calculated using $\epsilon = \frac{|C_{D,i_{simulation}} - C_{D,i_{h\ddot{o}lzer}|}}{C_{D,i_{simulation}}}$, has a maximum value of 47%. The mean relative error is 8.1% considering all the cases studied in our simulation. As a general formula which is applicable for various object geometries, this formula can provide a reasonable prediction for the drag on a tablet. However, a more precise correlation for the specific geometry is also necessary for research that requires higher accuracy for the drag data. To derive a more accurate correlation for the drag at various Reynold numbers and incidence angles, we start with the relationship in Eq. (A.18) for characterizing drag for bluff bodies at Reynolds numbers within the Stokes regime [109].

$$C_{D,\theta} = C_{D,\theta=0^\circ} + (C_{D,\theta=90^\circ} - C_{D,\theta=0^\circ})\sin^2\theta \quad (\text{A.18})$$

Sanjeevi and Padding[88] found that while this relationship works well for prolate spheroids, it does not work well for oblate spheroids like the cylinder shape in this study. They found that while the discrepancies are small at low Re, these become significant as the Reynolds number increases. Comparing the current simulation results and Eq. (A.18), similar to the findings of Sanjeevi and Padding [88], the discrepancy is negligible at Re=10 and 50, but for Re from 100 to 300, the relative error increases from a maximum value of 13.8% to 18.9%. The distribution of relative error with respect to θ is approximately bell-shaped with a peak near 45° and decreases towards 0° and 90° . Therefore, an extra term is added in our proposed formula to eliminate this discrepancy and the correlation has the form:

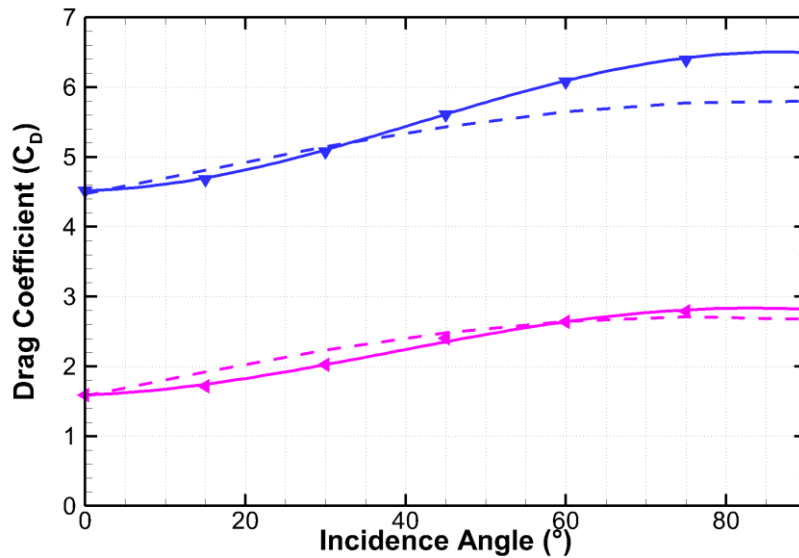
$$C_{D,\theta} = C_{D,\theta=0^\circ} + (C_{D,\theta=90^\circ} - C_{D,\theta=0^\circ})\sin^2\theta + 0.1280Re^{0.2171} \sin\theta \cos\theta \quad (\text{A.19})$$

$C_{D,\theta=90^\circ}$ and $C_{D,\theta=0^\circ}$ are predicted by the following relations:

$$C_{D,\theta=0^\circ} = \frac{24.3350}{Re} (1 + 0.2129Re^{0.6040}) \quad (\text{A.20})$$

$$C_{D,\theta=90^\circ} = \frac{24.2971}{Re^{0.5795}} + \frac{0.0210}{Re^{-0.6799}} \quad (\text{A.21})$$

The drag coefficient calculated using Eqs. (A.19) – (A.21) is shown in Fig A.11. It agrees very well with the original data. The mean relative error is 1.5% and the mean square error (MSE) is 1.5×10^{-3} .



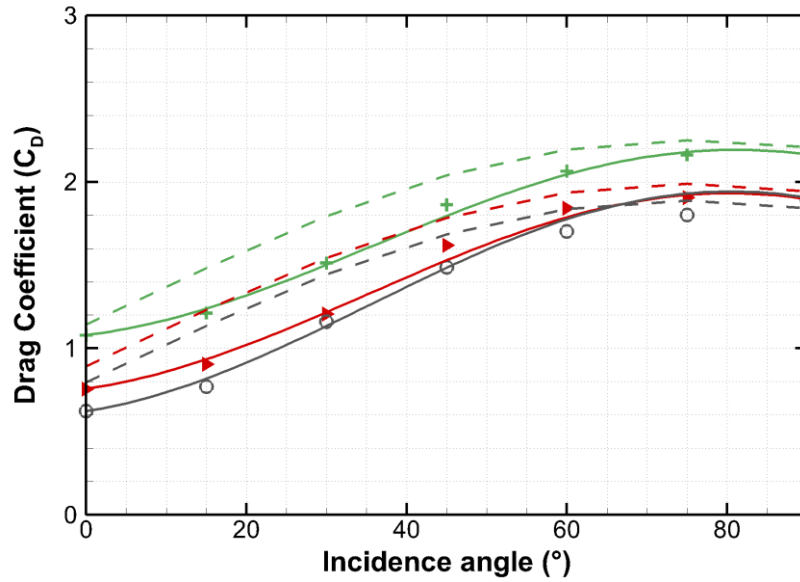
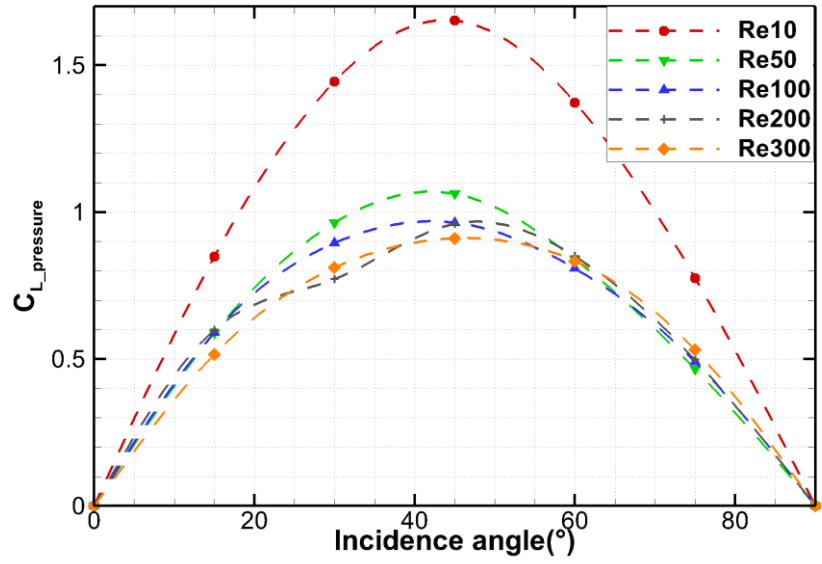


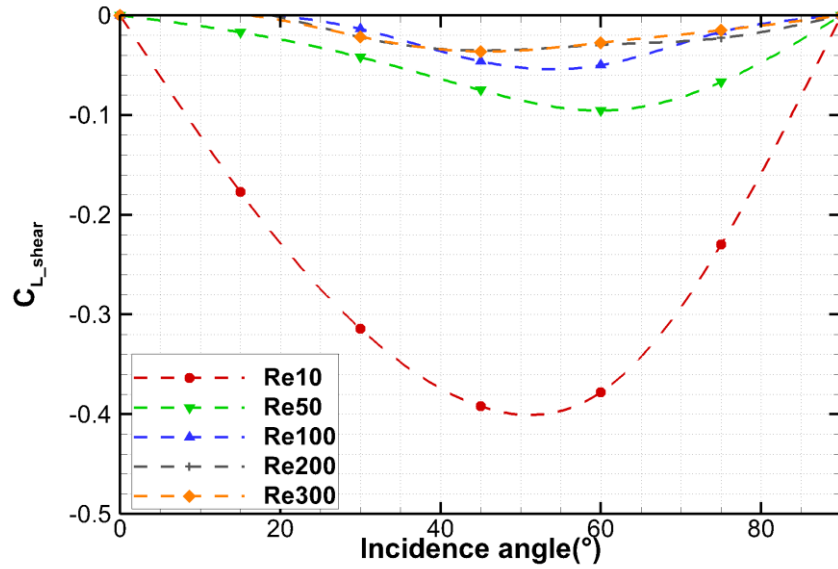
Fig. A. 11. Drag coefficient on the cylinder. (\blacktriangledown) Simulation at $Re=10$; (\blacktriangleleft) simulation at $Re=50$; ($+$) simulation at $Re=100$; (\blacktriangleright) simulation at $Re=200$; (\circ) simulation at $Re=300$; solid line: Present correlation; dashed line: Hölzer and Sommerfeld's correlation. (Same color represents the same Re .)

Lift coefficient

Lift force is defined as the force acting in the y-direction and has a finite value at angles other than 0° and 90° when the flow and pressure distribution on the windward and leeward surfaces of the cylinder are different. Data on lift coefficient on cylinder shaped object is not readily available in the literature. However, a similar geometry, oblate spheroid of aspect ratio 0.2 has been studied by Zastawny et al. [9] using IBM. In our simulation for the cylinder, lift coefficient due to pressure and shear are also calculated. The results are shown in Fig A.12 (a) and Fig A.12 (b).



(a) Pressure lift coefficient



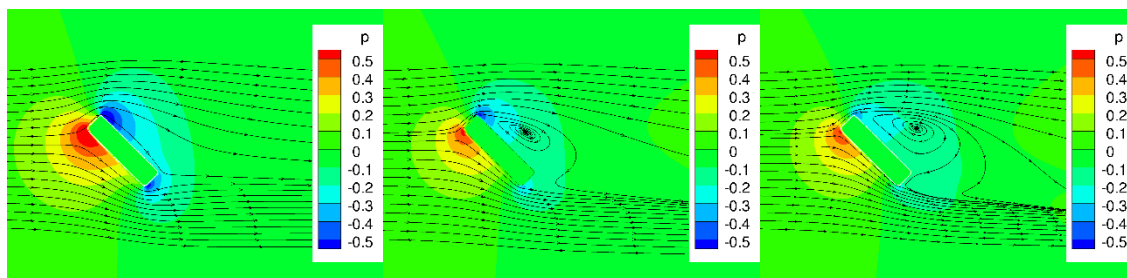
(b) Shear lift coefficient

Fig. A. 12. Lift coefficient from pressure and shear at different conditions

Both lift coefficients, that due to pressure and shear exhibit a bell shape, exhibiting zero values at $\theta = 0^\circ$ and 90° , and reaching a maximum or minimum in the vicinity of 45 degrees. Whereas pressure creates positive lift, shear acts opposite to pressure and decreases the total lift. While pressure acts normal to the surface, shear acts tangentially and is predominantly directed in the $-y$ -direction. The trends in both lift forces (and by association, lift coefficients) are dependent on the magnitude of the net stresses (pressure and shear) acting on the cylinder as well the projected area available for the stresses to act on. As θ increases from 0° to 90° , while the projected area for pressure in the y -direction decreases, the pressure differential increases between the windward and leeward sides of the cylinder. Between 0° and 45° , the increase in pressure differential dominates and overall pressure lift coefficient increases. As θ increases from 45° to 90° , the pressure differential between the windward and leeward side of the cylinder does not increase enough to compensate for the decrease in projected area, reducing the overall lift force and lift coefficient. On the hand, the projected area in the y -direction for shear stress increases from 0° to 90° , however in this case, the flow becomes increasingly symmetric about the x -axis as θ approaches 90° , producing near equal amounts of positive and negative shear, thus reducing the overall shear force contribution to the lift coefficient. An additional factor which comes into play, is the shear force in recirculation zones on the leeward side act in the $+ve$ y -direction, thus reducing the predominantly $-ve$ shear force that acts on the windward side of the cylinder.

The lift coefficient due to pressure and shear drop significantly from $Re=10$ to 50 , and gradually thereafter. At $Re=10$, maximum negative lift due to shear is approximately 30% of the lift generated by pressure. However, at $Re \geq 50$, the friction attenuation of lift drops rapidly to between 10%-15% of the positive lift generated by pressure. Fig A.13 shows the non-dimensional mean

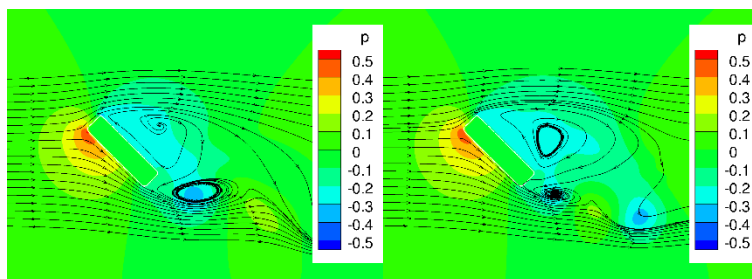
pressure (non-dimensionalized by $\rho_{ref}^* U_{\infty}^{*2}$) distribution near the cylinder's surface at $\theta=45^\circ$ for different Reynolds numbers. At $Re=10$, the stagnation pressure on the windward side is higher than that at $Re=50$, but the value and distribution does not change substantially for $Re>50$. On the leeward side at $Re=10$, in spite of an attached boundary layer, there is a region of negative pressure at the leading edge as the flow accelerates in this region. As the Reynolds number increases, the boundary layer separates on the leeward side with the formation of a recirculation region which grows in size with the consequence that a more uniform low pressure region forms on the leeward side but with a higher value (less negative) than at $Re=10$. The net result of non-dimensional pressure distribution on the windward and leeward sides leads to a sharp reduction in pressure lift coefficient from $Re=10$ to 50, followed by a gradual reduction for $Re>50$. As stated earlier, the onset of separation and recirculation on the leeward side introduce a component of shear force acting in the +ve y-direction, which together with the linear dependence of shear stresses on velocity lead to the sharp drop in negative shear lift coefficient for $Re \geq 50$.



(a) $Re=10$

(b) $Re=50$

(c) $Re=100$



(d) Re=200

(e) Re=300

Fig. A. 13. Pressure distribution around the cylinder at $\theta = 45^\circ$

Fig A.14 shows the total lift coefficient of the cylinder under different conditions. The overall trend shows a bell-shaped curve. The distribution is symmetric around incidence angle of 45° at Reynolds number of 10, but as the Reynolds number increases, the symmetry is broken. Research on flow over a two-dimensional flat plate [110] found similar characteristics for lift on the inclined flat plate. Since no reliable correlation for lift on a low-aspect ratio cylinder could be found in the literature, we derive a lift correlation for this shape. Based on linear theory in the Stokes regime [109], the lift coefficient can be expressed as:

$$C_{L,\theta} = (C_{D,\theta=90^\circ} - C_{D,\theta=0^\circ})\sin\theta\cos\theta \quad (\text{A.22})$$

The result is shown in Fig A.14, it can be seen that the lift coefficient calculated by Eq. (A.22) is noticeably smaller than the simulation results from this study. Similar observation was made by Sanjeevi and Padding [88] for an oblate spheroid. To derive a lift coefficient correlation for the low-aspect ratio cylinder in this study, a simplified form of that used by Zastawny et al. [9] is used. Eq. (A.23) presents the new correlation for lift coefficient on tablet at different Re and θ .

$$C_{L,\theta} = \left(1.688 + \frac{6.617}{Re^{1.063}}\right)(\sin\theta)^{0.8222}(\cos\theta)^{0.9796} \quad (\text{A.23})$$

The term within the parentheses presents dependence of lift on Reynolds number while the other two terms include the effect of the inclination. Comparing to the DNS simulation results calculated from this study, the relative error, which is calculated by:

$$\epsilon = \frac{|C_{L,i_{simulation}} - C_{L,i_{predict}}|}{C_{L,i_{simulation}}} \quad (\text{A.24})$$

has a mean value of 5.77% with a MSE of 1.90×10^{-3} . The largest relative error appears at $\theta=75^\circ$, $Re=50$, which is 16%.

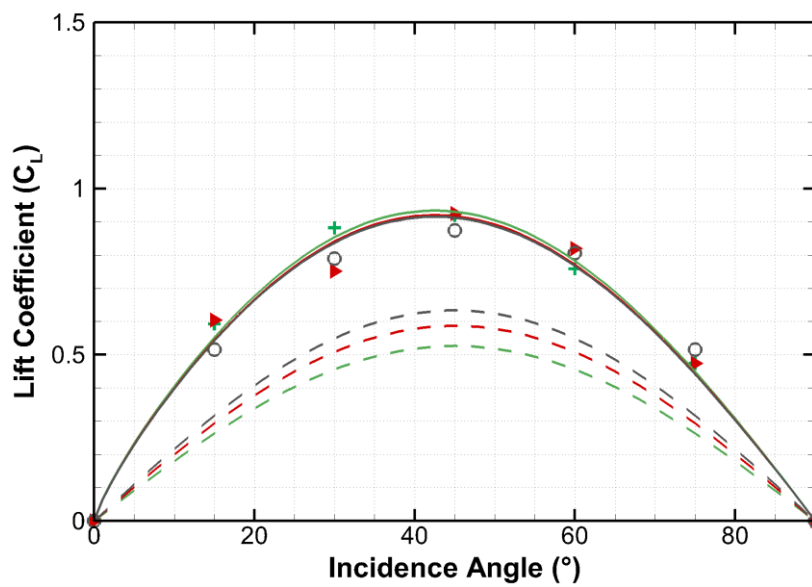
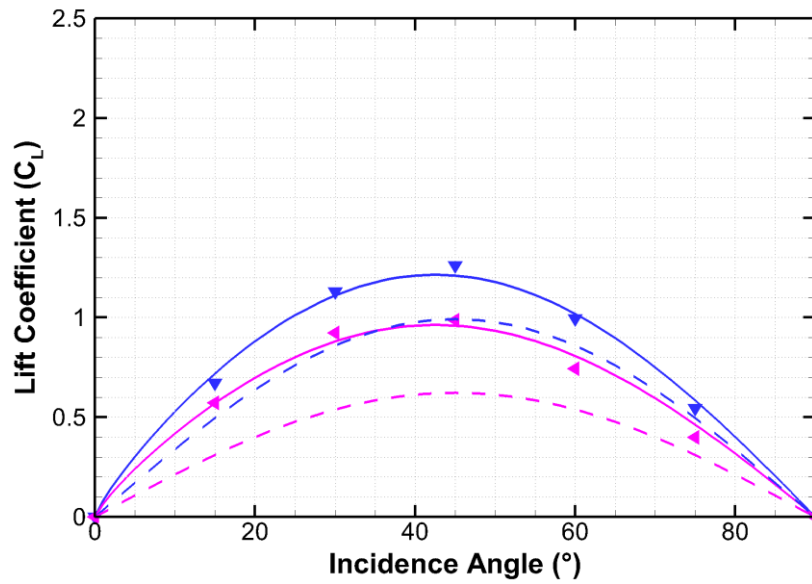


Fig. A. 14. Lift coefficient on cylinder. (▼) Simulation at Re=10; (◀) simulation at Re=50; (+) simulation at Re=100; (▶) simulation at Re=200; (○) simulation at Re=300; solid line: Present correlation; dashed line: Results of Eq. (22). (Same color represents the same Re.)

Pitching Torque Coefficient

Torque appears when the non-spherical object is inclined or when symmetry is broken in the flow field. In this study, the cylinder is symmetrical with respect to both x-y plane and x-z plane while inclined at $\theta = 0^\circ$ and 90° . Therefore, the flow remains symmetric around the cylinder and there is no torque while the flow is steady. At $Re \geq 200$ and $\theta = 90^\circ$, the unsteady vortex shedding from the cylinder, generates instantaneous torque on the object with a zero mean. Between $0^\circ < \theta < 90^\circ$, symmetry of the flow is broken and significant torque appears in the direction perpendicular to the x-y plane. As a representative case, Fig. A.13 for an inclination of 45° , shows the formation of a high pressure stagnation region on the windward side accompanied by separation and a low pressure region on the leeward side of the cylinder, leading to the generation of torque about the negative z-axis. The torque coefficient for the cylinder is shown in Fig. A.15. Similar to the lift coefficient, the variation of the torque coefficient is almost symmetric about an incidence angle of 45° at low Reynolds number but deviations from symmetry are observed as the Reynolds number increases. The correlation derived in this study for pitching torque coefficient is given by:

$$C_{T,\theta} = \left(19.28 - \frac{15.93}{Re^{-0.02476}}\right) (\sin\theta)^{0.8929} (\cos\theta)^{0.9769} \quad (\text{A.25})$$

Similar to the lift correlation for the cylinder, the term in the parentheses parametrizes the dependence of torque on Re and the other terms characterize the influence of θ . The curve plotted using Eq. (A.25) is illustrated in Fig. A.15. Good agreement can be observed between the

correlation and simulation results. Excluding torque at $\theta = 0^\circ$ and 90° , which are both 0, the mean relative error of the correlation is 4.7% and the largest relative error is 19.9%, which appears at Reynolds number of 200 and incidence angle of 15° . The MSE is 1.1×10^{-3} .

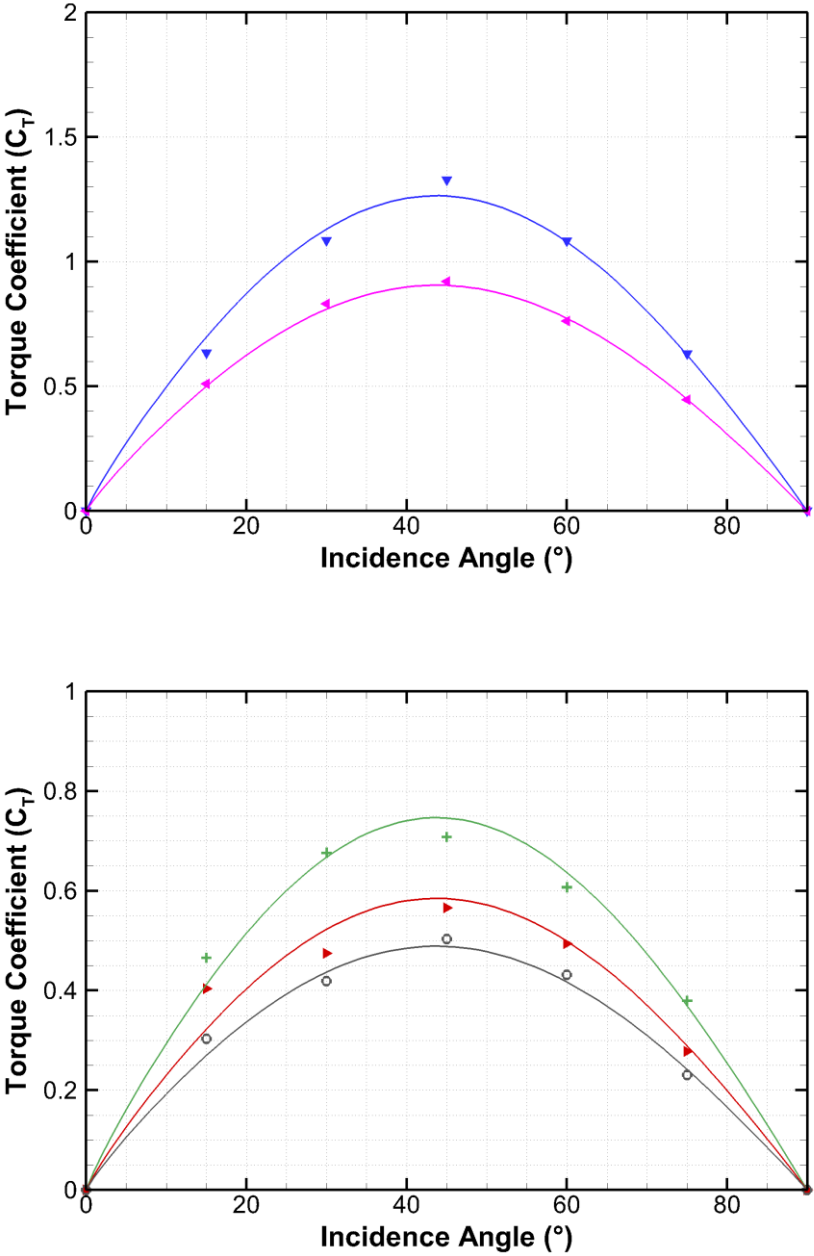


Fig. A. 15. Torque coefficient on the cylinder (▼). Simulation at Re=10; (◄) simulation at Re=50; (+) simulation at Re=100; (►) simulation at Re=200; (○) simulation at Re=300; solid line: Present correlation. (Same color represents the same Re.)

Summary and Conclusion

Fluid force data on non-spherical objects in the shape of a tablet or a low aspect ratio cylinder is not available in the literature. The current study uses direct numerical simulations to develop correlations for drag, lift, and pitching torque in the Reynolds number range between 10 to 300 at incidence angles between 0° to 90° on a cylinder with aspect ratio 1:4. An immersed boundary method is used for the simulations. It is validated by comparing results to past studies in the literature on spheres and also with a body-fitted grid. A grid independency study is used to show that 40 grid points per equivalent sphere diameter is sufficiently accurate to approximate the forces.

The flow around the cylinder is steady till $Re=200$ $\theta < 30^\circ$, after which it gets unsteady. As the inclination angle increases, large recirculation zone is formed on the leeward side of the cylinder which has a large influence on the forces acting on the object. As a result, the drag coefficient increases with incidence angle. The predicted drag coefficient is compared to the general correlation of Hölzer and Sommerfeld [1] for non-spherical objects. It is found that while the correlation compares well with the predicted drag coefficient at $\theta=0^\circ$ and 90° , it does not predict the variation of drag coefficient at intermediate angles very accurately. These differences get accentuated as the Reynolds number increases.

The lift coefficient has a symmetric distribution about the maximum value at $\theta=45^\circ$ at $Re=10$. However, as the Reynolds number increases the distribution becomes asymmetric. Pressure forces contribute positively to lift whereas shear forces reduce the lift force. The trends in the torque coefficient are quite similar to the lift coefficient reaching a maximum value near 45 degrees.

This study contributes to the literature by providing accurate drag, lift and torque coefficient data and correlations for a 1:4 aspect ratio cylinder for the full range of incidence angles up to $Re=300$. The correlations developed in this study can be used independently or provide additional force data to develop more general force correlations for non-spherical particles. These can also be used as foundational data to develop force correlations for random assemblies of this shape, which will be the focus of future studies.”

Acknowledgements

The authors would like to acknowledge computational resources and support provided by Advanced Research Computing at Virginia Tech.